Towards the Development of Sustainable Organic Thin-Film Transistors

By

Mohsin Ali

A Thesis Submitted to the University of Ottawa in Partial Fulfillment of the Requirements for the Doctor of Philosophy Degree in Chemical Engineering

Department of Chemical and Biological Engineering

University of Ottawa

© Mohsin Ali, Ottawa, Canada, 2026

All rights reserved

Abstract

Electronic devices are used for tasks ranging from health monitoring and environmental sensing to communication and consumer electronics. As demand for these devices grows, so does the volume of electronic waste (e-waste) they leave behind, most of which is exported, incinerated, or sent to landfills, where non-degradable components such as semiconductors, dielectrics, and metal electrodes can persist for years. This growing problem has motivated interest in transient electronics: devices designed to intentionally degrade after their functional lifetime. For biodegradable materials to be viable in these devices, they need to be solution-processable and capable of controlled degradation, all while maintaining the electrical performance expected of conventional electronic materials.

This thesis focuses on the development of low-voltage operation sustainable organic thin-film transistors (OTFTs) that combine strong electrical performance with reduced use of non-degradable materials and engineered, controllable degradation pathways. The first study focused on integrating a biodegradable dielectric with a biodegradable substrate to build a cytocompatible and fully disintegrable low-voltage n-type OTFT. I paired a fluorinated silicon phthalocyanine (F_{10}-SiPc) semiconductor with a bilayer poly(vinyl alcohol) (PVA) and poly(caprolactone) (PCL) dielectric deposited on a polylactic acid (PLA) substrate. This bilayer dielectric substantially lowered the threshold voltage ($V_{T)}$ compared to a conventional SiO_2 dielectric while maintaining comparable electron mobility (μ), and I showed that the complete device could disintegrate in phosphate-buffered saline solution within 20 days without producing degradation products toxic to cultured fibroblasts.

In the second study, I report that a non-biodegradable diketopyrrolopyrrole-based semiconducting polymer (DPP2T) can be blended with the biodegradable polymers PLA and PCL

to reduce the amount of active semiconductor (DPP2T) required in an OTFT by roughly 70-80%. Rather than sacrificing performance, the right PLA-PCL ratio actually improved device performance over neat DPP2T by increasing μ, lowering the V_T, and improving $I_{on/off}$, while also improving long-term stability under ambient air exposure.

In my last study, I built on this dielectric-and-substrate foundation to address a key limitation: once assembled, these devices dissolved into a single system, making it difficult to separate or recover individual materials. I designed a fully sustainable p-type OTFT using an imine-linked degradable semiconducting polymer (PDPP-TIT) paired with a PVA/UV-crosslinked-PCL bilayer dielectric on a PLA substrate, engineering each layer to respond to a different degradation trigger. This device also achieved a reduction in V_T relative to a conventional SiO_2 dielectric, and I demonstrated that the semiconductor and dielectric could be selectively dissolved under acidic conditions while the substrate degraded separately under basic conditions, leaving only recoverable gold micro/nanoparticles behind.

Finally, this work demonstrates that degradable, commercially available polymers can be systematically blended, stacked, and chemically engineered to produce OTFTs that match or exceed the performance of conventional devices, while reducing reliance on non-degradable materials and enabling controlled, multi-step degradation for environmentally responsible end-of-life electronics.

Résumé

Les dispositifs électroniques sont utilisés pour un large éventail de tâches, allant de la surveillance de la santé et de la détection environnementale à la communication et à l'électronique grand public. À mesure que la demande pour ces dispositifs augmente, le volume de déchets électroniques (déchets électroniques ou « e-waste ») qu'ils génèrent augmente également ; la plupart de ces déchets sont exportés, incinérés ou envoyés vers des sites d'enfouissement, où des composants non dégradables tels que les semi-conducteurs, les diélectriques et les électrodes métalliques peuvent persister pendant des années. Ce problème croissant a suscité un intérêt pour l'électronique transitoire : des dispositifs conçus pour se dégrader intentionnellement après leur durée de vie fonctionnelle. Pour que les matériaux biodégradables soient viables dans ces dispositifs, ils doivent être traitables en solution et capables d'une dégradation contrôlée, tout en maintenant les performances électriques attendues des matériaux électroniques conventionnels.

Cette thèse porte sur le développement de transistors à couches minces organiques (OTFT) durables, fonctionnant à basse tension, qui combinent de solides performances électriques avec une utilisation réduite de matériaux non dégradables et des voies de dégradation contrôlées et conçues à cet effet. La première étude a porté sur l'intégration d'un diélectrique biodégradable avec un substrat biodégradable afin de construire un OTFT de type n, à basse tension, cytocompatible et entièrement désintégrable. J'ai associé un semi-conducteur de phtalocyanine de silicium fluorée (F10-SiPc) à un diélectrique bicouche composé d'alcool polyvinylique (PVA) et de polycaprolactone (PCL), déposé sur un substrat d'acide polylactique (PLA). Ce diélectrique bicouche a considérablement réduit la tension de seuil par rapport à un diélectrique conventionnel de SiO2, tout en maintenant une mobilité électronique relative, et j'ai démontré que le dispositif

complet pouvait se désintégrer dans une solution saline tamponnée au phosphate en 20 jours, sans produire de sous-produits de dégradation toxiques pour des fibroblastes en culture.

Dans la deuxième étude, je rapporte qu'un polymère semi-conducteur non biodégradable à base de dicétopyrrolopyrrole (DPP2T) peut être mélangé aux polymères biodégradables PLA et PCL afin de réduire d'environ 70 à 80 % la quantité de semi-conducteur actif (DPP2T) nécessaire dans un OTFT. Plutôt que de sacrifier les performances, le bon rapport PLA-PCL a en réalité amélioré les performances du dispositif par rapport au DPP2T pur, en augmentant la mobilité, en abaissant la tension de seuil et en améliorant les rapports courant on/off, tout en améliorant également la stabilité à long terme sous exposition à l'air ambiant.

Dans ma dernière étude, je me suis appuyé sur cette base diélectrique-substrat pour répondre à une limitation majeure : une fois assemblés, ces dispositifs se dissolvaient en un seul système, rendant difficile la séparation ou la récupération des matériaux individuels. J'ai conçu un OTFT de type p entièrement durable, utilisant un polymère semi-conducteur dégradable à liaison imine (PDPP-TIT) associé à un diélectrique bicouche PVA/PCL réticulé aux UV sur un substrat de PLA, en concevant chaque couche pour qu'elle réponde à un déclencheur de dégradation différent. Ce dispositif a également permis une réduction importante de la tension de seuil par rapport à un diélectrique conventionnel de SiO2, et j'ai démontré que le semi-conducteur et le diélectrique pouvaient être sélectivement dissous en conditions acides, tandis que le substrat se dégradait séparément en conditions basiques, ne laissant derrière lui que des micro/nanoparticules d'or récupérables.

Enfin, ces travaux démontrent que des polymères dégradables et disponibles dans le commerce peuvent être systématiquement mélangés, empilés et modifiés chimiquement pour

produire des OTFT égalant ou dépassant les performances des dispositifs conventionnels, tout en réduisant la dépendance aux matériaux non dégradables et en permettant une dégradation contrôlée et en plusieurs étapes, en vue d'une électronique responsable en fin de vie sur le plan environnemental.

Acknowledgements

First off, I would like to thank my supervisor, Professor Benoit Lessard, for giving me the opportunity to learn and grow as a researcher within his group. Professor Lessard gave me the opportunity to work with him as a Ph.D. student when I was doing my Masters in Turkey. Throughout my academic journey, Professor Lessard has continuously provided me with support and helped me grow and improve my skills as a researcher. It has been a pleasure to work with the Lessard Research Group and see the group's knowledge and skills grow over the years.

I would also like to thank all of my group members from the Lessard Research Group for providing a research environment where I felt I could continuously grow and learn. I would like to give a special thank you to Dr. Joseph Manion for all the support during my research, for making cool schematic figures for all my papers, and for keeping the lab so well-maintained. I would also like to thank Raluchukwu B. Ewenike, Bahar Ronnasi, May Ourabi, Sofia G. Pascual for all their support and collaboration on projects over the years.

I would also like to thank all the collaborators and support staff that I've worked with for their knowledge and expertise. Thank you to beamline scientist Dr. Arnaud Hemmerle for always ensuring our trips to synchrotron facilities are a success. Thank you to Dr. Chang-Hyun Kim and Joonhyung Park for performing OTFT simulation analysis for my studies. Thank you to Dr. Spyridon Ntais at the University of Ottawa for performing AFM. Thank you to Dr. Simon Rondeau-Gagné at the University of Windsor for conducting GPC analysis. Thank you to Patrick Pageau for helping me build the necessary equipment during my graduate studies.

Thank you so much to my friends for everything you do for me. Thank you to Hisham Butt and Muhammad Umer Abid for being my best friends. Thank you to Saeed Sarvazizi for always

being there for me. I will miss our coffee runs and lunchtime together at CBY. I would also like to thank Mohammad Farzanullah and Shan Ali for listening to my rants about research and life. Thank you to Fooqia Khalid and Shivani Sharma, whom I met during my research visit in Finland, for making my time enjoyable. I will miss the food and cakes made by Fooqia Khalid.

Special thanks to my parents, Muhammad Ashraf and Abida Parveen, and my siblings, Ahsan Ali, Ali Hamza, and Munazza. I am endlessly grateful for all your love and support.

Table of Contents

Chapter 1: Introduction 1

1.1 Overview 1

1.1.1 The Electronic Waste Crisis: A Call for Sustainable Electronics 1

1.2 Cytocompatibility and Cytotoxicity of Organic Electronic Materials 4

1.3 Organic Thin Film Transistors Structure 6

1.3.1 OTFT Operation and Charge Transport 7

1.3.2 Electrical Characterization 9

1.4 Thin-Film Growth by Solution Deposition 11

1.4.1 Deposition Techniques 11

1.4.2 Thermodynamics and Kinetics 13

1.4.3 Effect of Deposition Parameters 16

1.5 Towards Sustainable OTFTs 18

1.5.1 Degradable Substrates: Building on a Foundation That Disappears 19

1.5.2 Degradable Dielectrics: The Interface That Controls Everything 22

1.5.3 Degradable Semiconductor 30

1.5.4 Degradable Conductors 34

1.6 OTFT Applications 37

1.7 Scope of Thesis 40

References 41

Chapter 2: Cytocompatible, Disintegrable, Low-Voltage Operation n-Type Organic Thin Film Transistors 65

2.1 Abstract 66

2.2 Introduction 66

2.3 Results and discussion 70
2.4 Conclusion 84
2.5 Experimental Section 85
2.5.1 Materials 85
2.5.2 Preparation of Self-Assembled Monolayer solution 85
2.5.3 Preparation of Substrate and Dielectric 85
2.5.4 Fabrication of TFT 86
2.5.5 Device Characterization 87
2.5.6 Thin Film Characterization 88
2.5.7 Numerical Simulation 89
2.5.8 Cytotoxicity Evaluation 90
2.6 Acknowledgements 91
2.7 Supporting Information 91
References 91
Chapter 3: Two Is Better Than One: How the Addition of Multiple Biodegradable Polymers Can Improve Organic Thin Film Transistor Performance 105
3.1 Abstract 106
3.2 Introduction 106
3.3 Results and Discussion 109
3.4 Conclusion 121
3.5 Experimentation 122
3.5.1 Materials 122
3.5.2 Preparation of DPP2T/PLA-PCL blend solution 122
3.5.3 OTFT fabrication 122
3.6 Acknowledgements 123

3.7 Supporting Information 123
3.7.1 Thin Film Characterization 123
3.7.2 OTFT Characterization 125
References 147
Chapter 4: Degradation by Design: Sequentially Degradable Organic Transistors for Sustainable Electronics 155
4.1 Abstract 156
4.2 Introduction 157
4.3 Experimentation 163
4.3.1 Materials 163
4.3.2 Gel permeation chromatography (GPC) 163
4.3.3 Preparation of the substrate and dielectric 164
4.3.4 Fabrication of OTFTs 164
4.3.5 Device characterization 165
4.3.6 Thin film characterization 165
4.4 Results And Discussion 167
4.5 Conclusion 182
4.6 Supporting Information 183
4.6.1 Device characterization 183
4.6.2 Synthesis of a degradable semiconductor: P(DPP-TIT) 191
References 192
Chapter 5: Conclusion and Recommendations for Future Work 206
5.1 Overall Conclusion 206
5.2 Recommendations for Future Work 208

List of Figures

Figure 1.1. (a) Fully disintegrable OTFT with bottom-gate-top-contact configuration. (b) Degradation of PDPP-PD-based OTFT device in cellulase buffer solution. (c) Bio-resorbable OTFT based on 5′-bis-(7-dodecyl-9H-fluoren-2-yl)-2,2′-bithiophene (DDFTTF) and other biodegradable materials. (d) ZnO-based degradable thin film transistor. 4

Figure 1.2. (a) BGBC (b) BGTC (c) TGBC (d) TGTC architecture. 7

Figure 1.3. (a) Cross-section illustration of a bottom-gate top-contact OTFT. (b) Energy-level schematic illustrating charge injection in p-type and n-type devices. 8

Figure 1.4. (a) Output curve, (b) forward and reverse transfer curves, and (c) Graph of $\sqrt{I_{SD}}$ against V_{GS} for an n-type OTFT, with a dashed tangent line used to extract μ and V_T. 9

Figure 1.5. Demonstration of various deposition methods 12

Figure 1.6. AFM images (5 x 5 μm) of CuPc thin films fabricated by drop casting, spin coating, dip coating, and spray coating. 18

Figure 1.7. A typical degradable electronic device is built up from four main classes of materials: biodegradable semiconductors, conductors, dielectrics, and substrates. 19

Figure 1.8. Chemical structures of natural and synthetic polymers used as substrates: Cellulose, Fibroin, polyethylene glycol (PEG), PLGA, PLA, PCL, and PGS.[83] 21

Figure 1.9. Impedance spectra of an ideal capacitor presented as (left) a Nyquist plot and (right) a Bode plot. 23

Figure 1.10. Chemical structures of both natural and synthetic polymers, highlighting the specific bonding sites susceptible to hydrolysis or oxidation. The degradation pathways for these materials, including the enzymatic breakdown of PVA and acid-catalyzed ester hydrolysis, as reproduced from Hosseini et al.[106] 30

Figure 1.11. Conjugated polymers (dark blue) are used in semiconductors and conductors to form channels for electronic conduction inside the matrix (light blue). In Type I materials, only the matrix can break down fully into small molecular building blocks, while the nondegradable active components stay intact. Only the matrix can break down completely. However, type II materials' matrix and active ingredients can both completely break down into monomers or oligomers, suggesting that these entirely biodegradable materials may be recyclable. 33

Figure 1.12. (a) The chemical structure of a fully degradable semiconductor, named diketopyrrolopyrrole-p-phenylenediamine (DPP-PPD) is based on imine bonds, which are acid-

labile. (b) The chemical structure of the elastomer is based on PCL, a widely used biodegradable material. (c) An illustration of the z-phase segregation in the thin-film morphology that results from blending the semiconductor and elastomer, forming a distinct layered structure.[18] 34
Figure 1.13. (a) Schematic representation of a P3HT-based OTFT for ammonia gas sensing.[164] (b) Flexible OTFT temperature sensor array with an integrated mini heater.[170] 39
Figure 2.1. (a) Chemical structures of semiconductor, substrate, and dielectric materials: F10-SiPc, PLA, PVA, and UV-PCL. (b) Schematic illustration of disintegrable BGTC transistor device. (c) Digital photo of PLA substrate with an array of OTFTs. 71
Figure 2.2. (a) Water contact angle measurements of gold film coated on PLA substrate as bottom gate electrode with and without thiol treatment. (b) The average surface roughness of the gate electrode surface measured with profilometer. (c) Optical microscopic images of gate electrode film after annealing at different temperatures. 74
Figure 2.3. Contact angle measurements for neat PVA and PVA/UV-PCL. 75
Figure 2.4. Output curves of (a) SiO_2/OTS and (b) PVA/UV-PCL, Transfer curves of (c) OTFT on OTS treated SiO_2 and (d) on PVA/UV-PCL. The transfer characteristics curve versus V_{GS} were obtained for V_{SD} = 50 V and V_{SD} = 3 V, respectively. 1D XRD pattern for F_{10}-SiPc on (e) OTS treated SiO_2 and (f) on PVA-UV-PCL dielectric. 79
Figure 2.5. Comparison between experimentally measured and numerically simulated transfer curves of the OTFT based on (a) SiO_2/OTS and (b) PVA/UV-PCL dielectric. Electron density (n) distribution in log scale showing the (c) channel formation and (d) pinch-off achieved by a low voltage in the OTFT based on the PVA/UV-PCL dielectric. 81
Figure 2.6. Photographs of OTFTs taken at different intervals after being submerged in a 1M PBS (pH ~10) for accelerated degradation. 83
Figure 2.7. (a) Metabolic activity of NIH 3T3 mouse fibroblasts following a 24 hour incubation with degradation product extracts resulting from the incubation of OTFTs in culture medium for 7 days compared to incubation with fresh medium free of the degradation products, and (b-c) representative fluorescence images of the cells cultured with (b) and without (c) the degradation products and incubated with Calcein-AM to label live cells (green fluorescence) and Ethidium homodimer-1 to label dead cells (red fluorescence). 84

Figure 3.1. (a) Chemical structure of the conjugated polymer (DPP2T), biodegradable polymer PLA and PCL. (b) Schematic illustration of the fabrication process for DPP2T/PLA-PCL blend films and integration into an OTFT. 110
Figure 3.2. Transfer curves (V_{SD} = -50) of (a) neat DPP2T and (b) a DPP2T/PLA-PCL blend (dashed lines, square root of drain current). (c) The mobility and (d) threshold voltage of a FET device at different ratios of PLA and PCL with the same DPP2T content. 113
Figure 3.3. XRD spectra (a) and (b) normalized UV-vis spectra for neat DPP2T and blend thin films with varying PLA-PCL content while keeping the DPP2T content the same. (c) Raman spectra of neat DPP2T and DPP2T blends with different PLA-PCL ratios and the same DPP2T content. 115
Figure 3.4. (a-f) AFM topographic images of thin films of DPP2T:PLA-PCL (30:70) with varied PLA-PCL compositions (g-l), Raman maps (19 x 19 μm), and (m-r) distribution histograms of the same films. 121
Figure S3.1. Output (left) and corresponding transfer (right) curves of neat DPP2T dissolved in chloroform..... 126
Figure S3.2. Output (left) and corresponding transfer (right) curves of neat DPP2T dissolved in dichloromethane. 127
Figure S3.3. Output (left) and corresponding transfer (right) curves of DPP2T/PLA-PCL blend with varied DPP2T and PLA-PCL (40-60 % according to the matrix ratio) content, with DPP2T dissolved in chloroform. 128
Figure S3.4. Output (left) and corresponding transfer (right) curves of DPP2T/PLA-PCL blend with varied DPP2T and PLA-PCL (80-20 % according to the matrix ratio) content, with DPP2T dissolved in chloroform. 129
Figure S3.5. Output (left) and corresponding transfer (right) curves of DPP2T/PLA-PCL blend with varied DPP2T and PLA-PCL (40-60 % according to the matrix ratio) content, with DPP2T dissolved in dichloromethane. 130
Figure S3.6. Output (left) and corresponding transfer (right) curves of DPP2T/PLA-PCL blend with varied DPP2T and PLA-PCL (80-20 % according to the matrix ratio) content, with DPP2T dissolved in dichloromethane. 131
Figure S3.7. Output (left) and transfer (right) curves for neat DPP2T (2 mg/ml) dissolved in chlorobenzene. 132

Figure S3.8. Output (left) and transfer (right) characteristics curves of varied DPP2T blend with neat PLA. 133
Figure S3.9. Output (left) and transfer (right) characteristics curves of varied DPP2T blend with neat PCL..... 134
Figure S3.10. Output (left) and transfer (right) characteristics curves of varied DPP2T/PLA-PCL blend with varied DPP2T and PLA-PCL (20-80 % according to the matrix ratio) content. 135
Figure S3.11. Output (left) and transfer (right) characteristics curves of varied DPP2T/PLA-PCL blend with varied DPP2T and PLA-PCL (40-60 % according to the matrix ratio) content. 136
Figure S3.12. Output (left) and transfer (right) characteristics curves of varied DPP2T/PLA-PCL blend with varied DPP2T and PLA-PCL (60-40 % according to the matrix ratio) content. 137
Figure S3.13. Output (left) and transfer (right) characteristics curves of varied DPP2T/PLA-PCL blend with varied DPP2T and PLA-PCL (80-20 % according to the matrix ratio) content. 138
Figure S3.14. a) and b) Output and corresponding c) and d) transfer curves of OTFTs made with neat DPP2T (a, c) and optimal blend, 30:56-14 (b, d) after 7 months of exposure to air. 144
Figure S3.15. AFM image of neat DPP2T film. 145
Figure S3.16. Raman spectra of neat DPP2T and DPP2T blends with different PLA-PCL ratios and same DPP2T content. 145
Figure 4.1. a) Chemical structures of biodegradable polymers: polylactic acid (PLA), polyvinyl alcohol (PVA), benzodioxinone-terminated poly caprolactone (UV-PCL), and poly diketopyrrolopyrrole-thiophene-imine-thiophene P(DPP-TIT). b) Schematic illustration of the sequential degradation of an OTFT device. All elements in this figure were developed using ChemDraw and Blender. 162
Figure 4.2. Output curves of (a) SiO2/OTS and (b) PVA/UV-PCL, and characteristic transfer curves of (c) OTFTs on OTS-treated SiO2 and (d) on PVA/UV-PCL. The transfer curves versus VGS were acquired at VDS = -50 V and VDS = -5 V, respectively. Transfer curves and leakage current are plotted under identical bias conditions for four times for a representative device in the SI (**Figure S4.3).** 171
Figure 4.3. GIWAXS scattering patterns of DPP-imine conjugated polymer thin films deposited on (a) the bilayer dielectric (PVA/UV-PCL) and (b) on SiO_2/OTS 175
Figure 4.4. Raman spectra (a) and maps (19 x 19 μm2) (b-c) of degradable P(DPP-TIT) semiconductor on bilayer dielectric (PVA/UV-PCL) and OTS-treated SiO_2. 20 × 20 μm AFM

topography images of thin films of P(DPP-TIT) deposited on (d) the degradable polymer dielectric and (e) OTS-treated SiO_2. 177
Figure 4.5. a) UV-vis spectra of the $\lambda_{0\text{-}1}$-based normalized absorbance of P(DPP-TIT) thin films on quartz substrates upon submersion in aqueous 1M HCl solution at selected time intervals. b) Line plot of UV-Vis spectra quantifying the decrease in $\lambda_{0\text{-}1}$ over a period of one hour (60 minutes). 179
Figure 4.6. (a) Raman spectrum of the degradable OTFT device at different stages of degradation. (b-d) Photos of OTFTs before the immersion in 1 M HCl, after immersion in 1 M HCl, and after the immersion in basic buffer solution (pH ~ 10), respectively. (e-g) Free-standing images of OTFT before the immersion in 1 M HCl, after immersion in 1 M HCl, and after the immersion in basic buffer solution, respectively. 181
Figure S4.1. High-temperature gel permeation chromatogram of P(DPP-TIT) recorded in 1,2,4-trichlorobenzene at 180 °C. Molecular weight measured against polystyrene standards. 185
Figure S4.2. Transfer curves (a-d) of a representative device run under identical bias stress (V_{GS}=-5) 186
Figure S4.3. Transfer curves and leakage current are plotted under identical bias conditions for four times for a representative device. 187
Figure S4.4. Experimental and theoretically reconstructed transfer curves for (a) non-degradable and (b) degradable TFT. (c) Values of N_{int} estimated in (a) and (b). 188
Figure S4.5. Simulation results visualizing the effects of N_{int} on transfer characteristics. N_{int} is the only variable between these seven curves. All the other materials parameters were kept identical to those extracted for the degradable TFT in **Figure S4.4**. 188
Figure S4.6. Corresponding azimuthally integrated diffraction profiles of P(DPP-TIT) on PVA/UV-PCL and SiO_2/OTS 189
Figure S4.7. GIWAXS pattern of PVA/UV-PCL dielectric on PLA substrate 189
Figure S4.8. χ-cuts of the (100) diffraction peak extracted from the GIWAXS patterns of P(DPP-TIT) thin films deposited on SiO_2 and on the polymer substrate. The integrated (100) intensity was normalized by film thickness 190
Figure S4.9. 1D line profiles of P(DPP-TIT) in a) Q_z out-of-plane vector direction and b) Q_{xy} in-plane vector direction. Data were processed with a standard Savitzky-Golay filter for clarity.. 191

Figure 5.1. Proposed future research directions for addressing the current on/off ratio and hysteresis trade-offs observed in the PVA/PCL bilayer dielectric devices. 210
Figure 5.2. Proposed complementary inverter circuit combining the n-type OTFT developed in Chapter 2 with the p-type OTFT developed in Chapter 4, as a first step toward evaluating circuit-level performance and degradation. 210
Figure 5.3. Future expansion of degradation analyses from laboratory conditions to real-world environments (soil, compost, freshwater, seawater, and biological systems), with degradation kinetics, degradation products, and environmental impact evaluated across each. 211
Figure 5.4. (a) Custom-built gas-sensing setup used to evaluate the sensing performance of the OTFTs under controlled analyte exposure.[12] (b) Preliminary sensing results from OTFTs under ammonia exposure fabricated using P(DPP-TIT) semiconductor and SiO_2 dielectric. 212

List of Tables

Table 2.1. Average dielectric properties of PVA/UV-PCL at 10 Hz..... 76
Table 2.2. Electrical data for OTFTs fabricated with SiO2/OTS and biodegradable bilayer PVA/UV-PCL dielectrics..... 80
Table S2.1. Key material parameters used as input to the numerical simulation..... 91
Table 3.1. Summary of the field effect properties of DPP2T/PLA-PCL semiconductor blends in OTFTs. 114
Table S3.1. Performance parameters computed from blend films prepared by dissolving DPP2T in chlorobenzene, chloroform and dichloromethane, and PLA-PCL in chloroform (40-60 % according to the matrix ratio) in chloroform..... 139
Table S3.2. Performance parameters computed from blend films prepared by dissolving DPP2T in chlorobenzene, chloroform and dichloromethane, and PLA-PCL in chloroform (80-20 % according to the matrix ratio) in chloroform..... 141
Table S3.3. Summary of averaged μ values for DPP2T/PLA-PCL blends with varied DPP2T (dissolved in chlorobenzene) and PLA-PCL (dissolved in chloroform)..... 142
Table S3.4. Thickness, density, and mass of material used in device. 143
Table S3.5. Trap density of the semiconducting blend films 143
Table S3.6. Summary of the OTFT properties of devices made with neat DPP2T and optimal blend (30:56-14) after 7 months of sitting in air. 144

Table S3.7. Summary of the percentage crystallinity of the semiconducting blends..... 146
Table 4.1. Dielectric properties of bilayer dielectric (PVA/UV-PCL) at 10 Hz 168
Table 4.2. Summary of the field effect properties of the degradable and non-degradable OTFT 172
Table 4.3. Stacking parameters and crystallization data of P(DPP-TIT) on OTS-SiO_2 and degradable polymer substrates. Crystal Coherence Length (CCL) was calculated using the Scherrer equation with a correction factor (K) of 0.9. 175
Table S4.1. Synthesis of P (DPP-TIT) polymer and its physical and optoelectronic properties 185
Table S4.2. Summary of the field effect properties of the representative device, swept consecutively four times 186

List of Abbreviations

A: single fitting parameter that combines all temperature-independent variables

Aa: area of amorphous region

Ac: area of crystalline region

AFM: atomic force microscope

Ag: silver

AL_2O_3: aluminium oxide

Au: gold

BGBC: bottom gate bottom contact

BGTC: bottom gate top contact

BioMEMS: biomedical microelectromechanical system

C: capacitance

C: concentration present during growth

C_∞: equilibrium solution concentration

CCL*:* crystal coherence length

C_i: capacitance density

CNC: cellulose nanocrystals

Cr: chromium

CTE: coefficient of thermal expansion

CuPc: copper phthalocyanine

CV: cyclic voltammetry

D-A: donor-acceptor

DCPU: dopant-free conductive polyurethane

DDFTTF: 5′-bis-(7-dodecyl-9*H*-fluoren-2-yl)-2,2′-bithiophene

DI: deionized

DMEM: Dulbecco's modified Eagle's medium

DMPA: dimethylolpropionic acid

D_n: electron diffusion coefficient

DOS: density of states

D_p: hole diffusion coefficient

DPP: diketopyrrolopyrroles

DPP2T: poly[[2,3,5,6-tetrahydro-2,5-bis(2-octyldodecyl)-3,6-dioxopyrrolo[3,4-c]pyrrole-1,4-diyl]-2,5-thiophenediylthieno[3,2-b]thiophene-2,5-diyl-2,5-thiophenediyl]

E: energy

E_c: energy of the conduction band

$\vec{E}$: electric field vector,

ECCM: effective conjugation coordinate model

EIS: electrochemical impedance spectroscopy

E-waste: electronic waste

F: farads

f: frequency

F_{10}-SiPc: bis(pentafluorophenoxy) silicon phthalocyanine

FBS: fetal bovine serum

FDA: Food and Drug Administration

$Fe(ClO_4)_3$: ferric perchlorate

Fe: iron

$FeCl_3$: ferric chloride

FWHM: full width half maximum

GIWAXS: grazing-incidence wide-angle X-ray scattering

g_m: transconductance

GPC: gel permeation chromatography

H: hysteresis

H_A: total density of acceptor-like trap states

HDFs: human dermal fibroblasts

high-k: dielectric constant > 3.9

HOMO: highest occupied molecular orbital

I_{GS}: source-gate current

$I_{on/off}$: on/off current ratio

IS: Impedance Spectroscopy

I_{SD}: source-drain current

ITO: indium tin oxide

$\overrightarrow{J_n}$: electron current density vector

$\overrightarrow{J_p}$: hole current density vector

k: dielectric constant (relative permittivity)

k_B: Boltzmann constant

L: channel length (distance between the source and drain electrodes)

low-k: dielectric constant < 3.9

LUMO: lowest unoccupied molecular orbital

Mg: magnesium

MIM: metal-insulator-metal

MMT: million metric tonnes

Mn: number-average molecular weight

Mo: molybdenum

MOSFET: metal-oxide semiconductor field-effect transistor

MPcs: metal phthalocyanines

MTT assay: (3-(4,5-dimethylthiazol-2-yl)-2,5-diphenyltetrazolium bromide)

Mw: weight-average molecular weight

n: electron concentration

NaOH: sodium hydroxide

N_{int}: charge density at the semiconductor/insulator interface

NIR: near-infrared

NMR: nuclear magnetic resonance

OLED: organic light-emitting diode

OPV: organic photovoltaic

OSCs: organic semiconductors

OTFT: organic thin film transistor

OTS: octyltrichlorosilane

P(DPP-TIT): poly(diketopyrrolopyrrole-thiophene-imine-thiophene)

P(MMA-co-DMAEMA): dimethyl aminoethyl methacrylate copolymers

p: hole concentration

P3HT: poly-3-hexylthiophene

P3TMA: poly(3-thiophene methyl acetate)

PANI: polyaniline

PBS: phosphate buffer saline (Chapter 2)

PBS: polybutylene succinate (Chapter 1)

Pc: phthalocyanines

PCBs: polychlorinated biphenyls

PCL: poly(caprolactone)

PDI: polydispersity index

PDPP-PD: poly(diketopyrrolopyrrole-phenylenediamine)

PEDOT: poly(3,4-ethylenedioxythiophene)

PEG: polyethylene glycol

PEU: poly(ester urea)

PGS: poly(glycerol sebacate)

PHAs: polyhydroxyalkanoates

PHBv: poly(3-hydroxybutyrate-*co*-3-hydroxyvalerate)

PLA: poly(lactic acid)

PLGA: poly(lactic-co-glycolic acid)

PMMA: polymethyl methacrylate

POC: poly(1,8-octanediol-co-citrate)

PPC: polypropylene carbonate

PPy: polypyrrole

PS: polystyrene

PSS: poly(styrenesulfonate)

PTFE: polytetrafluoroethylene

PVA: poly(vinyl alcohol)

PVD: physical vapor deposition

PVP: polyvinyl phenol

q: elementary charge,

R_2-SiPc: axially substituted silicon phthalocyanines

RFID: radio frequency identification

RH: relative humidity

RMS: root mean square

SAM: self-assembled monolayer

SEC: size exclusion chromatography

SiO_2: silicon dioxide

SWCNT: Single-walled carbon nanotubes

t: thickness of the dielectric layer

T_A: characteristic temperature dictating the energetic width of acceptor-like traps

Tan_{φ}: tangent loss

T_b: boiling point of solvent at atmospheric pressure

TCB: trichlorobenzene

TDI: toluene-2, 4-diisocyanate

TFSI: bis(trifluoromethylsulfonyl)imide

T_g: glass transition temperature

TGBC: top gate bottom contact

TGTC: top gate top contact

TiO_2: titanium dioxide

TIP-CuPc: tetrakis-(isopropoxy-carbonyl)-CuPc

T_m: melting point

TPCL: toluene diisocyanate terminated polycaprolactone

TPU: thermoplastic polyurethane

T_s: substrate temperature

UV-PCL: Benzodioxinone terminated polycaprolactone

V_{GS}: gate-source voltage

V_m: molar volume of solvent

V_{SD}: source-drain voltage

V_T: threshold voltage

W: tungsten

W: channel width

XRD: x-ray diffraction

Z: impedance

Z': real portion of the impedance

Z": imaginary portion of the impedance

Zn: zinc

ZnO: zinc oxide

γ_{SD}: dispersive component of the surface energy

γ_{SP}: polar component of the surface energy

ΔS_{vap}: entropy of vaporization of solvent

$\Delta\mu$: difference in chemical potential

ε_s: semiconductor permittivity

μ: mobility

μ_c: crystalline phase

μ_h, μp: hole mobility

μ_l: Liquid phase

μ_n: electron mobility

ν_c: coating speed

ν_e: evaporation rate

ρ: space charge density

φ: electrostatic potential (Chapter 2)

φ: phase angle (Chapter 1)

ω: angular frequency

Chapter 1: Introduction

1.1 Overview

1.1.1 The Electronic Waste Crisis: A Call for Sustainable Electronics

The growing demand for cutting-edge technologies and short-term consumer electronics has resulted in a rapidly expanding global surplus of electronic waste (e-waste). The yearly disposal of personal computers, cellphones, tablets, and other devices has increased, prompting considerable environmental concerns.[1] Consequently, there is an urgent need to develop energy-efficient and environmentally sustainable electronics.[2] Electronic devices present significant recycling challenges owing to their intricate and varied compositions. The sustainable recycling of e-waste is labor-intensive and often requires expensive equipment to prevent environmental contamination by harmful pollutants. Nowadays, less than 20% of e-waste is sufficiently recycled,[3] with the bulk disposed of in landfills, posing hazards of toxic leaks, incineration that emits hazardous fumes, or being exported to underdeveloped nations with lenient environmental rules, where laborers encounter high exposure risks. Improper handling of e-waste results in the release or leaching of hazardous compounds such as lead, cadmium, and polychlorinated biphenyls (PCBs) into the environment, with foreseeable detrimental effects on human health and the ecosystem.[4] The difficulty of handling e-waste can be partly ascribed to the insufficient advancement in the development of materials utilized in electronics. Recently, initiatives have been undertaken to address the global e-waste issues, including the revision of outdated e-waste management regulations and the minimization of hazardous material usage.[4,5] Transient or "green" electronics, a new class of technology intended to "disappear" after use or disposal have been introduced as a solution to these problems.[6–13] Transient electronics not only benefit the

environment but also open up new applications. For example, they can be used to make secure electronics that can completely disintegrate in a controlled manner and become untraceable, or they can be used to make implantable medical devices that can absorb into the body without the need for follow-up surgery.[12]

In the pursuit of achieving these objectives, silicon-based transient electronics have recently been fabricated,[6,7] representing the ability to degrade under mild alkaline conditions. However, devices fabricated with inorganic materials like silicon are mechanically brittle and require high-vacuum, high-temperature, and generally expensive fabrication processes. In contrast, organic materials, composed of abundant carbon-based components, can be synthesized and processed at lower temperatures. More importantly, they hold promise as environmentally friendly alternatives for electronic applications.[8] Transient or biodegradable electronic devices are attainable through the utilization of organic electronic components. These active materials can be fabricated by solution-based methods, such as roll-to-roll printing.[14] Various forms of organic electronics exist, with the most widely used being organic light-emitting diodes (OLEDs), organic photovoltaics (OPVs), and organic thin film transistors (OTFTs). Each of these devices presents distinct architectures and applications.[15] For instance, OTFTs are utilized in disposable packaging, biological and chemical sensing,[14,16] health monitors,[17] stretchable devices,[18] and electronic skin.[19] In numerous cases, these sensors are engineered for one-time usage, hence amplifying their environmental impact.[20–22] For instance, biodegradable electronic devices have potential advantages in optoelectronic, electronic, and sensing systems since they are constructed of materials that break down into safe and biocompatible byproducts.[23]

Transient and degradable electronics devices engineered to physically disintegrate, dissolve, or biodegrade after their intended functional lifetime have emerged as a compelling

strategy to mitigate e-waste. This thesis investigates the design, fabrication, and characterization of OTFTs built largely from biodegradable and biocompatible materials, with the aim of advancing the scientific foundation for truly sustainable electronic systems. Recently, researchers have developed completely biocompatible and degradable OTFTs using a degradable substrate (cellulose), dielectric aluminum oxide (Al_2O_3), and poly(diketopyrrolopyrrole-phenylenediamine) (PDPP-PD) semiconducting materials. For instance, Lei et al.[24] reported a degradable and biocompatible semiconducting polymer and a totally disintegrable OTFT device (**Figure 1.1a**). They demonstrated that a fully decomposable conjugated polymer with high charge-carrier mobility (μ) can be synthesized using reversible imine chemistry. This polymer provides solution processability and electrical performance comparable to those of traditional conjugated polymers. **Figure 1.1b** shows the full degradation of the device within 30 days in cellulase buffer solution (pH 4.6). Bettinger and Bao[9] described in detail the design, synthesis, and testing of degradable OTFTs that are water-stable and composed of biocompatible and biodegradable polymers **(Figure 1.1c).** The development of high-performance dielectric and semiconducting materials with biocompatibility and biodegradability, which yield non-toxic and ecologically acceptable monomers, may be prompted by the possible applications of resorbable organic electronics. Kettle et al.[25] reported fully degradable OTFT fabricated using zinc oxide (ZnO) as semiconducting material, Poly(3-hydroxybutyrate-*co*-3-hydroxyvalerate) (PHBv) as substrate, Molybdenum (Mo) as biodegradable electrodes and Al_2O_3 as dielectric material **(Figure 1.1d).** ZnO is very useful since it hydrolyses and yields benign and non-toxic byproducts. ZnO is distinguished by its exceptional transparency, chemical stability, and high mobility. These properties have been successfully applied in memory devices, TFTs, and LEDs in the past.

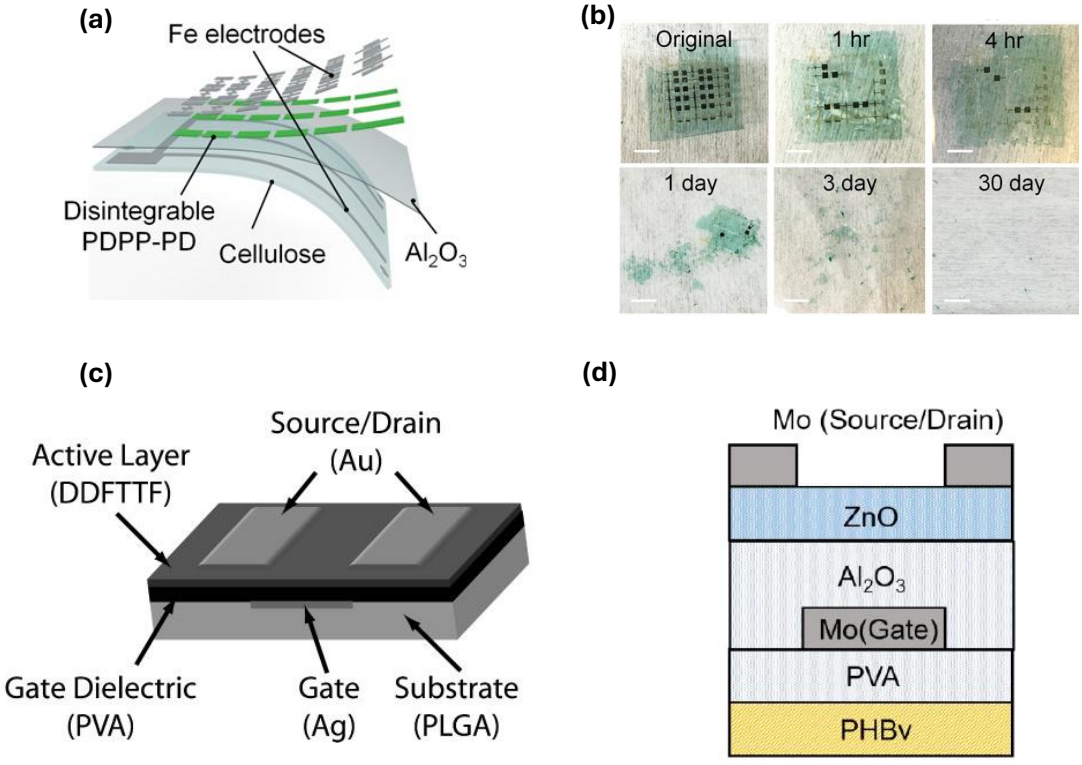


Figure 1.1. (a) Fully disintegrable OTFT with bottom-gate-top-contact configuration. (b) Degradation of PDPP-PD-based OTFT device in cellulase buffer solution. (c) Bio-resorbable OTFT based on 5′-bis-(7-dodecyl-9H-fluoren-2-yl)-2,2′-bithiophene (DDFTTF) and other biodegradable materials. (d) ZnO-based degradable thin film transistor.

1.2 Cytocompatibility and Cytotoxicity of Organic Electronic Materials

As degradable OTFTs move closer to biomedical applications, including implantable sensors, transient electronics, and wearable health monitors that contact biological tissue, the biological safety of their constituent materials becomes an equally critical design criterion

alongside electrical performance. In this context, cytotoxicity, defined as the degree to which a material or its degradation products cause damage or death to living cells, must be rigorously assessed before any organic electronic device can be considered suitable for use in or near biological environments.[26]

Cytotoxicity evaluation serves two distinct but complementary purposes in the context of degradable organic electronics. First, it assesses whether the intact material, in its processed thin-film form, elicits any harmful cellular response upon direct or indirect contact. Second, and equally importantly in degradable systems, it evaluates whether the products generated upon material breakdown, oligomers, monomers, solvents, or inorganic residues, are themselves biologically safe.[27] Since degradable OTFTs are specifically designed to disintegrate under physiological or environmental conditions, the toxicological profile of their degradation products is as important as that of the pristine material.

Cytotoxicity is most commonly assessed using standardized in vitro cell viability assays, in which a selected cell line, typically one relevant to the intended application, such as human dermal fibroblasts (HDFs) for skin-contact devices, or neuroblastoma cells for neural implant applications, is exposed to either the material directly or to an extract of the material incubated in cell culture medium.[28] The most widely employed quantitative assays include the MTT assay (3-(4,5-dimethylthiazol-2-yl)-2,5-diphenyltetrazolium bromide), which measures mitochondrial metabolic activity as a surrogate for cell viability, and the alamarBlue (resazurin reduction) assay, which quantifies cellular metabolic activity fluorometrically and is particularly well-suited to real-time, non-destructive monitoring.[29,30] Live/dead fluorescence staining, in which membrane-impermeant dyes (e.g. propidium iodide) selectively label compromised cells while membrane-permeant dyes (e.g. calcein-AM) label viable cells, provides complementary morphological

information on cell health and is frequently used alongside metabolic assays to give a more complete picture of cytotoxic response.[28–30]

In the organic electronics literature, cytotoxicity evaluation has been reported for a growing number of degradable and biocompatible material systems. Irimia-Vladu et al. demonstrated that OFETs fabricated with natural, biocompatible materials, including adenine, guanine, and glucose as active layers, elicited no adverse cellular response, thereby establishing an early benchmark for biologically benign organic semiconductors.[31] These studies collectively highlight that cytocompatibility is achievable in high-performing organic semiconductor systems, provided that material selection, processing solvents, and degradation chemistry are all considered within an integrated biocompatibility design framework.

1.3 Organic Thin Film Transistors Structure

The architecture of an OTFT is defined by the arrangement of its components in layers. Devices can be fabricated with either a top gate top contact (TGTC) or a top gate bottom contact (TGBC) arrangement, with the primary difference being the placement of the source-drain electrodes, as depicted in **Figure 1.2c-d**. Alternative designs comprise bottom gate bottom contact (BGBC) and bottom gate top contact (BGTC), as seen in **Figure 1.2a-b.** The BGTC structure is the most common configuration utilized in our laboratory.

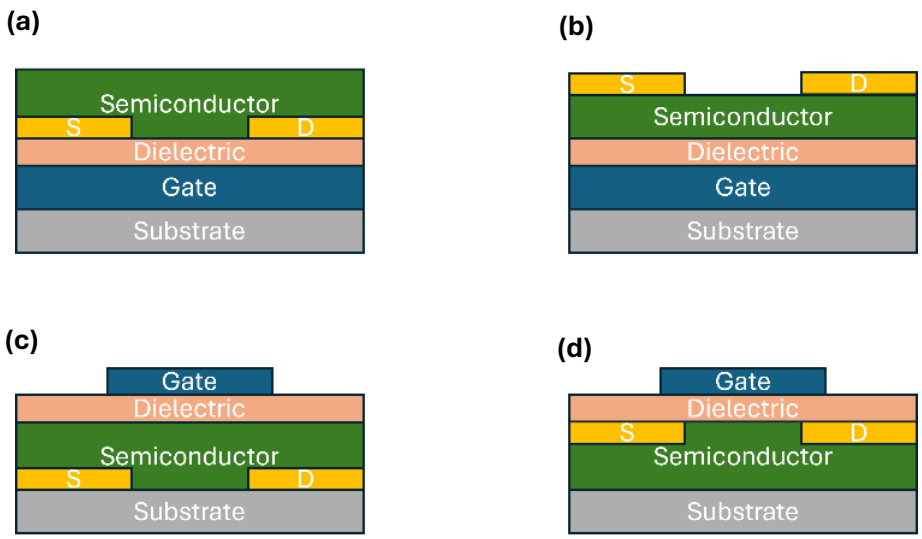


Figure 1.2. (a) BGBC (b) BGTC (c) TGBC (d) TGTC architecture.

1.3.1 OTFT Operation and Charge Transport

OTFTs belong to a class of three-terminal devices built from a gate electrode, an insulating dielectric, an organic semiconducting layer, and a pair of source and drain electrodes (**Figure 1.3**a). In operation, voltage is applied at the gate and drain while the source is held at ground, so the resulting source-drain current (I_{SD}) depends on the gate voltage (V_{GS}) applied across the dielectric. At low bias, almost no current passes through the semiconductor channel, and the device is in its off state. Once the bias exceeds a threshold voltage (V_T), charge accumulates at the dielectric-semiconductor interface and forms a conducting channel, allowing current to flow between source and drain. This state is considered to be the on state.

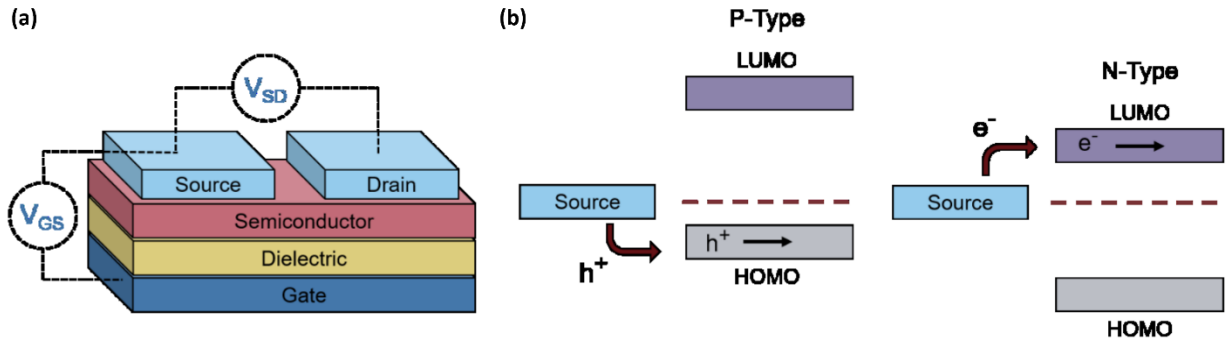


Figure 1.3. (a) Cross-section illustration of a bottom-gate top-contact OTFT. (b) Energy-level schematic illustrating charge injection in p-type and n-type devices.

Depending on the semiconductor and electrode materials chosen, OTFTs can behave as p-type, n-type, or ambipolar devices. In p-type operation, a negative bias pushes holes (positive charge carriers) from the source into the semiconductor, forming a channel that carries current from source to drain. N-type operation works the opposite way, using a positive bias to move electrons between the two electrodes. For charge injection to occur efficiently, the electrode material's work function needs to align well with either the semiconductor's highest occupied molecular orbital (HOMO) level (for p-type) or its lowest unoccupied molecular orbital (LUMO) level (for n-type) (**Figure 1.3b**). Ambipolar devices show a mix of both p- and n-type behavior, but usually one dominates and gives better device performance. Generally, p-type organic semiconductors outperform n-type ones in mobility and stability, since n-type materials tend to be air-sensitive and poorly soluble. N-type OTFTs are particularly difficult to fabricate because applying a positive voltage generates radical anions[32,33] that react readily with water and oxygen, which interferes with charge transport and requires both fabrication and operation in an inert atmosphere, limiting their practical use.[34,35]

1.3.2 Electrical Characterization

To electrically characterize these devices, researchers sweep either the source-drain voltage (V_{SD}) or the gate voltage (V_{GS}) while recording I_{SD}, producing an output curve (**Figure 1.4a**) or a transfer curve (**Figure 1.4b**), respectively. Output curves show how I_{SD} changes with V_{SD} at discrete V_{GS} values, while transfer curves display how I_{SD} changes with V_{GS} at a constant V_{SD}, measured in either the linear or saturation regime; sweeping forward and backward also reveals hysteresis. When V_{SD} is small, charge carriers are uniformly distributed along the channel, and the current rises linearly, following Ohm's law; this is the linear regime. Pushing V_{SD} higher eventually leads to the saturation regime, where current becomes independent of V_{SD}.

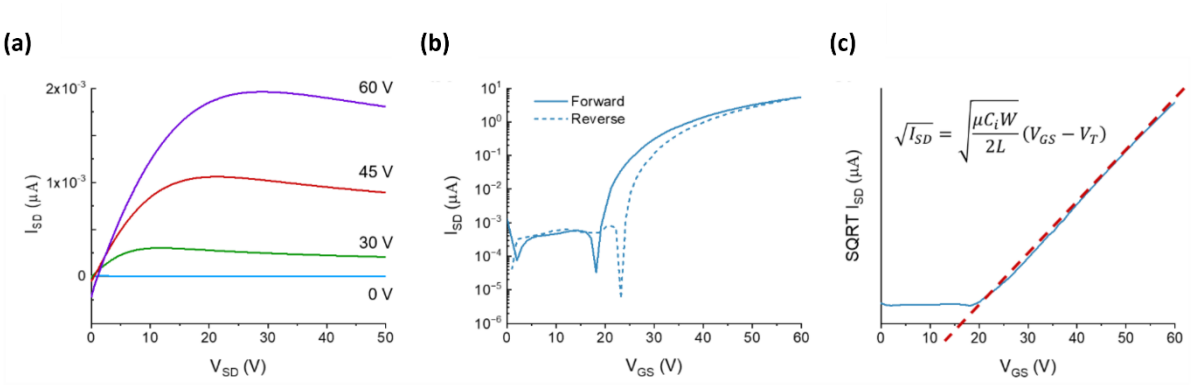


Figure 1.4. (a) Output curve, (b) forward and reverse transfer curves, and (c) Graph of $\sqrt{I_{SD}}$ against V_{GS} for an n-type OTFT, with a dashed tangent line used to extract μ and V_T.

Device performance is typically summarized using field-effect mobility (μ), V_T, and the on/off current ratio ($I_{on/off}$). Mobility reflects how quickly charge moves through the semiconducting channel, and is conventionally calculated using the metal-oxide semiconductor field-effect transistor (MOSFET) model, even though the underlying charge-transport physics differs between the two device types.[36–38] Standard MOSFETs generate charge carriers by inverting the conductivity of doped silicon at the dielectric interface, whereas OTFTs rely on intrinsic

semiconductors that contact the electrodes directly, with carriers building up at that interface.[36–38] Mobility can be extracted from the transfer curve in either the saturation or linear regime using **Equations 1.1** and **1.2.** In these equations, W and L represent the channel width and length, and C_i is the capacitance density, determined from the dielectric layer's thickness and dielectric constant. In the saturation regime specifically, taking the square root of **Equation 1.1** produces a linear relationship between $\sqrt{I_{SD}}$ and V_{GS}; plotting this lets you extract μ and V_T from the slope and x-intercept of a tangent line fit over the measured V_{GS} range (**Figure 1.4c**).

$$I_{SD,saturation} = \frac{W\mu C_i}{2L}(V_{GS} - V_T)^2 \tag{1.1}$$

$$I_{SD,linear} = \frac{W\mu C_i}{L}\left(V_{GS} - V_T)V_{SD} - \frac{{V_{SD}}^2}{2}\right) \tag{1.2}$$

V_T of an OTFT is the V_{GS} at which the device switches on and current begins flowing between source and drain. Its value is heavily influenced by the choice of semiconductor and dielectric, as dielectrics with higher capacitance allow the device to switch on at lower V_{GS}, lowering V_T. Organic devices also tend to show V_T drifting over time; this bias-stress effect appears as a positive shift in V_T and shows up as hysteresis between forward and reverse transfer sweeps (**Figure 1.4b**).[36–38] This drift is often caused by charge traps at the dielectric-semiconductor interface, which arise from impurities, defects, and grain boundaries within the semiconducting film, and these traps have a strong effect on V_T.[35,39,40] Finally, $I_{on/off}$ is defined as the ratio of measured current in the on and off states at a given V_{GS} and should be as high as possible for efficient switching behaviour.[36–38] High performing OTFT operation is characterized by a high μ and a V_T close to 0 V, typically observed in highly-ordered low-defect crystalline films which promote efficient charge transport pathways between source-drain electrodes.[37] This means μ, V_T,

and $I_{on/off}$ are not determined solely by material choice and device architecture, but also by how the semiconducting film forms and how its molecules are arranged.

1.4 Thin-Film Growth by Solution Deposition

1.4.1 Deposition Techniques

Substrate, dielectric, and semiconducting materials can be solution-deposited by first dissolving the material in an organic solvent, then depositing using one of four principal approaches: drop casting, spin coating, printing, or meniscus-guided coating (**Figure 1.5**). As the solvent evaporates, the solution enters a supersaturated state, which drives nucleation and crystal growth, ultimately producing a thin film. This nucleation and growth process is made more complex by solvent-vapour, solvent-substrate, solute-solvent, and solute-substrate interactions.[41] Because nucleation, crystallization, and growth can all progress within seconds, precisely controlling film formation during solution processing remains difficult.[42]

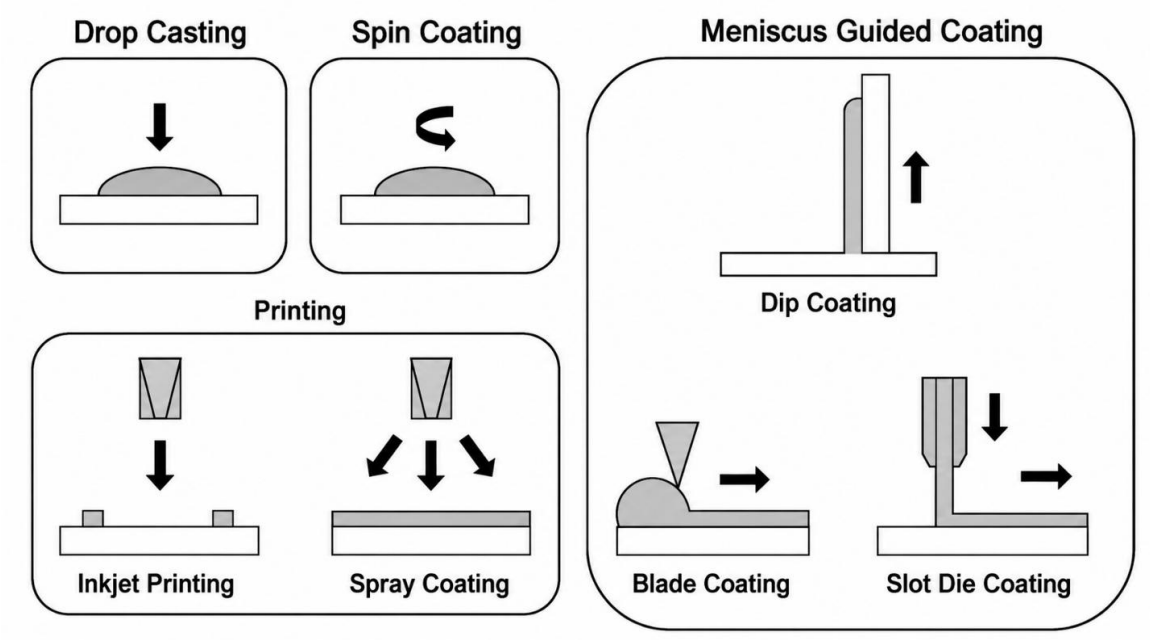


Figure 1.5. Demonstration of various deposition methods

At the laboratory scale, drop casting and spin coating are the two most widely used deposition methods for small-area substrates. In drop casting, droplets of solution with a defined size and momentum are placed onto a stationary substrate and allowed to evaporate slowly, forming a thin film.[41] Since no external force drives the process, nucleation initiates at the edge of the droplet, and crystals grow along the direction in which the contact line recedes. Because this recession tends to occur irregularly, drop casting frequently produces non-uniform films. Spin coating, by contrast, offers more reproducible results: the solution is dispensed onto a rotating substrate, where centrifugal force spreads it into a film while the solvent evaporates rapidly.[41]

Printing encompasses a broad set of deposition methods, generally referring to large-area solution-processing techniques that do not depend primarily on directional, shear-induced alignment, distinguishing them from meniscus-guided coating.[41] Inkjet printing is among the most widely used printing techniques, in which a piezoelectric or thermal actuator ejects a jet of solution

from a chamber onto the substrate.[41] Spray coating operates similarly, using an inert gas to aerosolize the solution into fine droplets that are then deposited from a nozzle.[41] Both inkjet printing and spray coating are well-suited to roll-to-roll manufacturing, making them attractive for high-throughput fabrication.

Meniscus-guided coating methods are another scalable, large-area approach, relying on the linear motion of either the substrate or the coating tool to produce films with uniformly aligned crystal growth.[41,43] Common examples include dip coating, in which the substrate is withdrawn vertically from a solution bath; blade coating, in which a flat, rectangular edge spreads solution across the substrate; and slot-die coating, in which solution flows through an orifice and shaping device onto a horizontally moving substrate.[41,43] In all of these methods, the size and alignment of the growing crystallites are governed by the shear forces that direct solution flow, which are in turn strongly dependent on the speed of the relative motion.

1.4.2 Thermodynamics and Kinetics

Once a solution is applied to a substrate, solvent evaporation causes the concentration of the solution to rise until it reaches supersaturation, at which point the dissolved molecules begin to precipitate and form a thin film. Achieving precise control over film formation, including grain structure and morphology, remains difficult in solution processing because nucleation and growth proceed so quickly. The thermodynamic driving force behind nucleation is the difference in chemical potential between organic molecules in the liquid phase (μ_l) and the crystalline phase (μ_c).[44] For solution deposition specifically, this difference in chemical potential, $\Delta\mu$, reflects the gap between the equilibrium solution concentration (C_∞) and the concentration present during growth (C), and can be written as a function of substrate temperature (T_s), as shown in **Equation 1.3**.[44]

$$\Delta\mu = \mu_l - \mu_c = kT_s \ln\left(\frac{C}{C_\infty}\right) \quad (1.3)$$

While C and T_s are, thermodynamically, the two parameters that dictate nucleation and crystallite growth during solution deposition, in practice, these processes are driven largely by kinetics and crystallization rates.[45] Specifically, the kinetic driving force for nucleation is the solvent evaporation rate, which directly sets the crystallization rate and is therefore central to producing reproducible thin films.[41,46] Because different solution-processing methods evaporate solvent under different conditions, the governing rules for evaporation rate vary from one method to the next.

In drop casting and printing, one or more solution droplets are released, strike the substrate, and spread, either merging into a continuous film before drying or drying separately into isolated island-like deposits. Because neither rotation nor shear is applied in these methods, the rate of solvent evaporation, and by extension the stages of nucleation and growth, is governed entirely by the properties of the solvent and substrate.[47–49] The solution and substrate surface properties can influence the deposition by causing splashing, spreading, receding, and/or rebounding.[50–52] Furthermore, temperature and concentration gradients that develop within individual droplets can give rise to coffee-ring and Marangoni effects, resulting in poorly controlled film formation.[47,48]

For spin coating, film formation can be demonstrated accurately by accounting for the evaporation rate of the solvent, the increase in viscosity that accompanies increasing solute concentration, the vapour phase above the substrate, and the intrinsic properties of the solvent.[53,54] The earliest and simplest treatments of liquid flow on a spinning surface rest on three assumptions: (i) both the gas and liquid phases behave as Newtonian fluids; (ii) the flow is laminar and axially symmetric; and (iii) the rotating surface is flat and effectively infinite in extent.[47,48] It is generally

accepted that spin coating proceeds in two stages: an early, flow-dominated stage, followed by a later stage governed by solvent evaporation. At the point where these two effects balance, the evaporation rate (ν_e) becomes a function of the rotational speed (ω), giving **Equation 1.4**.[53–57]

$$v_e \propto \omega^{\frac{1}{2}} \tag{1.4}$$

This relationship has been confirmed experimentally in polymer thin films, with only minor variation observed in the exponent across studies.[53,54,57–61] As the solvent evaporates, however, the solution's physical properties shift, giving rise to non-Newtonian behavior. More detailed models of spin coating, therefore, incorporate heat and momentum transfer, as well as solution viscosity and solvent volatility.[54,59,60] In situ measurements on spin-coated polymer films have supported this two-stage picture:[62,63] The rapid, flow-dominated crystallization step, which unfolds in under a second, proceeds independently of rotational speed, whereas the slower evaporation-dominated step depends on it.[62,63] **Equation 1.4**, therefore, captures the solvent evaporation rate during spin coating.

Meniscus-guided coating, by contrast, depends mainly on solvent properties and coating speed. In these methods, evaporation is concentrated at the meniscus, driving the solution there toward supersaturation and eventually precipitation and nucleation. Most meniscus-guided techniques also apply an external shear force to improve film uniformity and align the crystallites; the strength of this force scales with the coating speed (ν_c), which falls into two regimes: fast ($\nu_c \approx$ 1 mm s^{-1}) and slow ($\nu_c \approx$ 1-100 μm s^{-1}). At fast coating speeds, shear forces spread the solution while evaporation occurs away from the meniscus; this is known as the Landau-Levich-Derjaguin regime, in which the evaporation rate depends on ν_c.[64,65] At slow coating speeds, deposition instead falls into the evaporation regime, where ν_c roughly matches ν_e of a pinned droplet whose edge

recedes primarily due to solvent loss.[64] Unlike the Landau-Levich-Derjaguin regime, where evaporation and deposition are effectively decoupled, the evaporation regime involves a more intricate coupling between solvent loss, fluid flow, and film formation.[64–66] Several models have been put forward to describe v_e in this regime, most sharing the general form shown in **Equation 1.5.**[43,64,67]

$$v_e = AV_m T_s^{0.7} \exp\left(-\frac{\Delta S_{vap} T_b}{RT_s}\right) \quad (1.5)$$

Here, V_m denotes the solvent's molar volume, ΔS_{vap} its entropy of vaporization, T_b its boiling point at atmospheric pressure, R the universal gas constant, and A is a single fitting parameter that combines all temperature-independent variables.[64,67]

1.4.3 Effect of Deposition Parameters

Thin-film microstructure produced by solution deposition can vary widely based on factors like solution concentration, solvent choice, substrate temperature, and the surface chemistry of the substrate. The concentration of the solution affects how completely the film covers the substrate: dilute solutions tend to form a thin, incomplete sub-monolayer, while more concentrated solutions produce better coverage and connectivity, eventually forming mesh-like layers and multilayer structures. This pattern has been observed in spin-coated copper phthalocyanine (CuPc) films, where dilute solutions yield a sub-monolayer network of connected ribbon-shaped structures.[68–70] As CuPc concentration increases, the film builds up additional layers, though full single-layer coverage is never reached because CuPc's anisotropic shape alters how molecules diffuse and nucleate on the surface.[68–70]

The solvent used also strongly shapes film formation. Because the speed at which a solvent evaporates governs how fast crystallization occurs, it ultimately determines the film's morphology

and structure. Faster-evaporating solvents tend to produce rougher films because they form isolated clusters rather than a continuous surface. Chloroform, for example, evaporates quickly enough that molecules have little opportunity to diffuse or rearrange on the substrate, resulting in weaker aggregation and a disconnected film structure. In contrast, slower-evaporating solvents like dimethylformamide give molecules more time to move across the surface, typically producing denser, better-ordered films. This behavior has been observed for tetrakis-(isopropoxy-carbonyl)-CuPc (TIP-CuPc) as well as several other small-molecule semiconductors.[49,71–73]

The method of solution processing itself also substantially affects the resulting film structure. Gojzewski and colleagues compared CuPc film formation across drop casting, spin coating, dip coating, and spray coating (**Figure 1.6**).[68] In their work, CuPc was dissolved in trifluoroacetic acid, which spread readily across the hydrophilic substrate to form a uniform liquid layer. With drop casting, capillary flow moving outward from the drop's center carried CuPc molecules toward the edges, producing a characteristic ring-like structure **(Figure 1.6).** Spin coating with the same solution generated multilayered nanoribbons resembling the drop-cast result, but the additional spinning force sped up solvent evaporation, giving the film a rougher surface.[68] Dip coating produced films with similar roughness, coverage, and volume to the drop-cast samples, but with a distinct morphology: a sub-monolayer mesh composed of long, irregularly curved, interlinked nanoribbons, with the CuPc molecules lying flat relative to the substrate.[68] Spray-coated films, meanwhile, closely resembled spin-coated films in morphology, roughness, coverage, and volume, featuring large, rod-shaped CuPc aggregates.[68]

Although the extra spinning force in spin coating might be expected to create clear morphological differences compared to spray coating, both methods produced similar large rod-like aggregates in this case, because, as noted, morphology is ultimately governed by solvent evaporation rate rather than the deposition method itself.[68] This finding reinforces the central role solvent evaporation plays in driving nucleation and growth during solution-based thin-film deposition.

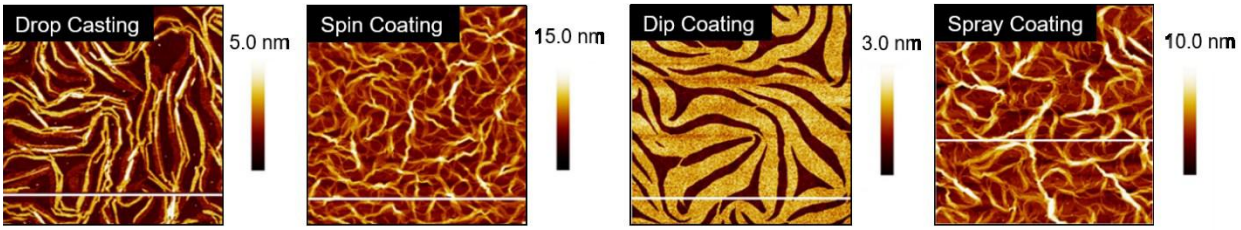


Figure 1.6. AFM images (5 × 5 μm) of CuPc thin films fabricated by drop casting, spin coating, dip coating, and spray coating.

1.5 Towards Sustainable OTFTs

There are two primary types of polymers utilized in organic electronics: insulating polymers and conjugated, conducting polymers. In electronic devices, insulators function as substrates or dielectrics, and conjugated polymers as semiconductors. The selection of a polymer for the substrate is mainly influenced by its compatibility with the processing requirements of the device, whereas dielectric insulators also need to be polarizable by an electric field. Depending on their Fermi level, conjugated polymers can have conducting or semiconducting characteristics. To fabricate sustainable OTFT devices, alternative materials need to be investigated for biodegradable substrates, insulators, metals, semiconductors, and encapsulation **(Figure 1.7)**. For any of these parts to be practical for future commercial applications, each must provide adequate performance, dependability, and degradability. Substrate, dielectric, conducting, and semiconducting polymers

provide the foundation for flexible electronics, owing to the extensive chemical design flexibility of polymers, which enables the tuning of their electrical, mechanical, and transient properties.[27] This tunability is particularly beneficial for the advancement of biodegradable electronics, since it obviates the necessity for complex structures and patterns to attain certain capabilities.[27] The vision of a fully biodegradable OTFT, however, demands that every layer of the device answer the same question simultaneously: the substrate, the dielectric, the semiconductor, and the electrodes must each degrade on a useful timescale without releasing toxic byproducts.[25] The methods employed in chemistry and engineering to overcome the challenges of developing degradable, biocompatible versions of these four material types will be discussed in the following sections.



Figure 1.7. A typical degradable electronic device is built up from four main classes of materials: biodegradable semiconductors, conductors, dielectrics, and substrates.

1.5.1 Degradable Substrates: Building on a Foundation That Disappears

The majority of the weight of the device is based on the substrate (99.89%),[9] with micrometer-scale thicknesses compared to other components that may only be hundreds of nanometers thick. As a result, substrates largely determine the overall degradation behavior of the device. In electronic devices, the substrate serves as a solid platform upon which multiple functional layers, such as semiconducting, dielectric, electrode, and encapsulation layers, are

deposited.[74] Thus, replacing traditional substrates with biodegradable alternatives could significantly reduce e-waste.

Biocompatible and biodegradable polymer substrates are increasingly viewed as promising solutions for next-generation electronic devices, as they can safely degrade within the environment or reduce electronic waste.[75] However, the physical attributes of degradable substrates provide constraints for further device processing as a result of (i) a low melting point (T_m) and glass transition temperature (T_g), and (ii) low chemical resistance when exposed to organic solvents. During the fabrication process of OTFT (e.g., annealing of dielectric and semiconductor layer), a biodegradable polymer substrate such as poly(lactic acid) (PLA) is particularly susceptible to dimensional instability because its coefficient of thermal expansion (CTE) is typically much higher.[76] These characteristics indicate the need to use mild downstream processing conditions. Therefore, as the substrate is exposed to high temperatures, it shrinks, leading to buckling and high surface roughness, which is not conducive to OTFT fabrication.[30] Recently, several natural polymers have been explored as substrates, including cellulose and paper, offering excellent biocompatibility and biodegradability for use in OTFT devices.[24,77–79] Well-established polymers used in biocompatible transient devices, such as PLA, poly(caprolactone) (PCL), polyhydroxyalkanoates (PHAs), poly(glycerol sebacate) (PGS), poly(1,8-octanediol-co-citrate) (POC), polypropylene carbonate (PPC), poly(lactic-co-glycolic acid) (PLGA), and dextran are being utilized in the development of organic electronic devices.[9,80–83] The chemical structures of some of the natural and synthetic biodegradable polymers are illustrated in **Figure 1.8.**

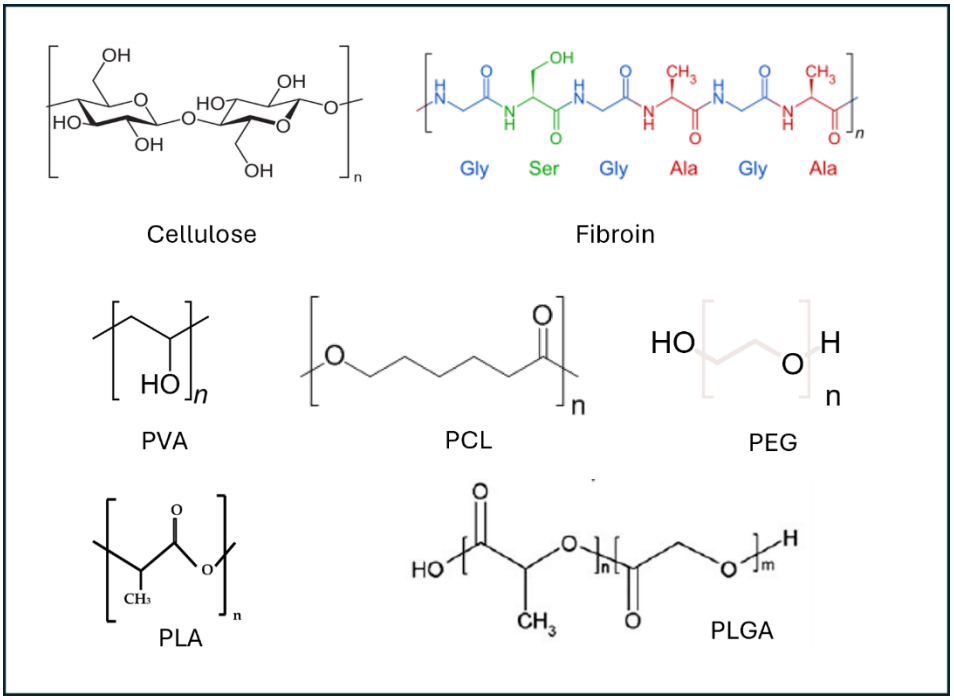


Figure 1.8. Chemical structures of natural and synthetic polymers used as substrates: Cellulose, Fibroin, polyethylene glycol (PEG), PLGA, PLA, PCL, and PGS.[83]

The earliest demonstration that organic transistors could be built on resorbable biomaterials came from Bettinger and Bao,[9] who fabricated OTFTs on PLGA substrates. Building on this foundation, PLA has since emerged as a substrate of particular interest. One challenge with biodegradable substrates such as PLA is their low T_g, which makes integration into high-temperature manufacturing processes difficult.[84,85] For organic electronics, the semiconductor is carbon-based and can be deposited at lower temperatures, enabling integration onto plastic substrates while providing low energy requirements and potential economic incentives.[86] PLA's Food and Drug Administration (FDA) approval, wide availability, and well-characterized degradation behavior in biological environments make it an attractive platform,[87] but its low thermal tolerance demands that every subsequent processing step be redesigned around it rather than the other way around.[9]

1.5.2 Degradable Dielectrics: The Interface That Controls Everything

The dielectric layer is one of the key active components of an OTFT. It acts as an insulator positioned between the gate electrode and the organic semiconductor. Its main function is to enable charge to build up at the interface between the semiconductor and the dielectric once a bias is applied across the source and gate electrodes. Specifically, applying a gate-source voltage (V_{GS}) draws mobile charge carriers in the semiconductor toward this interface, where they accumulate. Once this charge accumulation has occurred, applying a bias between the source and drain allows current to flow through the semiconductor.[88,89]A fundamental property of a dielectric material is capacitance. Higher capacitance promotes greater charge accumulation at the semiconductor/dielectric interface, thereby enhancing carrier mobility and lowering the threshold voltage (V_T).[90] To electrically characterize insulating layers, metal-insulator-metal (MIM) capacitors are fabricated and analyzed using electrochemical impedance spectroscopy (EIS). In EIS, a small sinusoidal voltage bias (approximately 10 mV) is applied across the device, and the resulting current response is measured. Impedance is normally expressed using the following equation:

$$Z(f) = \frac{V(f)}{I(f)} \tag{1.6}$$

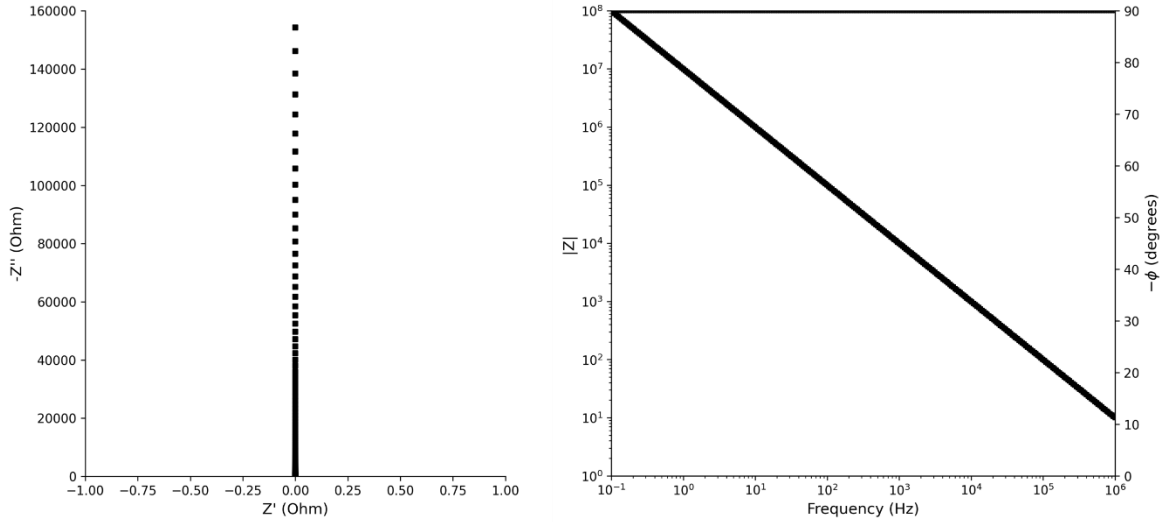


Figure 1.9. Impedance spectra of an ideal capacitor presented as (left) a Nyquist plot and (right) a Bode plot.

Unlike Ohm's law, where resistance is constant, impedance is frequency dependent and accounts for both resistive and capacitive contributions of the material.[91] The measured impedance is generally presented using Nyquist and Bode plots (**Figure 1.9**). A Nyquist plot represents the real component of impedance (Z′) along the x-axis and the negative imaginary component (−Z″) along the y-axis. The total impedance is expressed as:

$$Z = \mathrm{Z}' + \mathrm{jZ}'' \tag{1.7}$$

where *j* is the imaginary unit and the phase angle φ (**Figure 1.9**) is calculated from the ratio of these two components as

$$\varphi = \mathrm{Tan}^{-1}\left(\frac{\mathrm{Z}''}{\mathrm{Z}'}\right) \tag{1.8}$$

For an ideal capacitor, one exhibiting purely capacitive and no resistive behavior, corresponding to Z' = 0, the capacitance can be calculated directly from the imaginary impedance and the measurement frequency using:

$$C = \frac{1}{2\pi \times f \times -Z''} \tag{1.9}$$

In practice, however, polymer dielectrics rarely behave as ideal capacitors. Dipolar groups present along the polymer backbone or on pendant side chains contribute to both the dielectric constant and dielectric loss through local polarization effects. When a voltage bias is applied, the polymer dipoles reorient to polarize the material, but this realignment is not instantaneous; upon removal of the bias, a finite relaxation time is required for the polymer chains to return to their equilibrium random orientation. This delay gives rise to dielectric loss, quantified by the loss tangent (tan φ = Z''/Z'), which reaches a minimum when the polymer relaxation time is equal to or shorter than the period of the applied oscillating bias.[92] To account for these non-ideal polarization effects and calculate the dielectric constant and capacitance with greater accuracy, the following expressions are employed:[92,93]

$$k = \frac{t}{A\varepsilon_o \omega} \frac{Z''}{Z'^2 + Z''^2} \tag{1.10}$$

$$\text{Tan}\,(\varphi) = \left(\frac{Z''}{Z'}\right) \tag{1.11}$$

$$C = \frac{k\varepsilon_o A}{t} \tag{1.12}$$

In these equations, k is the dielectric constant, ω is the angular frequency (2πf), εo is the permittivity of free space, A is the electrode area, and t is the dielectric layer thickness. Dividing

the calculated capacitance by the electrode area yields the areal capacitance density (C_i), a parameter that is essential for accurately extracting field-effect mobility from OTFT transfer characteristics. Since the capacitance density of the gate dielectric directly governs both carrier mobility and threshold voltage in OTFTs, the fabrication and characterization of MIM capacitors provide an efficient route to isolating and optimizing dielectric properties independently before these materials are incorporated into full transistor stacks.

The dielectric layer in an OTFT is not merely an insulator; its surface chemistry, roughness, and dielectric constant collectively determine threshold voltage, carrier mobility, and device stability.[94,95] The dielectric constant, which can be high or low depending on the application, low dielectric loss to reduce electromagnetic energy dissipation, and high breakdown voltage for stability, are important performance indicators for dielectrics. Dielectrics are required in the fabrication of capacitors and thus have great significance in capacitive sensing and are critical for field-effect transistors (FETs). For reduced-voltage operation in transistors, high capacitance per unit area is preferred. The *k* is directly related to capacitance per unit area, whereas the thickness of an insulator film devoid of defects is inversely related. Thus, while choosing an appropriate dielectric, processing methods, as well as the material's inherent properties, are crucial. Because polarization mechanisms are time-dependent, the dielectric constant varies with frequency and depends on the number of polarizable groups in a material.[96] While k is commonly given for static fields, most electronic devices operate at high frequencies (>GHz).[97] When reducing the size of FETs, high-k dielectrics can help reduce leakage current.[98]

SiO_2 serves as the reference material, with a dielectric constant around 3.9, materials below that value are classified as low-k, and those above it as high-k.[89] Compostable or biodegradable natural and synthetic polymers can exhibit superior dielectric characteristics.

Examples of natural polymers include chitosan, alginate, and cellulose, many of which exhibit high capacitance and are classified as high-k materials.[99–102] Their dielectric performance in OTFTs is analogous to that of non-biodegradable synthetic polymers.[14,101,103] Alongside natural polymers, eco-friendly and biocompatible synthetic polymers, including PVA, PCL, PLA, and polybutylene succinate (PBS), are frequently utilized. It is essential to recognize that while several synthetic polymers are biodegradable and eco-friendly, they frequently necessitate particular microbes for their disintegration. This renders the term "compostable" more appropriate for such materials.[14] For example, PLA undergoes biodegradation in the presence of Bacillus licheniformis, but the decomposition of PVA is promoted by enzymes released by diverse soil microorganisms.[104,105] Additional examples of natural and synthetic polymers, together with an overview of how each undergoes biodegradation, are shown in Figure 1.10.[106]

Eco-friendly materials do not consistently match the performance of conventional polymer dielectrics and often pose challenges in processing, electrical characteristics, and scalability. Nevertheless, several approaches exist to enhance both the processability and electrical performance of these environmentally conscious dielectric materials. There are two main methods to increase the capacitance of a dielectric material: one is by increasing the dielectric constant (using a high-k material), and the other is by reducing the dielectric thickness. For low-k materials to achieve high capacitance, the dielectric layer must be extremely thin. Another strategy for enhancing the OTFT performance involves combining different dielectric layers through orthogonal processing. High-k dielectrics, for instance, tend to have rougher surfaces, which in turn lowers μ.[14] They also tend to exhibit greater dipolar disorder, which, in turn, degrades both μ and overall device performance.[107,108] Prior work has shown that this increased dipolar disorder at the semiconductor/dielectric interface broadens the density of states (DOS). In other words,

increasing the dielectric's polarity enhances capacitance but simultaneously increases the DOS, generating more trap states and lowering μ.[109] Masillamani et al. illustrated this trade-off directly: switching the dielectric from polystyrene (PS) ($k \approx 2.0$) to PMMA ($k \approx 3.6$) caused hole mobility to drop twentyfold, an effect attributed largely to DOS broadening.[110] Beyond reduced mobility, high-k dielectrics are also prone to higher leakage and off-state currents, largely because they contain mobile charges, whether from impurities or polarizable functional groups such as hydroxyls.[111] Low-k polymer dielectrics offer the opposite profile: less leakage and reduced polar disorder, but at the cost of lower capacitance. In short, high-k and low-k materials each bring their own strengths and weaknesses when used separately.

Combining the two into a bilayer, placing a thin low-k dielectric on top of a high-k layer, offers a way to offset the shortcomings of each. Such high-k/low-k bilayers have been shown to reduce gate leakage and charge trapping while improving OTFT mobility.[107,108,112,113] This bilayer approach also reduces the surface roughness and narrows the DOS, both of which further enhance μ.[14] Numerous studies have likewise reported that these bilayer structures lower gate leakage current (I_{GS}).[94,108,114] A wide range of low-k polymers has been employed toward this end. Crosslinked poly(vinyl phenol) (PVP), PMMA, and Octyltrichlorosilane (OTS), for example, have all been used as low-k layers to reduce I_{GS} and V_T.[112,114–116] Sun et al. combined PVA with an OTS treatment to create a low-k monolayer that lowered I_{GS}.[115] The same principle extends to eco-friendly materials: Rullyani et al. layered natural rubber over chitosan, thereby reducing I_{GS} and enhancing semiconductor film growth by tuning the dielectric's surface energy.[101]

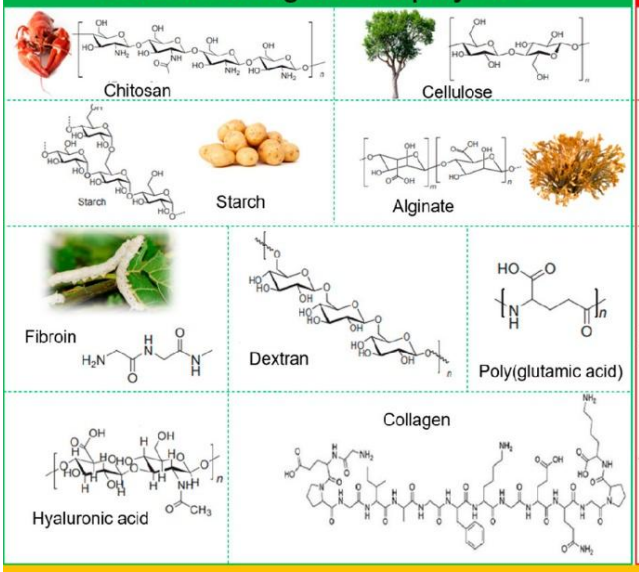
Placing a low-k layer between the gate electrode and the dielectric can also improve performance. Lee et al. found that charge injection from the gate into the dielectric deteriorates device hysteresis,[117] a problem because it shifts V_T and makes OTFT behavior less predictable.

Building on this, Wang et al. constructed a PMMA/PVA/PMMA trilayer dielectric that substantially reduced the hysteresis seen in plain PVA devices, pushing the on/off ratio to 10^4, V_T to −0.55 V, and mobility as high as 1.83 $cm^2V^{-1}s^{-1}$ with a pentacene semiconductor.[118] Similar high-k/low-k bilayer polymer systems have also improved the performance of single-wall carbon nanotube (SWCNT)-based OTFTs, yielding higher mobilities and improved on/off ratios.[119]

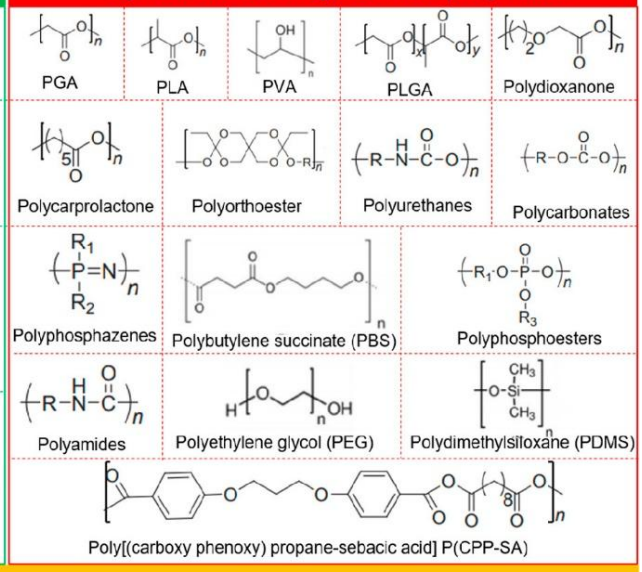
While these hybrid high-k/low-k systems achieve lower leakage currents, they still carry the inherent drawbacks of conventional inorganic dielectrics.[98,120–123] This means that when the goal is printable, environmentally friendly dielectrics, material selection needs to account for both performance and sustainability. Although much of the existing literature relies on inorganic-organic combinations or non-eco-friendly polymers, a number of fully environmentally friendly bilayer systems have also been reported, including chicken albumen/gelatin, chitosan/PLA, chitosan/gelatin, and PVA/PCL combinations, all used to enhance OTFT performance.[124–128]

Overall, layering a thin low-k dielectric over a high-k one consistently delivers benefits: higher mobility, reduced gate leakage, less hysteresis, and greater stability. This bilayer design also permits thicker overall dielectric films, which simplifies large-scale fabrication using standard printing methods.

Natural biodegradable polymers

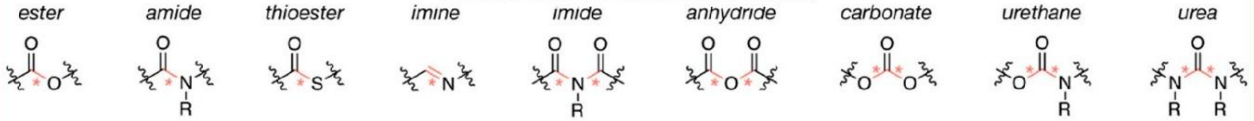


Synthetic biodegradable polymers

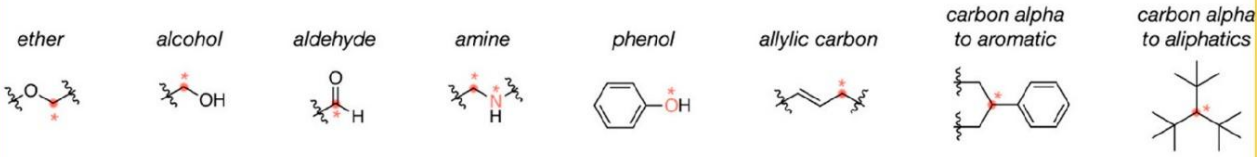


Mechanisms of polymer degradation

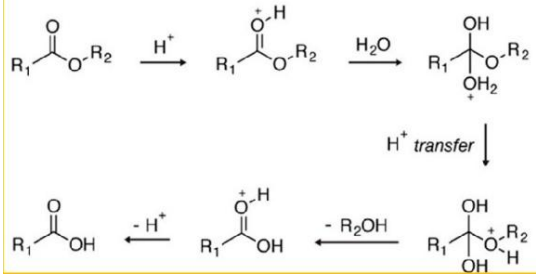
Linkages vulnerable to hydrolysis



Linkages vulnerable to oxidation



Acid catalyzed ester hydrolysis



Enzymatic degradation of PVA

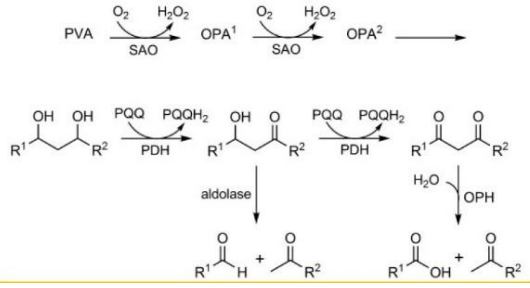


Figure 1.10. Chemical structures of both natural and synthetic polymers, highlighting the specific bonding sites susceptible to hydrolysis or oxidation. The degradation pathways for these materials, including the enzymatic breakdown of PVA and acid-catalyzed ester hydrolysis, as reproduced from Hosseini et al.[106]

1.5.3 Degradable Semiconductor

The performance of semiconducting polymers is generally assessed by μ, which signifies the velocity at which a charge transfers through the material under the influence of an electric field. Common semiconducting polymers comprise polythiophenes, exemplified as poly(3-hexylthiophene) (P3HT),[129] and donor-acceptor copolymers such as diketopyrrolopyrroles (DPP),[130,131] initially engineered for organic photovoltaics. To facilitate the development of increasingly complex biodegradable electronics, degradable semiconductors are needed. The sourcing of biodegradable semiconductor materials is a critical challenge in efforts to reduce e-waste.

There are several strategies for fabricating biodegradable semiconducting materials. Polymers that break apart physically without their chemical structure fully breaking down (type I), and those that can be broken back down into their monomer or oligomer components for recycling (type II). Achieving type I typically relies on engineering and materials-science approaches, while type II normally calls for deliberate synthetic pathways.[27]

Blending has been employed to fabricate semiconductors subject to type I degradation. To enhance miscibility with more polar biodegradable matrices, poly(3-thiophene methyl acetate) (P3TMA), a carboxylate-substituted derivative of P3HT, was selected for blending with polymers

such as PBS, PLA, poly(ester urea) (PEU), and thermoplastic polyurethane (TPU). Electrospinning semiconducting polymers with insulating, biodegradable polymers have been extensively researched. Degradable fibers of P3HT co-spun with PCL[132] and PLGA[133] have been developed, although they demonstrated reduced mobilities due to grain boundaries resulting from macroscopic phase segregation. Electrospun P3HT nanofibers exhibited a mobility of 1.7×10^{-2} $cm^2V^{-1}s^{-1}$; however, blending with 20 wt% PCL led to a mobility reduction by an order of magnitude, while 50 wt% PCL blends showed a two-order decline. Similar to blended transient conductors, these semiconducting polymer blends demonstrate type I degradation **(Figure 1.11)**, wherein the non-degradable semiconducting component depends on the biodegradable matrix to determine degradation characteristics.

Recent progress in understanding charge transport in semiconducting polymers may enable the development of future biodegradable semiconducting polymers. A significant challenge has been overcoming the inflexibility and rigidity of conjugated semiconducting molecules and their crystalline, charge-transporting aggregates, which restrict the application of conventional semiconducting polymers in stretchable and flexible electronics. In 2013, Noriega and co-workers reported that enhanced mobility may be attained in macroscopically disordered semiconducting polymers, including linked aggregates that facilitate effective local intra- and intermolecular charge transport.[134] In 2015, Wang and colleagues demonstrated that semiconducting polymers could sustain increased μ when incorporated with an insulating polymer matrix.[135] The foundation of this breakthrough was the development of semiconductors exhibiting great disorder resistance through the formation of linked aggregates that facilitate efficient local intermolecular charge transport.[134] The strategy of blending rigid semiconducting polymers with inert polymers possessing favorable properties could, in theory, be adapted to develop materials predominantly

made from an insulating, biodegradable matrix. This method involves optimizing both the semiconducting and inert polymer components to establish a linked morphology.

Biodegradability is facilitated through hydrolyzable connections such as ester bonds.[27] These bonds may be integrated into a secondary component within a mix, resulting in a semiconductor that is only partially degradable (type I), or directly inserted into the semiconducting polymer backbone, potentially disrupting the conjugation essential for enhanced mobilities.[27]

Lei et al.[24] demonstrated the first totally disintegrable and biocompatible semiconducting polymer for thin-film transistors. The polymer PDPP-PD was synthesized via a simple condensation reaction using reversible imine (–C=N–) bonds to connect DPP units with p-phenylenediamine, without noble-metal catalysts. The key design principle was that imine bonds are stable under neutral pH but hydrolyze readily under mild acidic conditions, enabling controlled disintegration. Lei et al. reported the utilization of reversible imine bonds as conjugated connections between DPP and p-phenylenediamine to obtain fully degradable type II semiconductors **(Figure 1.11)**.[24] The DPP-based semiconducting polymer preserves backbone conjugation, enabling hole mobilities of up to 0.34 $cm^2V^{-1}s^{-1}$ when spin-coated onto OTS-treated SiO_2/Si substrates.[24] The imine linkages deteriorate in somewhat acidic conditions (pH = 4.6), yielding aldehyde and amine precursors as byproducts. Devices underwent complete disintegration after 30 days when utilizing cellulose as a substrate, Al_2O_3 as the dielectric, and Iron (Fe) as the electrodes.

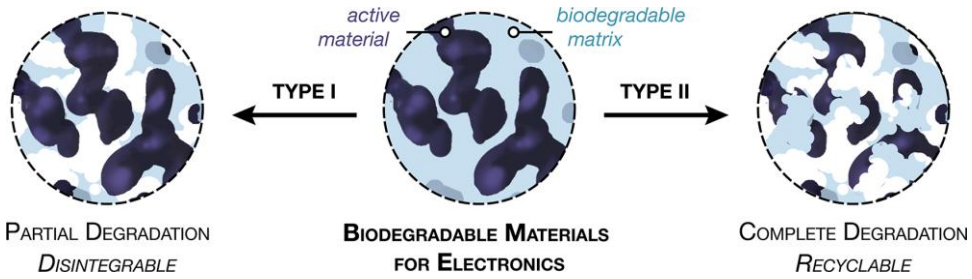


Figure 1.11. Conjugated polymers (dark blue) are used in semiconductors and conductors to form channels for electronic conduction inside the matrix (light blue). In Type I materials, only the matrix can break down fully into small molecular building blocks, while the nondegradable active components stay intact. Only the matrix can break down completely. However, type II materials' matrix and active ingredients can both completely break down into monomers or oligomers, suggesting that these entirely biodegradable materials may be recyclable.

Another example of a fully degradable (Type II) organic semiconductor comprises 5,5′-DDFTTF, which disintegrates in citrate buffer under physiological conditions, and DPP connected to p-phenylenediamine via conjugated imine bonds.[9,24] However, these polymers lack stretchability. Sugiyama et al.[136] subsequently presented a biodegradable semiconducting block copolymer consisting of rigid, conjugated DPP segments and flexible PCL segments. This design demonstrated enhanced hole mobility of approximately 0.1 $cm^2V^{-1}s^{-1}$, with mobility remaining steady despite the presence of up to 90% non-conductive material. PCL offers hydrolysis sites that facilitate breakdown in physiological settings, resulting in no detectable PCL after 12 weeks. This is a Type I system, in which the DPP component remains unchanged. Optimizing the block composition can enhance both mechanical flexibility and semiconducting performance. A combination of polymer chemistry and physics was employed to develop a completely degradable semiconducting polymer structure.[18,137] Tran et al.[18] reported DPP polymer with imine bonds as the semiconductor and PCL as the elastomer, both engineered to decompose into their fundamental components. The devices exhibited strain-independent performance across two distinct axes of

strain by encapsulating the semiconductors within nanoscale fibres in the elastomer via self-assembly **(Figure 1.12)**.

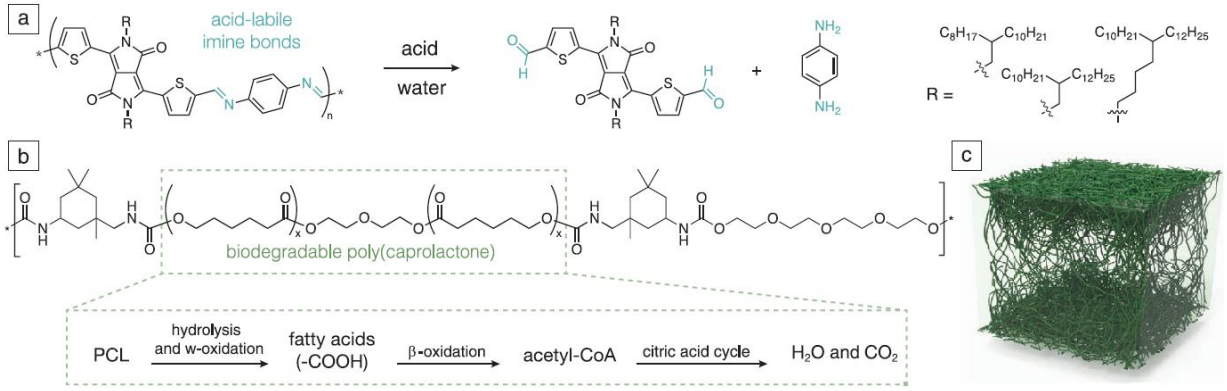


Figure 1.12. (a) The chemical structure of a fully degradable semiconductor, named diketopyrrolopyrrole-p-phenylenediamine (DPP-PPD) is based on imine bonds, which are acid-labile. (b) The chemical structure of the elastomer is based on PCL, a widely used biodegradable material. (c) An illustration of the z-phase segregation in the thin-film morphology that results from blending the semiconductor and elastomer, forming a distinct layered structure.[18]

1.5.4 Degradable Conductors

Conjugated polymers get their conductivity through doping, and once doped they are used to form interconnects and contacts in devices. Because doping is essential to switching these polymers into a conductive state, its biocompatibility becomes a design factor which needs to be considered. Well-known conjugated polymers that hold their conductivity once doped include polypyrrole (PPy), polyaniline (PANI), and poly(3,4-ethylenedioxythiophene) (PEDOT), the last of which, when doped with poly(styrenesulfonate) (PSS), can reach conductivities as high as 4.6 $\times 10^3$ S/cm.[138]

In these materials, conductivity travels through rigid, conjugated segments, which is why highly conductive films tend to be stiff and brittle. This trade-off can be overcome, though, since good electrical performance doesn't actually require much conjugated polymer; strong properties are achievable even at low loadings within a composite.[139–141] Following the same logic used for dielectric composites, one route to biodegradable conductors is blending conjugated polymers into a biodegradable, insulating matrix. These blends fall under type I degradation: the composite can break down physically, even though the conjugated polymer itself stays chemically intact. Since that conjugated component won't degrade, the goal becomes balancing conductivity against keeping its proportion in the blend as small as possible.[27]

Dispersing conjugated polymer nanoparticles through a biodegradable matrix works well for this, partly because doping can be done independently of the blending step. Unlike dielectric blends, though, the conductive filler here needs to exceed the percolation threshold so a continuous conduction pathway forms through the insulating matrix. However, keeping nanoparticle content low is key to good degradability.[142–144]

Type II degradation, by contrast, can be reached by inserting flexible, non-conjugated linkers that interrupt conjugation along the backbone, a strategy already used elsewhere to improve processability and mechanical behavior of conducting/semiconducting polymers without sacrificing much performance.[145–148] Similarly, polymers synthesized from short conjugated segments tied to biodegradable units still show reasonable charge transport. Because the resulting conjugated oligomers are small, they can plausibly be engulfed by macrophages that migrate to an implant site as part of the immune response,[149,150] making them a biocompatible degradation pathway. That said, type II conducting polymers still lag well behind type I materials in conductivity.[147,151–155]

Rivers and colleagues built a biodegradable polymer from pyrrole–thiophene–pyrrole trimers linked by ester bonds to aliphatic chains, reaching 10^{-4} S/cm with iodine doping; breakdown products appeared within two weeks in simulated body fluid with esterase present, and in vivo testing showed both the film and its degradation products were non-toxic, though the iodine dopant itself was cytotoxic.[156] To avoid iodine, Guimard's group doped a thiophene-oligomer copolymer with the non-toxic ions ferric chloride ($FeCl_3$) and ferric perchlorate ($Fe(ClO_4)_3$); rather than measuring conductivity directly, they confirmed successful doping through cyclic voltammetry (CV) (redox activity) and UV-vis (polaron signatures), and in vitro tests on Schwann cells showed near-total viability.[157]

Beyond biocompatibility, dopant mobility is a concern for long-term stability, since conductivity drops sharply once dopants diffuse out of the material. Xu's group addressed this with a dopant-free conductive polyurethane (DCPU) elastomer built from aniline trimers linked to biodegradable PCL, with dimethylolpropionic acid (DMPA) serving as a covalently-bound dopant.[158]

Overall, biodegradable conductors still fall short of the $>10^{-1}$ S/cm conductivity needed for practical electrodes and interconnects. However, most transient devices have utilized dissolvable metals such as magnesium (Mg), Zn, Fe, tungsten (W), and Mo in early biodegradable device demonstrations, but these materials offer limited mechanical flexibility.[159] Additionally, gold (Au) and silver (Ag) have been used as biocompatible conductors in the fabrication of biodegradable organic electronic devices.[160–163] Progress on intrinsically stretchable, highly conductive biodegradable electrodes will be important for next-generation sustainable electronics.

1.6 OTFT Applications

OTFTs have emerged as one of the most versatile transducing platforms in modern sensing technology. Unlike passive sensing elements that simply change resistance or capacitance upon analyte interaction, the OTFT is an active, three-terminal device capable of amplifying weak sensing signals directly at the point of detection, converting a chemical or physical stimulus into an easily measurable electrical output. This signal amplification capability, combined with the inherent tunability of organic semiconductors, compatibility with flexible and large-area substrates, low-temperature fabrication, and potential for low-cost, roll-to-roll manufacturing, has made OTFTs extremely attractive for a broad spectrum of sensing applications, ranging from chemical and biological detection to mechanical pressure sensing and ion recognition in physiological environments.

Numerous sensing technologies, such as gas,[164–166] temperature,[167,168] and humidity[169] sensors, have used OTFTs. Despite the impressive sensing capabilities of OTFTs documented above, the vast majority of conventional OTFT sensor platforms have been fabricated on substrates such as silicon wafers, glass, or non-biodegradable plastic films (e.g., polyethylene terephthalate, polyimide), and have employed conventional organic solvents, fluorinated dielectrics, or rare-earth-containing materials in their fabrication. As sensor applications increasingly demand single-use, disposable, or implantable devices, particularly in point-of-care diagnostics, environmental monitoring, and wearable health monitoring, the environmental footprint and sustainability of these materials become critical considerations. This has driven growing interest in sustainable OTFTs: devices that incorporate bio-based, biodegradable, or naturally derived materials in one or more components of the transistor stack, ideally without sacrificing sensing performance.

The proliferation of low-cost, single-use sensing devices based on conventional electronic materials poses an increasing challenge for electronic waste (e-waste) management. Plastic substrates are non-biodegradable, silicon-based electronics require energy-intensive processing, and many conventional gate dielectrics and electrode materials contain environmentally hazardous substances. In the context of OTFTs intended for disposable sensing applications, where devices are designed for single or limited use before disposal, the environmental and health implications of accumulating non-degradable e-waste are particularly pressing. A sustainable OTFT for sensing applications should ideally be fabricated from abundant, renewable, non-toxic materials that can biodegrade or be composted at the end of life, while maintaining sufficient electrical performance to enable sensitive and selective analyte detection.

For instance, Wu et al.[170] fabricated a flexible temperature sensor using gold, biocompatible PLA, and three distinct biocompatible organic semiconductors (OSCs) **(Figure 1.13b)**. The sensor exhibited a linear increase in mobility from 0.1 to 0.6 $cm^2V^{-1}s^{-1}$ as the temperature increased from 20 to 160 °C.[170] A three-arm PLA stereocomplex was used as both the flexible substrate and the dielectric. Yin et al.[169] reported a low-voltage operable flexible OTFT-based humidity sensor. PLA was employed as a dielectric and sensing layer for the fabrication of a humidity sensor. Verma et al.[164] demonstrated an ammonia gas-sensing OTFT device made using P3HT as the active layer **(Figure 1.13a)**. Another use for OTFT-based disposable sensors made for a single use is the detection of cannabinoids from cannabis plants.[171] These investigations have clearly demonstrated that sustainable materials can successfully replace specific layers within the transistor architecture while maintaining functional device operation. However, the majority of reported OTFTs remain only partially sustainable, as the remaining device layers, including the semiconductor, electrodes, dielectric, or substrate, continue to rely on conventional synthetic materials. Consequently, the

environmental benefits of these devices remain limited, particularly regarding end-of-life disposal and e-waste reduction. While these applications broadly motivate the development of degradable OTFTs, this thesis focuses specifically on establishing degradable substrate, dielectric, and semiconductor materials as the foundational building blocks. The application of these degradable OTFTs toward gas sensing is proposed as future work (**Chapter 5**).

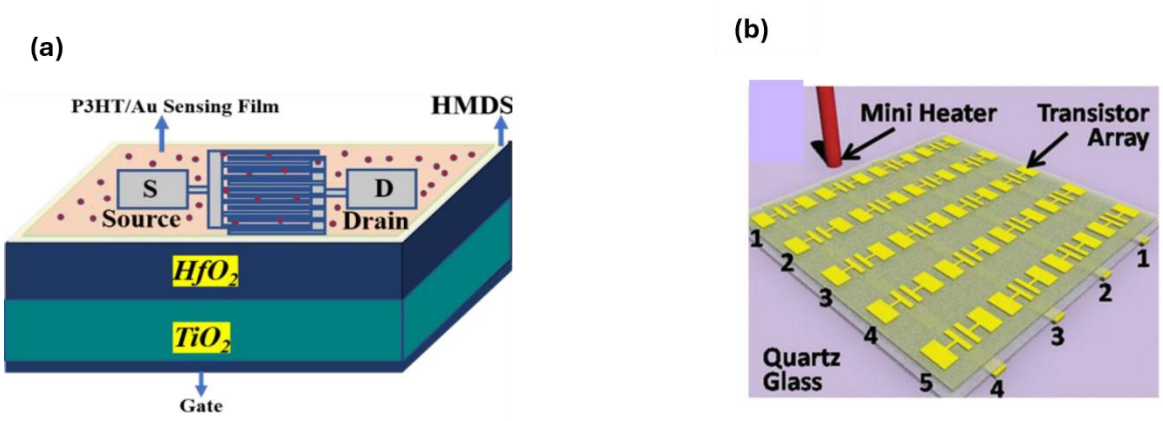


Figure 1.13. (a) Schematic representation of a P3HT-based OTFT for ammonia gas sensing.[164] (b) Flexible OTFT temperature sensor array with an integrated mini heater.[170]

1.7 Scope of Thesis

The remaining frontier is not simply to demonstrate degradability, but to achieve it without the compromises in electrical performance, operational stability, and processing scalability that have traditionally held biodegradable devices back from real-world adoption. This thesis addresses that frontier directly. Building on the reported literature on biocompatible and degradable polymers used in fabricating electronic devices (OTFT), and the materials insights established across the literature reviewed above, the work presented here pursues the following objectives:

- To investigate and optimize the processing conditions for sustainable OTFT fabrication on PLA substrates
- To evaluate the electrical performance of devices incorporating biodegradable dielectric and semiconductor components
- To characterize the degradation behavior and cytocompatibility of the resulting devices
- To advance the broader goal of a fully sustainable, high-performance OTFT platform suitable for transient bioelectronic applications

References

(1) Kumar, A.; Holuszko, M.; Espinosa, D. C. R. E-Waste: An Overview on Generation, Collection, Legislation and Recycling Practices. *Resour. Conserv. Recycl.* **2017**, *122*, 32–42.

(2) Irimia-Vladu, M.; Głowacki, E. D.; Voss, G.; Bauer, S.; Sariciftci, N. S. Green and Biodegradable Electronics. *Mater. Today* **2012**, *15* (7–8), 340–346.

(3) Wang, Z.; Zhang, B.; Guan, D. Take Responsibility for Electronic-Waste Disposal. *Nature* **2016**, *536* (7614), 23–25.

(4) Widmer, R.; Oswald-Krapf, H.; Sinha-Khetriwal, D.; Schnellmann, M.; Böni, H. Global Perspectives on E-Waste. *Environ. Impact Assess. Rev.* **2005**, *25* (5), 436–458.

(5) Li, J.; Zeng, X.; Chen, M.; Ogunseitan, O. A.; Stevels, A. "Control-Alt-Delete": Rebooting Solutions for the e-Waste Problem. *Environ. Sci. Technol.* **2015**, *49* (12), 7095–7108.

(6) Hwang, S.; Park, G.; Cheng, H.; Song, J.; Kang, S.; Yin, L.; Kim, J.; Omenetto, F. G.; Huang, Y.; Lee, K. 25th Anniversary Article: Materials for High-performance Biodegradable Semiconductor Devices. *Adv. Mater.* **2014**, *26* (13), 1992–2000.

(7) Hwang, S.-W.; Tao, H.; Kim, D.-H.; Cheng, H.; Song, J.-K.; Rill, E.; Brenckle, M. A.; Panilaitis, B.; Won, S. M.; Kim, Y.-S. A Physically Transient Form of Silicon Electronics. *Science.* **2012**, *337* (6102), 1640–1644.

(8) Irimia-Vladu, M. "Green" Electronics: Biodegradable and Biocompatible Materials and Devices for Sustainable Future. *Chem. Soc. Rev.* **2014**, *43* (2), 588–610.

(9) Bettinger, C. J.; Bao, Z. Organic Thin-film Transistors Fabricated on Resorbable Biomaterial Substrates. *Adv. Mater.* **2010**, *22* (5), 651–655.

(10) Bathaei, M. J.; Singh, R.; Mirzajani, H.; Istif, E.; Akhtar, M. J.; Abbasiasl, T.; Beker, L. Photolithography-Based Microfabrication of Biodegradable Flexible and Stretchable Sensors. *Adv. Mater.* **2023**, *35* (6), 2207081.

(11) Istif, E.; Ali, M.; Ozuaciksoz, E. Y.; Morova, Y.; Beker, L. Near-Infrared Triggered Degradation for Transient Electronics. *ACS omega* **2024**, *9* (2), 2528–2535.

(12) Boutry, C. M.; Beker, L.; Kaizawa, Y.; Vassos, C.; Tran, H.; Hinckley, A. C.; Pfattner, R.; Niu, S.; Li, J.; Claverie, J. Biodegradable and Flexible Arterial-Pulse Sensor for the Wireless Monitoring of Blood Flow. *Nat. Biomed. Eng.* **2019**, *3* (1), 47–57.

(13) Ali, M.; Hoseyni, S. M.; Das, R.; Awais, M.; Basdogan, I.; Beker, L. A Flexible and Biodegradable Piezoelectric-Based Wearable Sensor for Non-Invasive Monitoring of Dynamic Human Motions and Physiological Signals. *Adv. Mater. Technol.* 2023, 8, 2300347.

(14) Tan, M. J.; Owh, C.; Chee, P. L.; Kyaw, A. K. K.; Kai, D.; Loh, X. J. Biodegradable Electronics: Cornerstone for Sustainable Electronics and Transient Applications. *J. Mater. Chem. C* **2016**, *4* (24), 5531–5558.

(15) Kumar, B.; Kaushik, B. K.; Negi, Y. S. Organic Thin Film Transistors: Structures, Models, Materials, Fabrication, and Applications: A Review. *Polym. Rev.* **2014**, *54* (1), 33–111.

(16) Surya, S. G.; Raval, H. N.; Ahmad, R.; Sonar, P.; Salama, K. N.; Rao, V. R. Organic Field Effect Transistors (OFETs) in Environmental Sensing and Health Monitoring: A Review.

TrAC Trends Anal. Chem. **2019**, *111*, 27–36.

(17) Song, J.; Liu, H.; Zhao, Z.; Lin, P.; Yan, F. Flexible Organic Transistors for Biosensing: Devices and Applications. *Adv. Mater.* **2024**, *36* (20), 2300034.

(18) Tran, H.; Feig, V. R.; Liu, K.; Wu, H.-C.; Chen, R.; Xu, J.; Deisseroth, K.; Bao, Z. Stretchable and Fully Degradable Semiconductors for Transient Electronics. *ACS Cent. Sci.* **2019**, *5* (11), 1884–1891.

(19) Wang, S.; Xu, J.; Wang, W.; Wang, G.-J. N.; Rastak, R.; Molina-Lopez, F.; Chung, J. W.; Niu, S.; Feig, V. R.; Lopez, J.; Lei, T.; Kwon, S.-K.; Kim, Y.; Foudeh, A. M.; Ehrlich, A.; Gasperini, A.; Yun, Y.; Murmann, B.; Tok, J. B.-H.; Bao, Z. Skin Electronics from Scalable Fabrication of an Intrinsically Stretchable Transistor Array. *Nature* **2018**, *555* (7694), 83–88. https://doi.org/10.1038/nature25494.

(20) Elkington, D.; Cooling, N.; Belcher, W.; Dastoor, P. C.; Zhou, X. Organic Thin-Film Transistor (OTFT)-Based Sensors. *Electronics* **2014**, *3* (2), 234–254.

(21) Mabeck, J. T.; Malliaras, G. G. Chemical and Biological Sensors Based on Organic Thin-Film Transistors. *Anal. Bioanal. Chem.* **2006**, *384*, 343–353.

(22) Lin, P.; Yan, F. Organic Thin-film Transistors for Chemical and Biological Sensing. *Adv. Mater.* **2012**, *24* (1), 34–51.

(23) Yu, X.; Shou, W.; Mahajan, B. K.; Huang, X.; Pan, H. Materials, Processes, and Facile Manufacturing for Bioresorbable Electronics: A Review. *Adv. Mater.* **2018**, *30* (28), 1707624.

(24) Lei, T.; Guan, M.; Liu, J.; Lin, H.-C.; Pfattner, R.; Shaw, L.; McGuire, A. F.; Huang, T.-C.;

Shao, L.; Cheng, K.-T. Biocompatible and Totally Disintegrable Semiconducting Polymer for Ultrathin and Ultralightweight Transient Electronics. *Proc. Natl. Acad. Sci.* **2017**, *114* (20), 5107–5112.

(25) Kettle, J.; Kumar, D. Biodegradable Zinc Oxide Thin Film Transistors. In *2021 23rd European Microelectronics and Packaging Conference & Exhibition (EMPC)*; IEEE, 2021; pp 1–4.

(26) Askin Celik, T. Introductory Chapter: Cytotoxicity; Askin Celik, T., Ed.; IntechOpen: London, 2018. https://doi.org/10.5772/intechopen.77244.

(27) Feig, V. R.; Tran, H.; Bao, Z. Biodegradable Polymeric Materials in Degradable Electronic Devices. *ACS Cent. Sci.* **2018**, *4* (3), 337–348.

(28) International Organization for Standardization. Biological Evaluation of Medical Devices—Part 5: Tests for in Vitro Cytotoxicity; ISO 10993-5:2009; ISO: Geneva, Switzerland, 2009.

(29) Van Meerloo, J.; Kaspers, G. J. L.; Cloos, J. Cell Sensitivity Assays: The MTT Assay. In *Cancer cell culture: methods and protocols*; Springer, 2011; pp 237–245.

(30) Ali, M.; Ronnasi, B.; Ourabi, M.; Park, J. H.; St-Pierre, J.-P.; Kim, C.-H.; Lessard, B. H. Cytocompatible, Disintegrable, Low-Voltage Operation n-Type Organic Thin Film Transistors. *Mater. Adv.* **2025**, *6* (2), 557–568.

(31) Irimia-Vladu, M.; Troshin, P. A.; Reisinger, M.; Shmygleva, L.; Kanbur, Y.; Schwabegger, G.; Bodea, M.; Schwödiauer, R.; Mumyatov, A.; Fergus, J. W. Biocompatible and Biodegradable Materials for Organic Field-effect Transistors. *Adv. Funct. Mater.* **2010**, *20*

(23), 4069–4076.

(32) Facchetti, A. Gels Excel. *Nat. Mater.* **2008**, *7* (11), 839–840.

(33) Lan, S.; Yan, Y.; Yang, H.; Zhang, G.; Ye, Y.; Li, F.; Chen, H.; Guo, T. Improving Device Performance of N-Type Organic Field-Effect Transistors via Doping with a p-Type Organic Semiconductor. *J. Mater. Chem. C* **2019**, *7* (15), 4543–4550.

(34) Griggs, S.; Marks, A.; Bristow, H.; McCulloch, I. N-Type Organic Semiconducting Polymers: Stability Limitations, Design Considerations and Applications. *J. Mater. Chem. C* **2021**, *9* (26), 8099–8128.

(35) Quinn, J. T. E.; Zhu, J.; Li, X.; Wang, J.; Li, Y. Recent Progress in the Development of N-Type Organic Semiconductors for Organic Field Effect Transistors. *J. Mater. Chem. C* **2017**, *5* (34), 8654–8681.

(36) Zaumseil, J.; Sirringhaus, H. Electron and Ambipolar Transport in Organic Field-Effect Transistors. *Chem. Rev.* **2007**, *107* (4), 1296–1323.

(37) Klauk, H. Organic Thin-Film Transistors. *Chem. Soc. Rev.* **2010**, *39* (7), 2643–2666.

(38) Horowitz, G. Organic Thin Film Transistors: From Theory to Real Devices. *J. Mater. Res.* **2004**, *19* (7), 1946–1962.

(39) Padma, N.; Sawant, S. N.; Sudarsan, V.; Sen, S.; Gupta, S. K. Comparison of the Role of Holes and Electrons in Hysteresis and Threshold Voltage Stability of Organic Field Effect Transistors. *Phys. status solidi* **2013**, *210* (10), 2111–2120.

(40) Bolognesi, A.; Berliocchi, M.; Manenti, M.; DiCarlo, A.; Lugli, P.; Lmimouni, K.; Dufour,

C. Effects of Grain Boundaries, Field-Dependent Mobility, and Interface Trap States on the Electrical Characteristics of Pentacene TFT. *IEEE Trans. Electron Devices* **2004**, *51* (12), 1997–2003.

(41) Diao, Y.; Shaw, L.; Bao, Z.; Mannsfeld, S. C. B. Morphology Control Strategies for Solution-Processed Organic Semiconductor Thin Films. *Energy Environ. Sci.* **2014**, *7* (7), 2145–2159.

(42) Lee, S. S.; Kim, C. S.; Gomez, E. D.; Purushothaman, B.; Toney, M. F.; Wang, C.; Hexemer, A.; Anthony, J. E.; Loo, Y. Controlling Nucleation and Crystallization in Solution-processed Organic Semiconductors for Thin-film Transistors. *Adv. Mater.* **2009**, *21* (35), 3605–3609.

(43) Lu, Z.; Wang, C.; Deng, W.; Achille, M. T.; Jie, J.; Zhang, X. Meniscus-Guided Coating of Organic Crystalline Thin Films for High-Performance Organic Field-Effect Transistors. *J. Mater. Chem. C* **2020**, *8* (27), 9133–9146.

(44) Sunagawa, I. *Crystals: Growth, Morphology, & Perfection*; Cambridge University Press, 2007.

(45) Li, R.; Khan, H. U.; Payne, M. M.; Smilgies, D.; Anthony, J. E.; Amassian, A. Heterogeneous Nucleation Promotes Carrier Transport in Solution-processed Organic Field-effect Transistors. *Adv. Funct. Mater.* **2013**, *23* (3), 291–297.

(46) Wedl, B.; Resel, R.; Leising, G.; Kunert, B.; Salzmann, I.; Oehzelt, M.; Koch, N.; Vollmer, A.; Duhm, S.; Werzer, O. Crystallisation Kinetics in Thin Films of Dihexyl-Terthiophene: The Appearance of Polymorphic Phases. *RSC Adv.* **2012**, *2* (10), 4404–4414.

(47) Yang, X.; Chhasatia, V. H.; Shah, J.; Sun, Y. Coalescence, Evaporation and Particle Deposition of Consecutively Printed Colloidal Drops. *Soft Matter* **2012**, *8* (35), 9205–9213.

(48) Kumar, A. K. S.; Zhang, Y.; Li, D.; Compton, R. G. A Mini-Review: How Reliable Is the Drop Casting Technique? *Electrochem. commun.* **2020**, *121*, 106867.

(49) Kim, C. S.; Lee, S.; Gomez, E. D.; Anthony, J. E.; Loo, Y.-L. Solvent-Dependent Electrical Characteristics and Stability of Organic Thin-Film Transistors with Drop Cast Bis (Triisopropylsilylethynyl) Pentacene. *Appl. Phys. Lett.* **2008**, *93* (10).

(50) Rein, M. Phenomena of Liquid Drop Impact on Solid and Liquid Surfaces. *Fluid Dyn. Res.* **1993**, *12* (2), 61–93.

(51) Josserand, C.; Thoroddsen, S. T. Drop Impact on a Solid Surface. *Annu. Rev. Fluid Mech.* **2016**, *48*, 365–391.

(52) Yarin, A. L. Drop Impact Dynamics: Splashing, Spreading, Receding, Bouncing…. *Annu. Rev. Fluid Mech.* **2006**, *38* (1), 159–192.

(53) Ohara, T.; Matsumoto, Y.; Ohashi, H. The Film Formation Dynamics in Spin Coating. *Phys. Fluids A Fluid Dyn.* **1989**, *1* (12), 1949–1959.

(54) Norrman, K.; Ghanbari-Siahkali, A.; Larsen, N. B. 6 Studies of Spin-Coated Polymer Films. *Annu. Reports Sect. C (Physical Chem.)* **2005**, *101*, 174–201.

(55) Schubert, D. W.; Dunkel, T. Spin Coating from a Molecular Point of View: Its Concentration Regimes, Influence of Molar Mass and Distribution. *Mater. Res. Innov.* **2003**, *7* (5), 314–321.

(56) Sahu, N.; Parija, B.; Panigrahi, S. Fundamental Understanding and Modeling of Spin Coating Process: A Review. *Indian J. Phys.* **2009**, *83* (4), 493–502.

(57) Meyerhofer, D. Characteristics of Resist Films Produced by Spinning. *J. Appl. Phys.* **1978**, *49* (7), 3993–3997.

(58) Lai, J. H. An Investigation of Spin Coating of Electron Resists. *Polym. Eng. Sci.* **1979**, *19* (15), 1117–1121.

(59) Chen, B. T. Investigation of the Solvent-evaporation Effect on Spin Coating of Thin Films. *Polym. Eng. Sci.* **1983**, *23* (7), 399–403.

(60) Spangler, L. L.; Torkelson, J. M.; Royal, J. S. Influence of Solvent and Molecular Weight on Thickness and Surface Topography of Spin-coated Polymer Films. *Polym. Eng. Sci.* **1990**, *30* (11), 644–653.

(61) Daughton, W. J.; Givens, F. L. An Investigation of the Thickness Variation of Spun-on Thin Films Commonly Associated with the Semiconductor Industry. *J. Electrochem. Soc.* **1982**, *129* (1), 173–179.

(62) Wei Chou, K.; Ullah Khan, H.; Niazi, M. R.; Yan, B.; Li, R.; Payne, M. M.; Anthony, J. E.; Smilgies, D.-M.; Amassian, A. Late Stage Crystallization and Healing during Spin-Coating Enhance Carrier Transport in Small-Molecule Organic Semiconductors. *J. Mater. Chem. C* **2014**, *2* (28), 5681–5689.

(63) Manley, E. F.; Strzalka, J.; Fauvell, T. J.; Marks, T. J.; Chen, L. X. In Situ Analysis of Solvent and Additive Effects on Film Morphology Evolution in Spin-Cast Small-Molecule and Polymer Photovoltaic Materials. *Adv. Energy Mater.* **2018**, *8* (23), 1800611.

(64) Janneck, R.; Vercesi, F.; Heremans, P.; Genoe, J.; Rolin, C. Predictive Model for the Meniscus-Guided Coating of High-Quality Organic Single-Crystalline Thin Films. *Adv. Mater* **2016**, *28* (36), 8007–8013.

(65) Janneck, R.; Karagiannis, D.; Heremans, P.; Genoe, J.; Rolin, C. Influence of Solute Concentration on Meniscus-Guided Coating of Highly Crystalline Organic Thin Films. *Adv. Mater. Interfaces* **2019**, *6* (19), 1900614.

(66) Shaw, L.; Yan, H.; Gu, X.; Hayoz, P.; Weitz, R. T.; Kaelblein, D.; Toney, M. F.; Bao, Z. Microstructural Evolution of the Thin Films of a Donor–Acceptor Semiconducting Polymer Deposited by Meniscus-Guided Coating. *Macromolecules* **2018**, *51* (11), 4325–4340.

(67) Chen, M.; Peng, B.; Huang, S.; Chan, P. K. L. Understanding the Meniscus-guided Coating Parameters in Organic Field-effect-transistor Fabrications. *Adv. Funct. Mater.* **2020**, *30* (1), 1905963.

(68) Gojzewski, H.; Ghani, F.; Szybowicz, M. Thin Films of Copper Phthalocyanine Deposited by Solution Processing Methods. *Mater. Sci.* **2020**, *38* (1), 79–90.

(69) Ghani, F.; Gojzewski, H.; Riegler, H. Nucleation and Growth of Copper Phthalocyanine Aggregates Deposited from Solution on Planar Surfaces. *Appl. Surf. Sci.* **2015**, *351*, 969–976.

(70) Ghani, F.; Bochukov, I.; Fostiropoulos, K.; Riegler, H. Hybrid Solution/Vacuum-Processed Bilayer Heterojunction Organic Solar Cells: Structural Characterization and Performance. *Thin Solid Films* **2012**, *525*, 177–181.

(71) Chiong, J. A.; Zheng, Y.; Zhang, S.; Ma, G.; Wu, Y.; Ngaruka, G.; Lin, Y.; Gu, X.; Bao, Z.

Impact of Molecular Design on Degradation Lifetimes of Degradable Imine-Based Semiconducting Polymers. *J. Am. Chem. Soc.* **2022**, *144* (8), 3717–3726. https://doi.org/10.1021/jacs.1c12845.

(72) Kim, Y.-H.; Lee, Y. U.; Han, J.-I.; Han, S.-M.; Han, M.-K. Influence of Solvent on the Film Morphology, Crystallinity and Electrical Characteristics of Triisopropylsilyl Pentacene OTFTs. *J. Electrochem. Soc.* **2007**, *154* (12), H995–H998.

(73) Rubinger, C. P. L.; Haneef, H. F.; Hewitt, C.; Carroll, D.; Anthony, J. E.; Jurchescu, O. D. Influence of Solvent Additives on the Morphology and Electrical Properties of DiF-TES ADT Organic Field-Effect Transistors. *Org. Electron.* **2019**, *68*, 205–211.

(74) Wang, B.; Huang, W.; Chi, L.; Al-Hashimi, M.; Marks, T. J.; Facchetti, A. High-k Gate Dielectrics for Emerging Flexible and Stretchable Electronics. *Chem. Rev.* **2018**, *118* (11), 5690–5754.

(75) Park, D. Y.; Lee, H.; Kim, S.; Sim, Y.; Kang, Y.; Jang, G.; Kim, S.; Kwon, K.; Ryu, H. Recent Advances in Bioresorbable Biomedical Applications: From Materials to Devices. *Adv. Electron. Mater.* **2025**, *11* (10), 2400997.

(76) Kuciel, S.; Mazur, K.; Hebda, M. The Influence of Wood and Basalt Fibres on Mechanical, Thermal and Hydrothermal Properties of PLA Composites. *J. Polym. Environ.* **2020**, *28* (4), 1204–1215.

(77) Kim, Y.-H.; Moon, D.-G.; Han, J.-I. Organic TFT Array on a Paper Substrate. *IEEE Electron Device Lett.* **2004**, *25* (10), 702–704. https://doi.org/10.1109/LED.2004.836502.

(78) Zocco, A. T.; You, H.; Hagen, J. A.; Steckl, A. J. Pentacene Organic Thin-Film Transistors

on Flexible Paper and Glass Substrates. *Nanotechnology* **2014**, *25* (9), 94005.

(79) Kim, Y. H.; Moon, D. G.; Kim, W. K.; Han, J. I. Organic Thin-film Devices on Paper Substrates. *J. Soc. Inf. Disp.* **2005**, *13* (10), 829–833.

(80) Yang, Y.; Sun, B.; Zhao, X.; Yu, H.; Wang, B.; Li, J.; Tong, Y.; Tang, Q.; Liu, Y. Edible Polysaccharide-Based Ultraflexible Organic Transistors for Nutritive Electronics. *J. Mater. Chem. C* **2023**, *11* (26), 8808–8817.

(81) Rullyani, C.; Sung, C.-F.; Lin, H.-C.; Chu, C.-W. Flexible Organic Thin Film Transistors Incorporating a Biodegradable CO2-Based Polymer as the Substrate and Dielectric Material. *Sci. Rep.* **2018**, *8* (1), 8146.

(82) Hwang, S.; Song, J.; Huang, X.; Cheng, H.; Kang, S.; Kim, B. H.; Kim, J.; Yu, S.; Huang, Y.; Rogers, J. A. High-performance Biodegradable/Transient Electronics on Biodegradable Polymers. *Adv. Mater.* **2014**, *26* (23), 3905–3911.

(83) Cao, Y.; Uhrich, K. E. Biodegradable and Biocompatible Polymers for Electronic Applications: A Review. *J. Bioact. Compat. Polym.* **2019**, *34* (1), 3–15.

(84) Goument, C.; Gerges, T.; Lombard, P.; Lakhdar, H.; Arli, M.; Gilmus, V. M.; Lambert, S. A.; Allard, B.; Charmeau, J.-Y.; Cabrera, M. In-Mold Electronics on Poly (Lactic Acid): Towards a More Sustainable Mass Production of Plastronic Devices. *Int. J. Adv. Manuf. Technol.* **2023**, *125* (5), 2643–2660.

(85) Mittal, P.; Yadav, S.; Negi, S. Advancements for Organic Thin Film Transistors: Structures, Materials, Performance Parameters, Influencing Factors, Models, Fabrication, Reliability and Applications. *Mater. Sci. Semicond. Process.* **2021**, *133*, 105975.

(86) Yi, H. T.; Payne, M. M.; Anthony, J. E.; Podzorov, V. Ultra-Flexible Solution-Processed Organic Field-Effect Transistors. *Nat. Commun.* **2012**, *3* (1), 1259.

(87) Elmowafy, E. M.; Tiboni, M.; Soliman, M. E. Biocompatibility, Biodegradation and Biomedical Applications of Poly (Lactic Acid)/Poly (Lactic-Co-Glycolic Acid) Micro and Nanoparticles. *J. Pharm. Investig.* **2019**, *49* (4), 347–380.

(88) Aguirre, C. M.; Levesque, P. L.; Paillet, M.; Lapointe, F.; St-Antoine, B. C.; Desjardins, P.; Martel, R. The Role of the Oxygen/Water Redox Couple in Suppressing Electron Conduction in Field-Effect Transistors. *Adv. Mater* **2009**, *21* (30), 3087–3091.

(89) Su, Y.; Wang, C.; Xie, W.; Xie, F.; Chen, J.; Zhao, N.; Xu, J. Low-Voltage Organic Field-Effect Transistors (OFETs) with Solution-Processed Metal-Oxide as Gate Dielectric. *ACS Appl. Mater. Interfaces* **2011**, *3* (12), 4662–4667.

(90) Lee, E.; Ko, J.; Lim, K.; Kim, K.; Park, S. Y.; Myoung, J. M.; Kim, Y. S. Gate Capacitance-dependent Field-effect Mobility in Solution-processed Oxide Semiconductor Thin-film Transistors. *Adv. Funct. Mater.* **2014**, *24* (29), 4689–4697.

(91) Bardini, L. EIS 101, an Introduction to Electrochemical Spectroscopy. *What was a website is now available as a self-contained PDF. Available online https://www.researchgate.net/publication/280009629_EIS_101_an_introduction_to_electrochemical_spectroscopy_What_was_a_website_is_now_available_as_a_selfcontained_PDF (accessed 24 April 2020)* **2015**.

(92) Ahmad, Z. Polymer Dielectric Materials. In *Dielectric material*; IntechOpen, 2012.

(93) Joshi, J. H.; Kanchan, D. K.; Joshi, M. J.; Jethva, H. O.; Parikh, K. D. Dielectric Relaxation,

Complex Impedance and Modulus Spectroscopic Studies of Mix Phase Rod like Cobalt Sulfide Nanoparticles. *Mater. Res. Bull.* **2017**, *93*, 63–73.

(94) Teja Karri, B. R.; Gupta, N. Hybrid Bilayer Gate Dielectric-Based Organic Thin Film Transistors. *Bull. Mater. Sci.* **2019**, *42* (1), 2.

(95) Chen, X.; Zhang, Y.; Guan, X.; Zhang, H. Facile Synthesis of Solution-Processed Silica and Polyvinyl Phenol Hybrid Dielectric for Flexible Organic Transistors. *Nanomaterials* **2020**, *10* (4), 806.

(96) Psarras, G. C. Fundamentals of Dielectric Theories. In *Dielectric polymer materials for high-density energy storage*; Elsevier, 2018; pp 11–57.

(97) Gupta, T.; Gupta, T. Dielectric Materials. *Copp. Interconnect Technol.* **2009**, 67–110.

(98) Ortiz, R. P.; Facchetti, A.; Marks, T. J. High-k Organic, Inorganic, and Hybrid Dielectrics for Low-Voltage Organic Field-Effect Transistors. *Chem. Rev.* **2010**, *110* (1), 205–239.

(99) Luo, Q.; Shen, H.; Zhou, G.; Xu, X. A Mini-Review on the Dielectric Properties of Cellulose and Nanocellulose-Based Materials as Electronic Components. *Carbohydr. Polym.* **2023**, *303*, 120449.

(100) Petritz, A.; Wolfberger, A.; Fian, A.; Irimia-Vladu, M.; Haase, A.; Gold, H.; Rothländer, T.; Grießer, T.; Stadlober, B. Cellulose as Biodegradable High-k Dielectric Layer in Organic Complementary Inverters. *Appl. Phys. Lett.* **2013**, *103* (15).

(101) Rullyani, C.; Ramesh, M.; Sung, C.-F.; Lin, H.-C.; Chu, C.-W. Natural Polymers for Disposable Organic Thin Film Transistors. *Org. Electron.* **2018**, *54*, 154–160.

(102) Liu, Y. H.; Qiang Zhu, L.; Shi, Y.; Wan, Q. Proton Conducting Sodium Alginate Electrolyte Laterally Coupled Low-Voltage Oxide-Based Transistors. *Appl. Phys. Lett.* **2014**, *104* (13).

(103) Seck, M.; Mohammadian, N.; Diallo, A. K.; Faraji, S.; Erouel, M.; Bouguila, N.; Ndiaye, D.; Khirouni, K.; Majewski, L. A. Organic FETs Using Biodegradable Almond Gum as Gate Dielectric: A Promising Way towards Green Electronics. *Org. Electron.* **2020**, *83*, 105735.

(104) Chiellini, E.; Corti, A.; D'Antone, S.; Solaro, R. Biodegradation of Poly (Vinyl Alcohol) Based Materials. *Prog. Polym. Sci.* **2003**, *28* (6), 963–1014.

(105) Fukushima, K.; Abbate, C.; Tabuani, D.; Gennari, M.; Camino, G. Biodegradation of Poly (Lactic Acid) and Its Nanocomposites. *Polym. Degrad. Stab.* **2009**, *94* (10), 1646–1655.

(106) Hosseini, E. S.; Dervin, S.; Ganguly, P.; Dahiya, R. Biodegradable Materials for Sustainable Health Monitoring Devices. *ACS Appl. bio Mater.* **2020**, *4* (1), 163–194.

(107) Li, J.; Tang, W.; Wang, Q.; Sun, W.; Zhang, Q.; Guo, X.; Wang, X.; Yan, F. Solution-Processable Organic and Hybrid Gate Dielectrics for Printed Electronics. *Mater. Sci. Eng. R Reports* **2018**, *127*, 1–36.

(108) Nketia-Yawson, B.; Noh, Y. Recent Progress on High-capacitance Polymer Gate Dielectrics for Flexible Low-voltage Transistors. *Adv. Funct. Mater.* **2018**, *28* (42), 1802201.

(109) Veres, J.; Ogier, S. D.; Leeming, S. W.; Cupertino, D. C.; Mohialdin Khaffaf, S. Low-k Insulators as the Choice of Dielectrics in Organic Field-effect Transistors. *Adv. Funct. Mater.* **2003**, *13* (3), 199–204.

(110) Merari Masillamani, A.; Orgiu, E.; Samorì, P. Effect of the Molecular Weight of the Polymer Gate Dielectric on the Performances of Solution-Processed Ambipolar OTFTs. *J. Mater. Chem. C* **2013**, *1* (46), 7725–7730.

(111) Lee, S.; Koo, B.; Shin, J.; Lee, E.; Park, H.; Kim, H. Effects of Hydroxyl Groups in Polymeric Dielectrics on Organic Transistor Performance. *Appl. Phys. Lett.* **2006**, *88* (16).

(112) Yang, F.-Y.; Chang, K.-J.; Hsu, M.-Y.; Liu, C.-C. Low-Operating-Voltage Polymeric Transistor with Solution-Processed Low-k Polymer/High-k Metal-Oxide Bilayer Insulators. *Org. Electron.* **2008**, *9* (5), 925–929.

(113) Zhang, H.; Zhang, F.; Sun, J.; Zhang, M.; Hu, Y.; Lou, Z.; Hou, Y.; Teng, F. Solution-Processed Organic Field-Effect Transistors with Cross-Linked Poly (4-Vinylphenol)/Polyvinyl Alcohol Bilayer Dielectrics. *Appl. Surf. Sci.* **2019**, *478*, 699–707.

(114) Faraji, S.; Hashimoto, T.; Turner, M. L.; Majewski, L. A. Solution-Processed Nanocomposite Dielectrics for Low Voltage Operated OFETs. *Org. Electron.* **2015**, *17*, 178–183.

(115) Sun, Y.; Liu, Y.; Wang, Y.; Di, C.; Wu, W.; Yu, G. Polymer Gate Dielectrics with Self-Assembled Monolayers for High-Mobility Organic Thin-Film Transistors Based on Copper Phthalocyanine. *Appl. Phys. A* **2009**, *95*, 777–780.

(116) Jin, S. H.; Yu, J. S.; Kim, J. W.; Lee, C. A.; Park, B.; Lee, J. D.; Lee, J. H. 34.2: PMMA Buffer-Layer Effects on Electrical Performance of Pentacene OTFTs with a Cross-linked PVA Gate Insulator on a Flexible Substrate. In *SID Symposium Digest of Technical Papers*; Wiley Online Library, 2003; Vol. 34, pp 1088–1091.

(117) Lee, C. A.; Park, D. W.; Jin, S. H.; Park, I. H.; Lee, J. D.; Park, B.-G. Hysteresis Mechanism and Reduction Method in the Bottom-Contact Pentacene Thin-Film Transistors with Cross-Linked Poly (Vinyl Alcohol) Gate Insulator. *Appl. Phys. Lett.* **2006**, *88* (25).

(118) Wang, W.; Ma, D.; Pan, S.; Yang, Y. Hysteresis Mechanism in Low-Voltage and High Mobility Pentacene Thin-Film Transistors with Polyvinyl Alcohol Dielectric. *Appl. Phys. Lett.* **2012**, *101* (3).

(119) Lee, S.-H.; Kim, D.-Y.; Noh, Y.-Y. Solution-Processed Polymer-Sorted Semiconducting Carbon Nanotube Network Transistors with Low-k/High-k Bilayer Polymer Dielectrics. *Appl. Phys. Lett.* **2017**, *111* (12).

(120) Subbarao, N. V. V; Gedda, M.; Iyer, P. K.; Goswami, D. K. Enhanced Environmental Stability Induced by Effective Polarization of a Polar Dielectric Layer in a Trilayer Dielectric System of Organic Field-Effect Transistors: A Quantitative Study. *ACS Appl. Mater. Interfaces* **2015**, *7* (3), 1915–1924.

(121) Li, Q.; Li, S.; Yang, D.; Su, W.; Wang, Y.; Zhou, W.; Liu, H.; Xie, S. Designing Hybrid Gate Dielectric for Fully Printing High-Performance Carbon Nanotube Thin Film Transistors. *Nanotechnology* **2017**, *28* (43), 435203.

(122) Wang, C.-Y.; Fuentes-Hernandez, C.; Liu, J.-C.; Dindar, A.; Choi, S.; Youngblood, J. P.; Moon, R. J.; Kippelen, B. Stable Low-Voltage Operation Top-Gate Organic Field-Effect Transistors on Cellulose Nanocrystal Substrates. *ACS Appl. Mater. Interfaces* **2015**, *7* (8), 4804–4808.

(123) Subbarao, N. V. V; Mandal, S.; Gedda, M.; Iyer, P. K.; Goswami, D. K. Effect of

Temperature on Hysteresis of Dipolar Dielectric Layer Based Organic Field-Effect Transistors: A Temperature Sensing Mechanism. *Sensors Actuators A Phys.* **2018**, *269*, 491–499.

(124) Tousignant, M. N.; Lin, Z. S.; Brusso, J.; Lessard, B. H. Interfacial Ultraviolet Cross-Linking of Green Bilayer Dielectrics. *ACS Appl. Mater. Interfaces* **2023**, *15* (2), 3680–3688.

(125) Tousignant, M. N.; Rice, N. A.; Niskanen, J.; Richard, C. M.; Ritaine, D.; Adronov, A.; Lessard, B. H. High Performance Organic Electronic Devices Based on a Green Hybrid Dielectric. *Adv. Electron. Mater.* **2021**, *7* (10), 2100700.

(126) Ronnasi, B.; Tousignant, M. N.; Lessard, B. H. Chitosan Based Dielectrics for Use in Single Walled Carbon Nanotube-Based Thin Film Transistors. *J. Mater. Chem. C* **2023**, *11* (9), 3197–3205.

(127) Konwar, G.; Saxena, P.; Raghuwanshi, V.; Rahi, S.; Tiwari, S. P. High Performance Flexible Organic Transistors with Biodegradable Natural-Protein Based Gate Dielectrics. In *2022 29th International Workshop on Active-Matrix Flatpanel Displays and Devices (AM-FPD)*; IEEE, 2022; pp 190–193.

(128) Konwar, G.; Saxena, P.; Raghuwanshi, V.; Rahi, S.; Tiwari, S. P. Solution-Processed Biopolymer Dielectric Based Organic Field-Effect Transistors for Sustainable Electronics. In *2022 6th IEEE Electron Devices Technology & Manufacturing Conference (EDTM)*; IEEE, 2022; pp 107–109.

(129) Bao, Z.; Dodabalapur, A.; Lovinger, A. J. Soluble and Processable Regioregular Poly (3-hexylthiophene) for Thin Film Field-effect Transistor Applications with High Mobility.

Appl. Phys. Lett. **1996**, *69* (26), 4108–4110.

(130) Qiao, Y.; Guo, Y.; Yu, C.; Zhang, F.; Xu, W.; Liu, Y.; Zhu, D. Diketopyrrolopyrrole-Containing Quinoidal Small Molecules for High-Performance, Air-Stable, and Solution-Processable n-Channel Organic Field-Effect Transistors. *J. Am. Chem. Soc.* **2012**, *134* (9), 4084–4087.

(131) Chen, H.; Guo, Y.; Yu, G.; Zhao, Y.; Zhang, J.; Gao, D.; Liu, H.; Liu, Y. Highly Π-extended Copolymers with Diketopyrrolopyrrole Moieties for High-performance Field-effect Transistors. *Adv. Mater.* **2012**, *24* (34), 4618–4622.

(132) Lee, S.; Moon, G. D.; Jeong, U. Continuous Production of Uniform Poly (3-Hexylthiophene)(P3HT) Nanofibers by Electrospinning and Their Electrical Properties. *J. Mater. Chem.* **2009**, *19* (6), 743–748.

(133) Subramanian, A.; Krishnan, U. M.; Sethuraman, S. Axially Aligned Electrically Conducting Biodegradable Nanofibers for Neural Regeneration. *J. Mater. Sci. Mater. Med.* **2012**, *23*, 1797–1809.

(134) Noriega, R.; Rivnay, J.; Vandewal, K.; Koch, F. P. V; Stingelin, N.; Smith, P.; Toney, M. F.; Salleo, A. A General Relationship between Disorder, Aggregation and Charge Transport in Conjugated Polymers. *Nat. Mater.* **2013**, *12* (11), 1038–1044.

(135) Wang, S.; Fabiano, S.; Himmelberger, S.; Puzinas, S.; Crispin, X.; Salleo, A.; Berggren, M. Experimental Evidence That Short-Range Intermolecular Aggregation Is Sufficient for Efficient Charge Transport in Conjugated Polymers. *Proc. Natl. Acad. Sci.* **2015**, *112* (34), 10599–10604.

(136) Sugiyama, F.; Kleinschmidt, A. T.; Kayser, L. V; Alkhadra, M. A.; Wan, J. M.-H.; Chiang, A. S.-C.; Rodriquez, D.; Root, S. E.; Savagatrup, S.; Lipomi, D. J. Stretchable and Degradable Semiconducting Block Copolymers. *Macromolecules* **2018**, *51* (15), 5944–5949.

(137) Xu, J.; Wang, S.; Wang, G.-J. N.; Zhu, C.; Luo, S.; Jin, L.; Gu, X.; Chen, S.; Feig, V. R.; To, J. W. F. Highly Stretchable Polymer Semiconductor Films through the Nanoconfinement Effect. *Science.* **2017**, *355* (6320), 59–64.

(138) Worfolk, B. J.; Andrews, S. C.; Park, S.; Reinspach, J.; Liu, N.; Toney, M. F.; Mannsfeld, S. C. B.; Bao, Z. Ultrahigh Electrical Conductivity in Solution-Sheared Polymeric Transparent Films. *Proc. Natl. Acad. Sci.* **2015**, *112* (46), 14138–14143.

(139) Machado, J. M.; Karasz, F. E.; Lenz, R. W. Electrically Conducting Polymer Blends. *Polymer (Guildf).* **1988**, *29* (8), 1412–1417.

(140) Cao, Y.; Smith, P.; Heeger, A. J. Counter-Ion Induced Processibility of Conducting Polyaniline and of Conducting Polyblends of Polyaniline in Bulk Polymers. *Synth. Met.* **1992**, *48* (1), 91–97.

(141) Knackstedt, M. A.; Roberts, A. P. Morphology and Macroscopic Properties of Conducting Polymer Blends. *Macromolecules* **1996**, *29* (4), 1369–1371.

(142) Wang, S.; Guan, S.; Wang, J.; Liu, H.; Liu, T.; Ma, X.; Cui, Z. Fabrication and Characterization of Conductive Poly (3, 4-Ethylenedioxythiophene) Doped with Hyaluronic Acid/Poly (l-Lactic Acid) Composite Film for Biomedical Application. *J. Biosci. Bioeng.* **2017**, *123* (1), 116–125.

(143) Armelin, E.; Gomes, A. L.; Pérez-Madrigal, M. M.; Puiggali, J.; Franco, L.; Valle, L. J. del; Rodriguez-Galan, A.; Campos, J. S. de C.; Ferrer-Anglada, N.; Aleman, C. Biodegradable Free-Standing Nanomembranes of Conducting Polymer: Polyester Blends as Bioactive Platforms for Tissue Engineering. *J. Mater. Chem.* **2011**, *22* (2), 585–594.

(144) Shi, G.; Rouabhia, M.; Wang, Z.; Dao, L. H.; Zhang, Z. A Novel Electrically Conductive and Biodegradable Composite Made of Polypyrrole Nanoparticles and Polylactide. *Biomaterials* **2004**, *25* (13), 2477–2488.

(145) Schroeder, B. C.; Chiu, Y.; Gu, X.; Zhou, Y.; Xu, J.; Lopez, J.; Lu, C.; Toney, M. F.; Bao, Z. Non-conjugated Flexible Linkers in Semiconducting Polymers: A Pathway to Improved Processability without Compromising Device Performance. *Adv. Electron. Mater.* **2016**, *2* (7), 1600104.

(146) Gasperini, A.; Bivaud, S.; Sivula, K. Controlling Conjugated Polymer Morphology and Charge Carrier Transport with a Flexible-Linker Approach. *Chem. Sci.* **2014**, *5* (12), 4922–4927.

(147) Zhao, Y.; Zhao, X.; Zang, Y.; Di, C.; Diao, Y.; Mei, J. Conjugation-Break Spacers in Semiconducting Polymers: Impact on Polymer Processability and Charge Transport Properties. *Macromolecules* **2015**, *48* (7), 2048–2053.

(148) Oh, J. Y.; Rondeau-Gagné, S.; Chiu, Y.-C.; Chortos, A.; Lissel, F.; Wang, G.-J. N.; Schroeder, B. C.; Kurosawa, T.; Lopez, J.; Katsumata, T. Intrinsically Stretchable and Healable Semiconducting Polymer for Organic Transistors. *Nature* **2016**, *539* (7629), 411–415.

(149) Temenoff, J. S.; Mikos, A. G. *Biomaterials: The Intersection of Biology and Materials Science*; Pearson/Prentice Hall Upper Saddle River, NJ, USA, 2008; Vol. 1.

(150) Champion, J. A.; Walker, A.; Mitragotri, S. Role of Particle Size in Phagocytosis of Polymeric Microspheres. *Pharm. Res.* **2008**, *25* (8), 1815–1821.

(151) Runge, M. B.; Dadsetan, M.; Baltrusaitis, J.; Knight, A. M.; Ruesink, T.; Lazcano, E. A.; Lu, L.; Windebank, A. J.; Yaszemski, M. J. The Development of Electrically Conductive Polycaprolactone Fumarate–Polypyrrole Composite Materials for Nerve Regeneration. *Biomaterials* **2010**, *31* (23), 5916–5926.

(152) Li, M.; Guo, Y.; Wei, Y.; MacDiarmid, A. G.; Lelkes, P. I. Electrospinning Polyaniline-Contained Gelatin Nanofibers for Tissue Engineering Applications. *Biomaterials* **2006**, *27* (13), 2705–2715.

(153) Guo, B.; Finne-Wistrand, A.; Albertsson, A. C. Enhanced Electrical Conductivity by Macromolecular Architecture: Hyperbranched Electroactive and Degradable Block Copolymers Based on Poly(ε-Caprolactone) and Aniline Pentamer. *Macromolecules* **2010**, *43* (10), 4472–4480. https://doi.org/10.1021/ma100530k.

(154) Huang, L.; Hu, J.; Lang, L.; Wang, X.; Zhang, P.; Jing, X.; Wang, X.; Chen, X.; Lelkes, P. I.; MacDiarmid, A. G. Synthesis and Characterization of Electroactive and Biodegradable ABA Block Copolymer of Polylactide and Aniline Pentamer. *Biomaterials* **2007**, *28* (10), 1741–1751.

(155) Li, L.; Ge, J.; Guo, B.; Ma, P. X. In Situ Forming Biodegradable Electroactive Hydrogels. *Polym. Chem.* **2014**, *5* (8), 2880–2890.

(156) Rivers, T. J.; Hudson, T. W.; Schmidt, C. E. Synthesis of a Novel, Biodegradable Electrically Conducting Polymer for Biomedical Applications. *Adv. Funct. Mater.* **2002**, *12* (1), 33–37.

(157) Guimard, N. K. E.; Sessler, J. L.; Schmidt, C. E. Towards a Biocompatible, Biodegradable Copolymer Incorporating Electroactive Oligothiophene Units. *Macromolecules* **2009**, *42* (2), 502.

(158) Xu, C.; Huang, Y.; Yepez, G.; Wei, Z.; Liu, F.; Bugarin, A.; Tang, L.; Hong, Y. Development of Dopant-Free Conductive Bioelastomers. *Sci. Rep.* **2016**, *6* (1), 34451.

(159) Choi, Y.; Koo, J.; Rogers, J. A. Inorganic Materials for Transient Electronics in Biomedical Applications. *MRS Bull.* **2020**, *45* (2), 103–112.

(160) Konwar, G.; Rahi, S.; Tiwari, S. P. Decomposable Flexible Organic Transistors with a Cellulose-Based Gate Dielectric and Substrate for Biodegradable Electronics. *ACS Appl. Mater. Interfaces* **2023**, *15* (29), 35261–35271.

(161) Zhao, C.; Cheung, K. M.; Huang, I.-W.; Yang, H.; Nakatsuka, N.; Liu, W.; Cao, Y.; Man, T.; Weiss, P. S.; Monbouquette, H. G. Implantable Aptamer–Field-Effect Transistor Neuroprobes for in Vivo Neurotransmitter Monitoring. *Sci. Adv.* **2021**, *7* (48), eabj7422.

(162) Lee, W.; Kobayashi, S.; Nagase, M.; Jimbo, Y.; Saito, I.; Inoue, Y.; Yambe, T.; Sekino, M.; Malliaras, G. G.; Yokota, T. Nonthrombogenic, Stretchable, Active Multielectrode Array for Electroanatomical Mapping. *Sci. Adv.* **2018**, *4* (10), eaau2426.

(163) Wu, M.; Yao, K.; Huang, N.; Li, H.; Zhou, J.; Shi, R.; Li, J.; Huang, X.; Li, J.; Jia, H. Ultrathin, Soft, Bioresorbable Organic Electrochemical Transistors for Transient

Spatiotemporal Mapping of Brain Activity. *Adv. Sci.* **2023**, 2300504.

(164) Verma, A.; Mishra, V. N.; Prakash, R. Self-Assembled Au/P3HT, High-k Bilayer Dielectric-Based Solution Processed Low Voltage OTFT for Multiparametric Ammonia Sensor at Room Temperature. *IEEE Trans. Electron Devices* **2022**, *70* (1), 281–287.

(165) Verma, A.; Mishra, V. N.; Prakash, R. A Self-Aligned, Solution-Processed Low-Voltage Operated Organic Thin-Film Transistor for Ammonia Gas Sensing at Room Temperature. *IEEE Sens. J.* **2023**, *23* (6), 5561–5568.

(166) Zhuang, X.; Zhang, D.; Wang, X.; Yu, X.; Yu, J. Biocompatible and Degradable Gelatin Dielectric Based Low-Operating Voltage Organic Transistors for Ultra-High Sensitivity NH3 Detection. *Appl. Phys. Lett.* **2018**, *113* (26).

(167) Li, B.; Lai, P. T.; Tang, W. M. Temperature Dependence of Sensing Characteristics for OTFT-Based Hydrogen Sensor. *IEEE Trans. Electron Devices* **2020**, *67* (4), 1776–1780. https://doi.org/10.1109/TED.2020.2973288.

(168) Zhu, C.; Wu, H. C.; Nyikayaramba, G.; Bao, Z.; Murmann, B. Intrinsically Stretchable Temperature Sensor Based on Organic Thin-Film Transistors. *IEEE Electron Device Lett.* **2019**, *40* (10), 1630–1633. https://doi.org/10.1109/LED.2019.2933838.

(169) Yin, M.-J.; Li, Z.-R.; Lv, T.-R.; Yong, K.-T.; An, Q.-F. Low-Voltage Driven Flexible Organic Thin-Film Transistor Humidity Sensors. *Sensors Actuators B Chem.* **2021**, *339*, 129887.

(170) Wu, X.; Ma, Y.; Zhang, G.; Chu, Y.; Du, J.; Zhang, Y.; Li, Z.; Duan, Y.; Fan, Z.; Huang, J. Thermally Stable, Biocompatible, and Flexible Organic Field-effect Transistors and Their

Application in Temperature Sensing Arrays for Artificial Skin. *Adv. Funct. Mater.* **2015**, *25* (14), 2138–2146.

(171) Comeau, Z. J.; Boileau, N. T.; Lee, T.; Melville, O. A.; Rice, N. A.; Troung, Y.; Harris, C. S.; Lessard, B. H.; Shuhendler, A. J. On-the-Spot Detection and Speciation of Cannabinoids Using Organic Thin-Film Transistors. *ACS sensors* **2019**, *4* (10), 2706–2715.

Chapter 2: Cytocompatible, Disintegrable, Low-Voltage Operation n-Type Organic Thin Film Transistors

This chapter was published in the journal "Materials Advances": M. Ali, B. Ronnasi, M. Ourabi, J.H. Park, J.-P. St-Pierre, C.-H. Kim, B.H. Lessard, Cytocompatible, disintegrable, low-voltage operation n-type organic thin film transistors, Mater. Adv. 2025, 6, 557–568.

Context

For this work, I investigated the design and fabrication of a fully disintegrable, biocompatible n-type OTFT capable of operating at low voltages. As outlined in Chapter 1, one of the major barriers to sustainable organic electronics is the reliance on non-degradable dielectric and substrate materials, which contribute to growing electronic waste. Building on our group's prior work combining a PVA/PCL bilayer dielectric, I aimed to pair this biodegradable dielectric with a biodegradable PLA substrate and an n-type bis(pentafluorophenoxy) silicon phthalocyanine (F_{10}-SiPc) semiconductor. I hypothesized that this combination could reduce the V_T of the device relative to a conventional SiO_2 dielectric while remaining fully disintegrable in aqueous conditions and non-cytotoxic to mammalian cells. I was particularly interested in identifying the processing conditions, including gate electrode surface treatment and annealing temperature, needed to fabricate working devices on a temperature-sensitive PLA substrate, and in evaluating the resulting devices' electrical performance, degradation behavior, and cytocompatibility.

Contribution

I fabricated the OTFT devices, performed electrical characterization, and carried out the degradation studies. Ronnasi and Ourabi assisted in device fabrication and processing optimization. Park and Dr. Kim performed the numerical device simulations. Dr. St-Pierre

performed the cytotoxicity evaluation of the degradation products. I wrote the manuscript with input and revisions from Dr. Lessard and other co-authors.

2.1 Abstract

The constant demands for better performance of consumer electronics have led to shorter usage lifespans, resulting in a significant increase in electronic waste (e-waste). Developing electronics which can be easily broken down and recycled is a promising strategy to tackle this growing e-waste challenge. Herein, we report a biocompatible and degradable OTFT utilizing a biocompatible semiconductor with a biodegradable dielectric and substrate. We present the first OTFT based on F_{10}-SiPc with integrating PVA and PCL bilayer as the dielectric, leading to a drop in V_T from 12.7 V to -0.97 V, versus using SiO_2 while maintaining similar μ values. We demonstrate the importance of the annealing temperature on PLA substrate roughness and gate electrode surface chemistry for the fabrication of working OTFT devices. We then demonstrate that the bendable OTFTs could easily be dissolved in PBS solution at room temperature in under a month, which is a crucial aspect for ensuring eco-sustainability in electronic devices. Finally, incubation of the degradation products with fibroblastic cells did not affect cell viability, suggesting that they are non-cytotoxic. These cytocompatible disintegrable OTFTs with low operating voltages will find applications in bioresorbable electronics and constitute a step towards minimizing e-waste.

2.2 Introduction

In 2021, the United Nations released a report estimating that every person will produce roughly 7.6 kg of e-waste, leading to 57.4 million metric tonnes (MMT)[1] of e-waste. This number is predicted to rise to 74 MMT by 2030 if left uncontrolled. The need to consider the environmental effects of essential electronic components like transistors and capacitors during production and

disposal is growing due to the increasing demand for these devices worldwide. Sustainable and environmentally friendly electronics are becoming increasingly important, from reducing the risks linked to e-waste to paving the way for new generation of wearable and implantable electronics.[2–5] The growing number of transient electronic applications such as food package sensors or single-use biosensors is also causing concern for the e-waste problem and providing an opportunity for the development of non-toxic biodegradable electronics.[6,7]

The use of thin, plastic substrates in the fabrication of electrical devices has the advantage of lowering the total mass of the systems and imparting flexible characteristics which can lead to new applications such as wearable electronics.[8,9] Nevertheless, there are intrinsic disadvantages to using plastic substrates, including their disintegration into microplastics that can then find their way into our soil and groundwater, contributing to environmental contamination.[10] Consequently, the use of plastic substrates in flexible electronics that are not biodegradable or recyclable is unsustainable.[11] One of the challenges associated with using biodegradable substrates such as PLA is that the T_g of these materials is very low, which makes it challenging to integrate into high-temperature manufacturing processes like the manufacturing of silicon semiconductors. For organic electronics, the semiconductor is carbon-based and can be deposited at lower temperatures, enabling integration onto plastic substrates while providing low energy requirements and potential economic incentives.[12] OTFTs are electrical switches and are basic components in more complex circuits finding applications in next generation biological and chemical sensors,[13] health monitors,[14] stretchable devices,[15] and electronic skin.[16] Research on OTFT development has focused primarily on improving device performance with little attention to assessing the biocompatibility and environmental impact of the resulting materials.[17,18]

Biodegradable OTFTs require biodegradable substrates, dielectrics, electrodes, semiconductors, and peripheral materials such as encapsulating materials. Biobased materials, such as PLA, PHAs, starch blends, or cellulose-based polymers, are promising substrates if the processing temperatures can be kept <150°C.[19] However, biodegradable dielectrics with desired physical and electrical properties are rare. PVA is a bioresorbable dielectric that can be easily dissolved in environmentally friendly solvents such as water and breaks down naturally when exposed to suitable microorganisms.[20] PVA has been previously used as a dielectric material in sensors[21] and OTFTs, either as a homopolymer or as a blend of other materials.[22,23] However, PVA also presents challenges; its printing is difficult often requiring careful optimization such as the addition of a viscosity enhancer[24] and the resulting hydrophilic film is susceptible to moisture resulting in reduced reliability and stability of fabricated devices.[25,26] Our group recently developed PVA with thermally crosslinked diisocyanate-terminated polycaprolactone (TPCL) high-k/low-k bilayer dielectrics. The bilayer combined the desired electrical properties and high dielectric constant of the PVA with the moisture resistance of PCL, which also provides better surface matching for the subsequent deposition of the semiconductor. To further improve the shelf life and the ease of large-scale processing we then synthesized benzodioxinone-terminated PCL layer, which can be coupled to the PVA dielectric surface via UV radiation.[27] High-k/low-k bilayer dielectrics have shown several advantages, such as reduced charge trapping, improved device stability, facilitation of orthogonal processing, and prevention of direct interaction between the hydroxyl groups of PVA and the semiconductor.[28–30] The PCL layer acts as a protective coating for the PVA layer, creating a less polar environment at the interface between the dielectric and semiconductor.[31,32]

Phthalocyanines (Pc) are promising semiconductors used in OTFTs that are produced on the ton scale annually and are commonly used as blue and green pigments in a variety of applications, including textiles, plastics, automotive paints, and others.[33–35] Silicon Phthalocyanines (R_2-SiPc) are a class of tetravalent Pc with axial groups that can be used as handles to impart functionalities onto the molecule such as solubility or solid state engineering amenability. Their strong near-infrared (NIR) emission has also stimulated their prospective use in both in vitro and in vivo bioimaging.[36–40] Our group has demonstrated relatively better n-type performance of various R_2-SiPc derivatives in OTFTs.[41–45] In most cases R_2-SiPc based OTFTs suffer from high V_T making them unsuitable for use in consumer electronics (< 3 V) or in combination with printed batteries (< 1.5 V).[46,47] The interface between the dielectric and semiconductor in OTFT devices plays a pivotal role in enhancing charge transport by mitigating charge traps and reducing V_T.[48–50] Hybrid gate dielectric combinations of inorganic/organic bilayers are commonly employed to achieve high-performance organic transistors.[51] Nevertheless, their non-degradability emphasizes the need for pristine layers of biodegradable materials with a high *k*. Recently, our group published the first R_2-SiPc paired with a polymer dielectric based on methyl methacrylate and dimethyl aminoethyl methacrylate copolymers (P(MMA-co-DMAEMA)), attaining near-zero V_T.[52] Therefore, this study demonstrates the potential for using polymer dielectrics in combination with R_2-SiPc semiconductors in OTFTs.

In this work, we present a disintegrable and biocompatible n-type OTFT with low V_T, based on R_2-SiPc OTFT utilizing a biodegradable bilayer PVA/UV-PCL as a gate dielectric with a biodegradable PLA substrate. Utilizing UV-PCL increased device stability and ease of processing while maintaining its encapsulation characteristics and moisture resistance for the PVA layer. We also demonstrate the aqueous disintegration of the resulting OTFTs into non-cytotoxic degradation

products. These results demonstrate the broad applicability of low-voltage n-type and bioresorbable polymer dielectrics that employ scalable, economically viable R_2-SiPc semiconductors.

2.3 Results and discussion

In selecting the active materials, we focused on utilizing polymers that exhibit both biocompatibility and biodegradability, exhibit adequate electrical properties, and are soluble in various solvent systems enabling solution processing into thin films. **Figure 2.1** illustrates schematically the design of biocompatible and disintegrable OTFTs fabricated with BGTC architecture based on a PLA substrate, a bilayer PVA/PCL dielectric and a R_2-SiPc semiconductor. The substrate, which makes up 99.89% of the overall mass of the device,[53] was chosen to be made of PLA, a linear biodegradable thermoplastic polyester. The physical attributes of PLA provided constraints for further device processing as a result of (i) a low T_m, low T_g, (ii) low chemical resistance when exposed to organic solvents, and incompatibility with orthogonal processing. These characteristics indicate the need to use mild downstream processing conditions. Here, we employ water-soluble PVA as a solution-processable dielectric. PLA, PVA, and PCL are economical, easily accessible, and have a well-established history in various biomedical devices used in clinical settings.[53] The development of ecologically benign semiconductor materials is another critical step to overcome when fabricating fully decomposable OTFT devices.[54] R_2-SiPcs exhibit non-hazardous and biocompatible properties, making them promising candidates for degradable OTFTs. Gold electrodes are used in the OTFTs due to their remarkable conductivity and biocompatible characteristics both in vitro and in vivo and because gold has been employed in a range of medical applications.[55–57] Gold, as an inert biomaterial, has demonstrated decreased

biofouling in living organisms for various biomedical implants, such as cardiovascular[58] and Biomedical microelectromechanical (BioMEMS) systems.[59]

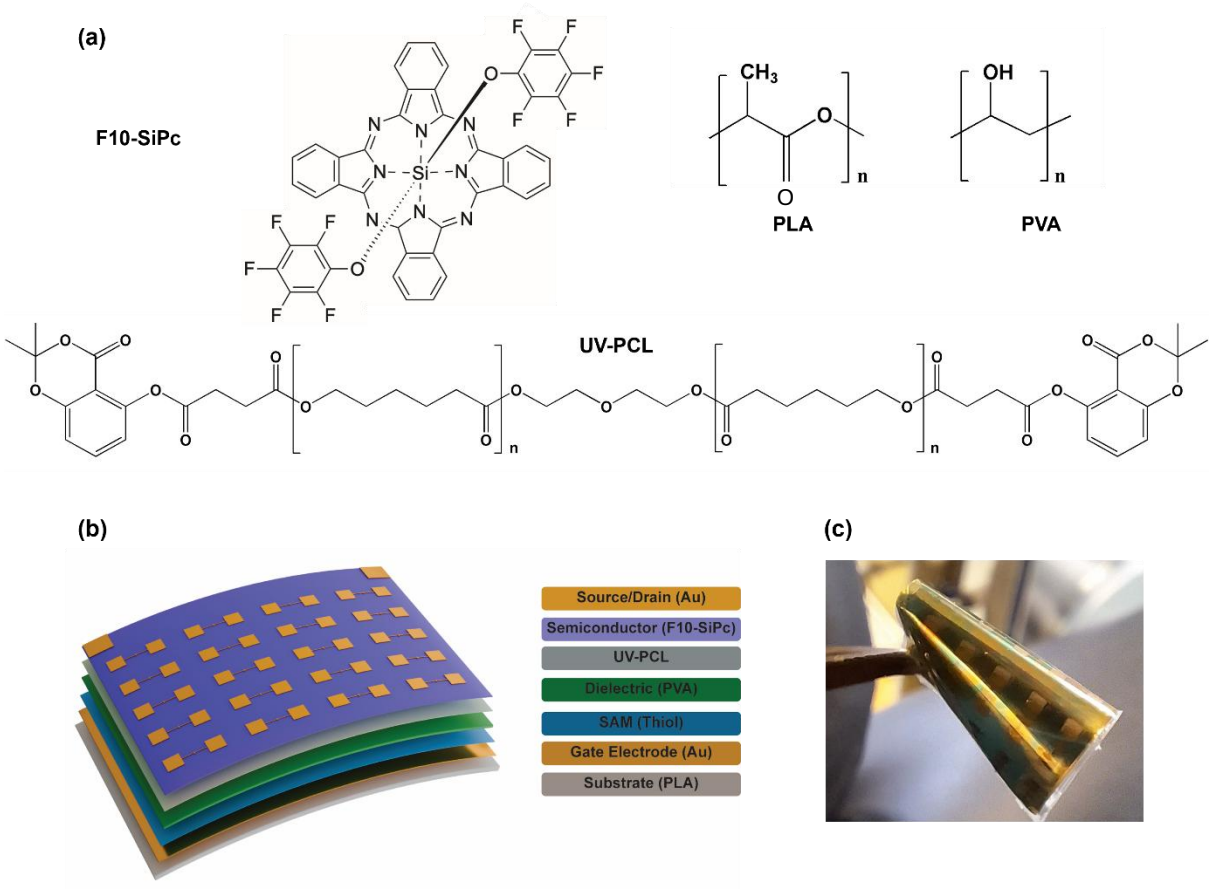


Figure 2.1. (a) Chemical structures of semiconductor, substrate, and dielectric materials: F10-SiPc, PLA, PVA, and UV-PCL. (b) Schematic illustration of disintegrable BGTC transistor device. (c) Digital photo of PLA substrate with an array of OTFTs.

The fabrication of OTFTs was accomplished by first spin-coating the PLA on quartz-coated glass substrate to make a uniform PLA layer. This was followed by a baking process to remove any trapped solvent, according to the literature.[60,61] The thickness of the biodegradable PLA substrate was approximately 3-4 μm which was then coated with chromium-gold (Cr-Au) where the Cr layer was used to improve the adhesion of Au on the PLA surface. The Au surface,

which was deposited to cover the entire PLA substrate surface to enable automated and robust testing[62], serves as the bottom gate electrode. However, the gold surface with a water contact angle at ~75° is not sufficiently hydrophilic for the PVA solution to be coated orthogonally and form a uniform layer. To overcome this, gold was treated with a self-assembled monolayer (SAM) of hydrophilic thiol for 1 hour to improve the hydrophilicity.[63] Excess thiol molecules were rinsed off with pure ethanol. A decrease in the water contact angle to ~40° was observed when gold films were treated with thiol (**Figure 2.2**a).

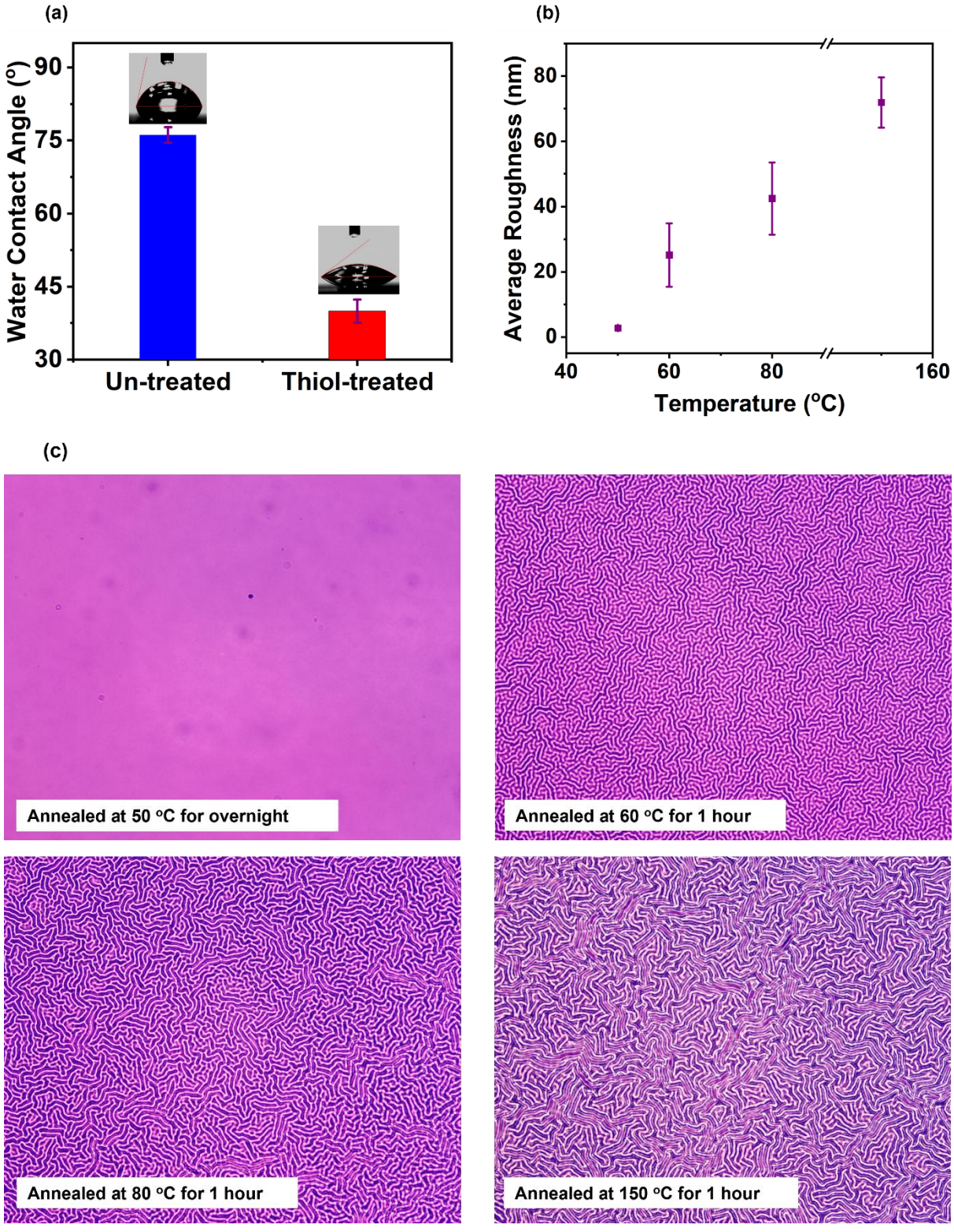

(a)
Water Contact Angle (°)
90
75
60
45
30
Un-treated
Thiol-treated
(b)
Average Roughness (nm)
80
60
40
20
0
40
60
80
160
Temperature (°C)
(c)
Annealed at 50 °C for overnight
Annealed at 60 °C for 1 hour
Annealed at 80 °C for 1 hour
Annealed at 150 °C for 1 hour

Figure 2.2. (a) Water contact angle measurements of gold film coated on PLA substrate as bottom gate electrode with and without thiol treatment. (b) The average surface roughness of the gate electrode surface measured with profilometer. (c) Optical microscopic images of gate electrode film after annealing at different temperatures.

The PVA dielectric was deposited by spin-coating onto the thiol-treated gold/PLA substrate followed by thermal annealing. In previous reports,[27,49] the PVA thin film were annealed at 150 ^{o}C for 1 hour to remove the solvent. Unlike our previous studies which annealed PVA on glass substrates, in this study the PVA is deposited on PLA which is temperature sensitive. Therefore, as the substrate is exposed to high temperatures it shrinks leading to buckling and high surface roughness, which is not conducive for OTFT fabrication. An average surface roughness of less than 10 nm is typically required to avoid surface traps at the dielectric-semiconductor interface and discontinuities of the semiconductor layer.[64] The gate electrode-coated PLA films were vacuum annealed at different temperatures: 150°C, 80°C, 60°C for 1 hour and 50°C overnight, and the roughness measurements were carried out utilizing a profilometer (**Figure 2.2**b). At annealing temperatures equal to or above 60°C, the average roughness of the gold layer was > 10 nm. We surmise this increase in roughness is a product of different thermal expansion of the PLA substrate and gold layer leading to changes in morphology. However, when the gold-coated PLA films were annealed at 50°C (below the T_g of PLA) overnight, the average roughness value was less than 10 nm. We also obtained microscopic images of the gold surface on PLA substrate when annealed at different temperatures (**Figure 2.2**c). These figures clearly show the roughness evolution upon increasing the temperature above the T_g of PLA. Consequently, no major change in the roughness of the gate electrode surface was observed when the film was annealed at 50°C overnight. Next,

the UV-PCL solution was spin coated onto the PVA layer, the films were UV-cross-linked prior to rinsing the excess PCL. To confirm the crosslinking of UV-PCL, the films were rinsed with toluene, and the water contact angle was measured. As shown in **Figure 2.3** we report the contact angle of PVA and UV-PCL-coated PVA before and after rinsing with toluene. UV-PCL would dissolve in toluene during the rinsing process if it wasn't crosslinked to the PVA layer, resulting in a drop in the contact angle to match that of the bare PVA film. The UV-PCL maintained a contact angle of around 78° after two rinsing steps once crosslinking conditions were optimized (**Figure 2.3)**. The cross-linking reaction between PCL and PVA also secures the PCL layer in position[65], inhibiting aggregation and reducing the interfacial hydroxy groups, which can act as charge traps during OTFT operation.[66] Interfacial cross-linking also preserves a substantial amount of hydroxyl groups in the bulk of PVA, leading to a high dielectric constant, while simultaneously enabling orthogonal processing.[2,67]

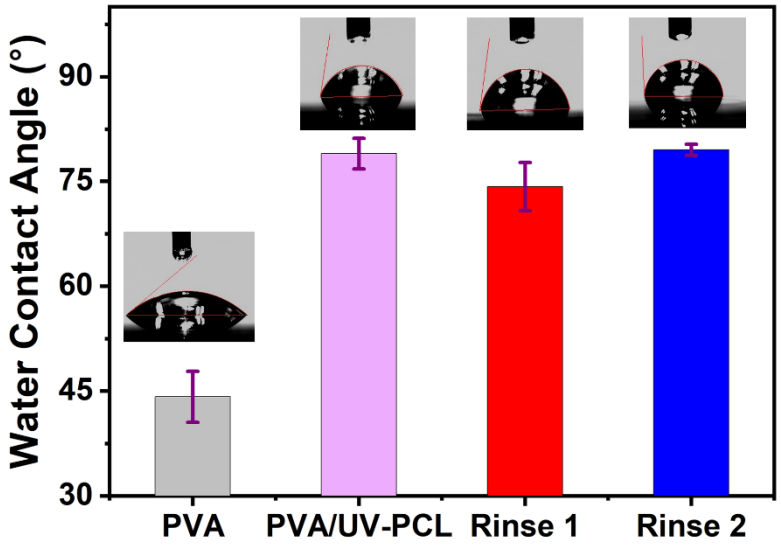


Figure 2.3. Contact angle measurements for neat PVA and PVA/UV-PCL.

The dielectric properties of the bilayer dielectric (PVA/UV-PCL) were characterized by impedance spectroscopy and summarized in **Table 2.1**. The bilayer dielectric constant values

found were well within the predicted range for PVA.[23,30,68] It has been reported that hygroscopic polymer dielectrics, when exposed to moisture, can experience an increase in capacitance density by up to 50 times at 10 Hz.[27] This change is explained by the fact that moisture acts as a plasticizer, facilitating hydroxyl group alignment under an applied electric field and thereby increasing the capacitance of PVA film.[69,70] However, for reliable transistors in flexible circuits, the dielectric properties need to be stable. Water molecules also introduce charge traps at the dielectric-semiconductor interface, increasing the device hysteresis which is also detrimental to the transistor performance. Therefore, a monolayer (~1-2 nm) of UV-cross-linkable PCL layer deposited on top of PVA functions as a moisture barrier, thereby reducing the impact of moisture on the dielectric properties of PVA.[27]

F_{10}-SiPc was deposited on the UV-PCL layer. F_{10}-SiPc OTFTs using OTS-treated SiO_2 as the gate dielectric were fabricated using a similar device configuration for device performance comparison. [23,27,30,68–70] Finally Cr then Au was deposited on the semiconductor as the source/drain electrodes using shadow masks. The Cr interlayer improves electrode durability[71] and reduce contact resistance by matching the work function of the electrode with the lowest unoccupied molecular orbital (LUMO) energy level of F_{10}-SiPc.[72,73]

Table 2.1. Average dielectric properties of PVA/UV-PCL at 10 Hz

Dielectric	Effective dielectric constant (*k*)	Capacitance density (nF/cm^2)
PVA/UV-PCL	10.6 ± 1.6	26.70 ± 0.04

Figure 2.4a–d depicts characteristics output and transfer curves of the F_{10}-SiPc OTFTs on both PVA/UV-PCL dielectric and OTS-treated SiO_2 dielectric. The V_T, electron mobility (μ_e) and

$I_{on/off}$ were determined and are presented in **Table 2.2**. The V_T of F_{10}-SiPc OTFTs was reduced noticeably from 12.7 ± 1.7 V when using OTS-treated SiO_2 as the gate dielectric to -0.97 ± 1.4 V when using PVA/UV-PCL bilayer as the gate dielectric. The decrease in V_T implies reduction in polarity at the semiconductor/dielectric interface, minimizing the amount of charge trapping[29,74–76], which is likely due to the higher dielectric constant (10.6) of PVA/UV-PCL compared to SiO_2 (3.9), at frequencies below 1 kHz.[77] This represents a significant improvement compared to previous studies[53] where biocompatible and bioresorbable OTFTs were fabricated utilizing PVA as gate dielectric with V_T values of approximately -15.4 V. A statistically similar μ_e was observed, going from $(2 \pm 0.7) \times 10^{-2}$ $cm^2V^{-1}s^{-1}$ on OTS/SiO_2 gate dielectric to $(1.03 \pm 1.6) \times 10^{-2}$ $cm^2V^{-1}s^{-1}$ when PVA/UV-PCL was used. This is consistent with previous research on bottom-gate devices that include the deposition of F_{10}-SiPc on PMMA dielectric, which provided an electron mobility of 1.1×10^{-2} $cm^2V^{-1}s^{-1}$, lower than that obtained with F_{10}-SiPc deposited on SiO_2.[52] Although the $I_{on/off}$ ratios are comparatively low, this aligns with the literature reported for PVA dielectrics.[78] The high off current observed in **Figure 2.4**d might be due to the ambipolarity of the device as the F_{10}-SiPc has been demonstrated as ambipolar semiconducting material. It is important to note that devices made on OTS/SiO_2 had a higher current than devices made on PVA/UV-PCL which is a function of several factors including the operating conditions used to obtain the transfer and output curves, which are different in terms of the V_{GS} and V_{SD}. With PVA/UV-PCL devices tested at V_{GS} and V_{SD} = 4V we obtain a current of ≈0.073 μA, but when using OTS/SiO_2 at the same V_{GS} and V_{SD} the device does not turn on, highlighting the low voltage requirements when using PVA/UV-PCL. A comparable current is only obtained at ~25 V when using OTS/SiO_2. Enhanced crystallinity in metal phthalocyanines (MPcs) deposited by PVD generally results in enhanced charge transport characteristics in OTFTs, leading to greater mobility and on-current values, while

amorphous MPcs typically show higher numbers of defect sites, which decreases the conductivity and mobility of the semiconductor.[79] The crystallization of MPcs is impacted by substrate characteristics, molecular order of the sub-layer, surface roughness, chemistry, and deposition rate.[80,81] **Figure 2.4**e-f compares XRD patterns of F_{10}-SiPc films deposited on OTS-treated SiO_2 and PVA/UV-PCL dielectric. A reduction in peak intensity at 2θ = 8.43° for F_{10}-SiPc films deposited on PVA/UV-PCL was observed compared to those on the OTS-treated SiO_2 surface which might be attributed to the change in structure and orientation of crystallites. This discrepancy can be attributed to the differing surface diffusion behaviour of F_{10}-SiPc molecules on PVA/UV-PCL compared to OTS-treated SiO_2 during the nucleation of F_{10}-SiPc vapours on the substrate and is consistent with the observed slight drop in device μ_e.[52] Overall, these results demonstrate that PVA/UV-PCL is an effective green dielectric for the development of R_2-SiPc-based OTFTs with low V_T.

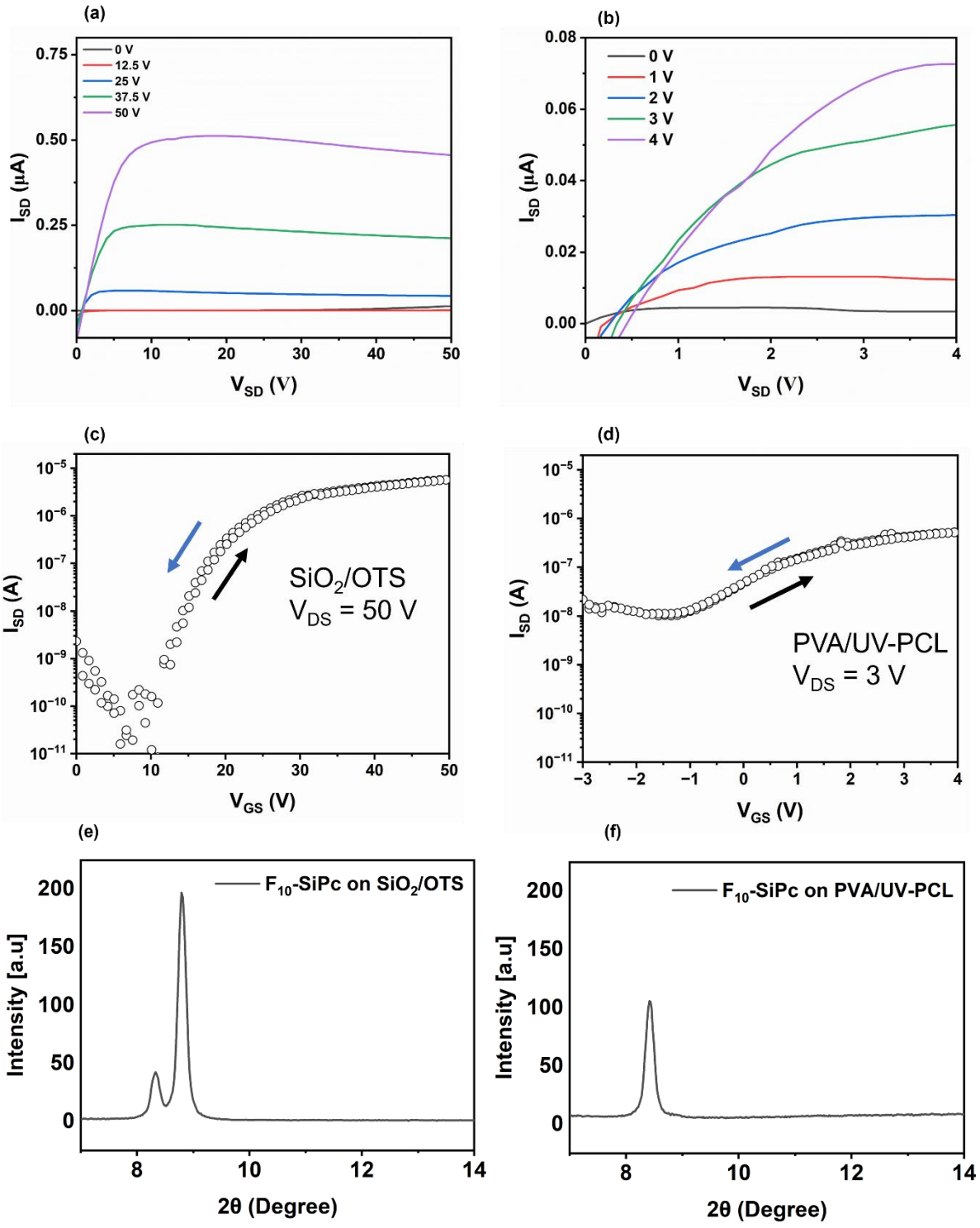


Figure 2.4. Output curves of (a) SiO_2/OTS and (b) PVA/UV-PCL, Transfer curves of (c) OTFT on OTS treated SiO_2 and (d) on PVA/UV-PCL. The transfer characteristics curve versus V_{GS} were

obtained for V_{SD} = 50 V and V_{SD} = 3 V, respectively. 1D XRD pattern for F_{10}-SiPc on (e) OTS treated SiO_2 and (f) on PVA-UV-PCL dielectric.

Table 2.2. Electrical data for OTFTs fabricated with SiO2/OTS and biodegradable bilayer PVA/UV-PCL dielectrics.

Dielectric	**μ_e ($cm^2V^{-1}s^{-1}$)**	**V_T (V)**	**$I_{on/off}$**
SiO_2/OTS	0.02 ± 0.007	12.7 ± 1.7	10^5 (at V_{GS} = 50 V)
PVA/UV-PCL	0.01 ± 0.016	-0.97 ± 1.4	10^1 (at V_{GS} = 4 V)

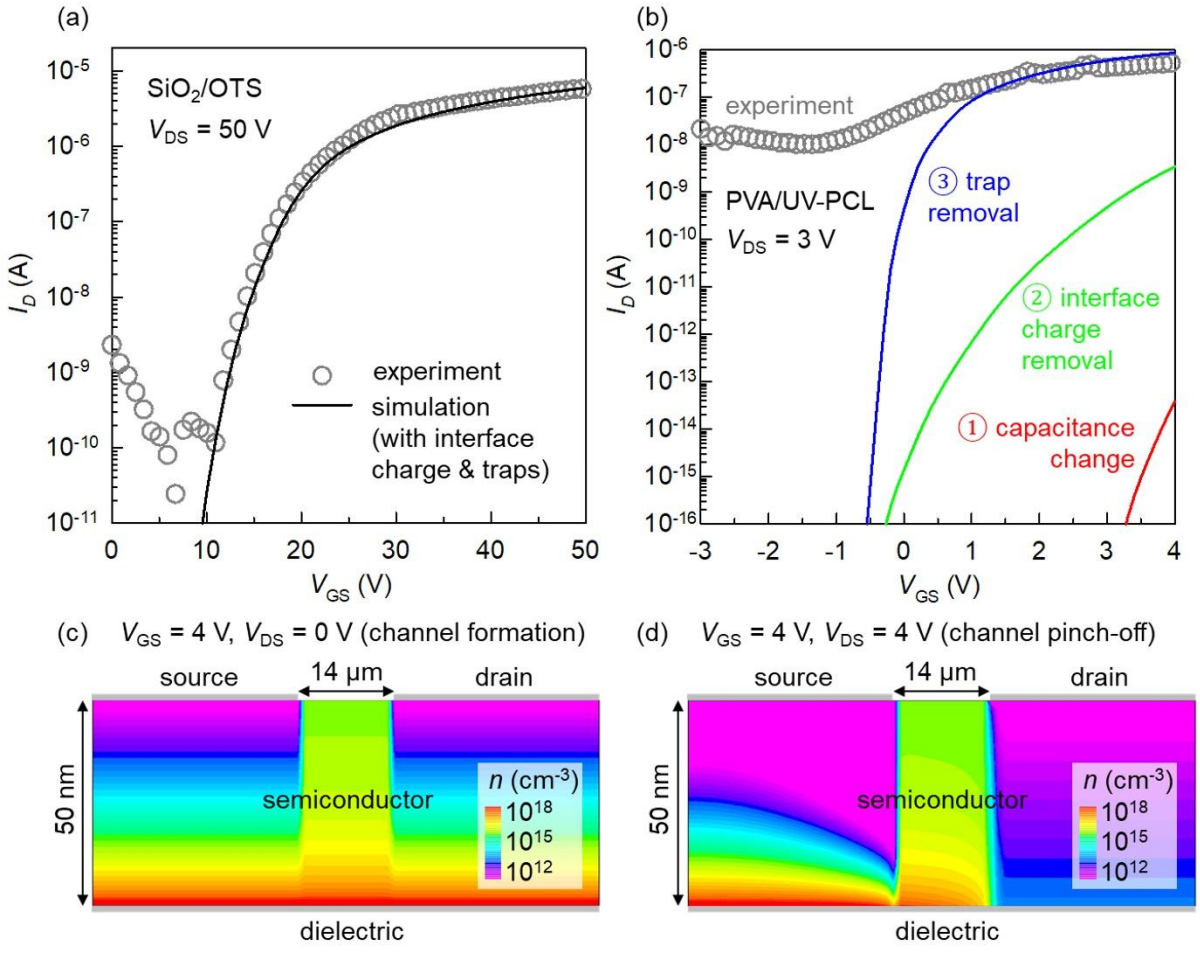


Figure 2.5. Comparison between experimentally measured and numerically simulated transfer curves of the OTFT based on (a) SiO_2/OTS and (b) PVA/UV-PCL dielectric. Electron density (n) distribution in log scale showing the (c) channel formation and (d) pinch-off achieved by a low voltage in the OTFT based on the PVA/UV-PCL dielectric.

Numerical simulation was carried out to investigate device physics of the corresponding transistors.[82–84] We determined a set of models and parameters that reproduce the major characteristics of the OTFT based on the SiO_2/OTS dielectric including both bulk traps and fixed charge at the semiconductor/insulator interface as shown in **Figure 2.5a**. It is worth mentioning that we will focus on the ON-state simulation data because the simulation returns purely theoretically achievable OFF currents that are typically orders-of-magnitude lower than those realistically measurable. We then took a step-by-step approach in modelling the OTFT based on the PVA/UV-PCL dielectric to identify an origin for the different behaviors of the two transistors. First, we increased the capacitance from 15 nF/cm^2 (SiO_2/OTS) to 27 nF/cm^2 (PVA/UV-PCL), without changing any other materials parameters (curve "1"). This simple transformation is not enough to reflect the experimental data, especially because the V_T is still too high. Next, to reduce the V_T, we removed the interface charge, obtaining curve "2". Finally, we removed the trap states, obtaining curve "3", which shows an excellent agreement between experiment and simulation, in terms of both the V_T and the ON-state current levels. A detailed list of parameters used for the optimized simulation curves in **Figure 2.5**a, and **b** can be found in **Table S2.1**, Supporting Information.

Our simulation reveals that PVA/UV-PCL does not only offer a large capacitance, but it also creates a charge-neutral and trap-minimized surface to enable low-voltage switching. Note that simple conversion of the subthreshold slope to the trap density would lead to the values of 3.5

$\times 10^{12}$ cm^{-2} eV^{-1} and 3.3 $\times 10^{12}$ cm^{-2} eV^{-1} for the transistors on SiO_2 and the polymer bilayer dielectric, respectively. The value for the SiO_2 based OTFT may reflect the actual trap DOS in this device probed by numerical simulation (**Table S2.1**). However, this method is likely to overestimate the trap density in the PVA/UV-PCL based OTFT as the subthreshold slope in this sample is not only determined by trap filling but also affected by leakage currents. To further emphasize this argument, we calculated internal distribution of electrons in the PVA/UV-PCL based OTFT. **Figure 2.5c** shows strongly depleted source/drain regions due to the injection barrier of 0.5 eV, yet the electron accumulation is clearly visible at the semiconductor/insulator interface at a V_{GS} of only 4 V. **Figure 2.5**d shows that, by increasing V_{SD} from 0 to 4 V, this channel is successfully pinched off at the drain side.

We demonstrated that these devices are capable of undergoing degradation under aqueous conditions. PLA resorption is influenced by temperature and pH, and degradation occurs slowly in PBS with a pH of 7.4 at room temperature.[85] To investigate the resorption behaviour of the device, an accelerated in vitro degradation experiment was performed by immersing the OTFTs in a PBS solution (1 M, pH ~ 10) at room temperature. The accelerated degradation test demonstrates the complete disintegration of the device in 20 days (**Figure 2.6**). We noticed that the PVA readily dissolved in PBS, and R_2-SiPc completely disintegrated from the device within 5 hours. Afterward, a loss of structural integrity was seen, leaving PLA and gold. After 20 days, the whole device was disintegrated completely, leaving micro/nano gold particles in the PBS solution which are known to be excreted or absorbed by the human body.[86]

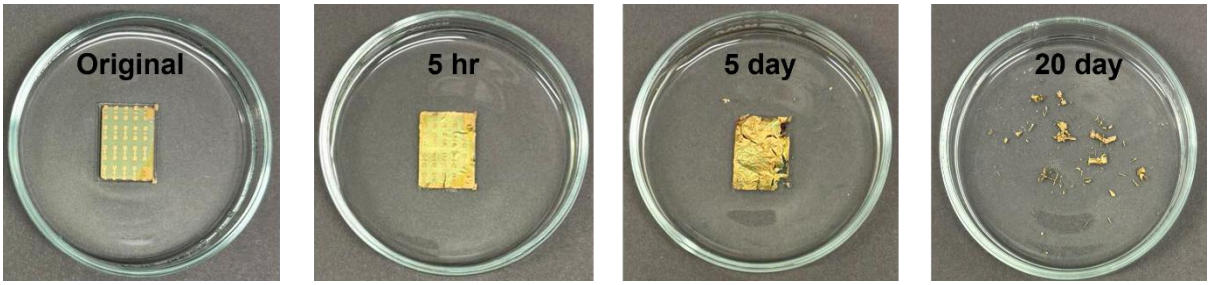


Figure 2.6. Photographs of OTFTs taken at different intervals after being submerged in a 1M PBS (pH ~10) for accelerated degradation.

We also investigated whether the degradation products from the incubation of OTFT devices in an aqueous medium elicit cytotoxicity to mammalian cells. Degradation product extracts were prepared by incubating devices in culture medium at 37 °C° for 7 days following a protocol modified from that in the study by Deng et al.[87] The metabolic activity of NIH 3T3 mouse fibroblast cultures following a 24 hour incubation with these (OTFT) extracts was not significantly different from that of cultures incubated in fresh medium without the degradation products, whereby metabolic activity is an accepted metric for evaluating cell viability (**Figure 2.7**a). The cells cultured in the presence and absence of degradation products were also incubated with Calcein-AM to label live cells (green fluorescence) and Ethidium homodimer-1 to label dead cells (red fluorescence). Fluorescence images show the presence of only a few dead cells in both culture conditions, confirming results from the metabolic activity assay (**Figure 2.7**b-c). Overall, these preliminary cell viability studies suggest that the use of UV-PCL, F10-SiPc, Au electrodes, thiol treatment and PLA as a substrate do not cause cytotoxicity to mammalian fibroblasts following degradation of the OTFT devices in aqueous solutions.

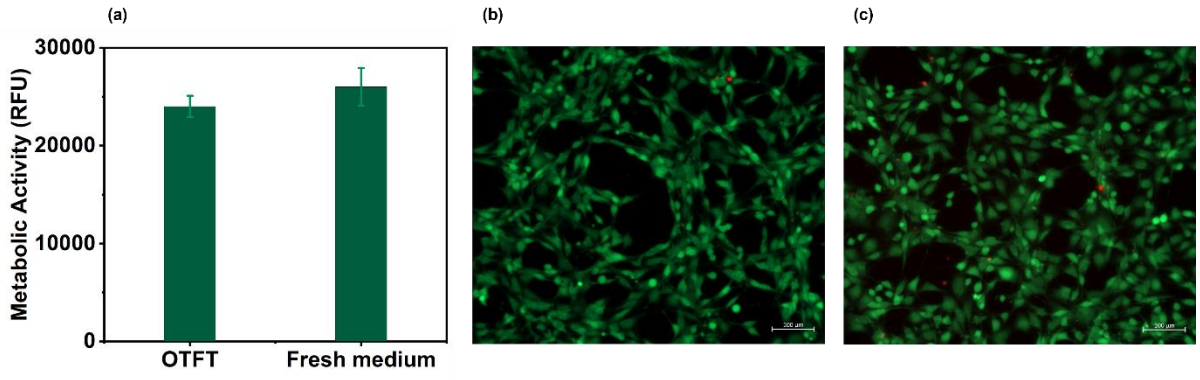


Figure 2.7. (a) Metabolic activity of NIH 3T3 mouse fibroblasts following a 24 hour incubation with degradation product extracts resulting from the incubation of OTFTs in culture medium for 7 days compared to incubation with fresh medium free of the degradation products, and (b-c) representative fluorescence images of the cells cultured with (b) and without (c) the degradation products and incubated with Calcein-AM to label live cells (green fluorescence) and Ethidium homodimer-1 to label dead cells (red fluorescence).

2.4 Conclusion

Biocompatible and degradable organic transistors were presented utilizing a water-soluble polymer gate dielectric (PVA) and biodegradable substrate (PLA). The use of a PCL and PVA bilayer gate dielectric effectively lowered the V_T of the R_2-SiPc n-type OTFT from 12.7 V to -0.97 V. Processing of the PLA device is critical for proper device function, including controlling the annealing conditions of the dielectric to avoid detrimental film roughening and thiol treating the gate for proper dielectric coating of the gate. Accelerated bio-disposability of OTFTs was shown by the successful disintegration of the developed devices in the PBS solution within 20 days. Cell viability assays were performed, demonstrating negligible cell death and the absence of apparent cytotoxicity for the degradation products of OTFT devices. Owing to the non-toxic, biodegradable nature and low voltage performance, these devices show great promise for next generation

environmentally friendly electronics and can minimize the effects of e-waste on the environment and ecosystem.

2.5 Experimental Section

2.5.1 Materials

All chemicals were obtained from Sigma-Aldrich and utilized as received unless otherwise specified. Octyltrichlorosilane (OTS) (97%) was diluted with toluene (anhydrous, 99.8%) to form a 1 v/v% solution in the glovebox. PCL diol (Mw = 2000 Da), toluene-2,4-diisocyanate (95%), PLA (230 kg/mol), PVA (Mw = 31,000–50,000 Da; 98–99% hydrolyzed) and 2-Aminoethanethiol hydrochloride were procured from Sigma-Aldrich. Chromium-coated tungsten rods (Cr) and gold (Au, 99.99%) were obtained from Angstrom Engineering. Quartz-coated glass substrates measuring 15 × 20 mm^2 were purchased from Ossila Limited. Si wafers with a SiO_2 thickness of 230 nm and shadow masks were obtained from WaferPro and Ossila Limited, respectively. Deuterated chloroform, with a purity of 99.8%, and benzene, with a purity of 98%, were acquired from Cambridge Isotope Laboratories Inc. The synthesis of F_{10}-SiPc was carried out according to the literature.[88] 2,2-dimethyl benzodioxinone-terminated PCL (UV-PCL) was synthesized according to literature.[27]

2.5.2 Preparation of Self-Assembled Monolayer solution

A solution of self-assembled mono layer of hydrophilic thiols was prepared by dissolving 10 mM of 2-aminoethanethiol hydrochloride in ethanol solvent.

2.5.3 Preparation of Substrate and Dielectric

PLA was selected to be used as biodegradable substrate for the fabrication of OTFTs. PLA solution of 80 mg/ml was prepared by dissolving granules of PLA (230 kg/mol) in chloroform

solvent followed by filtering with 0.45-micron PTFE filters. The PVA solution was prepared by dissolving 80 mg of PVA in 1 ml of distilled water, and then filtering it through a 0.45 μm cellulose filter. Next, the UV-PCL was weighted and transferred into an opaque vial, where it was dissolved in toluene to obtain a concentration of 2 mg/mL. Afterwards, the vial containing the UV-PCL was left on a hot plate set at 60°C for 1 hour to guarantee full dissolution. The UV-PCL solution obtained was subsequently passed through a 0.22 μm polytetrafluoroethylene (PTFE) filter into a separate opaque vial. These procedures were conducted under ambient conditions.

2.5.4 Fabrication of TFT

OTFTs were fabricated using quartz coated glass substrate (15 × 20 mm^2). The quartz substrates were used as temporary substrates. The substrates were cleaned using a four-step method. The substrates were first sonicated for five minutes by sequentially immersing them in detergent mixed with distilled water, distilled water, acetone, and methanol. Then, the substrates were rinsed with isopropanol and dried using a nitrogen stream. The PLA solution was then spin-coated at 2000 rpm for 90 seconds on glass substrates using a Laurell WS-650-23 spin coater. Subsequently, the PLA-coated glass substrates were vacuum annealed at 70 ^oC for 15 minutes. After baking the film of PLA, a film of ~3-4 micron was obtained. Next, using a shadow mask and the PVD method, a 2 nm layer of Cr (deposited at a rate of 0.5 Å s^{-1}) and a 50 nm layer of gold (deposited at a rate of 0.5 Å s^{-1}) were deposited on to the PLA substrate. Then, PLA substrates coated with gold were immersed in a hydrophilic thiol solution for one hour to form a self-assembled monolayer of thiols. The purpose of this monolayer is to enhance the hydrophilicity of gold layer on PLA. Next, a solution of PVA (80 mg/ml) was spin coated on gate electrode coated PLA substrate at 2000 rpm for 90 s followed by annealing at 50 ^oC for overnight to ensure that the PVA film is dried well. Afterwards, 2 mg/ml solution of UV-PCL was deposited on PVA dielectric

layer using spin coating at 2000 rpm for 90 s. The spin coated UV-PCL on PVA dielectric film was crosslinked using a UV lamp with a wavelength of 254 nm. After that, the samples were transferred to nitrogen glovebox connected to a thermal evaporator. The F_{10}-SiPc layer was thermally deposited by a PVD method, forming a 500 Å-thick film of F_{10}-SiPc using a square shadow mask. During the deposition procedure, the substrates were kept at room temperature, and the process was carried out at a rate of 0.2 Å s^{-1} under pressure of less than 2×10^{-6} Torr. Then, using a shadow mask, a 2 nm layer of chromium (deposited at a rate of 0.5 Å s^{-1}) and a 50 nm layer of gold (deposited at a rate of 0.5 Å s^{-1}) were deposited to obtain source-drain electrodes with dimensions of L = 30 μm and W = 1000 μm. Similar architecture was used for the fabrication of OTFTs with SiO_2 serving as the gate dielectric. SiO_2/Si wafers were first cleaned using the same cleaning process, then they were treated with oxygen plasma for 15 minutes. To create a monolayer of OTS on the SiO_2 surfaces, the wafers were then immersed in a 1v/v% OTS solution in toluene for an hour at 70°C. They were then rinsed with toluene and dried in a vacuum oven at 70°C. Following surface treatment, the substrates were placed in a glovebox and a 50 nm layer of F_{10}-SiPc was deposited. Next, Cr-Au source-drain electrodes were deposited using similar settings as previously mentioned.

2.5.5 Device Characterization

The OTFT devices were tested in a N_2 glovebox utilizing a custom-built auto tester[62] that was connected to a Keithley 2614B instrument. This configuration facilitated the control of the voltage between the source and drain (V_{SD}) and the voltage between the source and gate (V_{GS}), as well as the measurement of the current flowing between the source and drain (I_{SD}) in OTFTs. The output curves were obtained by sweeping the V_{SD} from 0 to 4 V, while the V_{GS} varied from -3 to 4 V. The transfer curves were obtained by setting the V_{SD} = 3 V for biodegradable polymer-gated

OTFTs and 50 V for SiO_2-gated OTFTs. The V_{GS} was then varied from -3 to 4 V for biodegradable polymer-gated devices and from 0 to 50 V for SiO_2-gated devices. The values of μ_e, V_T, and $I_{on/off}$ were computed by examining the transfer curves in the saturation regime which are modelled utilizing **Equation 2.1**:

$$I_{SD} = \frac{\mu_e C_i W}{2L} (V_{GS} - V_T)^2 \quad (2.1)$$

The V_T was calculated by linearizing Equation 2.1 and determining the point where the line fitted to the on-state of the transfer curve intersects the x-axis. The $I_{on/off}$ was determined by analyzing the highest and lowest currents on the transfer curves. The capacitance (C_i) was measured using impedance spectroscopy with a Metrohm PGSTAT204 potentiostat/galvanostat workstation at a frequency of 10 Hz. The voltage was varied from 0 to 10 V. **Equation 2.2** was used to compute C_i, using the angular frequency (ω), real (Z''), and imaginary (Z') parts of impedance.

$$C_i = \frac{1}{\omega A} \times \frac{Z''}{Z''^2 + Z'^2} \quad (2.2)$$

The calculation employed the total surface area (A) of each individual transistor. The mobility values were modified to compensate for variations in channel length caused by shadowing effects that occur when depositing the source-drain electrodes.

2.5.6 Thin Film Characterization

A Bruker D8 Endeavour apparatus was used to record the XRD patterns of 50 nm thick F_{10}-SiPc films on SiO_2 dielectric treated with OTS, as well as biodegradable bilayer dielectric (PVA/UV-PCL). The Cu Kα radiation (λ = 1.5418 Å) was used, and the scan rate was set to 0.5° min^{-1}, covering a range of $7° < 2\theta < 14°$.

Furthermore, each polymer film was subjected to a contact angle measurement (θ) with deionized (DI) water. This was obtained by dispensing 0.5 μL droplets of each reference liquid and taking an image of the drops with VCA Optima goniometer camera (AST Products Inc.).
A Bruker Dektak XT profilometer was used to measure the dielectric layer thickness and roughness of the gate electrode surface. The thickness values were then used to correct the mobilities that were measured.

2.5.7 Numerical Simulation

A physically based two-dimensional (2D) finite-element numerical solver was used for the simulation of OTFTs (ATLAS, Silvaco). The Poisson's equation is solved on a 2D coordinate system to relate the potential variation to the space charge density,

$$\mathrm{div}(\epsilon_s \nabla \varphi) = -\rho \tag{2.3}$$

where φ is the electrostatic potential, ε_s is the semiconductor permittivity, and ρ is the space charge density. The electrical currents are modelled by drift-diffusion mechanism,

$$\overrightarrow{J_n} = qn\mu_n \vec{E} + qD_n \nabla n \tag{2.4}$$

and

$$\overrightarrow{J_p} = qp\mu_p \vec{E} - qD_p \nabla p \tag{2.5}$$

where $\overrightarrow{J_n}$ and $\overrightarrow{J_p}$ are the electron and hole current density vectors, respectively, $\vec{E}$ is the electric field vector, μ_n and μ_p are the electron and hole mobility, respectively, D_n and D_p are the electron and hole diffusion coefficient, respectively, q is the elementary charge, n and p are the electron and hole concentration, respectively. The simulator self-consistently solves Equations (2.3)–(2.5) over a 2D mesh that is defined to mimic the cross-section of a fabricated device. The two major outcomes of this process are geometric solutions for the electrostatic parameters and terminal current-voltage characteristics that represent the integration of current densities under

different bias conditions. An exponential trap DOS at the LUMO edge and a fixed interface charge density were added for the simulation of OTFT with SiO_2/OTS. The functional form of trap DOS is:

$$\mathrm{DOS}(E) = \frac{H_A}{k_B T_A} \exp\left(-\frac{E_c - E}{k_B T_A}\right) \tag{2.6}$$

where E is the energy, H_A is the total density of acceptor-like trap states, k_B is the Boltzmann constant, T_A is the characteristic temperature dictating the energetic width of acceptor-like traps, and E_c is the energy of the conduction band (or LUMO) edge.

2.5.8 Cytotoxicity Evaluation

The cytotoxicity of degradation products from the incubation of OTFT devices in culture medium was carried out according to a protocol modified from the study by Deng et al.[87] Briefly, devices (15 × 20 mm^2) were sterilized by incubation in 70% ethanol for 10 minutes, rinsed twice in PBS and incubated in 1 mL of high glucose Dulbecco's Modified Eagle's Medium (DMEM) for 7 days at 37 °°C. The media samples comprising degradation products were then supplemented with fetal bovine serum (FBS) to a final concentration of 10% v/v before being used for cell experiments as degradation products extracts. NIH 3T3 mouse fibroblasts were seeded in DMEM supplemented with 10% FBS at a density of 10,000 cells per well in a 48 well plate and allowed to attach for 24 hours in an incubator at 37 °°C in an environment characterized by 5% CO_2 and 95% relative humidity. Subsequently, the medium was replaced with the degradation product extracts or fresh medium (control) and incubated for an additional 24 hours. Select cultures were evaluated for the metabolic activity of the cells with an alamarBlue assay (Thermo Fisher Scientific), according to manufacturer instructions. Additional cultures were incubated with 2 μM Calcein AM (Invitrogen; live cells stain; green fluorescence) and 4 μM Ethidium homodimer-1 (Sigma Aldrich; dead cells stain; red fluorescence) in DMEM for 10 minutes and imaged using a

Zeiss Axio Observer 7 microscope. The degradation products from 5 OTFT devices were tested for both cell viability assays.

2.6 Acknowledgements

The authors would like to thank the National Science and Engineering Research Council of Canada (NSERC), Canada Research Chair (CRC) program and the Canadian Foundation for Innovation (CFI) for funding this work.

2.7 Supporting Information

Table S2.1. Key material parameters used as input to the numerical simulation

Layer	Parameter	OTFT with SiO_2/OTS	OTFT with PVA/UV-PCL
Gate	Work function	4.0 eV	4.0 eV
Source/drain	Work function	4.35 eV	4.35 eV
Dielectric	Capacitance	15 nF/cm^2	27 nF/cm^2
	Interface charge	-6 ×10^{11} cm^{-2}	None
Semiconductor	Ionization energy (HOMO)	5.65 eV	5.65 eV
	Electron affinity (LUMO)	3.85 eV	3.85 eV
	HOMO effective density of states	10^{20} cm^{-3}	10^{20} cm^{-3}
	LUMO effective density of states	10^{20} cm^{-3}	10^{20} cm^{-3}
	Electron mobility	0.3 cm^{2}V^{-1}s^{-1}	0.3 cm^{2}V^{-1}s^{-1}
	Hole mobility	10^{-5} cm^{2}V^{-1}s^{-1}	10^{-5} cm^{2}V^{-1}s^{-1}
	Total trap density	10^{18} cm^{-3}	None
	Trap characteristic temperature	1200 K	None

References

(1) Murthy, V.; Ramakrishna, S. A Review on Global E-Waste Management: Urban Mining towards a Sustainable Future and Circular Economy. *Sustainability* **2022**, *14* (2), 647.

(2) Khan, Y.; Thielens, A.; Muin, S.; Ting, J.; Baumbauer, C.; Arias, A. C. A New Frontier of Printed Electronics: Flexible Hybrid Electronics. *Adv. Mater.* **2020**, *32* (15), 1905279.

(3) Wiklund, J.; Karakoç, A.; Palko, T.; Yiğitler, H.; Ruttik, K.; Jäntti, R.; Paltakari, J. A Review on Printed Electronics: Fabrication Methods, Inks, Substrates, Applications and Environmental Impacts. *J. Manuf. Mater. Process.* **2021**, *5* (3), 89.

(4) Kumar, A.; Holuszko, M.; Espinosa, D. C. R. E-Waste: An Overview on Generation, Collection, Legislation and Recycling Practices. *Resour. Conserv. Recycl.* **2017**, *122*, 32–42.

(5) Tan, M. J.; Owh, C.; Chee, P. L.; Kyaw, A. K. K.; Kai, D.; Loh, X. J. Biodegradable Electronics: Cornerstone for Sustainable Electronics and Transient Applications. *J. Mater. Chem. C* **2016**, *4* (24), 5531–5558.

(6) Hwang, S.; Park, G.; Cheng, H.; Song, J.; Kang, S.; Yin, L.; Kim, J.; Omenetto, F. G.; Huang, Y.; Lee, K. 25th Anniversary Article: Materials for High-performance Biodegradable Semiconductor Devices. *Adv. Mater.* **2014**, *26* (13), 1992–2000.

(7) Hwang, S.-W.; Tao, H.; Kim, D.-H.; Cheng, H.; Song, J.-K.; Rill, E.; Brenckle, M. A.; Panilaitis, B.; Won, S. M.; Kim, Y.-S. A Physically Transient Form of Silicon Electronics. *Science.* **2012**, *337* (6102), 1640–1644.

(8) Ma, Y.; Zhang, Y.; Cai, S.; Han, Z.; Liu, X.; Wang, F.; Cao, Y.; Wang, Z.; Li, H.; Chen, Y.

Flexible Hybrid Electronics for Digital Healthcare. *Adv. Mater.* **2020**, *32* (15), 1902062.

(9) Liu, K.; Ouyang, B.; Guo, X.; Guo, Y.; Liu, Y. Advances in Flexible Organic Field-Effect Transistors and Their Applications for Flexible Electronics. *npj Flex. Electron.* **2022**, *6* (1), 1.

(10) Chatterjee, S.; Sharma, S. Microplastics in Our Oceans and Marine Health. *F. Actions Sci. Reports. J. F. Actions* **2019**, No. Special Issue 19, 54–61.

(11) Wang, P.; Hu, M.; Wang, H.; Chen, Z.; Feng, Y.; Wang, J.; Ling, W.; Huang, Y. The Evolution of Flexible Electronics: From Nature, beyond Nature, and to Nature. *Adv. Sci.* **2020**, *7* (20), 2001116.

(12) Irimia-Vladu, M.; Głowacki, E. D.; Voss, G.; Bauer, S.; Sariciftci, N. S. Green and Biodegradable Electronics. *Mater. Today* **2012**, *15* (7–8), 340–346.

(13) King, B.; Lessard, B.H. Review Of Recent Advances In Sensing Mechanisms In Solid-State Organic Thin-Film Transistor (OTFT) Sensors. *Journal of Materials Chemistry C.* **2024**, 5654-5683.

(14) Kaltenbrunner, M.; Sekitani, T.; Reeder, J.; Yokota, T.; Kuribara, K.; Tokuhara, T.; Drack, M.; Schwödiauer, R.; Graz, I.; Bauer-Gogonea, S. An Ultra-Lightweight Design for Imperceptible Plastic Electronics. *Nature* **2013**, *499* (7459), 458–463.

(15) Sekitani, T.; Nakajima, H.; Maeda, H.; Fukushima, T.; Aida, T.; Hata, K.; Someya, T. Stretchable Active-Matrix Organic Light-Emitting Diode Display Using Printable Elastic Conductors. *Nat. Mater.* **2009**, *8* (6), 494–499.

(16) Tee, B. C.-K.; Chortos, A.; Berndt, A.; Nguyen, A. K.; Tom, A.; McGuire, A.; Lin, Z. C.;

Tien, K.; Bae, W.-G.; Wang, H. A Skin-Inspired Organic Digital Mechanoreceptor. *Science.* **2015**, *350* (6258), 313–316.

(17) Klauk, H.; Zschieschang, U.; Pflaum, J.; Halik, M. Ultralow-Power Organic Complementary Circuits. *Nature* **2007**, *445* (7129), 745–748.

(18) Henson, Z. B.; Müllen, K.; Bazan, G. C. Design Strategies for Organic Semiconductors beyond the Molecular Formula. *Nat. Chem.* **2012**, *4* (9), 699–704.

(19) Reichert, C. L.; Bugnicourt, E.; Coltelli, M.-B.; Cinelli, P.; Lazzeri, A.; Canesi, I.; Braca, F.; Martínez, B. M.; Alonso, R.; Agostinis, L. Bio-Based Packaging: Materials, Modifications, Industrial Applications and Sustainability. *Polymers (Basel).* **2020**, *12* (7), 1558.

(20) Chiellini, E.; Corti, A.; D'Antone, S.; Solaro, R. Biodegradation of Poly (Vinyl Alcohol) Based Materials. *Prog. Polym. Sci.* **2003**, *28* (6), 963–1014.

(21) Tousignant, M. N.; Tischler, V.; Wagner, K.; Lin, Z. S.; Brusso, J.; Izquierdo, R.; Lessard, B. Aerosol Jet Printed Temperature Sensors Using an Environmentally Friendly Bilayer Dielectric. *Flex. Print. Electron.* **2024**.

(22) Li, J.; Tang, W.; Wang, Q.; Sun, W.; Zhang, Q.; Guo, X.; Wang, X.; Yan, F. Solution-Processable Organic and Hybrid Gate Dielectrics for Printed Electronics. *Mater. Sci. Eng. R Reports* **2018**, *127*, 1–36.

(23) Van Etten, E. A.; Ximenes, E. S.; Tarasconi, L. T.; Garcia, I. T. S.; Forte, M. M. C.; Boudinov, H. Insulating Characteristics of Polyvinyl Alcohol for Integrated Electronics. *Thin Solid Films* **2014**, *568*, 111–116.

(24) Tousignant, M. N.; Rice, N. A.; Peltekoff, A.; Sundaresan, C.; Miao, C.; Hamad, W. Y.; Lessard, B. H. Improving Thin-Film Properties of Poly (Vinyl Alcohol) by the Addition of Low-Weight Percentages of Cellulose Nanocrystals. *Langmuir* **2020**, *36* (13), 3550–3557.

(25) Jin, S. H.; Yu, J. S.; Kim, J. W.; Lee, C. A.; Park, B.; Lee, J. D.; Lee, J. H. 34.2: PMMA Buffer-Layer Effects on Electrical Performance of Pentacene OTFTs with a Cross-linked PVA Gate Insulator on a Flexible Substrate. In *SID Symposium Digest of Technical Papers*; Wiley Online Library, 2003; Vol. 34, pp 1088–1091.

(26) Jin, S. H.; Yu, J. S.; Lee, C. A.; Kim, J. W.; Park, B.-G.; Lee, J. D. Pentacene OTFTs with PVA Gate Insulators on a Flexible Substrate. *Journal-Korean Phys. Soc.* **2004**, *44*, 181–184.

(27) Tousignant, M. N.; Lin, Z. S.; Brusso, J.; Lessard, B. H. Interfacial Ultraviolet Cross-Linking of Green Bilayer Dielectrics. *ACS Appl. Mater. Interfaces* **2023**, *15* (2), 3680–3688.

(28) TEJA KARRI, B. R.; Gupta, N. Hybrid Bilayer Gate Dielectric-Based Organic Thin Film Transistors. *Bull. Mater. Sci.* **2019**, *42* (1), 2.

(29) Zhang, H.; Zhang, F.; Sun, J.; Zhang, M.; Hu, Y.; Lou, Z.; Hou, Y.; Teng, F. Solution-Processed Organic Field-Effect Transistors with Cross-Linked Poly (4-Vinylphenol)/Polyvinyl Alcohol Bilayer Dielectrics. *Appl. Surf. Sci.* **2019**, *478*, 699–707.

(30) Subbarao, N. V. V; Mandal, S.; Gedda, M.; Iyer, P. K.; Goswami, D. K. Effect of Temperature on Hysteresis of Dipolar Dielectric Layer Based Organic Field-Effect Transistors: A Temperature Sensing Mechanism. *Sensors Actuators A Phys.* **2018**, *269*, 491–499.

(31) She, X.-J.; Liu, J.; Zhang, J.-Y.; Gao, X.; Wang, S.-D. Operational Stability Enhancement of Low-Voltage Organic Field-Effect Transistors Based on Bilayer Polymer Dielectrics. *Appl. Phys. Lett.* **2013**, *103* (13).

(32) Rullyani, C.; Ramesh, M.; Sung, C.-F.; Lin, H.-C.; Chu, C.-W. Natural Polymers for Disposable Organic Thin Film Transistors. *Org. Electron.* **2018**, *54*, 154–160.

(33) Pang, C.; Neubauer, N.; Boyles, M.; Brown, D.; Kanase, N.; Hristozov, D.; Fernandes, T.; Stone, V.; Wohlleben, W.; Marcomini, A. Releases from Transparent Blue Automobile Coatings Containing Nanoscale Copper Phthalocyanine and Their Effects on J774 A1 Macrophages. *NanoImpact* **2017**, *7*, 75–83.

(34) GÜnsel, A.; UsluoĞlu, A.; Bilgicli, A. T.; TOSUN, B.; Arabaci, G.; YaraŞir, M. N. The Use of Water-Soluble Phthalocyanines as Textile Dyes in Nylon/Elastane Fabric: Fastness and Antibacterial Effectiveness. *Turkish J. Chem.* **2020**, *44* (4), 923–931.

(35) Nie, L.; Chang, G.; Li, R. Preparation and Characterization of Self-Dispersing Phthalocyanine Blue 15: 4 Pigment for Dyeing of Wool Textiles. *Coatings* **2020**, *10* (8), 741.

(36) Mao, J.; Zhang, Y.; Zhu, J.; Zhang, C.; Guo, Z. Molecular Combo of Photodynamic Therapeutic Agent Silicon (IV) Phthalocyanine and Anticancer Drug Cisplatin. *Chem. Commun.* **2009**, No. 8, 908–910.

(37) Mitra, K.; Samsó, M.; Lyons, C. E.; Hartman, M. C. T. Hyaluronic Acid Grafted Nanoparticles of a Platinum (II)–Silicon (IV) Phthalocyanine Conjugate for Tumor and Mitochondria-Targeted Photodynamic Therapy in Red Light. *J. Mater. Chem. B* **2018**, *6* (45), 7373–7377.

(38) Li, K.; Dong, W.; Liu, Q.; Lv, G.; Xie, M.; Sun, X.; Qiu, L.; Lin, J. A Biotin Receptor-Targeted Silicon (IV) Phthalocyanine for in Vivo Tumor Imaging and Photodynamic Therapy. *J. Photochem. Photobiol. B Biol.* **2019**, *190*, 1–7.

(39) Mitsunaga, M.; Ogawa, M.; Kosaka, N.; Rosenblum, L. T.; Choyke, P. L.; Kobayashi, H. Cancer Cell–Selective in Vivo near Infrared Photoimmunotherapy Targeting Specific Membrane Molecules. *Nat. Med.* **2011**, *17* (12), 1685–1691.

(40) Lau, J. T. F.; Lo, P.-C.; Jiang, X.-J.; Wang, Q.; Ng, D. K. P. A Dual Activatable Photosensitizer toward Targeted Photodynamic Therapy. *J. Med. Chem.* **2014**, *57* (10), 4088–4097.

(41) Cranston, R. R.; Lanosky, T. D.; Ewenike, R.; Mckillop, S.; King, B.; Lessard, B. H. Polarized Raman Microscopy to Image Microstructure Changes in Silicon Phthalocyanine Thin-Films. *Small Sci.* **2024**, 2300350.

(42) Cranston, R. R.; Vebber, M. C.; Faleiro Berbigier, J.; Brusso, J.; Kelly, T. L.; Lessard, B. H. High Performance Solution Processed N-Type OTFTs through Surface Engineered F–F Interactions Using Asymmetric Silicon Phthalocyanines. *Adv. Electron. Mater.* **2022**, *8* (12), 2200696.

(43) King, B.; Vebber, M. C.; Ewenike, R.; Dupuy, M.; French, C.; Brusso, J. L.; Lessard, B. H. Peripherally Fluorinated Silicon Phthalocyanines: How Many Fluorine Groups Are Necessary for Air-Stable Electron Transport in Organic Thin-Film Transistors? *Chem. Mater.* **2023**, *35* (20), 8517–8528.

(44) Ewenike, R. B.; King, B.; Battaglia, A. M.; Quezada Borja, J. D.; Lin, Z. S.; Manion, J. G.; Brusso, J. L.; Kelly, T. L.; Seferos, D. S.; Lessard, B. H. Toward Weak Epitaxial Growth

of Silicon Phthalocyanines: How the Choice of the Optimal Templating Layer Differs from Traditional Phthalocyanines. *ACS Appl. Electron. Mater.* **2023**, *5* (12), 7023–7033.

(45) Lessard, B. H. The Rise of Silicon Phthalocyanine: From Organic Photovoltaics to Organic Thin Film Transistors. *ACS Appl. Mater. Interfaces* **2021**, *13* (27), 31321–31330.

(46) Brixi, S.; Radford, C. L.; Tousignant, M. N.; Peltekoff, A. J.; Manion, J. G.; Kelly, T. L.; Lessard, B. H. Poly (Ionic Liquid) Gating Materials for High-Performance Organic Thin-Film Transistors: The Role of Block Copolymer Self-Assembly at the Semiconductor Interface. *ACS Appl. Mater. Interfaces* **2022**, *14* (35), 40361–40370.

(47) Torricelli, F.; Adrahtas, D. Z.; Bao, Z.; Berggren, M.; Biscarini, F.; Bonfiglio, A.; Bortolotti, C. A.; Frisbie, C. D.; Macchia, E.; Malliaras, G. G.; McCulloch, I.; Moser, M.; Nguyen, T.-Q.; Owens, R. M.; Salleo, A.; Spanu, A.; Torsi, L. Electrolyte-Gated Transistors for Enhanced Performance Bioelectronics. *Nat. Rev. Methods Prim.* **2021**, *1* (1), 66. https://doi.org/10.1038/s43586-021-00065-8.

(48) Possanner, S. K.; Zojer, K.; Pacher, P.; Zojer, E.; Schürrer, F. Threshold Voltage Shifts in Organic Thin-Film Transistors Due to Self-Assembled Monolayers at the Dielectric Surface. *Adv. Funct. Mater.* **2009**, *19* (6), 958–967.

(49) Tousignant, M. N.; Ronnasi, B.; Tischler, V.; Lessard, B. H. N-Type Single Walled Carbon Nanotube Thin Film Transistors Using Green Tri-Layer Polymer Dielectric. *Adv. Mater. Interfaces* **2023**, *10* (14), 2300079.

(50) Hasan, M. M.; Islam, M. M.; Li, X.; He, M.; Manley, R.; Chang, J.; Zhelev, N.; Mehrotra, K.; Jang, J. Interface Engineering with Polystyrene for High-Performance, Low-Voltage Driven Organic Thin Film Transistor. *IEEE Trans. Electron Devices* **2020**, *67* (4), 1751–

1756.

(51) Konwar, G.; Saxena, P.; Raghuwanshi, V.; Rahi, S.; Tiwari, S. P. Multifunctional Flexible Organic Transistors with a High-k/Natural Protein Bilayer Gate Dielectric for Circuit and Sensing Applications. *ACS Appl. Electron. Mater.* **2022**, *4* (5), 2525–2533.

(52) Ronnasi, B.; King, B.; Brixi, S.; Swaraj, S.; Niskanen, J.; Lessard, B. H. Electron Donating Functional Polymer Dielectrics to Reduce the Threshold Voltage of N-Type Organic Thin-Film Transistors. *Adv. Electron. Mater.* **2024**, 2300810.

(53) Bettinger, C. J.; Bao, Z. Organic Thin-film Transistors Fabricated on Resorbable Biomaterial Substrates. *Adv. Mater.* **2010**, *22* (5), 651–655.

(54) Witte, F. 1.3.3D - Biodegradable Metals; Wagner, W. R., Sakiyama-Elbert, S. E., Zhang, G., Yaszemski, M. J. B. T.-B. S. (Fourth E., Eds.; Academic Press, 2020; pp 271–287. https://doi.org/https://doi.org/10.1016/B978-0-12-816137-1.00021-0.

(55) Voskerician, G.; Shawgo, R. S.; Hiltner, P. A.; Anderson, J. M.; Cima, M. J.; Langer, R. In Vivo Inflammatory and Wound Healing Effects of Gold Electrode Voltammetry for MEMS Micro-Reservoir Drug Delivery Device. *IEEE Trans. Biomed. Eng.* **2004**, *51* (4), 627–635. https://doi.org/10.1109/TBME.2003.821034.

(56) Wilson, G. S.; Hu, Y. Enzyme-Based Biosensors for in Vivo Measurements. *Chem. Rev.* **2000**, *100* (7), 2693–2704. https://doi.org/10.1021/cr990003y.

(57) Peng, M.; Wang, J.; Li, Z.; Ren, G.; Li, K.; Gu, C.; Lin, Y. Three-Dimensional Flexible and Stretchable Gold Foam Scaffold for Real-Time Electrochemical Sensing in Cells and in Vivo. *Talanta* **2023**, *253*, 123891.

https://doi.org/https://doi.org/10.1016/j.talanta.2022.123891.

(58) Edelman, E. R.; Seifert, P.; Groothuis, A.; Morss, A.; Bornstein, D.; Rogers, C. Gold-Coated NIR Stents in Porcine Coronary Arteries. *Circulation* **2001**, *103* (3), 429–434.

(59) Voskerician, G.; Shive, M. S.; Shawgo, R. S.; Von Recum, H.; Anderson, J. M.; Cima, M. J.; Langer, R. Biocompatibility and Biofouling of MEMS Drug Delivery Devices. *Biomaterials* **2003**, *24* (11), 1959–1967.

(60) Carvalho, J. R. G.; Conde, G.; Antonioli, M. L.; Dias, P. P.; Vasconcelos, R. O.; Taboga, S. R.; Canola, P. A.; Chinelatto, M. A.; Pereira, G. T.; Ferraz, G. C. Biocompatibility and Biodegradation of Poly (Lactic Acid)(PLA) and an Immiscible PLA/Poly (ε-Caprolactone)(PCL) Blend Compatibilized by Poly (ε-Caprolactone-b-Tetrahydrofuran) Implanted in Horses. *Polym. J.* **2020**, *52* (6), 629–643.

(61) Silva, C. C.; Thomazini, D.; Pinheiro, A. G.; Aranha, N.; Figueiro, S. D.; Góes, J. C.; Sombra, A. S. B. Collagen–Hydroxyapatite Films: Piezoelectric Properties. *Mater. Sci. Eng. B* **2001**, *86* (3), 210–218.

(62) Manion, J.; Lessard, B. H. High-Throughput Characterization Is Key to Report Reliable Organic Thin-Film Transistor Performance. *Nat. Rev. Mater.* **2024**, *9* (6), 377–378. https://doi.org/10.1038/s41578-024-00689-8.

(63) Notsu, H.; Kubo, W.; Shitanda, I.; Tatsuma, T. Super-Hydrophobic/Super-Hydrophilic Patterning of Gold Surfaces by Photocatalytic Lithography. *J. Mater. Chem.* **2005**, *15* (15), 1523–1527.

(64) Kettle, J.; Kumar, D. Biodegradable Zinc Oxide Thin Film Transistors. In *2021 23rd*

European Microelectronics and Packaging Conference & Exhibition (EMPC); IEEE, 2021; pp 1–4.

(65) KV, S. B.; Rama Teja, A. S.; Srinivas Babu, N.; Arunachalam, V.; Maheswar, C. V. S.; Reddy, A. Methods of Decontamination of Toluene Di-Isocyanate (TDI) Spills and Leftovers. *Res. J. Chem. Sci. ISSN 2231*, 606X.

(66) Tousignant, M. N.; Rice, N. A.; Niskanen, J.; Richard, C. M.; Ritaine, D.; Adronov, A.; Lessard, B. H. High Performance Organic Electronic Devices Based on a Green Hybrid Dielectric. *Adv. Electron. Mater.* **2021**, *7* (10), 2100700.

(67) Grau, G.; Subramanian, V. Dimensional Scaling of High-Speed Printed Organic Transistors Enabling High-Frequency Operation. *Flex. Print. Electron.* **2020**, *5* (1), 14013.

(68) Ortiz, R. P.; Facchetti, A.; Marks, T. J. High-k Organic, Inorganic, and Hybrid Dielectrics for Low-Voltage Organic Field-Effect Transistors. *Chem. Rev.* **2010**, *110* (1), 205–239.

(69) Amin, E. M.; Karmakar, N. C.; Winther-Jensen, B. Polyvinyl-Alcohol (PVA)-Based RF Humidity Sensor in Microwave Frequency. *Prog. Electromagn. Res. B* **2013**, *54*, 149–166.

(70) Tsai, T.; Chang, J.; Wen, T.; Guo, T. Manipulating the Hysteresis in Poly (Vinyl Alcohol)-Dielectric Organic Field-Effect Transistors Toward Memory Elements. *Adv. Funct. Mater.* **2013**, *23* (34), 4206–4214.

(71) Mirka, B.; Rice, N. A.; Richard, C. M.; Lefebvre, D.; King, B.; Bodnaryk, W. J.; Fong, D.; Adronov, A.; Lessard, B. H. Contact Engineering in Single-Walled Carbon Nanotube Thin-Film Transistors: Implications for Silane-Treated SiO2 Substrates. *ACS Appl. Nano Mater.* **2022**, *5* (9), 12487–12495.

(72) Melville, O. A.; Grant, T. M.; Lochhead, K.; King, B.; Ambrose, R.; Rice, N. A.; Boileau, N. T.; Peltekoff, A. J.; Tousignant, M.; Hill, I. G. Contact Engineering Using Manganese, Chromium, and Bathocuproine in Group 14 Phthalocyanine Organic Thin-Film Transistors. *ACS Appl. Electron. Mater.* **2020**, *2* (5), 1313–1322.

(73) Dallaire, N. J.; Brixi, S.; Claus, M.; Blawid, S.; Lessard, B. H. Benchmarking Contact Quality in N-Type Organic Thin Film Transistors through an Improved Virtual-Source Emission-Diffusion Model. *Appl. Phys. Rev.* **2022**, *9* (1).

(74) Nketia-Yawson, B.; Noh, Y. Recent Progress on High-capacitance Polymer Gate Dielectrics for Flexible Low-voltage Transistors. *Adv. Funct. Mater.* **2018**, *28* (42), 1802201.

(75) Nawaz, A.; Hümmelgen, I. A. Poly (Vinyl Alcohol) Gate Dielectric in Organic Field-Effect Transistors. *J. Mater. Sci. Mater. Electron.* **2019**, *30* (6), 5299–5326.

(76) Sun, Y.; Liu, Y.; Wang, Y.; Di, C.; Wu, W.; Yu, G. Polymer Gate Dielectrics with Self-Assembled Monolayers for High-Mobility Organic Thin-Film Transistors Based on Copper Phthalocyanine. *Appl. Phys. A* **2009**, *95*, 777–780.

(77) Puigdollers, J.; Voz, C.; Fonrodona, M.; Cheylan, S.; Stella, M.; Andreu, J.; Vetter, M.; Alcubilla, R. Copper Phthalocyanine Thin-Film Transistors with Polymeric Gate Dielectric. *J. Non. Cryst. Solids* **2006**, *352* (9–20), 1778–1782.

(78) Vasimalla, S.; Subbarao, N. V. V; Gedda, M.; Goswami, D. K.; Iyer, P. K. Effects of Dielectric Material, HMDS Layer, and Channel Length on the Performance of the Perylenediimide-Based Organic Field-Effect Transistors. *ACS omega* **2017**, *2* (6), 2552–2560.

(79) King, B.; Radford, C. L.; Vebber, M. C.; Ronnasi, B.; Lessard, B. H. Not Just Surface Energy: The Role of Bis (Pentafluorophenoxy) Silicon Phthalocyanine Axial Functionalization and Molecular Orientation on Organic Thin-Film Transistor Performance. *ACS Appl. Mater. Interfaces* **2023**, *15* (11), 14937–14947.

(80) Cranston, R. R.; King, B.; Dindault, C.; Grant, T. M.; Rice, N. A.; Tonnelé, C.; Muccioli, L.; Castet, F.; Swaraj, S.; Lessard, B. H. Highlighting the Processing Versatility of a Silicon Phthalocyanine Derivative for Organic Thin-Film Transistors. *J. Mater. Chem. C* **2022**, *10* (2), 485–495.

(81) Cranston, R. R.; Lessard, B. H. Metal Phthalocyanines: Thin-Film Formation, Microstructure, and Physical Properties. *RSC Adv.* **2021**, *11* (35), 21716–21737.

(82) Jo, S.-W.; Cho, S.; Kim, C.-H. Key Factors Affecting Contact Resistance in Coplanar Organic Thin-Film Transistors. *J. Phys. D. Appl. Phys.* **2022**, *55* (40), 405101.

(83) Lee, H.; Kim, Y. E.; Bae, J.; Jung, S.; Sporea, R. A.; Kim, C.-H. High-Performance Organic Source-Gated Transistors Enabled by the Indium-Tin Oxide–Diketopyrrolopyrrole Polymer Interface. *ACS Appl. Mater. Interfaces* **2023**, *15* (8), 10918–10925.

(84) Bae, J.; Park, S.; Jung, H.; Ko, E.-H.; Kymissis, I.; Kim, C.-H. Polymer Field-Effect Transistors with Inkjet-Printed Silver Electrodes: From Device Fabrication to Circuit Simulation. *J. Mater. Sci. Mater. Electron.* **2024**, *35* (2), 185.

(85) Ali, M.; Hoseyni, S. M.; Das, R.; Awais, M.; Basdogan, I.; Beker, L. A Flexible and Biodegradable Piezoelectric-Based Wearable Sensor for Non-Invasive Monitoring of Dynamic Human Motions and Physiological Signals. *Adv. Mater. Technol.* 2023, 8, 2300347.

(86) Wu, M.; Yao, K.; Huang, N.; Li, H.; Zhou, J.; Shi, R.; Li, J.; Huang, X.; Li, J.; Jia, H. Ultrathin, Soft, Bioresorbable Organic Electrochemical Transistors for Transient Spatiotemporal Mapping of Brain Activity. *Adv. Sci.* **2023**, 2300504.

(87) Deng, Y.; Qi, H.; Ma, Y.; Liu, S.; Zhao, M.; Guo, Z.; Jie, Y.; Zheng, R.; Jing, J.; Chen, K. A Flexible and Highly Sensitive Organic Electrochemical Transistor-Based Biosensor for Continuous and Wireless Nitric Oxide Detection. *Proc. Natl. Acad. Sci.* **2022**, *119* (34), e2208060119.

(88) Melville, O. A.; Grant, T. M.; Lessard, B. H. Silicon Phthalocyanines as N-Type Semiconductors in Organic Thin Film Transistors. *J. Mater. Chem. C* **2018**, *6* (20), 5482–5488.

Chapter 3: Two Is Better Than One: How the Addition of Multiple Biodegradable Polymers Can Improve Organic Thin Film Transistor Performance

This chapter was published in the journal "ACS Applied Materials & Interfaces": M. Ali, R.B. Ewenike, J.G. Manion, B.H. Lessard, Two Is Better than One: How the Addition of Multiple Biodegradable Polymers Can Improve Organic Thin-Film Transistor Performance, ACS Appl. Mater. Interfaces 2025, 17, 1734–1742.

Context

For this work, I examined whether blending a semiconducting polymer with multiple biodegradable polymers could reduce the amount of active semiconductor required in an OTFT without sacrificing device performance. As outlined in previous chapters, the push toward sustainable electronics requires materials that are either recyclable or degradable while still meeting the electrical performance demands of functional devices. In this study, I explored blends of a DPP2T with two biodegradable polymers, PCL and PLA, rather than either polymer alone. We hypothesized that combining PCL and PLA in different ratios with DPP2T could allow for a substantial reduction in semiconductor loading while maintaining, or even improving, field-effect μ, V_T, and $I_{on/off}$ relative to neat DPP2T films. We were interested in identifying the DPP2T:PLA:PCL ratio that provided the best balance of reduced active-material content and device performance, and in understanding how the biodegradable polymer matrix influenced the self-assembly and crystallization of DPP2T within the blended film.

Contribution

I prepared the DPP2T/PLA-PCL blend solutions, fabricated and characterized the OTFT devices, and performed the electrical measurements. Ewenike and Dr. Manion assisted with thin-film characterization. I interpreted the thin film and OTFT data and made all the figures used within the study. Dr. Lessard edited and reviewed the manuscript. I wrote and reviewed the submitted manuscript.

3.1 Abstract

Developing sustainable electronics requires using materials that are either recyclable or biodegradable without compromising electrical performance. Here, we introduce a solution-processed biodegradable polymer blend consisting of a DPP2T and different mixtures of two biodegradable polymers, PCL and PLA. We find that controlling the ratio of components enables a reduction in semiconductor polymer loading (~70-80% reduction) while maintaining or improving field-effect transistor performance. At a ratio of 30 wt% DPP2T versus 70 wt% of PLA and PCL (56:14 ratio) the DPP2T self-assembled and crystallized inside the biodegradable polymer matrix, exhibiting a high field effect μ (0.18 $cm^2V^{-1}s^{-1}$), reduced V_T (~ -17 V), and a high $I_{on/off}$ (~10^5). This study demonstrates that performance does not need to be sacrificed for biodegradability.

3.2 Introduction

The development of OTFT arrays and circuits for future large-area, flexible, and low-cost electronics requires semiconductors that are solution processable and exhibit suitable performance characteristics.[1–4] Organic conjugated polymers are considered ideal semiconductor candidates for OTFTs due to their mechanical flexibility[5–7], light weight, and the ability to be processed using high-throughput fabrication techniques like solution-printing, enabling their integration into next-

generation electronic application.[4,8,9] Low bandgap polymers containing donor-acceptor (D-A) repeat units are among the most promising polymers in terms of electrical performance (charge mobilities ≈ 0.1-1.0 $cm^2\ V^{-1}\ s^{-1}$).[10–12] These polymers are typically insoluble in most organic solvents, are not biodegradable and in order to achieve high charge mobilities require undesired processing methods like high-temperature annealing[13] and macroscopic alignment procedures,[10] which makes them challenging to incorporate into flexible and degradable electronics. Previous work has focused on incorporating degradable blocks or units into the semiconductor such as Sugiyama et al.[14] who developed a conjugated diketopyrrolopyrroles (DPP) block copolymer with an insulating PCL, (**Figure 3.1**) which exhibited stretchability and similar device performance compared to pure DPP polymers based devices. Tran et al. developed conjugated polymers with degradable imine groups[15] and DPP-based polymers with acid-labile groups enabling fully degradable polymers which show high performance in OTFTs.[11] While promising, these approaches are challenging due to their synthetic complexity.[16]

Recently, multicomponent, blended polymer systems have attracted considerable attention due to their ability to reduce the amount of semiconducting polymer required while imparting secondary functionality, such as stretchability[17] and improved air stability.[18–20] Under appropriate processing conditions, the addition of inert polymers can lead to similar or even improved device performance compared with the pristine semiconducting polymer.[17,21] To date the majority of studies have focused on improving device performance without considering the recyclability, toxicity or degradation of the final polymer blend.[1,18,21–25] Since the semiconducting portion of the blend is often non-biodegradable, an ideal blend must maximize electrical performance while minimizing the non-recyclable components. Depending on the intended use, it is not always essential to completely break down the polymer into its monomeric structural components while

using simple recycling strategies.[26] To date, multicomponent systems that incorporate biodegradable polymers in blends of DPP and PCL have been shown to exhibit reduced or similar device performance compared to the pristine conjugated polymer.[11] Thus, the potential for degradable materials with considerable electrical performance remained promising. To build on this foundation, we were curious to investigate the impact of using a mixture of PCL and PLA as both biodegradable polymers are known to have different properties that can have a significant influence on the phase separation and morphology of the blend. The specific ratios of PLA and PCL might result in desired stabilization of microstructures and charge pathways of conjugated polymer in the blend.

In this study, we introduce a ternary blend of poly[[2,3,5,6-tetrahydro-2,5-bis(2-octyldodecyl)-3,6-dioxopyrrolo[3,4-c]pyrrole-1,4-diyl]-2,5-thiophenediylthieno[3,2-b]thiophene-2,5-diyl-2,5-thiophenediyl] (DPP2T, **Figure 3.1**), a semiconducting copolymer, within a biodegradable polymer matrix of PLA, (**Figure 3.1**) and PCL. We explored the relationships between polymer ratio and OTFT performance and found that we can minimize the DPP2T composition, leading to improved OTFT device performance over the pristine DPP2T devices. The blend of PLA and PCL provides a matrix that helps increase the web-like formation of the DPP2T and increases its crystallinity, leading to devices that outperform both the use of PLA alone and PCL alone. We developed a structure property-relationship by systematically investigating the morphologies, crystalline structures, and electrical properties of the blends with varying DPP2T and PLA-PCL contents and demonstrated their suitability as active materials in OTFTs, demonstrating that the addition of biodegradable polymers can be beneficial to device performance.

3.3 Results and Discussion

Dyes, such as DPP and isoindigo, are common building blocks for conjugated polymers as their planar structures contain delocalized π-electrons that make them ideal for charge transport.[10,27] DPP derivatives are frequently used as pigments in tattoos, printing inks, and industrial coatings. DPP can undergo facile chemical functionalization and as a building block can easily be degraded under mild acidic conditions.[28] There are no discernible ecological or toxicological hazards to the environment or public health associated with DPP tattoo dyes.[29] The fabrication of DPP based OTFTs already uses a low concentration of DPP, however further minimizing its concentration can allow for improved degradability and biocompatibility.

Tran and coworkers reported using PCL[11,14] as an additive for DPP-based biodegradable semiconducting blends. While these blends exhibited reduced electrical performance compared to neat semiconducting polymers, the potential for biodegradable electronics was highlighted. To build on this foundation, we investigated the impact of using different biodegradable polymers including PLA and mixtures of PLA/PCL and established structure property relationships between DPP2T ternary composition and resulting electrical properties (**Figure 3.1**). **Figure 3.1**b illustrates the fabrication of the semiconducting polymer blend films and their integration into OTFTs. We also examined the effect of solvents on the electrical properties of the DPP2T/PLA-PCL blend. Devices were fabricated by dissolving DPP2T in either chloroform or dichloromethane (in which DPP2T is sparingly soluble), followed by mixing with a blend of PLA-PCL dissolved in chloroform. The blends of DPP2T (dissolved in chlorobenzene) and PLA-PCL exhibit better OTFT performance than the blends of DPP2T (separately dissolved in chloroform and dichloromethane) with PLA-PCL. The charge transport characteristics of these blends are shown in **Figure S3.1-**

S3.6. **Table S3.**1 and **S3.**2 summarize the mobility, current on/off ratio and threshold voltage computed from the characteristic curves.

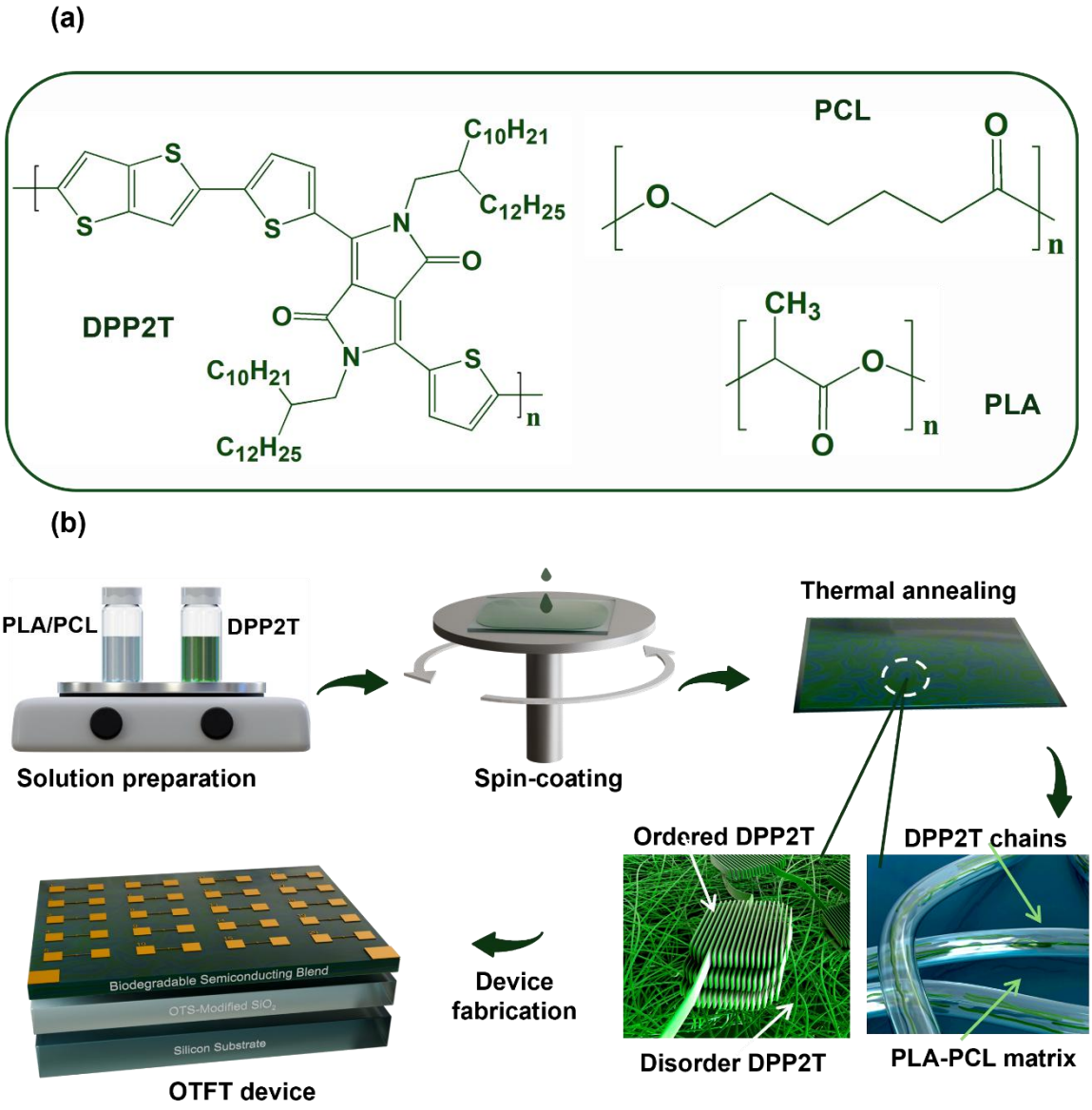


Figure 3.1. (a) Chemical structure of the conjugated polymer (DPP2T), biodegradable polymer PLA and PCL. (b) Schematic illustration of the fabrication process for DPP2T/PLA-PCL blend films and integration into an OTFT.

To identify the optimal blend ratio, we fabricated and electrically characterized bottom-gate, top-contact (BGTC) OTFTs **Figure 3.1**b while varying the DPP2T to PLA-PCL ratio from 10 to 100 wt%. We further optimized this by varying the amount of PLA and PCL from 0 to 100 wt% in the biodegradable fraction of the blend to analyse the effect of different ratios on the electrical properties. All output and transfer curves for the neat DPP2T and blended films (DPP2T/PLA-PCL) are shown in **Figure S3.7-S3.13 (SI)**. All the devices showed clear p-type charge transfer characteristics with negligible hysteresis. The μ in each device was extracted in the saturation regime. **Table 3.1** and **Table S3.3 (SI)** summarize the μ, V_T and $I_{on/off}$ for all devices. We found that the devices fabricated with varying DPP2T content (from 10-100 wt%) in neat PLA and PCL blend exhibited lower μ than the device fabricated with neat DPP2T, similar to reports by others.[11,14] However when using a 30 wt% DPP2T in 70 wt% PLA-PCL ternary blend with a 56-14 ratio, the devices exhibited greater μ than the neat DPP2T (**Figure 3.2**). Devices fabricated using 30 wt% DPP2T and 70 wt% PLA-PCL (56-14) exhibited a $\mu = (1.84 \pm 0.58) \times 10^{-1}$ $cm^2V^{-1}s^{-1}$ which outperformed neat DPP2T with a $\mu = (1.14 \pm 0.28) \times 10^{-1}$ $cm^{2}V^{-1}s^{-1}$. **Figure 3.2a** and **3.2b** depict the transfer characteristics of the neat DPP2T and DPP2T (30 wt%) blend with 70 wt% PLA-PCL (56-14), respectively. This 70 wt% reduction in DPP2T in the blend leads to a total DPP2T of roughly 0.041 $\mu g/mm^2$ DPP2T per device as calculated based on the procedure set out by Lei et al.[28] (**Table S3.4**). OTFTs fabricated with this blend exhibit greater $I_{on/off}$ that is absent in the transfer characteristics of the OTFTs made with neat DPP2T. This trend becomes clearer when examining the μ of ternary blends with different PLA-PCL ratios. **Figure 3.2c** and **3.2d** display the effect of PLA-PCL ratio on the μ and V_T, respectively, for the blends containing 30 wt% DPP2T and 70 wt% PLA-PCL. We observe a reduction in V_T from ~ -27 ± 4 V for neat DPP2T to as low as ~ -17 ± 1.0 V for PLA-PCL blend ratios. This reduction in the V_T implies reduced charge

trapping at the SiO_2/polymer blend interface.[1] We computed the interface trap density using extracted device parameters. The calculated trap density values (**Table S3.5**) confirmed significant decrease in trap density of the optimized device aligning well with the observed reduction in V_T. All devices were fabricated on OTS modified SiO_2 dielectric suggesting the drop in V_T must originate from the morphology of the semiconductor blend and its relative change in interfacial environment with the electrodes which is favourable when using a PLA-PCL mixture over both neat PLA or neat PCL. In our recent studies we have shown that PCL based dielectrics when used in OTFTs lead to significant reduction in V_T due to the elimination of interfacial charge traps.[30–32] We observe a slight improvement in $I_{on/off}$ for all blended DPP2T and PCL-PLA devices over the use of neat DPP2T with the most significant increase in the $I_{on/off}$ values for blend films of DPP2T:PCL-PLA (30:56-14), which exhibited $I_{on/off}$ of 10^5. For the PLA-PCL blends we observe a drop in off current (as a reason for increased $I_{on/off}$) which could be a result of the insulating properties of PLA-PCL, increasing the resistance in the film and reducing the leakage current. The improvement in electrical performance for the blends over neat DPP2T films are likely due to changes in morphology which has been well reported for DPP2T based blends.[1,11,14,21] The increase in μ is likely due to the formation of long-range, highly crystalline ordering of DPP2T within the PLA to PCL matrix.

In order to test the stability of the OTFT made with optimal blend, we ran the devices fabricated with optimal blend (30:56-14) after almost 7 months of exposure to air and the devices were still functioning. **Figure S3.**14 mentioned below shows the comparison of the output and corresponding transfer curves of neat DPP2T and optimal blend. **Table S3.**6 summarizes the performance parameters computed from the transfer curves of neat DPP2T and optimal blend. The degradation in the performance of the pristine DPP2T-based device is very pronounced. After 7

months of exposure to air current on/off ratio decreases from 10^3 to 10^1 and mobility value drops to 2×10^{-2} from 11×10^{-2}. On the contrary, the device made with optimal blend remains stable even after 7 months of exposure to air. Moreover, the percentage of functioning devices based on neat DPP2T is only 10% whereas 75% of the devices made with optimal blend worked suggesting prolonged air stability of semiconducting polymer when blended with degradable polymers.

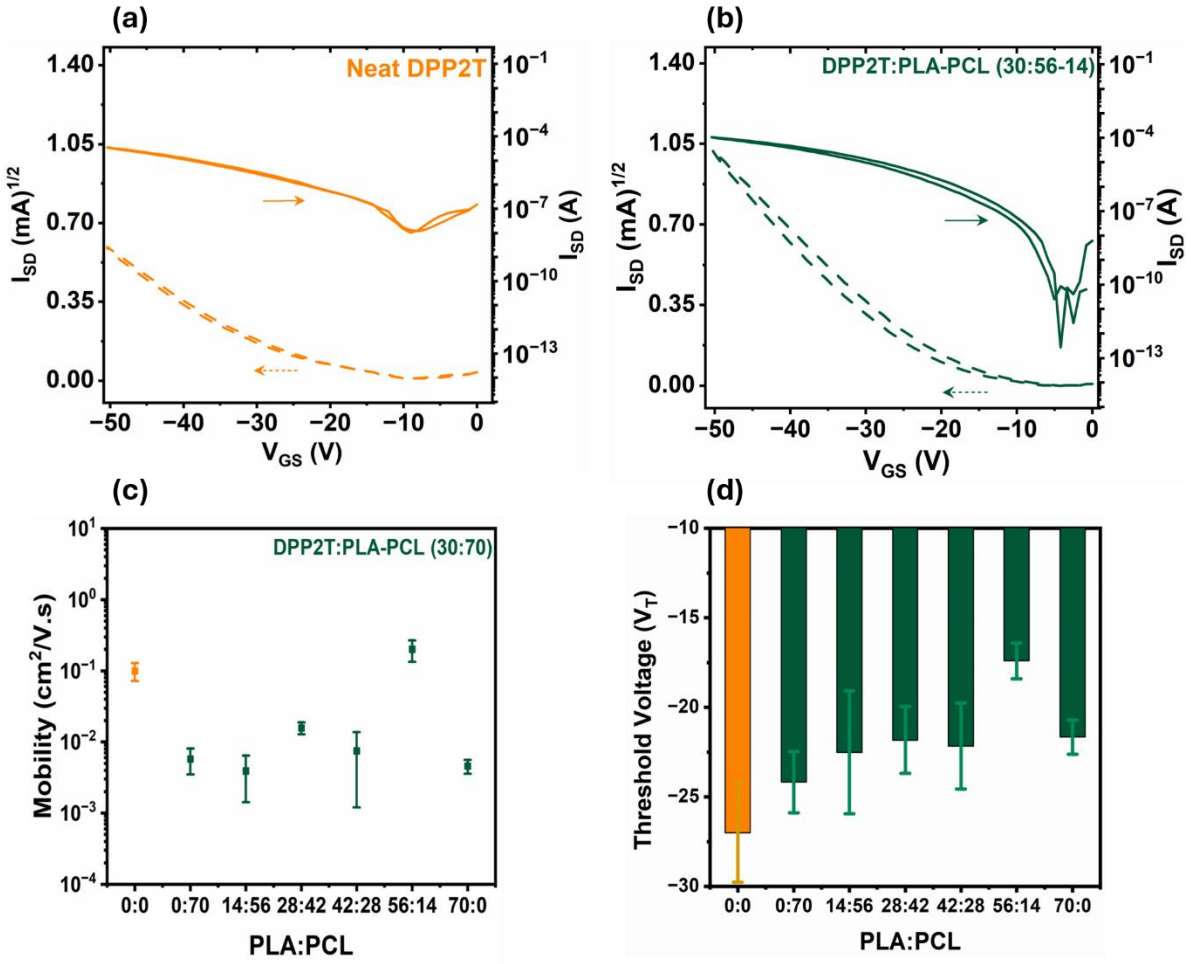


Figure 3.2. Transfer curves (V_{SD} = -50) of (a) neat DPP2T and (b) a DPP2T/PLA-PCL blend (dashed lines, square root of drain current). (c) The mobility and (d) threshold voltage of a FET device at different ratios of PLA and PCL with the same DPP2T content.

Table 3.1. Summary of the field effect properties of DPP2T/PLA-PCL semiconductor blends in OTFTs.

DPP2T:PLA-PCL[a]	Mobility ($cm^2 V^{-1}s^{-1}$)		$I_{on/off}$ [d]	$I_{on/off}$ [e]	V_T (V) [c]	Thickness (nm)[f]
	(Max. μ) [b] × 10^{-2}	(Ave. μ) [c] × 10^{-2}				
100:0	17	11 ± 2.8	2×10^3	2×10^3	-27 ± 4.0	80 ± 11.9
30:0-70	1.1	0.6 ± 0.2	5×10^3	9×10^3	-24 ± 1.7	119 ± 2.1
30:14-56	0.8	0.4 ± 0.2	4×10^3	3×10^3	-23 ± 3.4	85 ± 4.3
30:28-42	8.3	1.6 ± 2.2	5×10^3	7×10^3	-21 ± 1.9	149 ± 6.2
30:42-28	1.9	0.7 ± 0.4	6×10^3	1×10^4	-22 ± 2.4	136 ± 15.1
30:56-14	28	18 ± 5.8	7×10^5	8×10^5	-17 ± 1.0	144 ± 5.8
30:70-0	0.6	0.4 ± 0.1	7×10^3	7×10^3	-22 ± 1.0	128± 17.6

(a) Ratio of each component in the blend.
(b) Maximum mobility (μ) measured from at least 15 functional OTFT devices.
(c) Mobility and threshold voltage were computed using an average value.
(d) Ratio of on and off current was calculated using a median value.
(e) Ratio of on and off current was calculated using an average value.
(f) Thickness of the spin-coated DPP2T/PLA-PCL blends films obtained using profilometer.

XRD was performed to investigate the crystalline regions of the DPP2T/PLA-PCL films. The spectra of the films are found in **Figure 3.3a** along with the corresponding film thicknesses in Table 3.1. The neat DPP2T film displayed a sharp (100) lattice plane diffraction peak at 2θ = ~ 3.7° and a weak diffraction peak (200) at 2θ = ~ 5.6° which is consistent with the literature.[33,34] The XRD spectra of the blended films were characterized to have a similar peak location. While the film thicknesses vary due to slight changes in solution viscosity with substitution of PCL and

PLA the resulting films still exhibited relatively high signal intensity comparable to the neat DPP2T films. The percentage crystallinity of the blend thin films calculated using Equation S1[35] is listed in **Table S3.7** for comparison.

Figure 3.3b displays the solid-state UV-visible absorption spectra of neat DPP2T and its blend with the PLA-PCL matrix. Every sample displayed characteristic vibronic splitting of the dual-band absorption between 740–835 nm, typical of a highly ordered DPP2T structure.[36–39] As the loading of PLA increased from 0 to 42 wt% (while keeping loading of DPP2T constant at 30 wt%), the 0-0 vibrational peak (~825 nm) increased in intensity with respect to the 0-1 vibrational peak intensity (~750 nm). The greatest increase in 0-0 relative to 0-1 was observed for a ratio of DPP2T:PLA-PCL of 30:42-28 and was even greater than the neat DPP2T. This is consistent with the XRD spectra of the sample (30:42-28). These observations indicate that blending PLA and PCL under the right conditions leads to increased molecular ordering due to the formation of lamellar stacks of DPP2T[38] in the blend films.

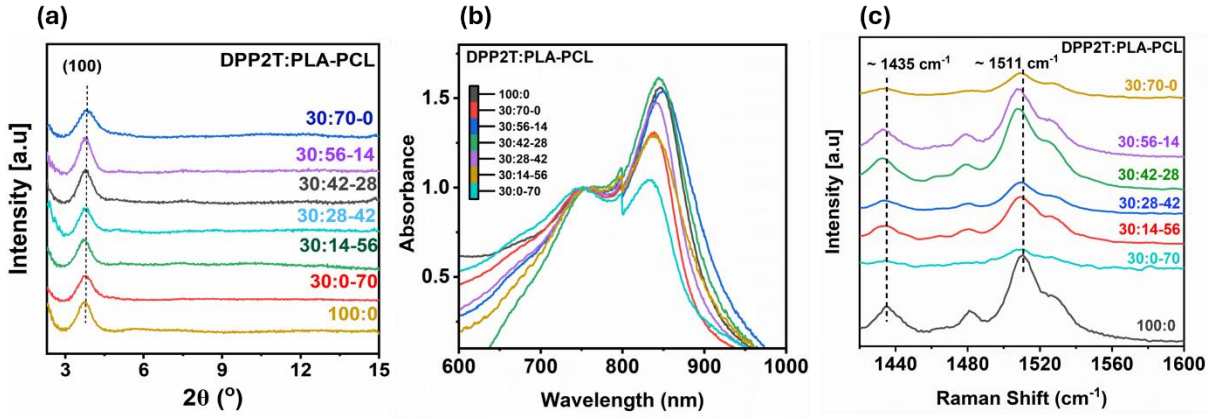


Figure 3.3. XRD spectra (a) and (b) normalized UV-vis spectra for neat DPP2T and blend thin films with varying PLA-PCL content while keeping the DPP2T content the same. (c) Raman

spectra of neat DPP2T and DPP2T blends with different PLA-PCL ratios and the same DPP2T content.

AFM was used to investigate semiconductor blend films to characterize film morphology. The neat DPP2T film exhibited diffuse and nanodomain features, with no long-range ordering, in AFM topographic images (**Figure S3.15**). Blended DPP2T (30 wt%) demonstrated a progressive development towards larger, more apparent nanowire-like structures as the PLA ratio relative to PCL was increased (**Figure 3.4a-f**). Three distinct regimes may be identified in the morphological evolution of DPP2T in the PLA-PCL matrix: (i) at low PLA content, the DPP2T forms nanodomain features with no long range orders (**Figure 3.4**b-c) (ii) at intermediate concentrations of PLA in the blend, DPP2T forms fully interconnected networks of long range (**Figure 3.4**e); and (iii) at high concentration (neat PLA), the crystalline domain structures break down which decreased the density of the nanowires and resulted in features with no long-range ordering of DPP2T (**Figure 3.4**f). These changes in morphology because of the different PLA content are likely responsible for changes in charge-transport characteristics as observed from the electrical performance of the OTFTs.

The processing of the blends with different PLA and PCL content likely led to the segregation and self-assembly of DPP2T crystalline domains in the PLA-PCL matrix similar to previously reported vertical phase separations of semiconductor/polymer blends that produced two separate layers.[40–44] The final morphology of the blend films depends on several factors, including the combination of processing solvents and the surface energy of the blending materials and substrate.[17,18,45] The segregation and distribution of DPP2T network on OTS-treated SiO_2 dielectric surface can be attributed to changes in surface energies of the blend components. The higher surface energy of PLA (~ 53 mN/m)[46] and PCL (~ 43 mN/m)[47] compared to DPP (~ 31 mN/m)[48]

results in preferential migration of PLA/PCL to the air/blend interface, whereas the DPP2T network structure migrated to the blend/substrate interface during spin coating owing to the closely matching surface energies of the SiO_2 (OTS-treated) (~ 28 mN/m)[49] and DPP2T. Moreover, when the blend solution is spin-coated on the SiO_2 substrate, the DPP2T immediately solidifies (segregated and self-assembled) as a result of the change in surface energy,[18,50] thereby forming the well-interconnected network structure of DPP2T. Subsequently annealing the blend films increased the size of the DPP2T-rich region while the size of the coexistence region decreased as the PLA-PCL move towards the air-film interface.[50] Consequently, the DPP2T network structures were evenly embedded throughout the PLA/PCL matrix to form a desirable structure for retaining suitable electrical properties within a high fraction of matrix material.

Raman microscopy was performed to obtain further insight into the DPP2T blend morphology. Raman microscopy is particularly sensitive to variations in the local ordering of polymers, enabling the detection of small differences in conjugation length or miscibility within the system.[51–54] Chemical or compositional maps can therefore be assembled by identifying corresponding spectroscopic peaks unique to the PLA/PCL and comparing them to those of DPP2T. DPP2T is characterized by intra-unit C=C backbone symmetric stretching vibrations of the thiophene ring at ~ 1435 cm^{-1}, C-N and C-C symmetric stretches related to the DPP acceptor (~ 1370 cm^{-1}) and DPP and thiophene lactam ring C=C asymmetric stretching (~ 1511 cm^{-1}) (**Figure S3.16**, **SI**).[52,55] PLA and PCL exhibit characteristic peaks at ~ 2945 cm^{-1} and ~ 2913 cm^{-1}, respectively. **Figure 3.4g-l** depicts the Raman intensity ratio maps for a 19 × 19 μm area of an OTFT device fabricated using blends with different ratios of PLA and PCL while keeping the DPP2T content constant at 30 wt%. These figures illustrate the normalized ratio of DPP2T (at ~ 1511 cm^{-1}) relative to PLA/PCL (~ 2945/2913 cm^{-1}) and provide a visual representation of the film

chemical uniformity to complement the AFM. Raman maps reveal that when blending with neat PCL (**Figure 3.4**g) we see very sharp contrast regions with high DPP2T ratios and while using neat PLA (**Figure 3.4**l) we see a completely homogeneous film with low DPP2T ratios. As we increase the PLA content from 0 to 56 wt% in the PCL blend we observe an increase in the intensity ratio of the DPP2T signal. Specifically, the sample with a PLA content of 56 wt% in the PLA-PCL blend showed a uniformly higher DPP2T intensity ratio. This indicates that a higher proportion of PLA within the blend uniformly enhances the DPP2T segregation and network formation. In addition, the Raman spectrum shown in **Figure 3.3**c demonstrates that the two backbone C=C peaks gradually shifted to lower wavenumbers for the blend films containing 42 and 56 wt% PLA in DPP2T:PLA-PCL blend which is indicative of improved crystallization and segregation of DPP2T in the blend with a particular amount of PLA.[55] The effective conjugation coordinate model (ECCM) states that the force constant resulting from the interaction between the centre unit and the units at a distance along the one-dimensional lattice increases as a conjugation length of the polymer increases.[56] As a result, the total force constant decreases, which causes the wavenumber of the Raman mode to be downshifted as the conjugation length and segmental order increase. Therefore, longer conjugation lengths, increased backbone planarity, and higher segmental order during crystallization are indicated by the shifting of C=C peaks to lower wavenumbers.[51,56] This suggests that while the specific amount of PLA in PLA-PCL blend improves DPP2T segregation and network formation, excessive/low PLA may inhibit optimal DPP2T network formation or interaction.

When combined, PLA and PCL are known to have different properties that affect phase separation and provide a different morphology. For instance, a study by Ostafinska et al. reported that a PLA-PCL blend with the ratio of 80-20 (similar to our optimized sample) demonstrated

improved material performance because of even distribution of PCL in the PLA-PCL matrix, particularly when the PLA proportion was higher.[57] This implies that the higher PLA content in DPP2T/PLA-PCL blend might aid in microstructure stabilization and improve DPP2T charge pathways, both of which are essential for semiconducting performance. Higher content of PLA (56 wt%) may form a rigid matrix, which might contribute to improving charge transport properties of the optimal blend film by forming nanostructures with long-range order of the conjugated polymer within the PLA-PCL matrix,[58] while the specific amount of PCL (10-20%) in the PLA-PCL blend improves the fluidity of PLA chains.[59] The distribution histograms presented in **Figure 3.4**m-r quantify the ratio's from the maps to help visualize the distribution of ratios. It can be seen from the distribution histograms that the optimal sample (30:56-14) exhibits a broad distribution. As these measurements were conducted for films fabricated with the same processing conditions, the difference in intensity of DPP2T is therefore caused by using different PLA-PCL content. The Raman microscopy further supports the XRD, UV-Vis and AFM suggesting that a ternary blend of DPP2T, PLA and PCL led to improved morphology, self-assembly and crystallization of the DPP2T domains, resulting in improved OTFT performance.

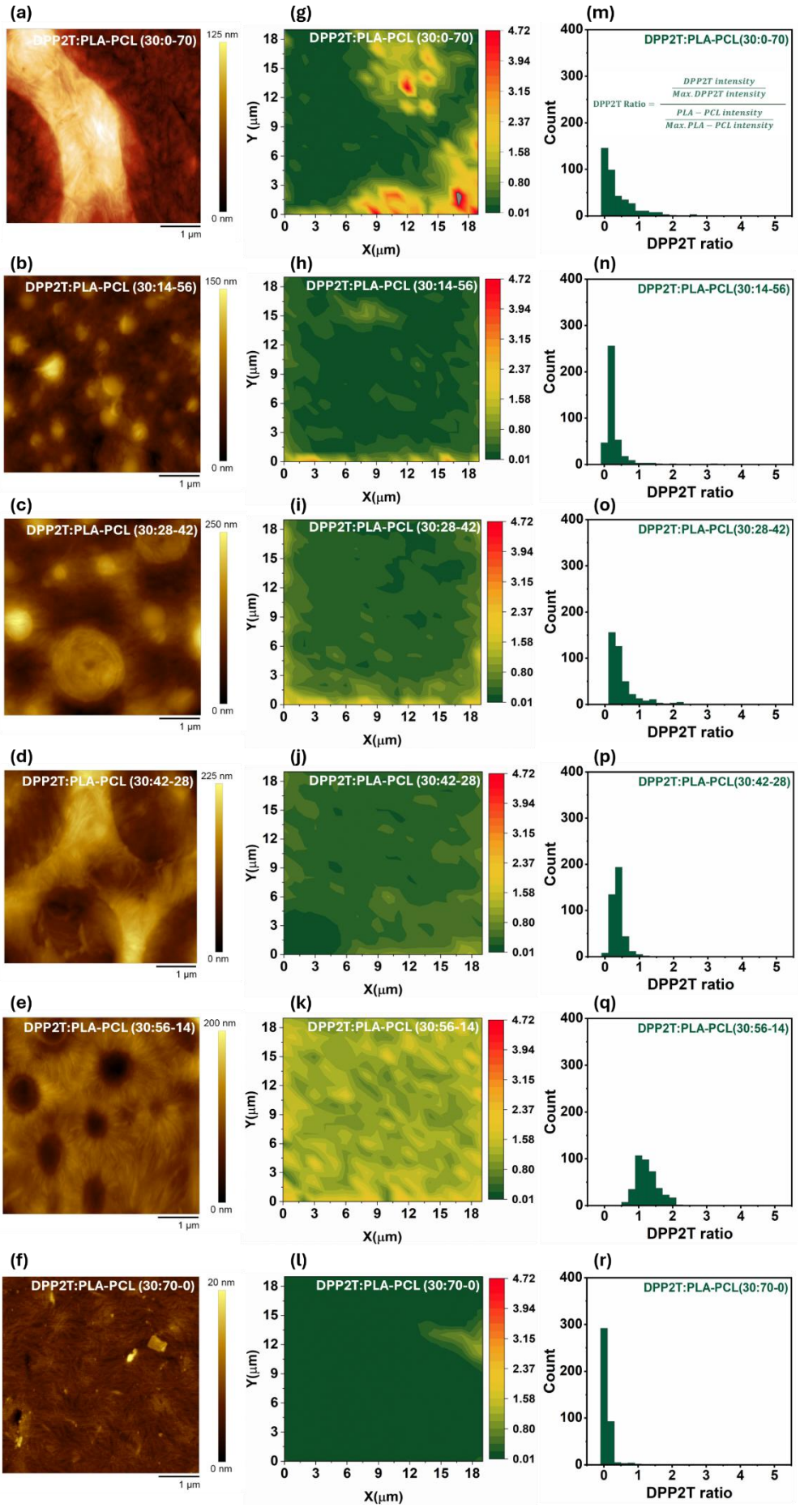

(a)
DPP2T:PLA-PCL (30:0-70)
125 nm
0 nm
1 μm
(g)
DPP2T:PLA-PCL (30:0-70)
Y (μm)
X(μm)
4.72
3.94
3.15
2.37
1.58
0.80
0.01
(m)
DPP2T:PLA-PCL(30:0-70)
DPP2T Ratio = (DPP2T intensity / Max. DPP2T intensity) / (PLA − PCL intensity / Max. PLA − PCL intensity)
Count
DPP2T ratio
(b)
DPP2T:PLA-PCL (30:14-56)
150 nm
0 nm
1 μm
(h)
DPP2T:PLA-PCL (30:14-56)
(n)
DPP2T:PLA-PCL(30:14-56)
(c)
DPP2T:PLA-PCL (30:28-42)
250 nm
0 nm
1 μm
(i)
DPP2T:PLA-PCL (30:28-42)
(o)
DPP2T:PLA-PCL(30:28-42)
(d)
DPP2T:PLA-PCL (30:42-28)
225 nm
0 nm
1 μm
(j)
DPP2T:PLA-PCL (30:42-28)
(p)
DPP2T:PLA-PCL(30:42-28)
(e)
DPP2T:PLA-PCL (30:56-14)
200 nm
0 nm
1 μm
(k)
DPP2T:PLA-PCL (30:56-14)
(q)
DPP2T:PLA-PCL(30:56-14)
(f)
DPP2T:PLA-PCL (30:70-0)
20 nm
0 nm
1 μm
(l)
DPP2T:PLA-PCL (30:70-0)
(r)
DPP2T:PLA-PCL(30:70-0)

Figure 3.4. (a-f) AFM topographic images of thin films of DPP2T:PLA-PCL (30:70) with varied PLA-PCL compositions (g-l), Raman maps (19 × 19 μm), and (m-r) distribution histograms of the same films.

3.4 Conclusion

We report a multicomponent, degradable, and flexible semiconducting polymer blend based on DPP2T, PLA and PCL using a facile solution processing method. Under the right ternary ratio, we developed OTFTs which outperformed the neat DPP2T based OTFTs as well as the DPP2T binary blends using only PLA or PCL. XRD and solid-state UV-Vis absorption spectroscopy suggest the combined use of PCL and PLA lead to improved crystallinity of the DPP2T domains while AFM and Raman microscopy illustrate improved morphology and self-assembly of the DPP2T. Our findings demonstrate that the combination of PLA and PCL lead to improved morphology and device performance while reducing the loading of non-degradable semiconductor by 70–80% paving the way towards high performing sustainable electronics.

3.5 Experimentation

3.5.1 Materials

All the chemicals were used as received unless otherwise specified. OTS (97%) was diluted with toluene (anhydrous, 99.8%) to prepare a 1 v/v% solution inside the glovebox. PCL (80 kg/mol) and PLA (230 kg/mol) were sourced from Sigma-Aldrich. DPP2T (Mw ~80 k, PDI ~3) conjugated polymer was acquired from 1-Material. Chromium-coated tungsten rods and gold (99.99%) were obtained from Angstrom Engineering. Silicon wafers with a thermally grown SiO_2 layer of 230 nm, and shadow masks were supplied by WaferPro and Ossila, respectively. Solvents were acquired from commercial suppliers and used as received, unless otherwise specified.

3.5.2 Preparation of DPP2T/PLA-PCL blend solution

Solutions of PLA and PCL polymers in chloroform (10 mg ml^{-1}) were prepared with varying the amounts of PLA (0 to 100 wt%) in PLA-PCL. The solution was then filtered using 0.22-micron size PTFE filters. DPP2T with the concentration of 2 mg mL^{-1} was prepared by dissolving it in chlorobenzene solvent and stirred for 1 hour at 60 ^{o}C. The solution of PLA-PCL and DPP2T were blended in various ratios and stirred for 90 min at room temperature to enhance the formation of crystalline DPP2T in the blend solution.

3.5.3 OTFT fabrication

OTFTs with BGTC were fabricated on n-doped silicon substrates measuring 15 mm by 20 mm. The substrates were procured from WaferPro with a 230 nm thick thermally grown SiO_2 dielectric layer. The substrates were cleaned by sonicating them for five minutes in distilled water, soapy water, acetone, and methanol sequentially. They were then nitrogen-dried and subjected to an air plasma treatment for 15 minutes. After being exposed to plasma, the substrates were cleaned

with isopropanol and water, dried with nitrogen, and then immersed in a 1% v/v solution of OTS and toluene at 70 ºC for 1 hour. Following the OTS treatment, the substrates were vacuum-dried for an hour at 70 °C after being washed with toluene and isopropanol. The blended solutions were spin cast onto the OTS-treated SiO_2 film using a Laurell WS-650-23 spin coater at 2500 rpm for 60 s under ambient conditions. Subsequently, the spin-coated films of the biodegradable semiconductor blend were annealed at 110 ºC for 15 minutes under vacuum. The samples were then transferred to a nitrogen glovebox connected to a thermal evaporator (Angstrom Engineering). Source-drain electrodes with dimensions of L = 30 μm and W = 1000 μm were fabricated by depositing a 2 nm layer of chromium and a 50 nm layer of gold at a rate of 0.5 Å s−1 using a shadow mask. All devices were then characterized using our in-house autotester.[60,61]

3.6 Acknowledgements

The authors would like to thank the National Science and Engineering Research Council of Canada (NSERC), Canada Research Chair (CRC) program and the Canadian Foundation for Innovation (CFI) for funding this work.

3.7 Supporting Information

3.7.1 Thin Film Characterization

XRD: XRD patterns of neat DPP2T and DPP2T/PLA-PCL films on SiO_2 dielectric treated with OTS was recorded using a Bruker D8 Endeavour apparatus. The measurements were conducted using Cu Kα radiation (λ = 1.5418 Å) at a scan rate of 0.5° min^{-1}, covering the range of $2° < 2\theta < 15°$. The percentage crystallinity of the XRD peaks was computed by using **Equation S3.1**.[35] The following equation is often expressed as the ratio of the area of the crystalline region (Ac) to the sum of the area of the crystalline region and the amorphous region (Ac + Aa):

$$W_{c,x} = \frac{A_c}{A_c + A_a} \times 100\% \quad \text{(S3.1)}$$

UV-Vis: The UV-vis spectra were measured by using an Agilent Technologies Cary 7000 UV-Vis-NIR spectrometer. Absorbance measurements were collected for solid -state thin films deposited onto glass substrate via spin coating (at 2500 rpm for 60 seconds) at ambient temperature within the range of 600-1000 nm.

AFM: Atomic force microscopy (AFM) was performed using a Park NX10 in tapping mode. Tap300Al-G silicon (AFM Probe with Aluminium Reflective Coating) tips were used, operating at 300 kHz with a force constant of 40 N/m and a tip radius of 10 nm.

Raman: A Renishaw in Via InSpec confocal Raman microscope was used to analyse non-polarized Raman spectra. The Leica Microsystems DM2700 bright field microscope was the instrument used. Using a 2400 l mm^{-1} grating and a 500 mW, 532 nm laser, the spectral range of 500 to 1700 cm^{-1} for neat DPP2T and 1000-3200 cm^{-1} for DPP2T/PLA-PCL blends was measured. Using a 50L lens with a 0.5 aperture, the laser was directed onto the sample via a Leica Microsystems bright field microscope equipped with a DM2700 light source. With this configuration, the Raman microscope was able to reach a theoretical depth of focus of about 3.0 μm, an estimated spatial resolution of 640 nm, and a spectral resolution of 0.3 cm^{-1} measured from full width half maximum (FWHM). Prior to every measurement, calibration was carried out using the 520 cm^{-1} silicon reference peaks within 0.5 cm^{-1}. Measurements without polarisation were conducted using a 10% laser power (50 mW) and a 10-second exposure duration. Using 361 distinct spectra, a 1.0 μm step size, 5% laser intensity (25 mW), and a 10-second exposure duration,

Raman maps (19 × 19 μm) were produced. The distribution intensity ratio of the DPP2T in the DPP2T/PLA-PCL blend was calculated using **Equation S3.**2. Cosmic ray disruptions were eliminated from all acquired data through processing.

$$\text{DPP2T Ratio} = \frac{\text{DPP2T intensity}/\text{Max.DPP2T intensity}}{\text{PLA}-\text{PCL intensity}/\text{Max.PLA}-\text{PCL intensity}} \quad \text{(S3.2)}$$

Profilometer: Bruker Dektak XT Profilometry was used to measure the thickness of semiconducting blend films.

3.7.2 OTFT Characterization

For electrical characterization, a custom-built auto tester and a Keithley 2614B source meter were used. The tips of the auto tester contacted the source, drain, and gate electrodes of the BGTC OTFTs. The Keithley 2614B source meter, controlled by a custom LabVIEW program, was used to set the V_{GS} and V_{SD} while measuring the I_{SD} in the devices. For each substrate, output curves were collected by sweeping the V_{SD} while maintaining a constant V_{GS}. Transfer curves were obtained by sweeping the V_{GS} and holding the V_{SD} constant. This process was repeated four times to ensure stable performance, and the fourth run was used to evaluate device performance. The device performance characteristics were analyzed in the saturation regime using **Equation S3.3**.

$$I_{SD} = \frac{\mu C_i W}{2L}(V_{GS} - V_T)^2 \quad \text{(S3.3)}$$

where μ is the field-effect μ of the semiconductor, and L and W represent the channel length and width, respectively. C_i is the capacitance of the dielectric layer, and V_T is the threshold voltage.

V_T and μ were computed by measuring the x-intercept and slope, respectively, of the linearized curve ($\sqrt{I_{SD}}$ *vs* V_{GS}) utilizing **Equation S3.4**.

$$\sqrt{I_{SD}} = \frac{\mu C_i W}{2L}(V_{GS} - V_T) \tag{S3.4}$$

The $I_{on/off}$ of the devices was calculated as the ratio of the measured maximum current (I_{on}) to the minimum current (I_{off}) achieved within the operational voltage range of the transfer curves.

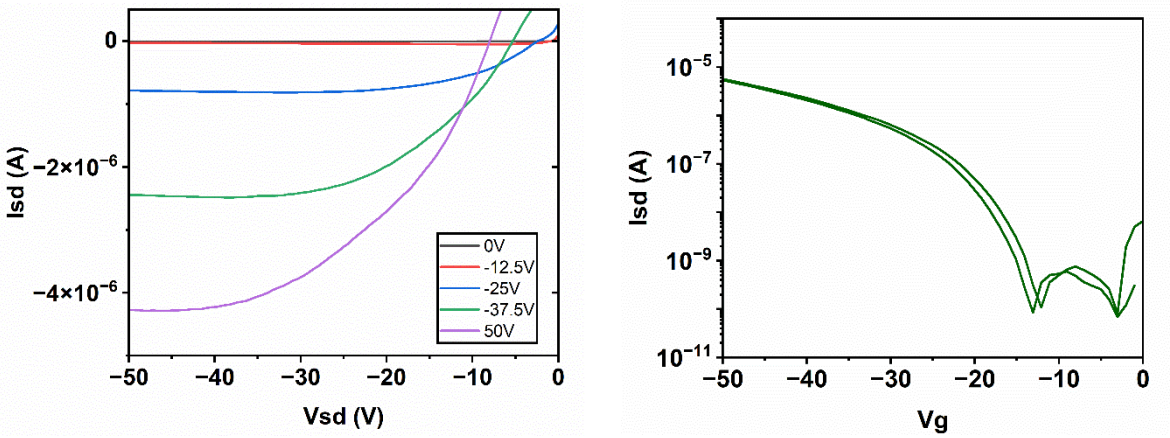


Figure S3.1. Output (left) and corresponding transfer (right) curves of neat DPP2T dissolved in chloroform.

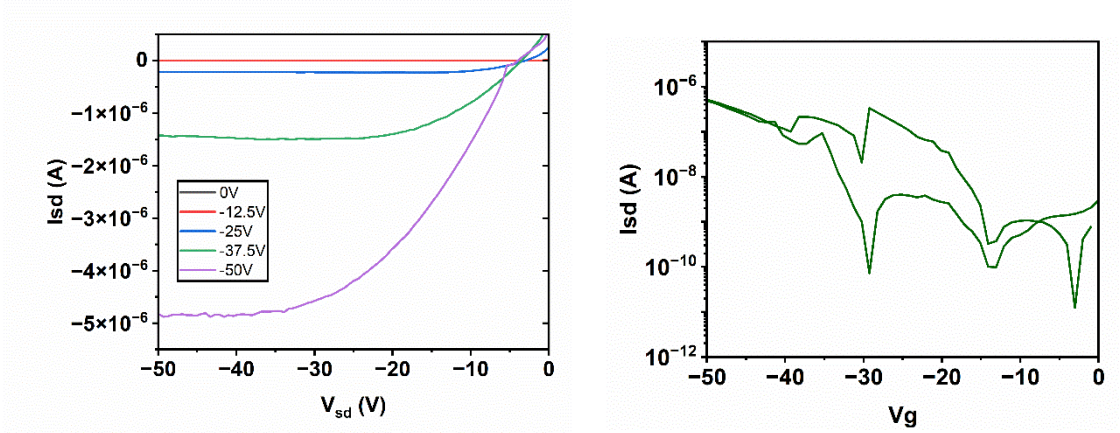


Figure S3.2. Output (left) and corresponding transfer (right) curves of neat DPP2T dissolved in dichloromethane.

Note: Electrical data using semiconducting blend films prepared by dissolving DPP2T in chloroform and PLA-PCL in chloroform

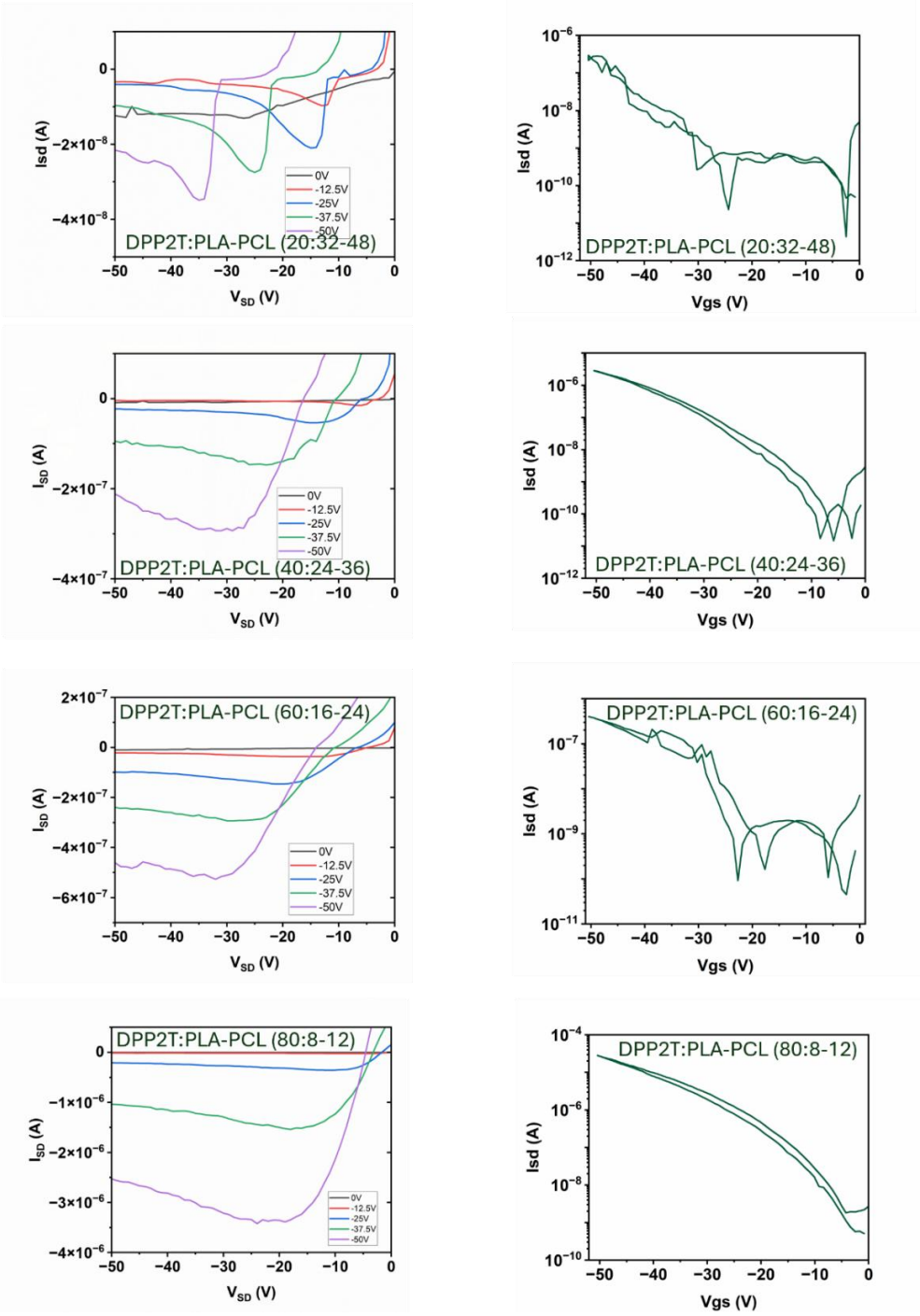


Figure S3.3. Output (left) and corresponding transfer (right) curves of DPP2T/PLA-PCL blend with varied DPP2T and PLA-PCL (40-60% according to the matrix ratio) content, with DPP2T dissolved in chloroform.

Note: Electrical data using semiconducting blend films prepared by dissolving DPP2T in chloroform and PLA-PCL in chloroform.

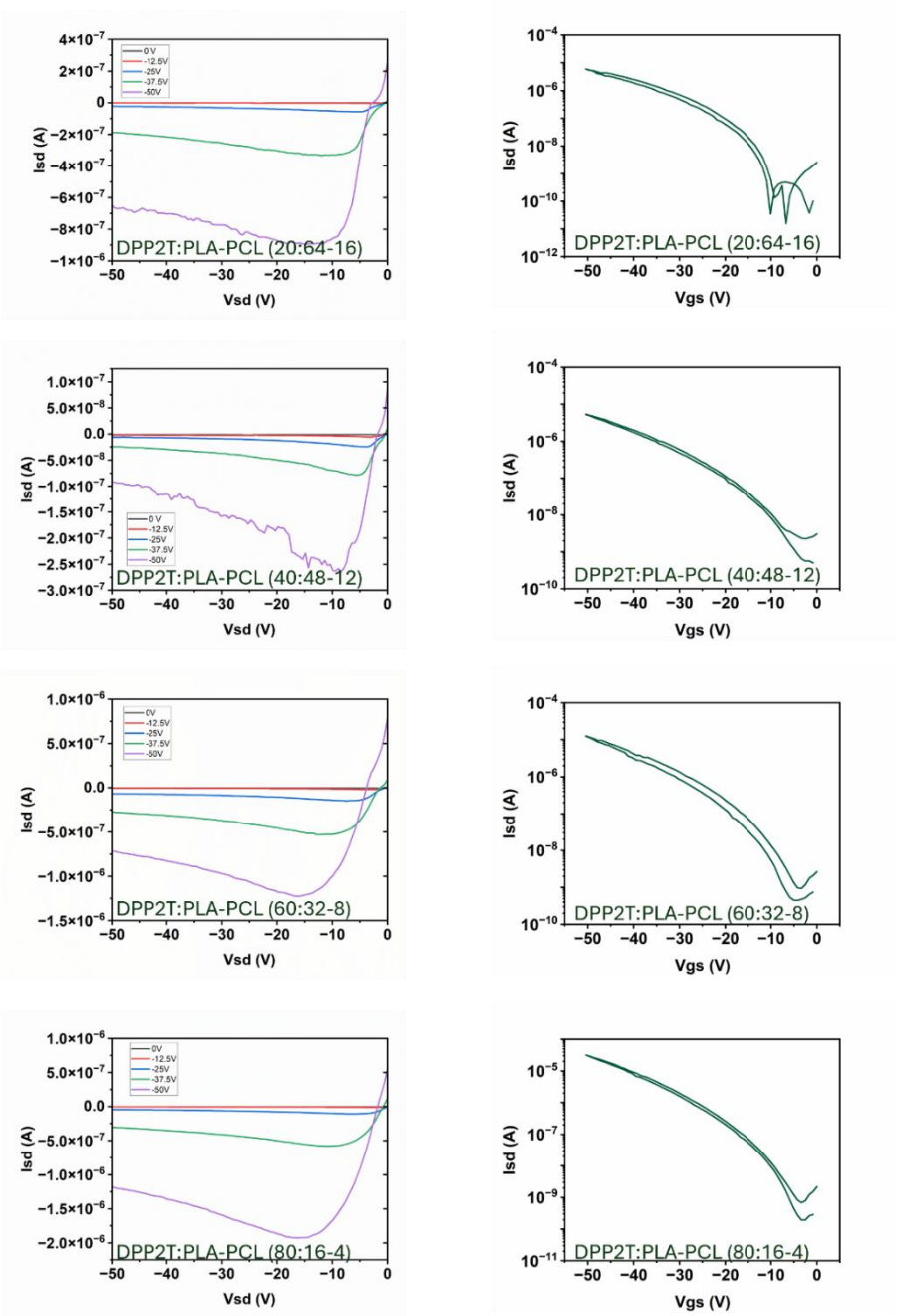


Figure S3.4. Output (left) and corresponding transfer (right) curves of DPP2T/PLA-PCL blend with varied DPP2T and PLA-PCL (80-20% according to the matrix ratio) content, with DPP2T dissolved in chloroform.

Note: Electrical data using semiconducting blend films prepared by dissolving DPP2T in dichloromethane and PLA-PCL in chloroform

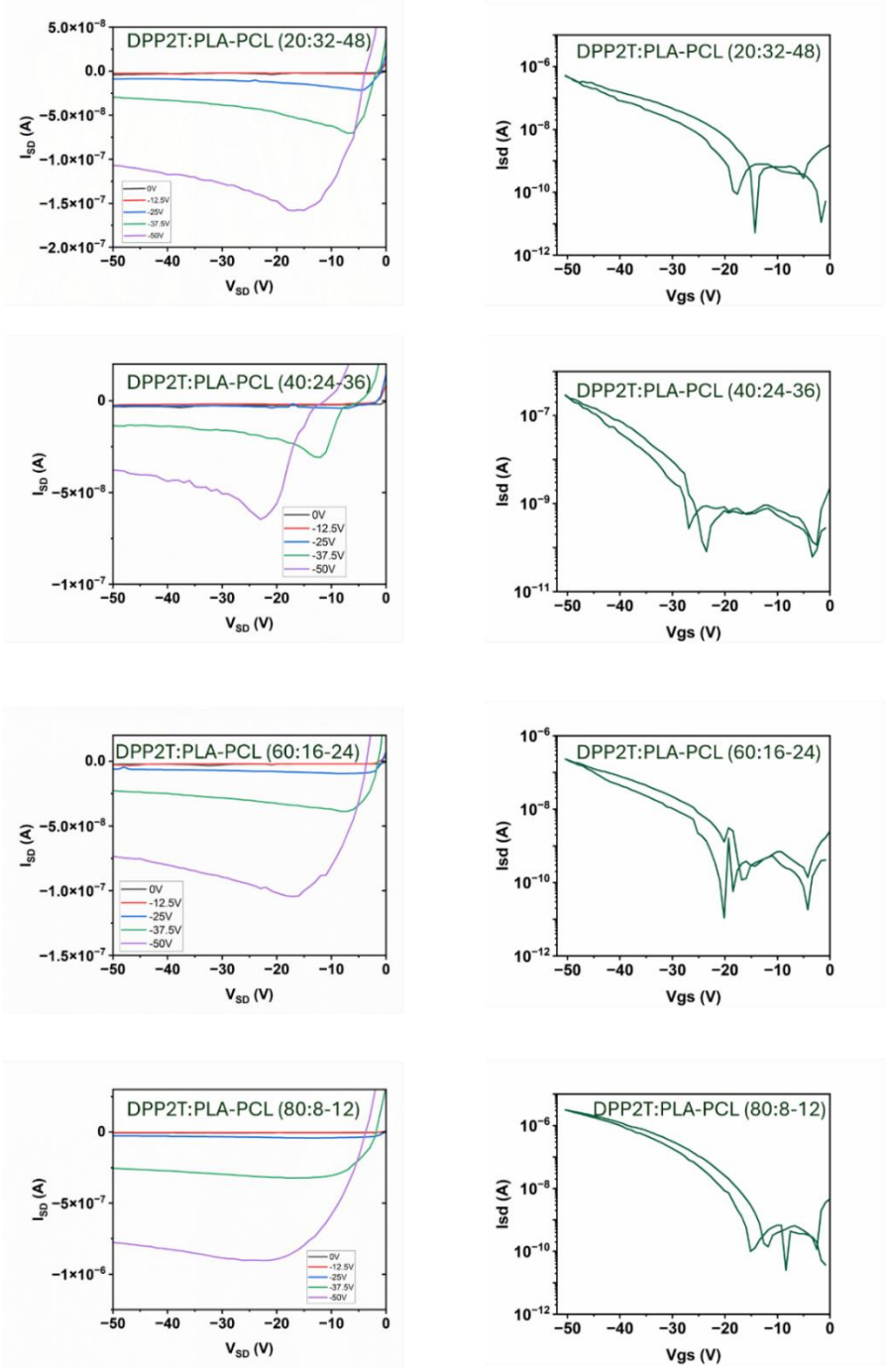


Figure S3.5. Output (left) and corresponding transfer (right) curves of DPP2T/PLA-PCL blend with varied DPP2T and PLA-PCL (40-60% according to the matrix ratio) content, with DPP2T dissolved in dichloromethane.

Note: Electrical data using semiconducting blend films prepared by dissolving DPP2T in dichloromethane and PLA-PCL in chloroform

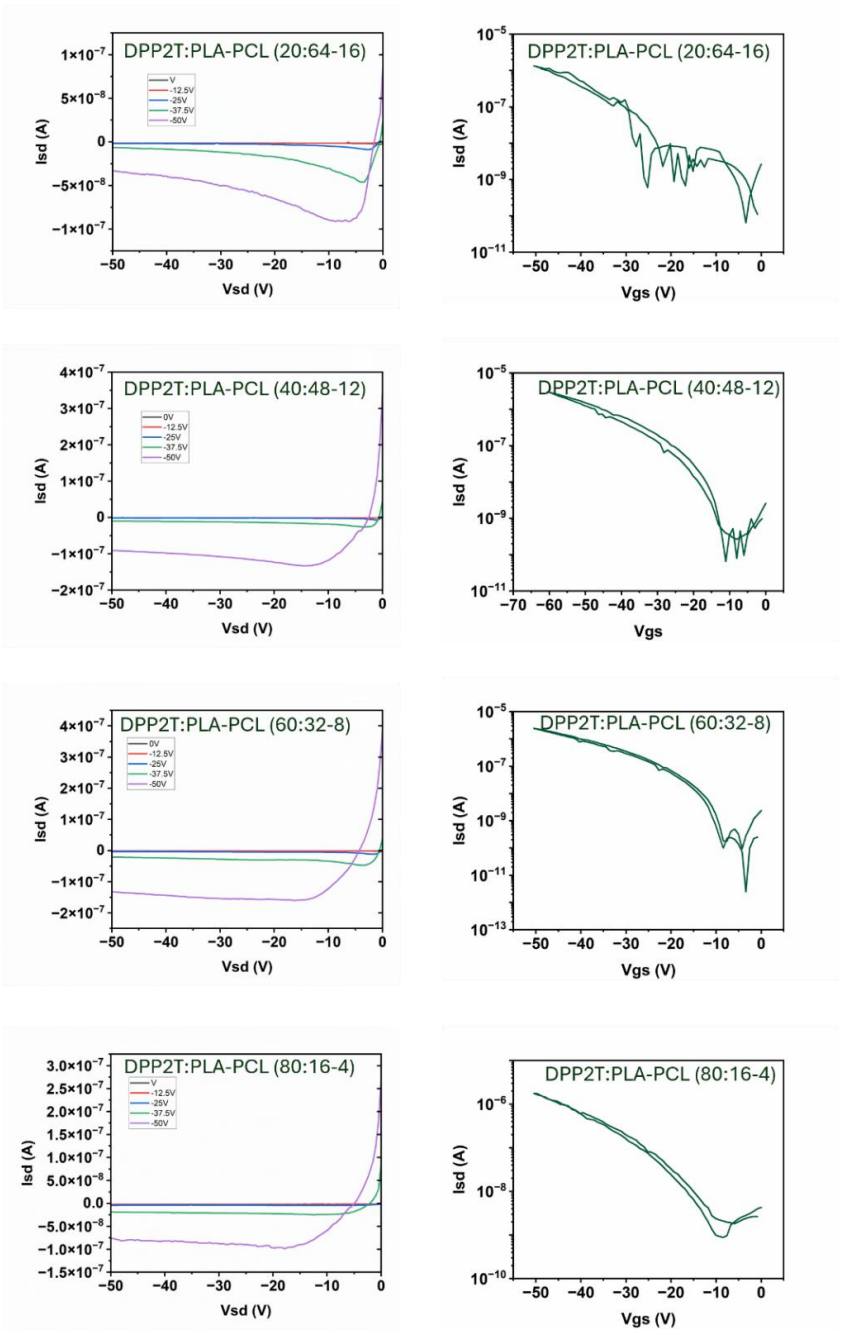


Figure S3.6. Output (left) and corresponding transfer (right) curves of DPP2T/PLA-PCL blend with varied DPP2T and PLA-PCL (80-20% according to the matrix ratio) content, with DPP2T dissolved in dichloromethane.

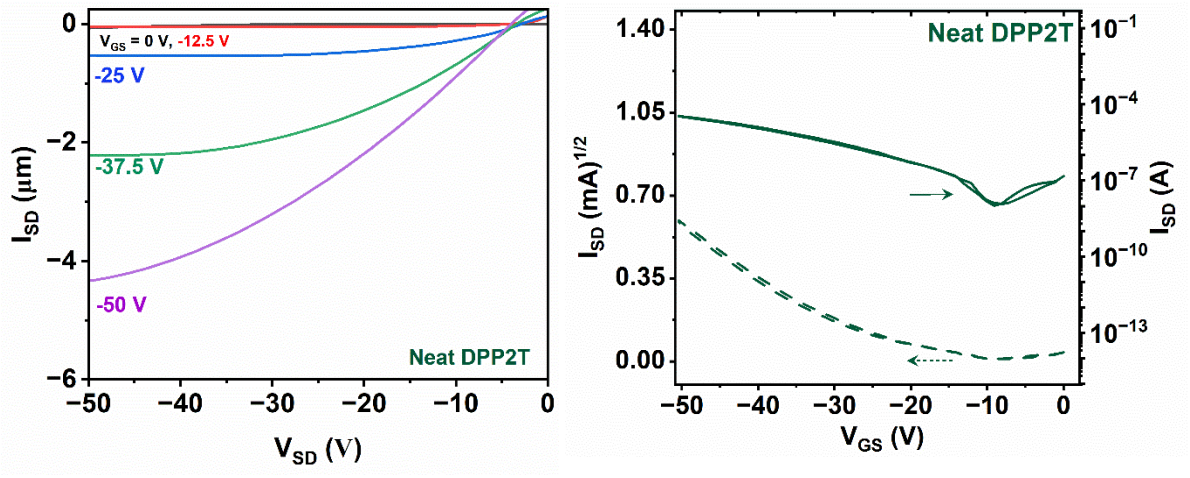


Figure S3.7. Output (left) and transfer (right) curves for neat DPP2T (2 mg/ml) dissolved in chlorobenzene.

Note: Electrical data using semiconducting blend films prepared by dissolving DPP2T in chlorobenzene and PLA/PCL in chloroform.

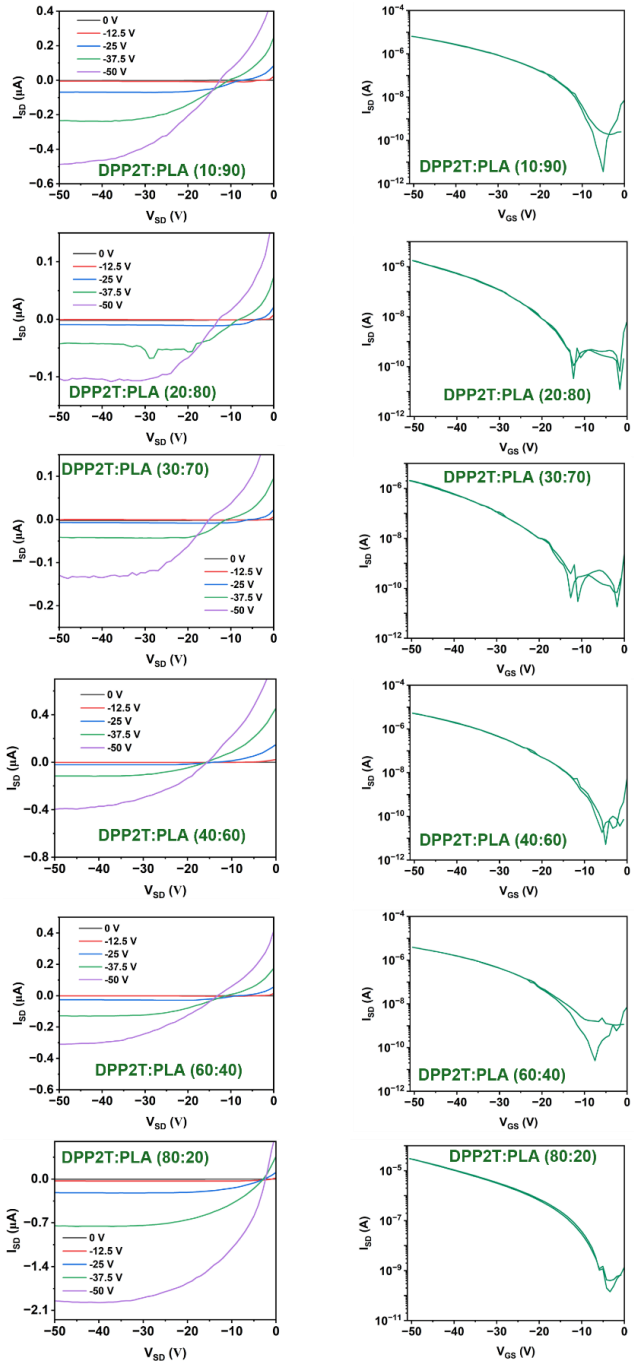


Figure S3.8. Output (left) and transfer (right) characteristics curves of varied DPP2T blend with neat PLA.

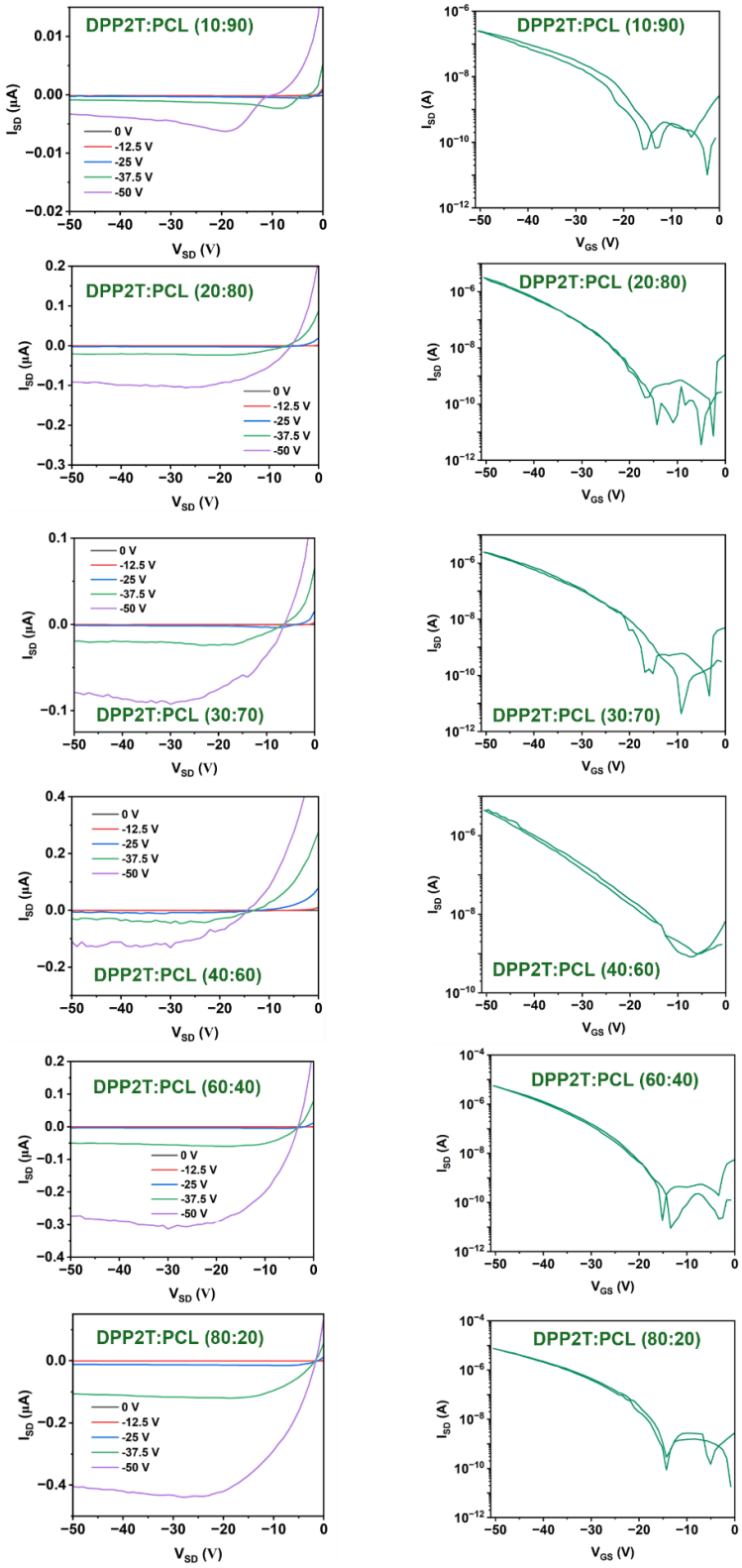


Figure S3.9. Output (left) and transfer (right) characteristics curves of varied DPP2T blend with neat PCL.

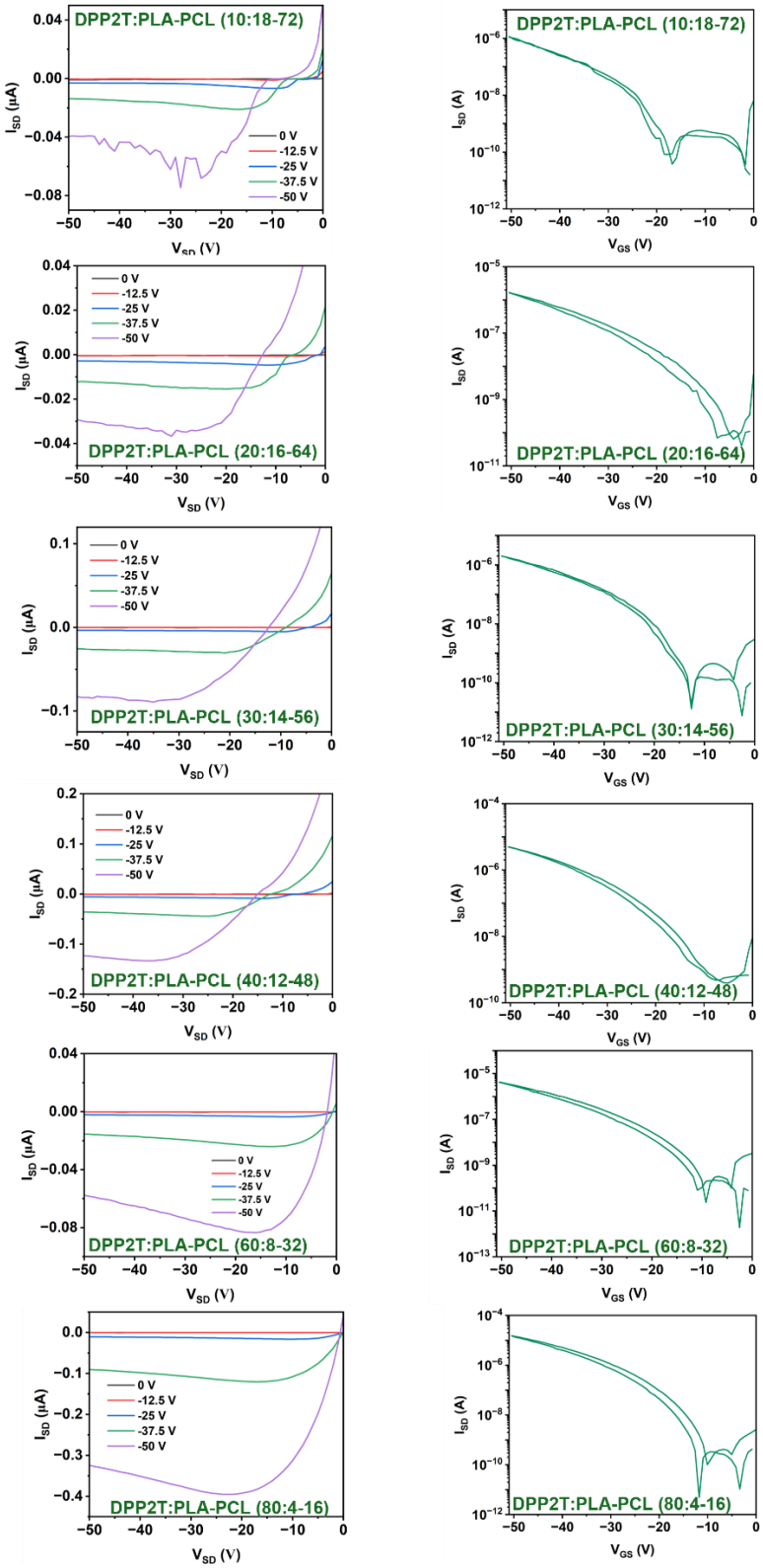


Figure S3.10. Output (left) and transfer (right) characteristics curves of varied DPP2T/PLA-PCL blend with varied DPP2T and PLA-PCL (20-80% according to the matrix ratio) content.

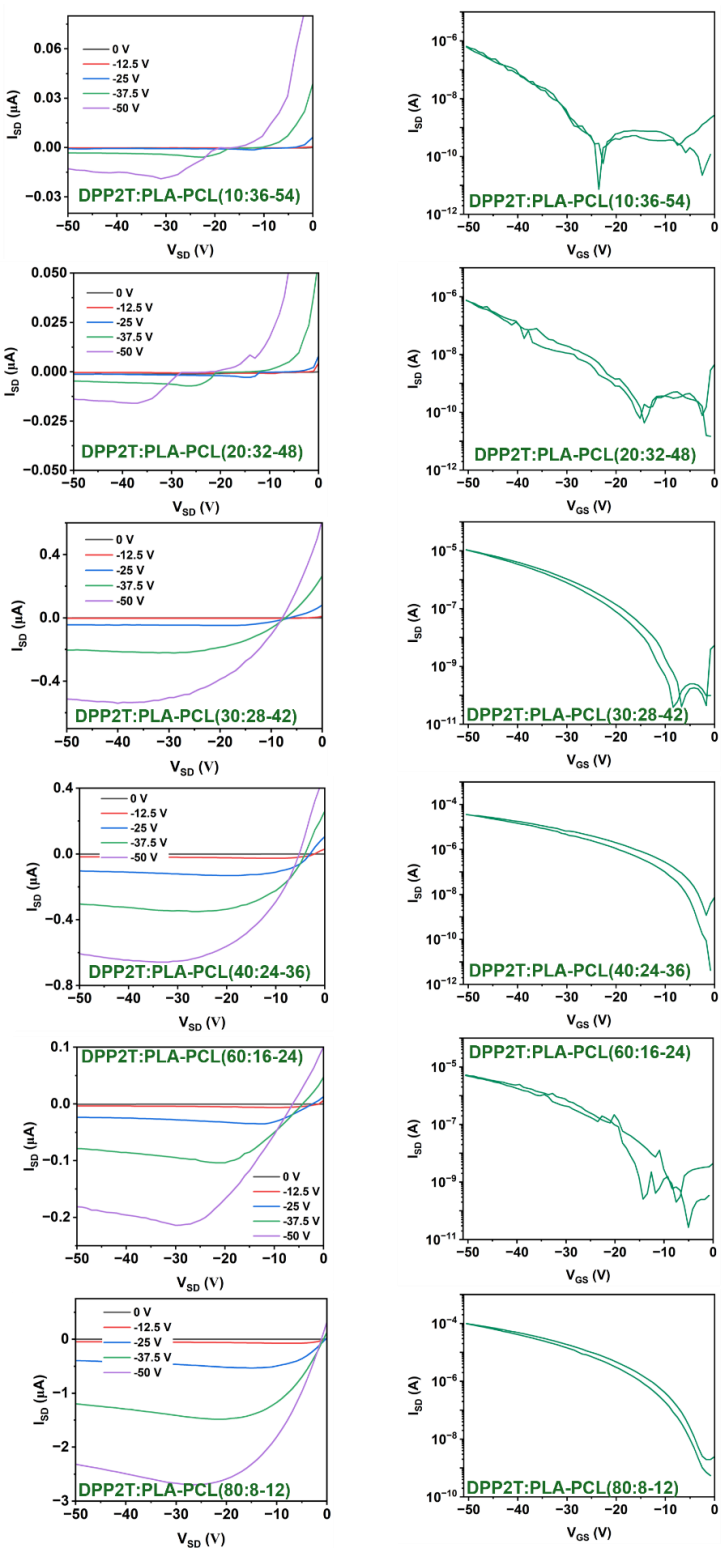


Figure S3.11. Output (left) and transfer (right) characteristics curves of varied DPP2T/PLA-PCL blend with varied DPP2T and PLA-PCL (40-60% according to the matrix ratio) content.

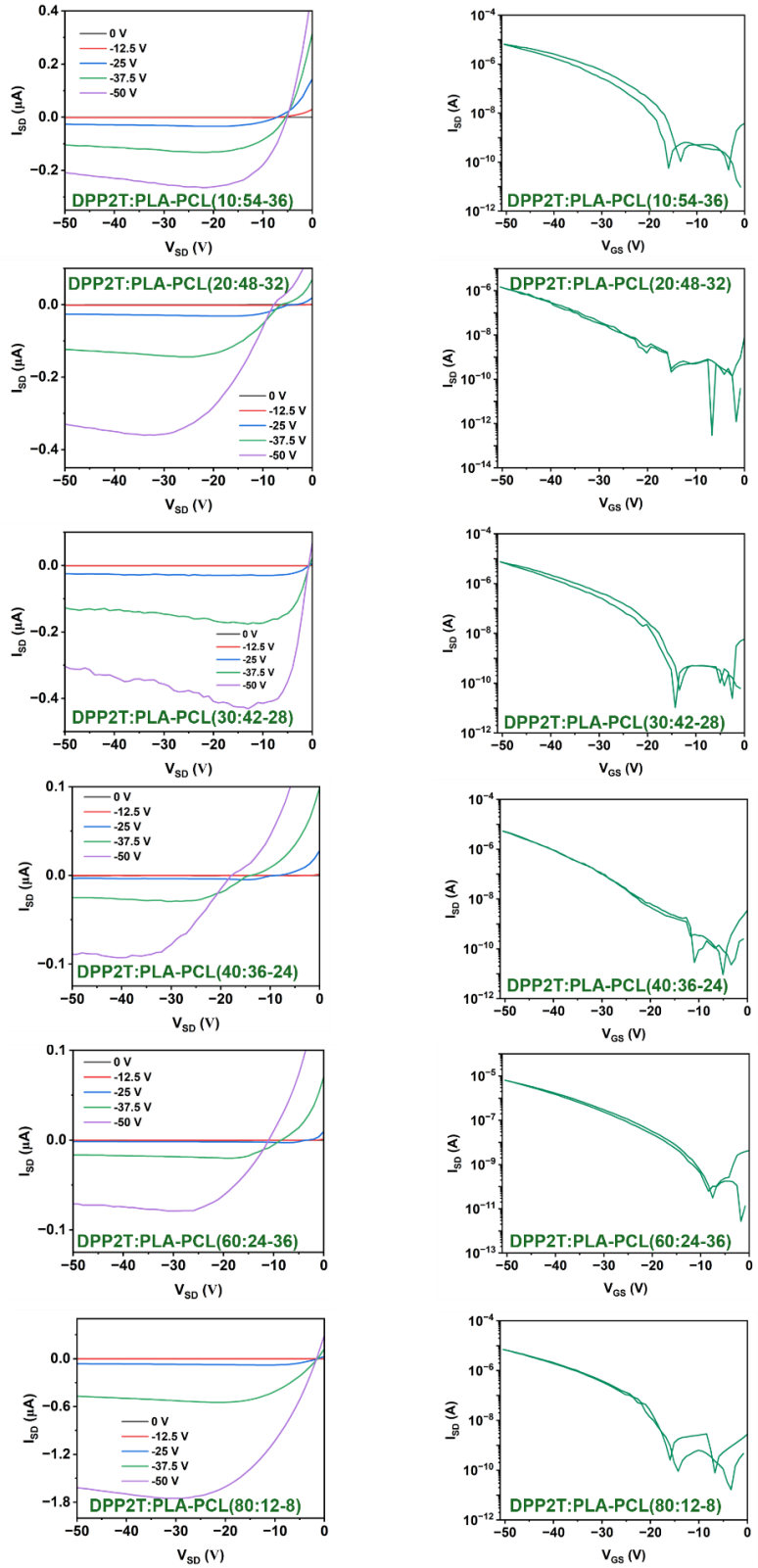


Figure S3.12. Output (left) and transfer (right) characteristics curves of varied DPP2T/PLA-PCL blend with varied DPP2T and PLA-PCL (60-40% according to the matrix ratio) content.

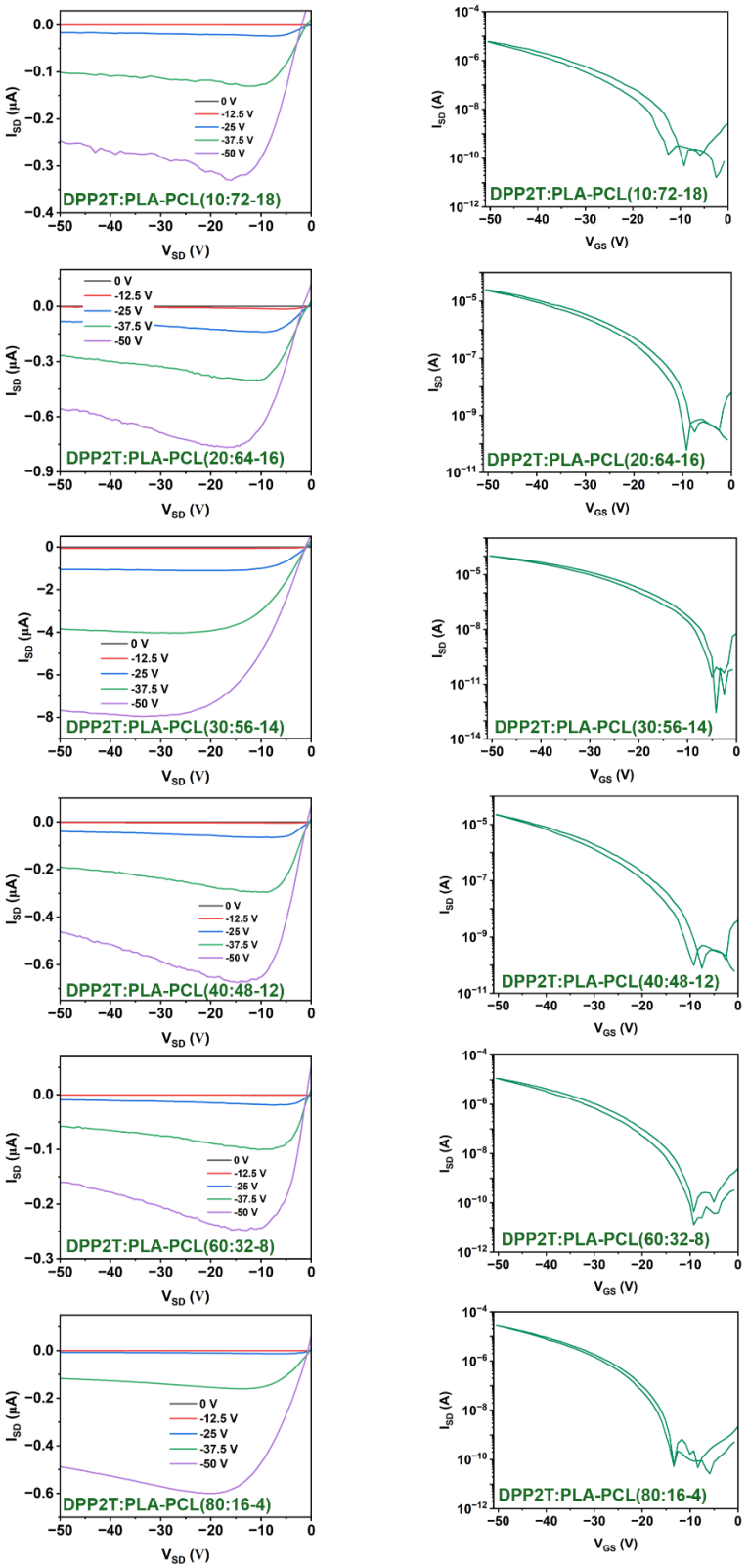


Figure S3.13. Output (left) and transfer (right) characteristics curves of varied DPP2T/PLA-PCL blend with varied DPP2T and PLA-PCL (80-20% according to the matrix ratio) content.

We compared the performance indicators computed from blends prepared by dissolving DPP2T in chlorobenzene, chloroform and dichloromethane. We observed that the DPP2T blends prepared with chlorobenzene exhibited better field effect μ and $I_{on/off}$ as compared to the blends prepared with chloroform and dichloromethane (**Table S3.1 and S3.2**).

Table S3.1. Performance parameters computed from blend films prepared by dissolving DPP2T in chlorobenzene, chloroform, and dichloromethane, and PLA-PCL in chloroform (40-60% according to the matrix ratio)

DPP2T dissolved in Chlorobenzene			
DPP2T:PLA-PCL	**μ*** **(Ave. μ)** **[c]** **$\times 10^{-2}$**	**$I_{on/off}$***	**V_T (V)***
100:0	11 ± 2.8	2×10^3	-27 ± 4.0
80:8-12	16 ± 4.1	5×10^4	-18 ± 0.8
60:16-24	1.6 ± 1.7	2×10^3	-21 ± 1.4
40:24-36	7.0 ± 4.6	6×10^3	-20 ± 1.0
20:32-48	0.3 ± 0.1	1×10^3	-26 ± 2.7
DPP2T dissolved in Chloroform			
100:0	2.0 ± 0.2	7×10^3	-24 ± 0.9
80:8-12	9.0 ± 3.1	1×10^4	-23 ± 1.4
60:16-24	0.2 ± 0.1	1×10^2	-23 ± 3.0
40:24-36	1.0 ± 0.3	3×10^3	-27 ± 1.5
20:32-48	0.2 ± 0.2	4×10^2	-28 ± 4.1

DPP2T dissolved in Dichloromethane			
100:0	0.4 ± 0.5	9×10^2	-33 ± 4.9
80:8-12	1.0 ± 0.4	3×10^3	-24 ± 1.7
60:16-24	0.05 ± 0.04	3×10^2	-22 ± 2.2
40:24-36	0.2 ± 0.02	5×10^2	-27 ± 2.5
20:32-48	0.2 ± 0.1	5×10^2	-25 ± 2.6

μ, V_T and $I_{on/off}$ was calculated using average values

Table S3.2. Performance parameters computed from blend films prepared by dissolving DPP2T in chlorobenzene, chloroform and dichloromethane, and PLA-PCL in chloroform (80-20% according to the matrix ratio)

DPP2T:PLA-PCL	μ^* (Ave. μ) × 10^{-2}	$I_{on/off}{}^*$	V_T (V)*
DPP2T dissolved in Chlorobenzene			
100:0	11 ± 2.8	2×10^3	-27 ± 4.0
80:16-4	6 ± 2.9	4×10^4	-22 ± 0.9
60:32-8	3 ± 1.0	1×10^4	-21 ± 0.3
40:48-12	7 ± 1.6	2×10^4	-21 ± 0.6
20:64-16	7 ± 1.7	1×10^4	-18 ± 0.6
DPP2T dissolved in Chloroform			
100:0	4 ± 0.5	7×10^3	-24 ± 0.9
80:16-4	6 ± 3.3	2×10^4	-19 ± 0.8
60:32-8	2 ± 1.4	7×10^3	-18 ± 0.8
40:48-12	0.8 ± 0.5	2×10^3	-17 ± 0.6
20:64-16	0.9 ± 0.2	5×10^3	-18 ± 0.2
DPP2T dissolved in Dichloromethane			
100:0	0.1 ± 1.1	9×10^2	-33 ± 4.9
80:16-4	0.3 ± 0.4	7×10^2	-19 ± 0.9
60:32-8	0.4 ± 0.1	2×10^3	-18 ± 1.3
40:48-12	0.3 ± 0.1	4×10^3	-17 ± 0.5
20:64-16	0.4 ± 0.2	1×10^3	-23 ± 1.6

**μ, V_T and $I_{on/off}$ was calculated using average values*

Table S3.3. Summary of averaged μ values for DPP2T/PLA-PCL blends with varied DPP2T (dissolved in chlorobenzene) and PLA-PCL (dissolved in chloroform)

Samples	**μ ($cm^2V^{-1}s^{-1}$)* x 10^{-2}**					
DPP2T	PLA-PCL (0-100)	PLA-PCL (20-80)	PLA-PCL (40-60)	PLA-PCL (60-40)	PLA-PCL (80-20)	PLA-PCL (100-0)
10	0.05 ± 0.05	0.14 ± 0.10	0.07 ± 0.04	1.13 ± 0.31	0.76 ± 0.40	1.29 ± 0.14
20	0.28 ± 0.11	0.31 ± 0.20	0.29 ± 0.14	1.79 ± 1.01	7.15 ± 1.75	0.20 ± 0.06
30	0.58 ± 0.24	0.40 ± 0.20	1.58 ± 2.20	0.75 ± 0.50	18 ± 5.80	0.45 ± 0.15
40	0.53 ± 0.10	0.68 ± 0.51	7.19 ± 4.62	0.43 ± 0.36	6.84 ± 1.70	0.81 ± 0.30
60	0.91 ± 0.24	0.51 ± 0.98	1.66 ± 1.71	0.10 ± 0.08	3.04 ± 1.01	0.57 ± 0.08
80	1.27 ± 0.75	2.02 ± 1.71	16 ± 4.12	9.52 ± 5.71	6.05 ± 2.92	3.24 ± 0.38
100 (Neat DPP2T)	11 ± 2.80					

*μ values for all blended samples were calculated using an average value of functional OTFT devices.

Table S3.4. Thickness, density, and mass of material used in device.

Material	Thickness (nm)	Density (g/cm^3)	Mass for a 1 cm^2 device (µg)
DPP2T	144 ± 5.8[a]	0.9-1.15[b]	4.1[c]

[a]Averaged thickness of the optimized semiconducting blend film DPP2T:PLA-PCL (30:56-14)

[b]Density of the conjugated polymer is in the range from 0.9-1.15 g/cm^3, estimated from the reference.[62]

[c]The film is a blend of 30 wt% DPP2T and 70 wt% PLA-PCL, therefore, mass is calculated based on this percentage (i.e. 13.77 µg is the total weight for a 1 cm^2 device and 4.1 µg is the 30 percent of 13.77 µg).

Table S3.5. Trap density of the semiconducting blend films

DPP2T:PLA-PCL	Trap density (cm^{-2}.eV^{-1})* x 10^{12}
100:0	9.6 ± 2.1
30:0-70	4.8 ± 0.7
30:14-56	4.1 ± 0.5
30:28-42	3.1 ± 0.7
30:42-28	4.2 ± 1.5
30:56-14	2.8 ± 0.9
30:70-0	3.6 ± 1.3

*Trap density values for all blended samples were calculated using an average value of functional OTFT devices.

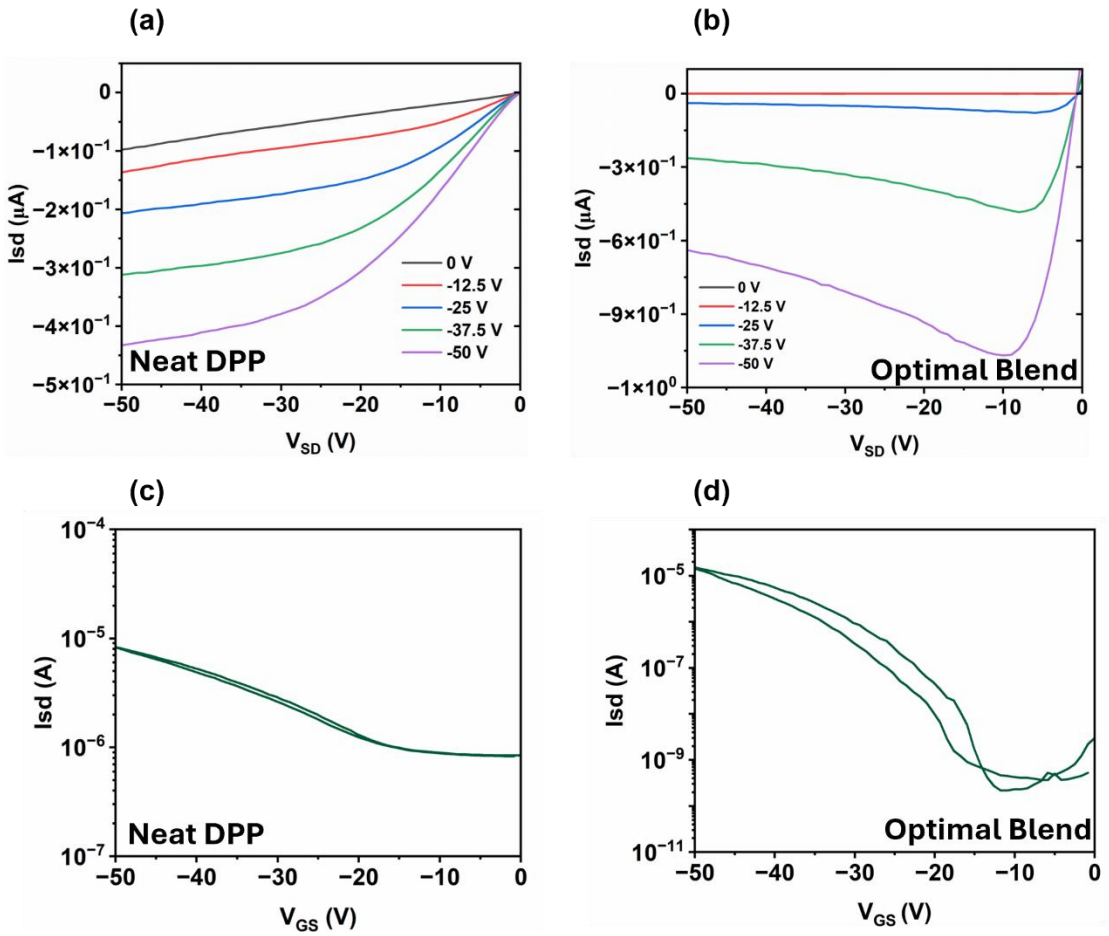


Figure S3.14. a) and b) Output and corresponding c) and d) transfer curves of OTFTs made with neat DPP2T (a, c) and optimal blend, 30:56-14 (b, d) after 7 months of exposure to air.

Table S3.6. Summary of the OTFT properties of devices made with neat DPP2T and optimal blend (30:56-14) after 7 months of sitting in air.

	μ ($cm^2\ V^{-1}s^{-1}$)		
DPP2T:PLA-PCL	**(Avg. μ) × 10^{-2}**	$I_{on/off}$	V_T (V)
100:0	2 ± 0.9	1 × 10^1	-1.2 ± 1.0
30:56-14	10 ± 2.3	1 × 10^4	-20 ± 0.6

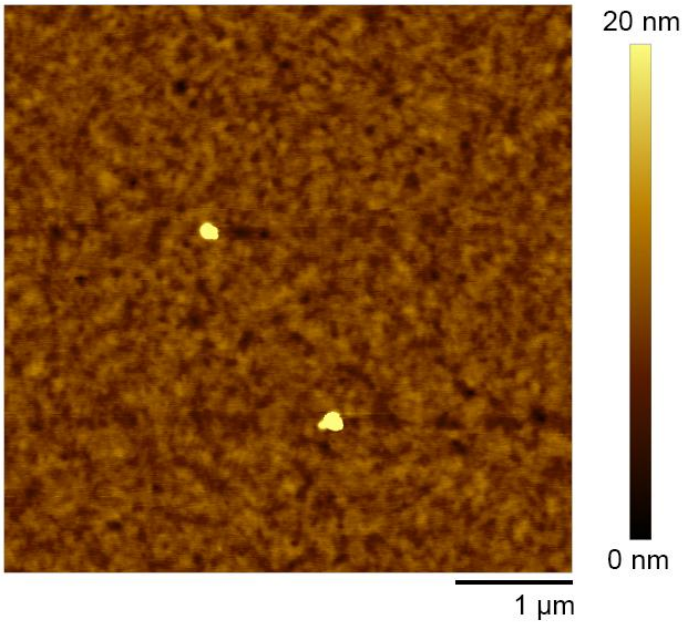


Figure S3.15. AFM image of neat DPP2T film.

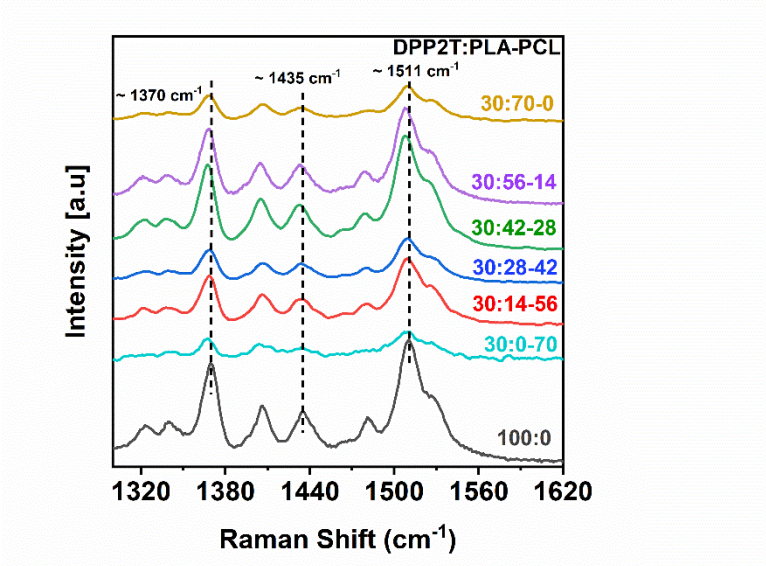


Figure S3.16. Raman spectra of neat DPP2T and DPP2T blends with different PLA-PCL ratios and same DPP2T content.

Table S3.7. Summary of the percentage crystallinity of the semiconducting blends

DPP2T:PLA-PCL	Percentage crystallinity	Thickness (nm)
100:0	29.4	80 ± 11.9
30:0-70	23.7	119 ± 2.16
30:14-56	26.2	85 ± 4.32
30:28-42	26.6	149 ± 6.17
30:42-28	33.6	136 ± 15.1
30:56-14	28.8	144 ± 5.8
30:70-0	26.3	128 ± 17.6

References

(1) Lei, Y.; Deng, P.; Li, J.; Lin, M.; Zhu, F.; Ng, T.-W.; Lee, C.-S.; Ong, B. S. Solution-Processed Donor-Acceptor Polymer Nanowire Network Semiconductors for High-Performance Field-Effect Transistors. *Sci. Rep.* **2016**, *6* (1), 24476.

(2) Guo, X.; Baumgarten, M.; Müllen, K. Designing π-Conjugated Polymers for Organic Electronics. *Prog. Polym. Sci.* **2013**, *38* (12), 1832–1908.

(3) Facchetti, A. π-Conjugated Polymers for Organic Electronics and Photovoltaic Cell Applications. *Chem. Mater.* **2011**, *23* (3), 733–758.

(4) King, B.; Lessard, B.H. Review Of Recent Advances In Sensing Mechanisms In Solid-State Organic Thin-Film Transistor (OTFT) Sensors. *Journal of Materials Chemistry C.* **2024**, 5654-5683.

(5) Liao, C.; Zhang, M.; Yao, M. Y.; Hua, T.; Li, L.; Yan, F. Flexible Organic Electronics in Biology: Materials and Devices. *Adv. Mater.* **2015**, *27* (46), 7493–7527.

(6) Kwon, K. Y.; Lee, J. S.; Ko, G.; Sunwoo, S. H.; Lee, S.; Jo, Y. J.; Choi, C. H.; Hwang, S.; Kim, T. Biosafe, Eco-friendly Levan Polysaccharide toward Transient Electronics. *Small* **2018**, *14* (32), 1801332.

(7) Wu, X.; Zhou, J.; Huang, J. Integration of Biomaterials into Sensors Based on Organic Thin-Film Transistors. *Macromol. Rapid Commun.* **2018**, *39* (15), 1800084.

(8) Hwang, S.; Park, G.; Cheng, H.; Song, J.; Kang, S.; Yin, L.; Kim, J.; Omenetto, F. G.; Huang, Y.; Lee, K. 25th Anniversary Article: Materials for High-performance Biodegradable Semiconductor Devices. *Adv. Mater.* **2014**, *26* (13), 1992–2000.

(9) Bettinger, C. J.; Bao, Z. Organic Thin-film Transistors Fabricated on Resorbable Biomaterial Substrates. *Adv. Mater.* **2010**, *22* (5), 651–655.

(10) Nielsen, C. B.; Turbiez, M.; McCulloch, I. Recent Advances in the Development of Semiconducting DPP-containing Polymers for Transistor Applications. *Adv. Mater.* **2013**, *25* (13), 1859–1880.

(11) Tran, H.; Feig, V. R.; Liu, K.; Wu, H.-C.; Chen, R.; Xu, J.; Deisseroth, K.; Bao, Z. Stretchable and Fully Degradable Semiconductors for Transient Electronics. *ACS Cent. Sci.* **2019**, *5* (11), 1884–1891.

(12) Oh, J. Y.; Rondeau-Gagné, S.; Chiu, Y.-C.; Chortos, A.; Lissel, F.; Wang, G.-J. N.; Schroeder, B. C.; Kurosawa, T.; Lopez, J.; Katsumata, T. Intrinsically Stretchable and Healable Semiconducting Polymer for Organic Transistors. *Nature* **2016**, *539* (7629), 411–415.

(13) Irimia-Vladu, M.; Troshin, P. A.; Reisinger, M.; Shmygleva, L.; Kanbur, Y.; Schwabegger, G.; Bodea, M.; Schwödiauer, R.; Mumyatov, A.; Fergus, J. W. Biocompatible and Biodegradable Materials for Organic Field-effect Transistors. *Adv. Funct. Mater.* **2010**, *20* (23), 4069–4076.

(14) Sugiyama, F.; Kleinschmidt, A. T.; Kayser, L. V; Alkhadra, M. A.; Wan, J. M.-H.; Chiang, A. S.-C.; Rodriquez, D.; Root, S. E.; Savagatrup, S.; Lipomi, D. J. Stretchable and Degradable Semiconducting Block Copolymers. *Macromolecules* **2018**, *51* (15), 5944–5949.

(15) Hsu, N. S. Y.; Lin, A.; Uva, A.; Huang, S. H.; Tran, H. Direct Arylation Polymerization of Degradable Imine-Based Conjugated Polymers. *Macromolecules* **2023**, *56* (21), 8947–8955.

(16) Uva, A.; Michailovich, S.; Hsu, N. S. Y.; Tran, H. Degradable π-Conjugated Polymers. *J. Am. Chem. Soc.* **2024**, *146* (18), 12271–12287.

(17) Song, E.; Kang, B.; Choi, H. H.; Sin, D. H.; Lee, H.; Lee, W. H.; Cho, K. Stretchable and Transparent Organic Semiconducting Thin Film with Conjugated Polymer Nanowires Embedded in an Elastomeric Matrix. *Adv. Electron. Mater.* **2016**, *2* (1), 1500250.

(18) Qiu, L.; Lee, W. H.; Wang, X.; Kim, J. S.; Lim, J. A.; Kwak, D.; Lee, S.; Cho, K. Organic Thin-film Transistors Based on Polythiophene Nanowires Embedded in Insulating Polymer. *Adv. Mater.* **2009**, *21* (13), 1349–1353.

(19) Goffri, S.; Müller, C.; Stingelin-Stutzmann, N.; Breiby, D. W.; Radano, C. P.; Andreasen, J. W.; Thompson, R.; Janssen, R. A. J.; Nielsen, M. M.; Smith, P. Multicomponent Semiconducting Polymer Systems with Low Crystallization-Induced Percolation Threshold. *Nat. Mater.* **2006**, *5* (12), 950–956.

(20) Brixi, S.; Dindault, C.; King, B.; Lamontagne, H. R.; Shuhendler, A. J.; Swaraj, S.; Lessard, B. H. Poly (2-vinylpyridine) as an Additive for Enhancing N-Type Organic Thin-Film Transistor Stability. *Adv. Electron. Mater.* **2024**, *10* (2), 2300660.

(21) Yu, K.; Park, B.; Kim, G.; Kim, C.-H.; Park, S.; Kim, J.; Jung, S.; Jeong, S.; Kwon, S.; Kang, H. Optically Transparent Semiconducting Polymer Nanonetwork for Flexible and Transparent Electronics. *Proc. Natl. Acad. Sci.* **2016**, *113* (50), 14261–14266.

(22) Park, B.; Kang, H.; Ha, Y. H.; Kim, J.; Lee, J.; Yu, K.; Kwon, S.; Jang, S.; Kim, S.; Jeong, S. Direct Observation of Confinement Effects of Semiconducting Polymers in Polymer Blend Electronic Systems. *Adv. Sci.* **2021**, *8* (14), 2100332.

(23) Guo, S.; Wang, X.; Sun, J.; Tong, Y.; Tang, Q.; Liu, Y. Intrinsically Stretchable N-Type Organic Transistor Based on Elastic Hybrid Network Semiconducting Film. *IEEE Electron Device Lett.* **2023**.

(24) Klauk, H.; Zschieschang, U.; Pflaum, J.; Halik, M. Ultralow-Power Organic

Complementary Circuits. *Nature* **2007**, *445* (7129), 745–748.

(25) Henson, Z. B.; Müllen, K.; Bazan, G. C. Design Strategies for Organic Semiconductors beyond the Molecular Formula. *Nat. Chem.* **2012**, *4* (9), 699–704.

(26) Feig, V. R.; Tran, H.; Bao, Z. Biodegradable Polymeric Materials in Degradable Electronic Devices. *ACS Cent. Sci.* **2018**, *4* (3), 337–348.

(27) Lei, T.; Wang, J.-Y.; Pei, J. Design, Synthesis, and Structure–Property Relationships of Isoindigo-Based Conjugated Polymers. *Acc. Chem. Res.* **2014**, *47* (4), 1117–1126. https://doi.org/10.1021/ar400254j.

(28) Lei, T.; Guan, M.; Liu, J.; Lin, H.-C.; Pfattner, R.; Shaw, L.; McGuire, A. F.; Huang, T.-C.; Shao, L.; Cheng, K.-T. Biocompatible and Totally Disintegrable Semiconducting Polymer for Ultrathin and Ultralightweight Transient Electronics. *Proc. Natl. Acad. Sci.* **2017**, *114* (20), 5107–5112.

(29) Hofmann, T.; Ma-Hock, L.; Strauss, V.; Treumann, S.; Rey Moreno, M.; Neubauer, N.; Wohlleben, W.; Gröters, S.; Wiench, K.; Veith, U. Comparative Short-Term Inhalation Toxicity of Five Organic Diketopyrrolopyrrole Pigments and Two Inorganic Iron-Oxide-Based Pigments. *Inhal. Toxicol.* **2016**, *28* (10), 463–479.

(30) Tousignant, M. N.; Lin, Z. S.; Brusso, J.; Lessard, B. H. Interfacial Ultraviolet Cross-Linking of Green Bilayer Dielectrics. *ACS Appl. Mater. Interfaces* **2023**, *15* (2), 3680–3688.

(31) Tousignant, M. N.; Ronnasi, B.; Tischler, V.; Lessard, B. H. N-Type Single Walled Carbon Nanotube Thin Film Transistors Using Green Tri-Layer Polymer Dielectric. *Adv. Mater. Interfaces* **2023**, *10* (14), 2300079.

(32) Tousignant, M. N.; Rice, N. A.; Peltekoff, A.; Sundaresan, C.; Miao, C.; Hamad, W. Y.; Lessard, B. H. Improving Thin-Film Properties of Poly (Vinyl Alcohol) by the Addition of

Low-Weight Percentages of Cellulose Nanocrystals. *Langmuir* **2020**, *36* (13), 3550–3557.

(33) Li, Y.; Singh, S. P.; Sonar, P. A High Mobility P-type DPP-thieno [3, 2-b] Thiophene Copolymer for Organic Thin-film Transistors. *Adv. Mater.* **2010**, *22* (43), 4862–4866.

(34) Kim, Y. J.; Jang, W.; Ahn, S.; Park, C. E.; Wang, D. H. Dramatically Enhanced Performances and Ideally Controlled Nano-Morphology via Co-Solvent Processing in Low Bandgap Polymer Solar Cells. *Org. Electron.* **2016**, *34*, 42–49. https://doi.org/10.1016/j.orgel.2016.04.010.

(35) Dai, R.; Ding, C.; Li, X.; Fan, N.; Minari, T.; Liu, X.; Sun, Q. Molecular Single Crystals Induce Chain Alignment in a Semiconducting Polymer. *Adv. Compos. Hybrid Mater.* **2023**, *6* (1), 35.

(36) Kang, I. L.; Yun, H.-J.; Chung, D. S.; Kwon, S.-K.; Kim, Y.-H. Record High Hole Mobility in Polymer Semiconductors via Side-Chain Engineering. *J. Am. Chem. Soc.* **2013**, *135* (40), 14896–14899.

(37) Ong, B. S.; Wu, Y.; Liu, P.; Gardner, S. Structurally Ordered Polythiophene Nanoparticles for High-performance Organic Thin-film Transistors. *Adv. Mater.* **2005**, *17* (9), 1141–1144.

(38) Lei, T.; Dou, J.; Pei, J. Influence of Alkyl Chain Branching Positions on the Hole Mobilities of Polymer Thin-film Transistors. *Adv. Mater.* **2012**, *24* (48), 6457–6461.

(39) Lei, T.; Dou, J.-H.; Cao, X.-Y.; Wang, J.-Y.; Pei, J. A BDOPV-Based Donor-Acceptor Polymer for High-Performance n-Type and Oxygen-Doped Ambipolar Field-Effect Transistors. *Adv. Mater* **2013**, *25* (45), 6589–6593.

(40) Qiu, L.; Lim, J. A.; Wang, X.; Lee, W. H.; Hwang, M.; Cho, K. Versatile Use of Vertical-phase-separation-induced Bilayer Structures in Organic Thin-film Transistors. *Adv. Mater.* **2008**, *20* (6), 1141–1145.

(41) Kimura, Y.; Nagase, T.; Kobayashi, T.; Hamaguchi, A.; Ikeda, Y.; Shiro, T.; Takimiya, K.; Naito, H. Soluble Organic Semiconductor Precursor with Specific Phase Separation for High-Performance Printed Organic Transistors. *Adv. Mater.* **2015**, *27* (4), 727–732.

(42) Yuan, Y.; Giri, G.; Ayzner, A. L.; Zoombelt, A. P.; Mannsfeld, S. C. B.; Chen, J.; Nordlund, D.; Toney, M. F.; Huang, J.; Bao, Z. Ultra-High Mobility Transparent Organic Thin Film Transistors Grown by an off-Centre Spin-Coating Method. *Nat. Commun.* **2014**, *5* (1), 3005.

(43) Arias, A. C.; Endicott, F.; Street, R. A. Surface-induced Self-encapsulation of Polymer Thin-film Transistors. *Adv. Mater.* **2006**, *18* (21), 2900–2904.

(44) Lu, G.; Blakesley, J.; Himmelberger, S.; Pingel, P.; Frisch, J.; Lieberwirth, I.; Salzmann, I.; Oehzelt, M.; Di Pietro, R.; Salleo, A. Moderate Doping Leads to High Performance of Semiconductor/Insulator Polymer Blend Transistors. *Nat. Commun.* **2013**, *4* (1), 1588.

(45) Janasz, L.; Borkowski, M.; Blom, P. W. M.; Marszalek, T.; Pisula, W. Organic Semiconductor/Insulator Blends for Elastic Field-Effect Transistors and Sensors. *Adv. Funct. Mater.* **2022**, *32* (7). https://doi.org/10.1002/adfm.202105456.

(46) Chen, K.; Zhou, C.; Yao, L.; Jing, M.; Liu, C.; Shen, C.; Wang, Y. Phase Morphology, Rheological Behavior and Mechanical Properties of Supertough Biobased Poly (Lactic Acid) Reactive Ternary Blends. *Int. J. Biol. Macromol.* **2023**, *253*, 127079.

(47) Wu, D.; Lin, D.; Zhang, J.; Zhou, W.; Zhang, M.; Zhang, Y.; Wang, D.; Lin, B. Selective Localization of Nanofillers: Effect on Morphology and Crystallization of PLA/PCL Blends. *Macromol. Chem. Phys.* **2011**, *212* (6), 613–626.

(48) Sun, Y.; Chien, S.-C.; Yip, H.-L.; Chen, K.-S.; Zhang, Y.; Davies, J. A.; Chen, F.-C.; Lin, B.; Jen, A. K.-Y. Improved Thin Film Morphology and Bulk-Heterojunction Solar Cell Performance through Systematic Tuning of the Surface Energy of Conjugated Polymers. *J.*

Mater. Chem. **2012**, *22* (12), 5587–5595.

(49) Lim, S. C.; Kim, S. H.; Lee, J. H.; Kim, M. K.; Kim, D. J.; Zyung, T. Surface-Treatment Effects on Organic Thin-Film Transistors. *Synth. Met.* **2005**, *148* (1), 75–79. https://doi.org/10.1016/j.synthmet.2004.08.034.

(50) Lee, W. H.; Lim, J. A.; Kwak, D.; Cho, J. H.; Lee, H. S.; Choi, H. H.; Cho, K. Semiconductor-Dielectric Blends: A Facile All Solution Route to Flexible All-Organic Transistors. *Adv. Mater.* **2009**, *21* (42), 4243–4248. https://doi.org/10.1002/adma.200900277.

(51) Yu, S. H.; Park, K. H.; Kim, Y.-H.; Chung, D. S.; Kwon, S.-K. Fine Molecular Tuning of Diketopyrrolopyrrole-Based Polymer Semiconductors for Efficient Charge Transport: Effects of Intramolecular Conjugation Structure. *Macromolecules* **2017**, *50* (11), 4227–4234.

(52) Mukhopadhyay, T.; Puttaraju, B.; Roy, P.; Dasgupta, J.; Meyer, A.; Rudnick, A.; Tscheuschner, S.; Kahle, F.; Köhler, A.; Patil, S. Facile Synthesis and Chain-Length Dependence of the Optical and Structural Properties of Diketopyrrolopyrrole-Based Oligomers. *Chem. Eur. J.* **2017**, *23* (55), 13718–13723.

(53) McPherson, T. E. Characterizing the Morphology of Solvent Annealed PCBM/P3HT Bilayers Using GIXRD and Raman Spectroscopy. M.S. Thesis, University of Tennessee, Knoxville, 2014.

(54) Cranston, R. R.; Lanosky, T. D.; Ewenike, R.; Mckillop, S.; King, B.; Lessard, B. H. Polarized Raman Microscopy to Image Microstructure Changes in Silicon Phthalocyanine Thin-Films. *Small Sci.* **2024**, 2300350.

(55) Luo, S.; Li, Y.; Li, N.; Cao, Z.; Zhang, S.; Ocheje, M. U.; Gu, X.; Rondeau-Gagné, S.; Xue,

G.; Wang, S. Real-Time Correlation of Crystallization and Segmental Order in Conjugated Polymers. *Mater. Horizons* **2024**, *11* (1), 196–206.

(56) Wood, S.; Hollis, J. R.; Kim, J.-S. Raman Spectroscopy as an Advanced Structural Nanoprobe for Conjugated Molecular Semiconductors. *J. Phys. D. Appl. Phys.* **2017**, *50* (7), 73001.

(57) Ostafinska, A.; Fortelny, I.; Nevoralova, M.; Hodan, J.; Kredatusova, J.; Slouf, M. Synergistic Effects in Mechanical Properties of PLA/PCL Blends with Optimized Composition, Processing, and Morphology. *RSC Adv.* **2015**, *5* (120), 98971–98982.

(58) Ho, V.; Boudouris, B. W.; McCulloch, B. L.; Shuttle, C. G.; Burkhardt, M.; Chabinyc, M. L.; Segalman, R. A. Poly (3-Alkylthiophene) Diblock Copolymers with Ordered Microstructures and Continuous Semiconducting Pathways. *J. Am. Chem. Soc.* **2011**, *133* (24), 9270–9273.

(59) Chen, Y.; Lu, T.; Li, L.; Zhang, H.; Wang, H.; Ke, F. Fully Biodegradable PLA Composite with Improved Mechanical Properties via 3D Printing. *Mater. Lett.* **2023**, *331*, 133543.

(60) Manion, J.; Lessard, B. H. High-Throughput Characterization Is Key to Report Reliable Organic Thin-Film Transistor Performance. *Nat. Rev. Mater.* **2024**, *9* (6), 377–378. https://doi.org/10.1038/s41578-024-00689-8.

(61) Dallaire, N.; Boileau, N. T.; Myers, I.; Brixi, S.; Ourabi, M.; Raluchukwu, E.; Cranston, R.; Lamontagne, H. R.; King, B.; Ronnasi, B. High Throughput Characterization of Organic Thin Film Transistors. *Adv. Mater.* **2024**, 2406105.

(62) Machui, F.; Rathgeber, S.; Li, N.; Ameri, T.; Brabec, C. J. Influence of a Ternary Donor Material on the Morphology of a P3HT: PCBM Blend for Organic Photovoltaic Devices. *J. Mater. Chem.* **2012**, *22* (31), 15570–15577.

Chapter 4: Degradation by Design: Sequentially Degradable Organic Transistors for Sustainable Electronics

This chapter was published in the journal "Soft Science": M. Ali, A. Nyayachavadi, S.G. Pascual, J. Park, C.H. Kim, A. Hemmerle, J.G. Manion, B.H. Lessard, Degradation by design: sequentially degradable organic transistors for sustainable electronics, Soft Sci. 2026, 6, 42. The section order of this chapter follows the layout of the published article.

Context

For this work, I studied how a fully degradable OTFT could be engineered so that each of its components degrades under a distinct, targeted trigger rather than all breaking down together in a single environment. As outlined in previous chapters, our group had already shown that pairing a PVA/PCL bilayer dielectric with a PLA substrate and gold electrodes could produce cytocompatible, disintegrable, low-voltage OTFTs, but the gold electrodes did not degrade and needed to be physically recovered afterward. Here, I paired this biodegradable dielectric/substrate platform with a new imine-containing p-type semiconducting polymer, poly(diketopyrrolopyrrole-thiophene-imine-thiophene) [P(DPP-TIT)], designed with symmetrical alkyl side chains to promote good charge transport while keeping the molecular weight low enough to allow rapid degradation. We hypothesized that combining this imine-based semiconductor with the PVA/UV-PCL dielectric and PLA substrate would allow the device to operate at a much lower V_T than an equivalent OTFT built on a conventional SiO_2 dielectric, while still enabling sequential, component-specific disassembly: the semiconductor and dielectric dissolving first under acidic conditions, followed by the substrate breaking down separately in basic conditions, leaving only recoverable gold particles behind. We were interested in benchmarking the electrical performance

of this fully degradable device against a non-degradable SiO_2-based control, understanding how the biodegradable dielectric affected the semiconductor's morphology and molecular packing, and demonstrating that the device could be disassembled step by step to enable separation and potential recycling of its individual layers.

Contribution

I conducted the experimental work, including device fabrication and degradation experiments, performed the data analysis, and wrote the initial draft of the manuscript. Dr. Nyayachavadi synthesized the semiconducting polymer, conducted the UV-Vis measurements, and assisted with data analysis and manuscript editing. Pascual interpreted the Grazing-Incidence Wide-Angle X-ray Scattering (GIWAXS) results. Park performed the numerical simulation analysis, which Dr. Kim then analyzed and used to help edit the manuscript. Dr. Hemmerle performed the GIWAXS measurements and collected the corresponding data at the SIRIUS beamline of Synchrotron SOLEIL. Dr. Manion helped design and create the schematic figures and edited the manuscript. Dr. Lessard acquired funding, supervised and directed the study, and assisted with writing and editing the manuscript.

4.1 Abstract

The growing accumulation of e-waste and demand for environmentally sustainable technologies have accelerated interest in transient degradable electronics, which physically disintegrate or biodegrade after their functional lifetime. Such devices offer promising pathways towards reducing ecological impact while enabling applications in biomedical implants, environmental sensors, and temporary wearable systems. Biodegradable OTFTs play a pivotal role as fundamental building blocks for fully transient electronic circuits, combining mechanical

flexibility, solution processability, and controlled disintegration. In this study, we report the development of a fully degradable OTFT fabricated using P(DPP-TIT) as the biodegradable semiconducting layer, integrated with a bilayer dielectric composed of PVA and PCL, and a PLA substrate. This configuration yields a significant reduction in V_T from −16.1 V to −2 V compared to devices fabricated on OTS/SiO_2, while maintaining comparable charge carrier μ. The OTFT can be selectively degraded through sequential steps, where the semiconductor and dielectric dissolve under acidic conditions (1 M hydrochloric acid (HCl)), followed by degradation of the substrate in basic buffer solution. This controlled disassembly enables separation and potential recycling of individual components, providing a straightforward strategy for environmentally responsible end-of-life management of transient electronics. Overall, this work represents an important step toward realizing low-voltage, fully degradable, and recyclable electronic systems for sustainable applications.

4.2 Introduction

The rapid growth of electronic devices across biomedical, environmental, and consumer applications has intensified concerns over electronic waste and the long-term persistence of electronic materials. Transient electronics address this challenge by incorporating materials that undergo controlled degradation after use, thereby reducing waste accumulation and environmental impact.[1–3] These biodegradable electronics have several advantages, such as (i) lowering the amount of electronic waste (e-waste) that accumulates, (ii) circumventing invasive surgeries to remove implanted devices, and (iii) enabling environmental transience, which allows sensors that are deployed remotely to function without retrieval.[4–7] OTFTs are electronic building blocks for circuits with applications in biological and chemical sensors,[8] health monitoring systems,[9] stretchable electronics,[10] and electronic skin.[11] While advances in materials design have greatly

improved OTFT performance, the environmental and biological safety of these materials remain underexplored.[12,13]

Advancing transient OTFT requires deliberate design and scalable fabrication of each component and layer to ensure both performance and sustainability.[14–17] *Lei et al.*[18] demonstrated the fabrication of a biocompatible and fully disintegrable OTFT, with respectable charge carrier mobility, using a semiconducting polymer with iron electrodes and a cellulose substrate. They reported complete disintegration of their OTFTs in acidic conditions after 30 days in-vitro. However, when all components degrade simultaneously in a single environment, it becomes difficult to separate, isolate, or recycle functional materials. Thus, advancing fully transient electronics requires OTFTs in which each component responds to distinct degradation triggers, enabling controlled disassembly and targeted recovery of valuable resources like gold/precious metals.

The substrate, which accounts for 99.89% of the overall device mass,[19] must be a biodegradable plastic. Biobased materials such as PLA, PHAs, starch blends, and cellulose-derived polymers are promising substrate options, contingent upon processing temperatures not exceeding ~150 °C.[20] However, biodegradable dielectrics exhibiting appropriate physical and electrical properties remain limited. PVA (**Figure 4.1**) is a bioresorbable dielectric that rapidly dissolves in environmentally benign solvents such as water and undergoes natural degradation when exposed to suitable bacteria.[21] PVA has been utilized as a dielectric in sensors and OTFTs, either in its pure polymer form or in combination with other materials.[22–24] Despite its benefits, PVA presents challenges: printing frequently necessitates optimization, such as the incorporation of viscosity enhancers, and its hydrophilic characteristics render the resultant films susceptible to moisture, undermining device stability and reliability.[25,26] Previously, our group demonstrated that

combining PVA with an interfacial, thermally crosslinked TPCL yields a high-performance, hydrophobic, and degradable high-k/low-k bilayer dielectric.[27,28] This architecture couples the high dielectric constant and electrical performance of PVA with the moisture resistance of PCL, while also improving surface compatibility for semiconductor deposition.[29,30] To enhance shelf stability and enable scalable processing, we further synthesized benzodioxinone-terminated PCL, which can be UV-coupled to the PVA surface (**Figure 4.1**).[24,26] PLA, PVA, and PCL are inexpensive, widely available, and have a long history of use in biomedical devices within clinical practice.[19]

A diverse array of processing and synthetic strategies have been developed and optimized towards designing transient organic semiconductors, primarily focused on integrating and balancing electronic functionality with environmental instability.[31] These approaches include encapsulation of semiconducting fillers within biodegradable polymer matrices, the synthesis of block copolymers featuring discrete semiconducting and degradable segments, the utilization of naturally occurring pigments susceptible to enzymatic breakdown, and the covalent tethering of conjugated motifs to degradable scaffolds via chemically cleavable linkages.[32–34] Among these strategies, the integration of acid-labile imine motifs directly within the backbone of organic conjugated polymers is a promising approach for designing materials possessing good electronic performance while also forgoing the requirement of complicated degradation triggers.[18,35] Compared to other strategies which rely on either disrupting the conjugated backbone or reducing the amount of semiconducting material within the device's active layer, imine-motifs possess sp^2-hybridization character, allowing for the double-bond to contribute and maintain the orbital delocalization of the conjugated polymer backbone, a parameter critical for obtaining good charge carrier mobility in OTFTs.[36–38] Furthermore, compared to other synthetic approaches for designing

transient organic semiconductors, imine-based conjugated polymers do not require complicated synthetic protocols or specialized processing procedures, and have shown potential promise for greener synthetic pathways in developing organic semiconductors.[39,40] When paired with an established high charge carrier performance chemical structure, particularly DPP, it has been demonstrated that imine-based conjugated polymers can be used to fabricate high performance transient OTFTs with measurable electronic properties comparable to conventionally used designs.[37] In addition to possessing good charge carrier mobility in OTFTs, DPP-based polymers have well-understood aqueous and photo-degradation mechanisms, further enforcing their role as promising chemical motifs for designing transient devices that are also environmentally benign.[41,42] Inspired by previous reports, DPP was copolymerized with a thiophene-imine-thiophene donor monomer to generate P(DPP-TIT), a conjugated polymer established to have good hole charge carrier mobility in OTFTs.[36,43]

To further synergize good electronic performance with degradation capabilities, we report a novel variant of P(DPP-TIT), as per **Figure 4.1**, designed with alkyl side chains where each branching arm has symmetrical carbon lengths, a structural feature known to enhance charge transport in thin films while simultaneously limiting excessive molecular weight growth during polymerization, allowing for relatively narrow dispersity in polycondensation-type reactions.[44,45] The combination of narrow dispersity and lower molecular weight of the organic semiconductor has implications in accelerating degradation time, a highly sought-after trait in transient electronic technologies.[46] By integrating the P(DPP-TIT) conjugated polymer with degradable polymeric substrates and dielectric layers, it is possible to design fully transient OTFTs that exhibit strong electrical performance while producing benign by-products during degradation. The combination of materials with distinct degradation triggers enables controlled, multi-step disassembly that

allows selective breakdown, separation, and potential recycling of individual layers. Finally, incorporating biocompatible, non-toxic electrodes alongside these materials completes the foundation for fully biodegradable and biocompatible electronic devices. We have previously fabricated cytocompatible and disintegrable OTFTs using gold electrodes; however, the gold electrodes did not degrade and therefore required recovery.[24] Gold combines high electrical conductivity and excellent biocompatibility in both in vitro and in vivo environments, and has a well-established role in various medical technologies.[47–49] Furthermore, as an inert biomaterial, gold has proven effective in reducing biofouling in biological systems,[50] particularly in implants such as cardiovascular devices and BioMEMS.[51]

This study presents a fully degradable and biocompatible *p*-type OTFT with high mobility and low threshold voltage, based on a P(DPP-TIT) conjugated polymer integrated with a biodegradable PLA substrate and a bilayer PVA/UV-PCL dielectric. Low-temperature surface engineering strategies, including the deposition of biodegradable hydrophobic interlayers, were employed to improve film quality and device reproducibility. Electrical performance and stability were benchmarked against conventional OTFT architectures, confirming competitive operation while highlighting the advantages of sustainable materials. Distinct from previous reports, each device component in this system degrades under a specific pH trigger, enabling sequential disassembly and selective recovery of individual layers (**Figure 4.1b**). The imine-containing P(DPP-TIT) semiconductor and the PVA/UV-PCL dielectric dissolve under acidic conditions, whereas the PLA substrate degrades in basic environments, allowing controlled separation and recycling. This dual-trigger design establishes a new paradigm for transient optoelectronics,

demonstrating how performance and sustainability can be co-engineered through programmable end-of-life disassembly.

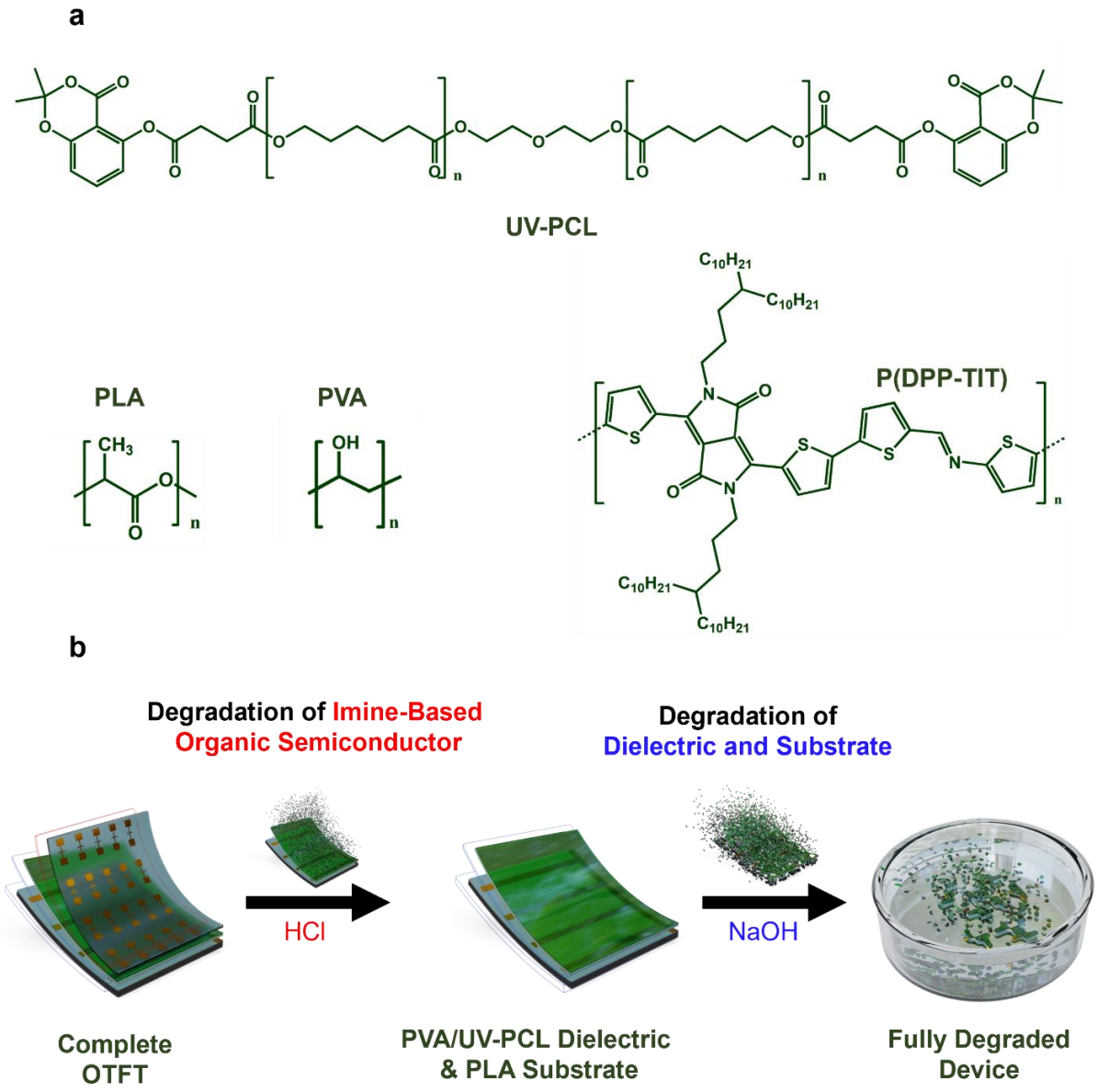


Figure 4.1. a) Chemical structures of biodegradable polymers: polylactic acid (PLA), polyvinyl alcohol (PVA), benzodioxinone-terminated poly caprolactone (UV-PCL), and poly diketopyrrolopyrrole-thiophene-imine-thiophene P(DPP-TIT). b) Schematic illustration of the sequential degradation of an OTFT device. All elements in this figure were developed using ChemDraw and Blender.

4.3 Experimentation

4.3.1 Materials

All reagents were acquired from Sigma-Aldrich and utilised without additional purification unless specified differently. OTS (97%) was dissolved in anhydrous toluene (99.8%) inside a glovebox to prepare a 1% v/v solution. Polycaprolactone (PCL) diol (Mw = 2000 Da), toluene-2,4-diisocyanate (95%), PLA (230 kg mol^{-1}), and PVA (Mw = 31,000–50,000 Da; 98–99% hydrolyzed) were procured from Sigma-Aldrich. Chromium-coated tungsten rods and high-purity gold (Au, 99.99%) were obtained from Angstrom Engineering. Quartz-coated glass substrates (15 × 20 mm^2) were acquired from Ossila Limited, whereas Si wafers featuring a 230 nm SiO_2 layer and shadow masks were provided by WaferPro and Ossila Limited, respectively. Deuterated chloroform (99.8% purity) and benzene (98% purity) were obtained from Cambridge Isotope Laboratories Inc. The synthesis of P(DPP-TIT) was conducted according to established protocols, and 2,2-dimethyl benzodioxinone-terminated PCL (UV-PCL) was synthesized using documented methods.[27]

4.3.2 Gel permeation chromatography (GPC)

Number average molecular weight (Mn), weight average molecular weight (Mw), and polydispersity index (PDI) of P(DPP-TIT) were evaluated by high temperature size exclusion chromatography (SEC) **(Figure S4.1 and Table S4.1, SI)** using 1,2,4-trichlorobenzene and performed on an EcoSEC HLC-8321GPC/HT (Tosoh Bioscience, Japan) equipped with a single TSKgel GPC column (GMHHR-H; 300 mm × 7.8 mm) calibrated with monodisperse polystyrene standards. The samples were prepared using 1 mg/mL of sample in trichlorobenzene (TCB), which were allowed to stir at 80 ºC for 12 h prior to injection. The analysis of the samples was performed

at 180 ºC with a flow rate of 1.0 mL/min with injection quantities of 300 µL. The data was collected and integrated using EcoSEC 8321GPC HT software suite.

4.3.3 Preparation of the substrate and dielectric

The Substrate (PLA) and dielectric (PVA/UV-PCL) solutions were prepared following the protocol reported in our previous study.[24] Briefly, the materials were dissolved in the appropriate solvent systems under continuous stirring until complete homogenization was achieved. The processing conditions, including concentration, temperature, and mixing duration, were maintained consistent with the previously optimized procedure. Detailed processing parameters and preparation steps can be found in our earlier publication.[24]

4.3.4 Fabrication of OTFTs

Glass substrates (15 × 20 mm^2) coated with quartz were used as temporary supports for the fabrication of OTFTs. Substrate cleaning and preparation were carried out according to the protocol described in our previous study.[52] A spin coater (Laurell WS-650-23, United States of America (USA)) was used to spin-coat the PLA solution in chloroform (70 mg/ml) filtered through 0.22-micron PTFE filters, onto the cleaned substrates for 90 seconds at 1200 rpm. The substrates were then vacuum annealed for 15 minutes at 70 °C. PLA films with a thickness of roughly 2 µm were produced by this method. The gate electrodes were deposited using a thermal evaporator (Angstrom Evovac, Canada), consisting of a 2 nm chromium (Cr) adhesion layer (0.5 Å s^{-1}) and a 50 nm gold (Au) layer (0.5 Å s^{-1}) applied to the PLA film through a shadow mask. After that, the PLA substrates coated with Cr/Au were air-plasma-treated using PDC-32G plasma cleaner (Harrick Plasma, USA) for 15 minutes, followed by rinsing with isopropanol and water, which improved surface wettability. Next, the biodegradable bilayer dielectric layers were deposited following our previously reported procedure.[24] After crosslinking the degradable semiconducting

layer was deposited by spin-coating a 3 mg/mL solution of P(DPP-TIT) dissolved in chlorobenzene at 2500 rpm for 60 seconds, followed by annealing at 50 °C for an hour in a vacuum oven. The average thickness of the semiconductor layer was measured around ~154 nm. Lastly, the devices were moved to a nitrogen glovebox linked with a thermal evaporator built in. A 50 nm Au layer (0.5 Å s^{-1}) was deposited via PVD using a shadow mask to obtain source–drain electrodes. This resulted in channel dimensions of L = 30 μm and W = 1000 μm. Si wafers were used as substrate and SiO_2 as a nondegradable dielectric in the fabrication of the control OTFT for comparison. Following the same four-step cleaning procedure, the wafers were exposed to air plasma for fifteen minutes. Wafers were immersed in a 1% v/v OTS solution in toluene at 70 °C for one hour. They were then rinsed with toluene and dried in a vacuum oven at 70 °C. A layer of degradable semiconductor was deposited by spin-coating following surface preparation, and then Au source/drain electrode deposition was carried as previously described.

4.3.5 Device characterization

OTFT were characterized using a Keithley 2614B source meter coupled to a specially designed auto-tester.[53] The complete device characterization procedure can be found in the supporting information.

4.3.6 Thin film characterization

Grazing-incidence wide-angle X-ray scattering (GIWAXS)

GIWAXS experiments were performed at the SOLEIL Synchrotron facility in Saint-Aubin, France, using the SIRIUS beamline.[54] The X-ray energy was set to 10 keV (λ = 1.24 Å) using a Si(111) double-crystal monochromator. The beam had a size of 500 × 120 μm^2 (H × V), and a beam stop was employed to block the direct and reflected beams. GIWAXS measurements were

taken directly from the polymer samples deposited on silicon substrates at an angle of incidence set according to the sample of 0.1°. GIWAXS patterns were collected with a DECTRIS PILATUS3 1M (172×172 μm pixel size), which was placed 312 mm from the sample center. The GIWAXS data were then calibrated against a silver behenate and P3HT standard and analyzed using the GIXSGUI software package.[55]

Atomic force microscopy (AFM)

AFM images were taken using an AFM (Bruker Dimension FastScan, USA) with ScanAsyst-Air tips in Peak Force Tapping Mode. Imaging processing was performed with NanoScope Analysis v.3.0. The samples per line used were 512.

Raman spectroscopy

A confocal Raman microscope (Renishaw *inVia InSpec*, United Kingdom (UK)) was used to record non-polarized Raman spectra, in conjunction with a *Leica Microsystems DM2700* bright-field microscope, Germany. Spectra and maps for P(DPP-TIT) films on SiO_2 and bilayer dielectrics were collected in the 500–2000 cm^{-1} range using a 532 nm laser (500 mW) and a 2400 l mm^{-1} grating. The laser beam was focused onto the sample through a 50 L with a 0.5 aperture integrated into the DM2700 optical system. This setup provided a theoretical depth of focus of approximately 3.0 μm, a spatial resolution of about 640 nm, and a spectral resolution of 0.3 cm^{-1} (FWHM). Calibration was performed before each measurement using the silicon reference peak at 520 cm^{-1}, maintained within ± 0.5 cm^{-1} accuracy. Raman spectra were collected without polarization at 10% laser power (50 mW) and a 10 s exposure time. Raman mapping (19 × 19 μm^2) was performed using 361 individual spectra, acquired with a 1.0 μm step size, 5% laser power (25 mW), and a 10 s exposure. All data were processed to remove cosmic ray artifacts.

UV-visible spectroscopy

A Cary 6000i UV-Vis-NIR spectrophotometer (Agilent Technologies, Malaysia) was used to collect spectra. Absorbance measurements were collected for solid-state thin films deposited onto a glass substrate via drop casting, followed by annealing at 50 ºC for an hour, within the range of 250-1000 nm.

Profilometer

A Dektak XT Profilometer (Bruker Corporation, USA) was used to measure the thickness of the PLA substrates, bilayer dielectrics, and P(DPP-TIT) films.

4.4 Results And Discussion

Fully transient OTFTs were fabricated using biocompatible and biodegradable polymers chosen for their electrical performance, processability, and distinct degradation behavior. The devices feature a BGTC architecture where **Figure 4.1** shows the chemical structures of the PLA substrate, PVA/UV-PCL bilayer dielectric, and P(DPP-TIT) semiconductor, along with a schematic of the stepwise degradation. A uniform biodegradable PLA film was obtained by spin coating PLA onto a quartz-coated glass substrate which was baked to eliminate residual solvent, following established literature.[56,57] The resulting PLA substrate was approximately 2 μm thick and was subsequently coated with patterned chromium and gold (Cr/Au) electrodes. The chromium interlayer facilitated strong adhesion between the gold film and the PLA surface and functioned as the bottom gate electrode, ensuring stable and reproducible electrical characterization.[53] Since the gold-patterned PLA surface exhibited hydrophobic characteristics,[24] air plasma treatment for 15 minutes was employed to enhance its surface hydrophilicity, thereby facilitating uniform coating of the subsequent dielectric layer. The PVA dielectric layer was deposited by spin-coating on the

gold/PLA substrate and was annealed at low temperatures (50°C for ~18 hours). We found that exposure of the PLA substrate to temperatures >50°C results in dimensional shrinkage, leading to surface buckling and increased roughness, conditions unfavorable for OTFT fabrication.[24] Hygroscopic polymer dielectrics, such as PVA, can demonstrate a capacitance density enhancement of up to x50 at 10 Hz upon moisture exposure.[58] This phenomenon occurs as water functions as a plasticizer, facilitating the alignment of hydroxyl groups in an electric field and thereby augmenting the capacitance of PVA films.[59,60] However, for flexible electronic circuits, it is essential to preserve constant dielectric characteristics and avoid water uptake. A thin PCL layer (about 1–2 nm) applied to the PVA layer provides efficient moisture barrier properties, hence leading to more reliable and predictable electronic performance.[24,60,61] Therefore, following the PVA annealing, we deposited a hydrophobic interlayer (UV-PCL) to improve film quality and device reproducibility. The optimal UV-crosslinking conditions were previously determined through solvent-resistance testing using toluene and by measuring the water contact angle before and after rinsing in our previous studies.[24,27] The interfacial cross-linking between PCL and PVA not only stabilizes the dielectric bilayer by anchoring the PCL film to the underlying PVA matrix[52,62] but also suppresses polymer aggregation and reduces the density of surface hydroxyl groups that can act as charge-trapping sites during OTFT operation.[63] The remaining hydroxyl functionalities within the bulk of the PVA contribute to a relatively high dielectric constant (k), while the cross-linked top layer enables orthogonal solution processing for subsequent semiconductor deposition.[64,65] The dielectric properties of the resulting bilayer dielectric (PVA/UV-PCL) were assessed by impedance spectroscopy, with the findings presented in **Table 4.1**. The reported dielectric constant values aligned with the anticipated range for PVA.[22,24,58,66]

Table 4.1. Dielectric properties of bilayer dielectric (PVA/UV-PCL) at 10 Hz

Dielectric	Effective dielectric constant (*k*)	Capacitance density (nF/cm²)
PVA/UV-PCL	6.6 ± 3.2	19.7 ± 9.7

P(DPP-TIT) was deposited on the UV-PCL layer by the spin-coating followed by vacuum annealing for an hour at 50 °C. For performance benchmarking, P(DPP-TIT)-based OTFTs were also fabricated using OTS-treated SiO_2 as the gate dielectric, employing an identical device architecture to ensure direct comparison with the degradable OTFTs.[22,58,60,66–68] Finally, gold contacts were deposited on the semiconducting layer as the source/drain electrodes. **Figure 4.2a-d** display the characteristic output and transfer curves of both OTFTs. Performance parameters, including field-effect hole mobility μ_h, V_T, and $I_{on/off}$ were extracted to quantify electrical performance (**Table 4.2**). The V_T of P(DPP-TIT) OTFTs reduced markedly from -16.1 ± 0.9 V on OTS-treated SiO_2 gate dielectrics to -2 ± 0.4 V with the application of a PVA/UV-PCL bilayer dielectric. The decrease in V_T indicates less polarity at the semiconductor/dielectric interface, hence mitigating charge trapping.[27,69–71] This can be attributed to the enhanced dielectric constant of the PVA/UV-PCL bilayer (~ 6.6) in comparison to SiO_2 (3.9) at frequencies under 1 kHz[72] as well as the elimination of hydroxy group-based charge traps due to the interfacial crosslinking with UV-PCL.[24] These values represent a significant improvement compared to previous studies[19] in which PVA was solely employed as a dielectric, yielding V_T values of around −15.4 V for biocompatible and bioresorbable OTFTs. The highest μ_h of the functional OTFT was statistically similar, measuring 0.17 $cm^2 V^{-1} s^{-1}$ for OTFT made with OTS-treated SiO_2 dielectric and 0.16 $cm^2 V^{-1} s^{-1}$ for OTFT fabricated with PVA/UV-PCL dielectric. The $I_{on/off}$ for PVA/UV-PCL based devices is low and typical for PVA-based dielectrics;[73] resulting from the low V_{GS} and V_{SD} needed to operate the device. For example, when the OTFT fabricated with PVA/UV-PCL bilayer

dielectric was tested at V_{GS} and V_{SD} = -5 V, we obtained approximately 0.85 μA, but the OTFT made using OTS/SiO_2 dielectric remained inactive under the same conditions, requiring approximately -10 V to obtain the same amount of current. While mild hysteresis is observed in the PVA/UV-PCL OTFTs due to the dielectric environment and interfacial characteristics, these results demonstrate an effective strategy for developing fully biodegradable, high-performing devices. The on-current value was extracted from the output characteristics at $V_{GS} = -5\text{V}$ and $V_{DS} = -5\text{V}$. A lower current level (~0.2 μA) is observed in the transfer characteristics measured under the same bias conditions, which can be attributed to transient charge trapping and bias-stress effects commonly observed in polymer dielectric-based field-effect transistors.

In our study, we observe the expected trade-off between fully green, transiently degradable dielectrics and OTFT performance. Hysteresis mainly originates from slow polarization and charge trapping associated with the polar hydroxyl groups in the PVA dielectric.[24,27] PVA contains a high density of hydroxyl groups, whose dipoles reorient under the applied gate field but relax on a timescale comparable to, or slower than, the voltage sweep, this time-dependent dipolar polarization makes the channel charge depend on the sweep direction, giving rise to a hysteretic shift and current. Moisture uptake can further facilitate reorientation of hydroxyl groups or introduce additional mobile charges, modifying but not eliminating this hysteresis, while added low-k interlayers (e.g., UV-PCL) mainly lower interfacial charge trapping and leakage but do not completely remove the intrinsic dipolar polarization effects.[24,27,28,61] In a previous study from our group,[27] we showed that hysteresis can be largely suppressed by lowering pulsing frequency, confirming that the dominant contribution is dielectric polarization. In addition, these devices were measured over a much lower voltage range (V_{GS} and V_{SD} = -5 V) compared to SiO_2-based devices (V_{GS} and V_{SD} = -50 V) to achieve their low-voltage operation, which explains the smaller drain

current values. Nevertheless, despite these trade-offs, the devices still exhibit clear transistor behavior with reproducible channel formation at low voltages, demonstrating that the PVA/UV-PCL dielectric system enables functional, low-voltage, transient electronics as intended.

Furthermore, to evaluate short-term bias stability, consecutive transfer characteristics were measured under identical bias conditions. **Figure S4.2** a-d, depicts the representative transfer curves. The device exhibited minimal variation in extracted parameters over four repeated sweeps (**Table S4.2**), indicating stable charge transport and limited bias-induced degradation within the measurement time scale.

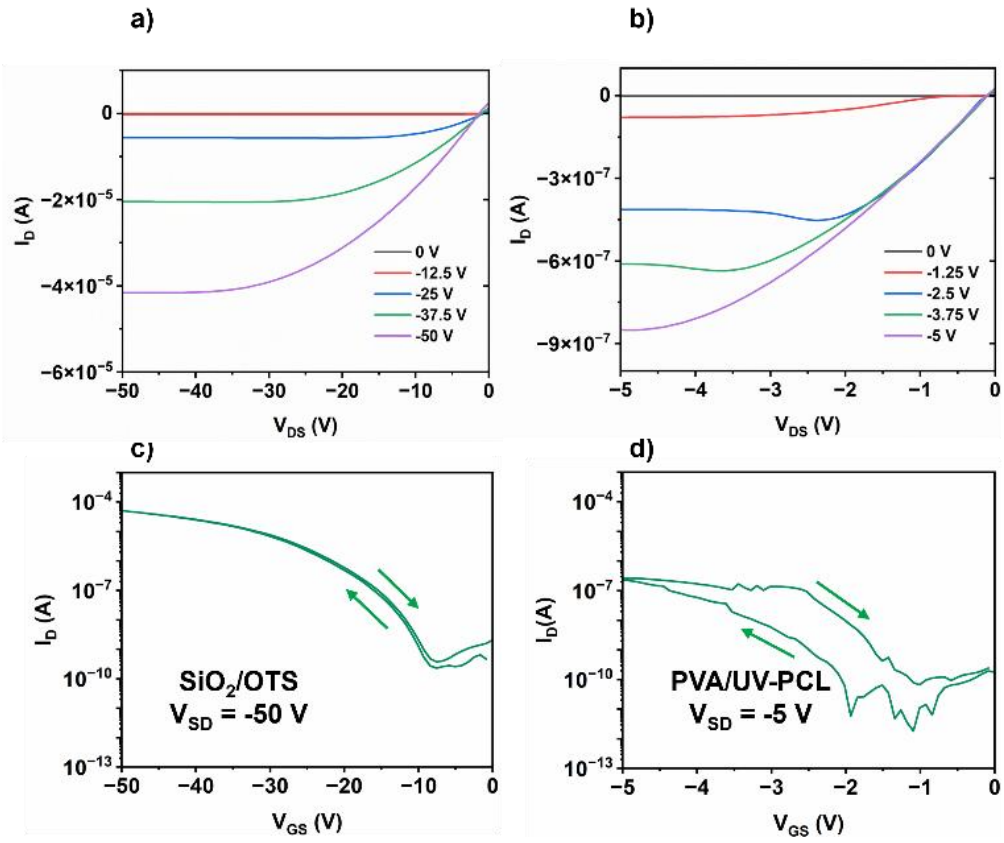


Figure 4.2. Output curves of (a) SiO2/OTS and (b) PVA/UV-PCL, and characteristic transfer curves of (c) OTFTs on OTS-treated SiO2 and (d) on PVA/UV-PCL. The transfer curves versus

VGS were acquired at V_{SD} = -50 V and V_{SD} = -5 V, respectively. Transfer curves and leakage current are plotted under identical bias conditions for four times for a representative device in the SI (**Figure S4.3).**

Table 4.2. Summary of the field effect properties of the degradable and non-degradable OTFT

Substrate/Gate/Dielectric[a]	Mobility ($cm^2V^{-1}s^{-1}$)		$I_{on/off}$[d]	V_T (V)[c]	n[e]
	μ_{max}[b]	μ_{avg}[c]			
Si/SiO_2	0.17	0.08 ± 0.04	10^4	-16.1 ± 0.9	38
PLA/Au/PVA/UV-PCL	0.16	0.03 ± 0.04	10^3	-2.0 ± 0.4	31

[a]OTFT fabricated with a silicon (Si) substrate and SiO_2 dielectric, or OTFT fabricated using a Biodegradable PLA substrate and PVA-based dielectric. Both devices were made using P(DPP-TIT) as the semiconductor.
[b]Maximum mobility (μ) measured from the functional OTFT.
[c]Mobility and threshold voltage were computed using an average value.
[d]Ratio of the on and off currents was calculated using the median value.
[e]Number of functioning devices used for the calculation of averages.

We performed numerical simulation to investigate the mechanism of the fabricated P(DPP-TIT) TFTs.[74–78] Our goal was to reconstruct the transfer characteristics measured under dual-sweep conditions for the devices representative for the non-degradable (SiO_2 dielectric) and degradable (PVA/UV-PCL dielectric) systems. We found that all curve groups measured in the saturation regime reasonably well follow the quadratic I_D–V_{GS} relationship, excluding the Schottky barrier and/or trap effects as a dominant contributor. We therefore took the hole mobility μ_{sim} (intrinsic mobility that serves as a simulation input) and the charge density at the semiconductor/insulator interface N_{int} as main fitting parameters.

Figure S4.4 (a) and (b), show the results of optimized simulation fitting to the experimental data. The fitting process yielded μ_{sim} of 0.112 $cm^2V^{-1}s^{-1}$ and 0.051 $cm^2V^{-1}s^{-1}$ for the

non-degradable and degradable devices, respectively. The dual-sweep measurement, conducted in the sequence of off-to-on and on-to-off scans, resulted in a hysteresis in opposite directions to a different extent in the two TFTs. The dynamic shift of the threshold voltage due to the hysteresis was modelled by the modulation of N_{int} in our simulation. As shown in **Figure S4.4**(c), the degradable TFT showed significantly lower N_{int} values as compared to the non-degradable TFT, confirming the suitability of the P(DPP-TIT) semiconductor–PVA/UV-PCL dielectric combination for low-voltage applications. The small hysteresis of the non-degradable TFT (**Figure 4.2c**) was tracked by a slight increase in N_{int} between the two scans. The larger and opposite-direction hysteresis of the degradable TFT (**Figure 4.2d**) was modelled by a decrease in N_{int}, which could originate from slower relaxation associated with charged species in the multi-component PVA/UV-PCL dielectric. N_{int} is the fixed two-dimensional charge density at the semiconductor/insulator interface that either partially screens or reinforces the externally applied gate field. A change in N_{int} therefore induces a systematic lateral shift of the transfer curve **(Figure S4.5).** This property was used to extract the N_{int} value corresponding to each transfer curve.

Synchrotron-based Grazing-Incidence Wide-Angle X-ray Scattering (GIWAXS) measurements were used to characterize the molecular packing and crystallographic orientation of the P(DPP-TIT) semiconductor deposited on both SiO_2 and PVA/UV-PCL dielectrics. The corresponding 2D scattering patterns (**Figure 4.3a–b**) and diffraction profiles (**Figure S4.6)** reveal comparable structural features across both systems. As shown in **Figure 4.3a**, the diffraction pattern of the semiconductor films deposited on the degradable dielectric includes additional reflections originating from the polymer substrate (PLA) (**Figure S4.7**) which partially overlap with the semiconductor's scattering signal. In contrast, the film deposited on SiO_2 (**Figure 4.3b**) exhibits sharper and more clearly resolved diffraction spots with higher intensity. To quantify this

difference, the integrated intensity of the (100) reflection was extracted from χ-cuts and normalized by film thickness (**Figure S4.8**). The resulting ratio between the semiconductor film deposited on SiO_2 and on PVA/UV-PCL was 1.11, indicating only a modest increase in the normalized (100) intensity for the SiO_2 sample and suggesting comparable crystallinity across both substrates. Aside from the substrate-related reflections, no significant differences in the overall diffraction pattern were observed (**Figure S4.6**), confirming that the polymer dielectric does not significantly affect the molecular packing or crystallographic texture of the P(DPP-TIT) semiconductor. Moreover, when examined under a 1D line profile plot as per **Table 4.3** and **Figure S4.9**, both device structures exhibit similar lamellar spacing parameters, indicating that the polymer dielectric substrate offers comparable morphological characteristics when compared to SiO_2/OTS. Notably, however, the lack of the 010 π-π spacing peak for P(DPP-TIT) on PVA/UV-PCL dielectric, as quantified in **Table 4.3**, indicates that P(DPP-TIT) exhibits less observable edge-on π-stacking properties in comparison to on SiO_2/OTS.[79,80] This observation is consistent with other organic polymer semiconductors deposited on non-monolayer substrates and polymer dielectrics.[16] Despite these differences, as per **Table 4.2**, this has little influence on the μ_h of P(DPP-TIT) itself, overall suggesting that the PVA/UV-PCL dielectric is a good substitute for SiO_2/OTS.

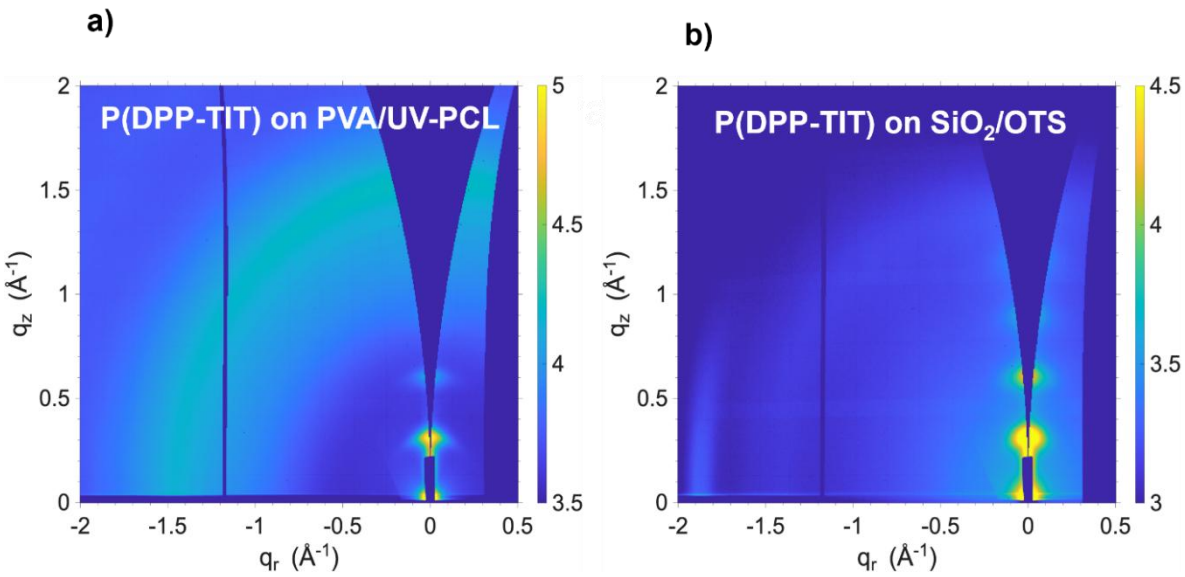


Figure 4.3. GIWAXS scattering patterns of DPP-imine conjugated polymer thin films deposited on (a) the bilayer dielectric (PVA/UV-PCL) and (b) on SiO_2/OTS

Table 4.3. Stacking parameters and crystallization data of P(DPP-TIT) on OTS-SiO_2 and degradable polymer substrates. Crystal Coherence Length (CCL) was calculated using the Scherrer equation with a correction factor (K) of 0.9.

Dielectrics	**Lamellar Spacing**		**π-π Spacing**		**FWHM [1/Å]**	**CCL [Å]**
	Peak Position [1/Å]	**d-d Distance [Å]**	**Peak Position [1/Å]**	**d-d Distance [Å]**		
SiO_2/OTS	0.247	25.438	1.75	3.590	0.101	55.988
PVA/UV-PCL	0.255	24.640	n/a	n/a	n/a	n/a

Raman microscopy was employed to gain a deeper understanding of the morphology of P(DPP-TIT) on OTS-treated SiO_2 and PVA/UV-PCL dielectric surface. This technique is highly

sensitive to local polymer ordering, permitting subtle variations in conjugation length or miscibility within the material to be detected.[81–84] By tracking characteristic vibrational peaks specific to the DPP-based semiconductor, chemical or compositional maps can be generated. **Figure 4.4a** compares Raman spectra for OTFT with P(DPP-TIT) deposited on OTS-treated SiO_2 and on PVA/UV-PCL. Distinct Raman features of the DPP-based semiconductor include the symmetric C═C stretching of the thiophene backbone at ~1412 cm^{-1}, symmetric C–N and C–C stretches associated with the DPP acceptor at ~1365 cm^{-1}, and asymmetric C═C stretching from the DPP and thiophene lactam rings at ~1512 cm^{-1} (**Figure 4.4a**). **Figure 4.4b** and **c** depict the Raman intensity maps for 19 × 19 μm^2 of an OTFT device fabricated by depositing P(DPP-TIT) on OTS-treated SiO_2 and on a degradable dielectric (PVA/UV-PCL), respectively. These figures demonstrate the normalized intensity value of the DPP-based semiconductor (at ~ 1512 cm^{-1}) and provide a visual representation of the chemical uniformity of the P(DPP-TIT) film to complement the Raman spectrum (**Figure 4.4a**). Raman maps reveal that the intensity of P(DPP-TIT) on PVA/UV-PCL dielectric is relatively more uniform than when deposited on OTS-treated SiO_2. A more packed and uniform structure of P(DPP-TIT) on a degradable dielectric surface can be attributed to fewer deep interfacial traps at the dielectric/semiconductor interface, enabling a more continuous conjugated network.

The effect of the degradable polymer substrate and dielectric on the thin-film morphology was further characterized by AFM. Thin films were cast via spin-coating onto the bilayer dielectric (PVA/UV-PCL) (**Figure 4.4d**) and on OTS-treated SiO_2 (**Figure 4.4e**) and were imaged over a 20 × 20 μm^2 area to evaluate large-scale surface features. In both cases, P(DPP-TIT) exhibited morphological characteristics typical of DPP-based semiconductors, with uniform grain-like domains and no evidence of phase separation or aggregation.[85,86] The root-mean-square (RMS)

roughness was 2.97 nm for the polymer substrate and 2.86 nm for SiO_2, indicating comparable surface topographies. This similarity in morphology suggests that the dielectric and substrate have a minimal influence on the thin-film formation, which is consistent with the negligible difference in charge-carrier mobility between the devices.[87,88] The AFM results are in good agreement with the Raman spectra (**Figure 4.4a**) and corresponding Raman mapping (**Figure 4.4b-c**), collectively confirming the uniformity and compositional consistency of the film. These results confirm that the semiconductor can be integrated into a fully biodegradable platform while maintaining its thin-film morphology.

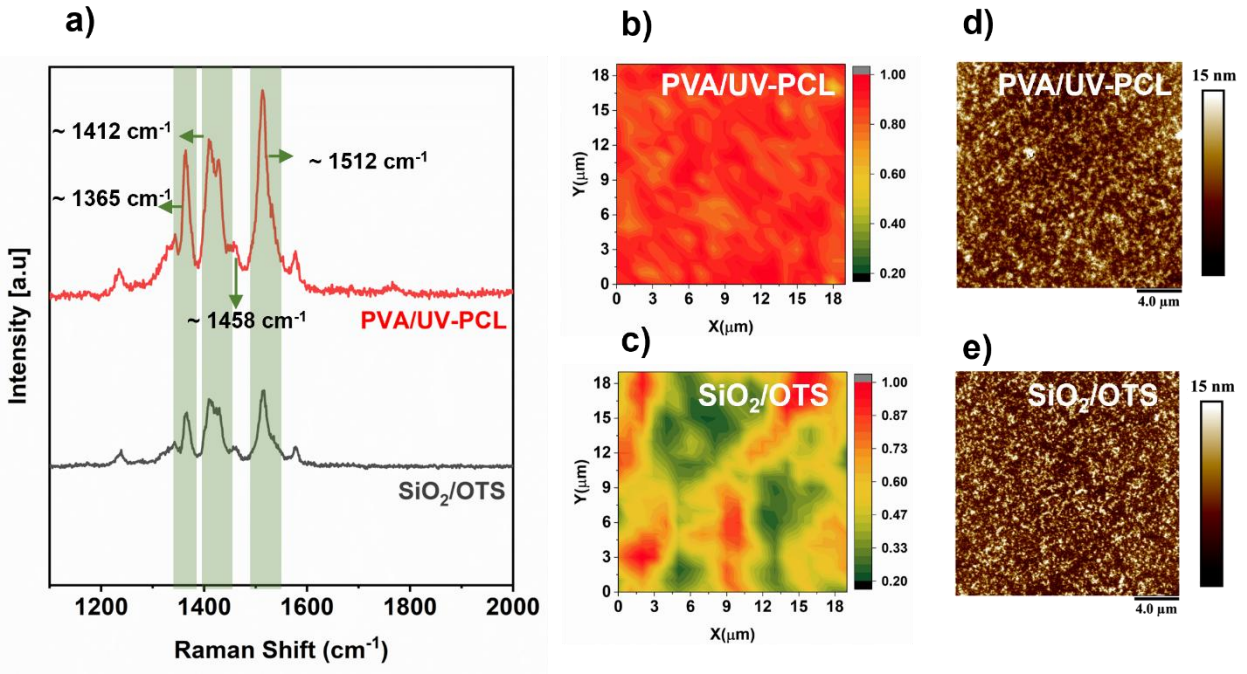


Figure 4.4. Raman spectra (a) and maps (19 × 19 μm2) (b-c) of degradable P(DPP-TIT) semiconductor on bilayer dielectric (PVA/UV-PCL) and OTS-treated SiO_2. 20 × 20 μm AFM topography images of thin films of P(DPP-TIT) deposited on (d) the degradable polymer dielectric and (e) OTS-treated SiO_2.

As depicted in **Figure 4.1b**, exposure of the fabricated OTFT to acidic medium (1 M HCl) for 7 days led to the degradation of P(DPP-TIT) layer and possibly the dissolution of bilayer dielectric layer based on PVA, while subsequent immersion of the degradable PLA substrate and patterned gold coated gate electrode in basic buffer solution (pH ~10) resulted in the gradual degradation of the PLA matrix in 20 days, leaving behind only dispersed gold micro and nanoparticles. This combination of structural design and sequential degradation demonstrates the feasibility of fabricating a high-performance yet transient OTFT system using biodegradable materials. UV–vis spectroscopy was employed to track the degradation of imine groups in the P(DPP-TIT) polymers thin film (**Figure 4.5).** The films were submerged in 1M HCl at specified time intervals of 15 minutes, 30 minutes, and 1 hour, upon which the spectral data was collected, as per **Figure 4.5a**. Progressive cleavage of the imine bonds results in the depolymerization of the material into oligomeric and monomeric species, which exhibit negligible absorption in the visible spectrum.[18,36,43] This can be observed in **Figure 4.5b**, by the progressive decrease in absorbance of the $\lambda_{0\text{-}1}$ after just 15 minutes of submersion, as well as an observable widening hyperchromic shift, indicating polymer chain scission.[16] The absorbance continues to decrease more drastically after 30 minutes, and by 1 hour, only approximately 20% of the initial $\lambda_{0\text{-}1}$ absorbance remains, suggesting that the solid-state film of P(DPP-TIT) can undergo rapid depolymerization under aqueous acidic conditions. In comparison with previously established reports of the degradation of P(DPP-TIT) based thin films, this variant of P(DPP-TIT) has a degree of polymerization of 11 repeat units, and relatively narrow dispersity of 1.55, as per **Table S4.1**. Both values are indicative that P(DPP-TIT) has a relatively low molecular weight, with polymer chains having relatively similar lengths.[89] The combination of these factors can provide faster degradation in comparison to previously established polymers possessing similar alkyl chains and conjugated backbones.[43]

This is noteworthy, as literature reports indicate that polymers with reduced molecular weights degrade more readily, which complements the other components of the OTFT system that are also engineered for rapid breakdown.[90,91] Together, these design features ensure that the material maintains strong charge transport characteristics during operation while facilitating efficient degradation after use. Notably, as shown in **Figure 4.5a**, the π–π* transition peak centered at 450 nm associated with intrachain charge delocalization diminished at a slower rate in comparison to $\lambda_{0\text{-}1}$ and $\lambda_{0\text{-}0}$ absorbance peaks. The decay in absorbance of this peak is associated with the hydrolysis and subsequent ring-opening of the DPP motif.[41] With these observations, we hypothesize that in the solid state, the polymer undergoes chain scission via hydrolysis of the imine bonds within the conjugated backbone, which is then followed by destruction of the DPP motif itself.[92]

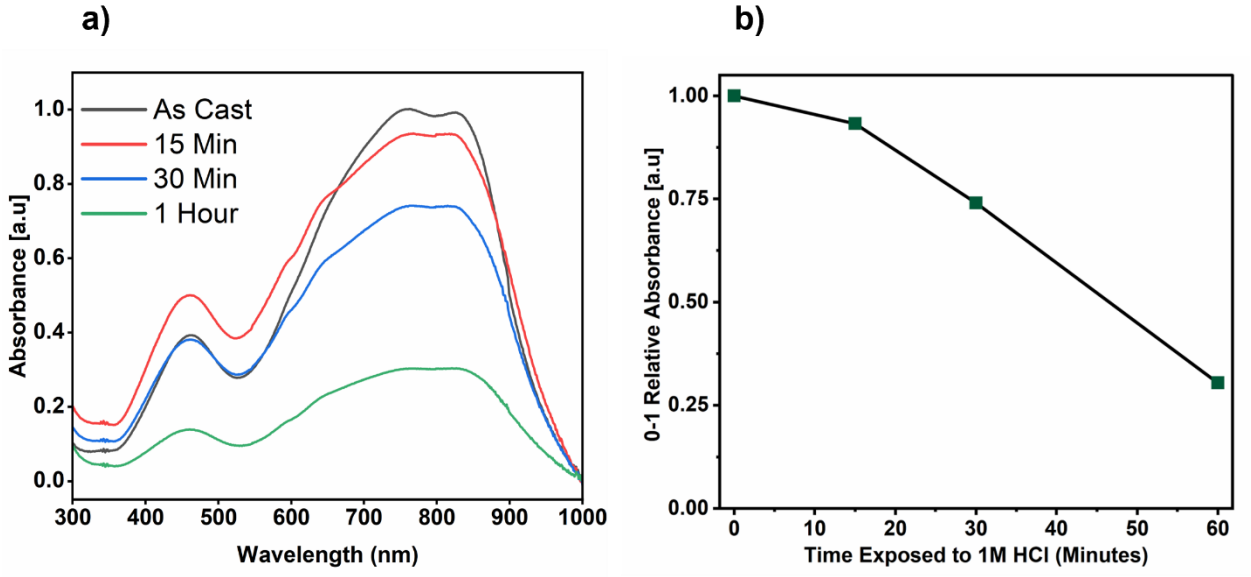


Figure 4.5. a) UV-vis spectra of the $\lambda_{0\text{-}1}$-based normalized absorbance of P(DPP-TIT) thin films on quartz substrates upon submersion in aqueous 1M HCl solution at selected time intervals. b) Line plot of UV-Vis spectra quantifying the decrease in $\lambda_{0\text{-}1}$ over a period of one hour (60 minutes).

We have also investigated the full device degradation and component recovery leveraging dual trigger dissolution: the imine-containing DPP-based semiconductor degrades under acidic conditions,[43] while the PLA substrate dissolves in basic environments,[24,93] enabling sequential separation and extraction of device layers. To demonstrate the degradation of the degradable P(DPP-TIT) semiconductor, a device was immersed in 1 M HCl solution and monitored for 7 days. Raman microscopy performed after exposure revealed the complete disappearance of the typical DPP polymer semiconductor peaks, as per **Figure 4.6a**, associated with the delocalized conjugated backbone alkene and aromatic spectral signatures. There was also a weak vibration peak observed at ~1458 cm^{-1}, which can be assigned to O-H and C-H bending for PVA film[94] (**Figure 4.6a**). Hence, the disappearance of characteristic peaks of P(DPP-TIT) and PVA confirms that the active semiconductor layer was fully degraded along with full dissolution of the thin bilayer dielectric. Subsequently, the remaining layers (PLA substrate and gate electrode) were immersed in a basic buffer solution with a pH of ~10 to facilitate degradation. Raman measurements following this treatment displayed no characteristic peaks of PLA, yielding a flat baseline, which indicates that all the OTFT layers, including the P(DPP-TIT) semiconductor, substrate (PLA), and dielectric (PVA/UV-PCL), were completely degraded, leaving micro/nano particles of gold. The corresponding optical images shown in **Figure 4.6b-d** depict the stepwise degradation process of the OTFT device in an acidic and basic medium. **Figure 4.6b** shows the intact device prior to immersion. **Figure 4.6c** demonstrates the complete degradation of the active semiconducting layer and dissolution of PVA and UV-PCL (monolayer), along with the visible disintegration of the source and drain electrodes during immersion. Finally, **Figure 4.6d** reveals the presence of only gold micro/nanoparticles remaining after the complete degradation of the substrate in basic buffer solution of sodium hydroxide (NaOH) (pH ~10). Similarly, **Figures 4.6e-g** illustrate the

degradation sequence for the free-standing OTFT structure. **Figure 4.6e** shows an OTFT device before it was immersed in 1 M HCl, **Figure 4.6f** displays the free-standing PLA layer with the remaining gate electrode pattern, and **Figure 4.6g** shows a free-standing gold particle following substrate degradation. Overall, these results and images clearly demonstrate a tiered degradation approach which enables separation of components and will facilitate separation, recovery and repurposing of the OTFT components.

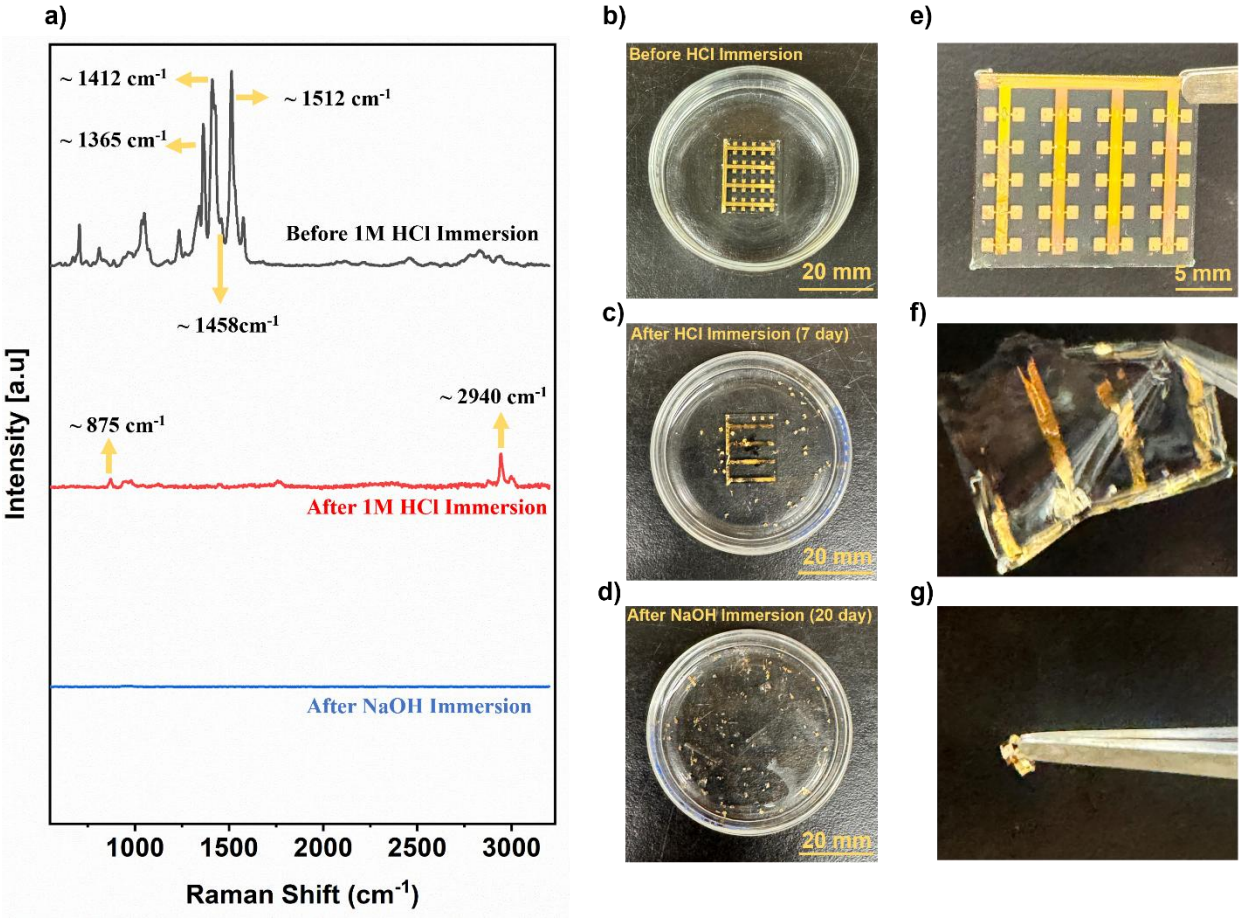


Figure 4.6. (a) Raman spectrum of the degradable OTFT device at different stages of degradation. (b-d) Photos of OTFTs before the immersion in 1 M HCl, after immersion in 1 M HCl, and after the immersion in basic buffer solution (pH ~ 10), respectively. (e-g) Free-standing images of OTFT

before the immersion in 1 M HCl, after immersion in 1 M HCl, and after the immersion in basic buffer solution, respectively.

Furthermore, the acid and base media employed in this work for the demonstration of sequential degradation are not intended to represent physiological or typical environmental conditions. Instead, they serve as accelerated conditions used to demonstrate selective layer removal and identify relative material stability within experimentally accessible time scales.[37,93,95–97] In potential industrial recovery or recycling scenarios, similar acceleration could be achieved through elevated temperatures and controlled pH to facilitate efficient material separation. Under natural environmental conditions, degradation would instead proceed more gradually through hydrolytic, enzymatic, or environmentally assisted processes. Over time, the material breaks into soluble fragments, supporting separation and reducing long-term persistence. Accordingly, the presented strategy demonstrates the feasibility of controlled disassembly while recognizing that degradation in real-world environments would occur at slower rates than those observed under accelerated laboratory conditions.

4.5 Conclusion

In summary, biocompatible and fully biodegradable OTFTs were prepared using an imine-based degradable semiconducting polymer P(DPP-TIT), coupled with a biodegradable substrate (PLA) and dielectric (PVA/UV-PCL). The use of a bilayer gate dielectric effectively reduced the V_T of P(DPP-TIT)-based *p*-type OTFTs from -16.1 V to -2 V while maintaining electrical performance comparable to OTFTs employing conventional SiO_2 dielectrics. Raman spectroscopy/microscopy, GIWAXS, and AFM analyses revealed similar morphological and structural characteristics consistent with the observed device performance. Finally, we demonstrated the stepwise degradation of each device layer under acidic and basic environments,

confirming the complete disintegration of the OTFT components. This work highlights a promising approach toward sustainable, transient electronics that combine reliable functionality with environmental degradability.

Acknowledgments

We acknowledge SOLEIL for beamtime provision on the beamline SIRIUS. We also thank Laura E. Dickson for her assistance in analyzing GIWAXS results.

4.6 Supporting Information

4.6.1 Device characterization

Our built-in autotester made it possible to measure the I_{SD}, control the source-drain voltage V_{SD}, and control the V_{GS}. While V_{GS} was adjusted between 0 and -5 V, output characteristics were obtained by sweeping V_{SD} from 0 to -5 V. For biodegradable polymer-gated devices, transfer characteristics were measured at V_{SD} = -5 V, while for SiO_2-gated devices, V_{SD} = -50 V. V_{GS} was modulated between 0 and -50 V for the latter and between 0 and -5 V for the former.

$$I_{SD} = \frac{\mu C_i W}{2L} (V_{GS} - V_T)^2 \quad \text{(S4.1)}$$

Equation (S4.1)[98] was used to extract the μ_h, V_T, and $I_{on/off}$ from transfer characteristics in the saturation regime. $I_{on/off}$ was derived from the ratio of the maximum to minimum I_{SD} values, whereas V_T was calculated by projecting the linear portion of the on-state transfer curve to its x-axis intercept. Using impedance spectroscopy (Metrohm PGSTAT204 potentiostat/galvanostat, Switzerland) at 10 Hz and an applied voltage sweep from 0 to 10 V, the gate dielectric capacitance (C_i) was measured. C_i was computed using equation (S4.2),[99] taking into account the real (Z') and imaginary (Z'') components of impedance as well as the angular frequency (ω). The active area of each device (A) was taken into account in the computation. To account for changes in channel

length brought on by electrode shadowing during source-drain deposition, reported mobility values were adjusted.

$$C_i = \frac{1}{\omega A} \times \frac{Z''}{Z''^2 + Z'^2} \tag{S4.2}$$

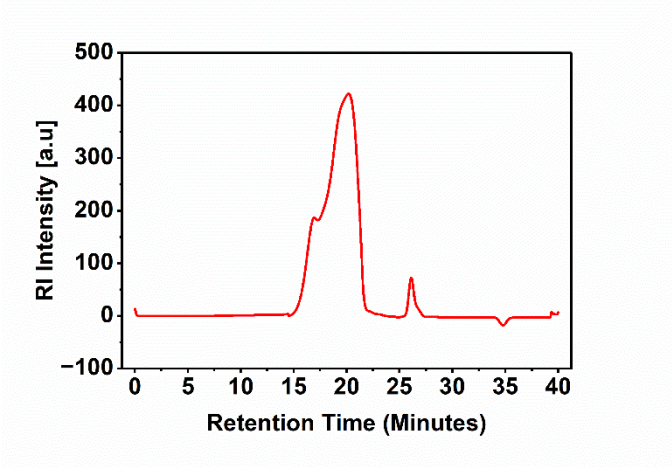


Figure S4.1. High-temperature gel permeation chromatogram of P(DPP-TIT) recorded in 1,2,4-trichlorobenzene at 180 °C. Molecular weight measured against polystyrene standards.

Table S4.1. Synthesis of P (DPP-TIT) polymer and its physical and optoelectronic properties

Polymer	**M_n (kDa)[a]**	**M_w (kDa)**	**$Đ_w$[b]**	**X_n[c]**	**Λ_{film}(nm)[d]**	**Eg_{opt}(eV)[e]**
P(DPP-TIT)	13.1	20.3	1.55	11	829.37	1.36

a) Number-average molecular weight estimated by high-temperature gel permeation chromatography in 1,2,4-trichlorobenzene at 180 °C using a polystyrene standard. b) Dispersity defined as Mw/Mn. c) Degree of polymerization defined as Mn/M0, where M0 is the molecular weight of the repeat unit of each polymer. d) Absorption maxima. e) Calculated by the following equation: gap = $1240/\lambda_{onset}$.

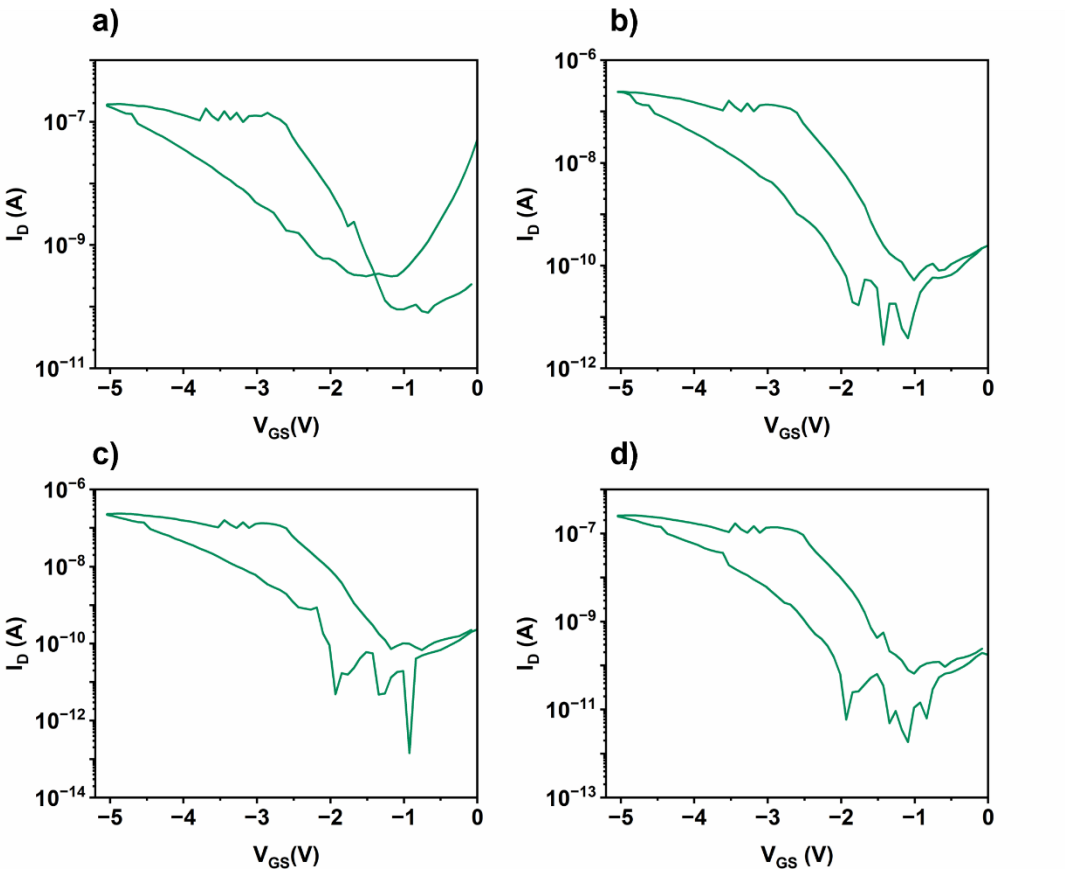


Figure S4.2. Transfer curves (a-d) of a representative device run under identical bias stress (V_{GS}=-5)

Table S4.2. Summary of the field effect properties of the representative device, swept consecutively four times

Transfer Curve*	Mobility ($cm^2V^{-1}s^{-1}$)	$I_{on/off}$	V_T (V)
a	0.015	10^2	-2.0
b	0.019	10^3	-2.1
c	0.021	10^3	-2.1
d	0.031	10^3	-2.2

*Extracted parameters from the representative transfer curve run under identical bias conditions.

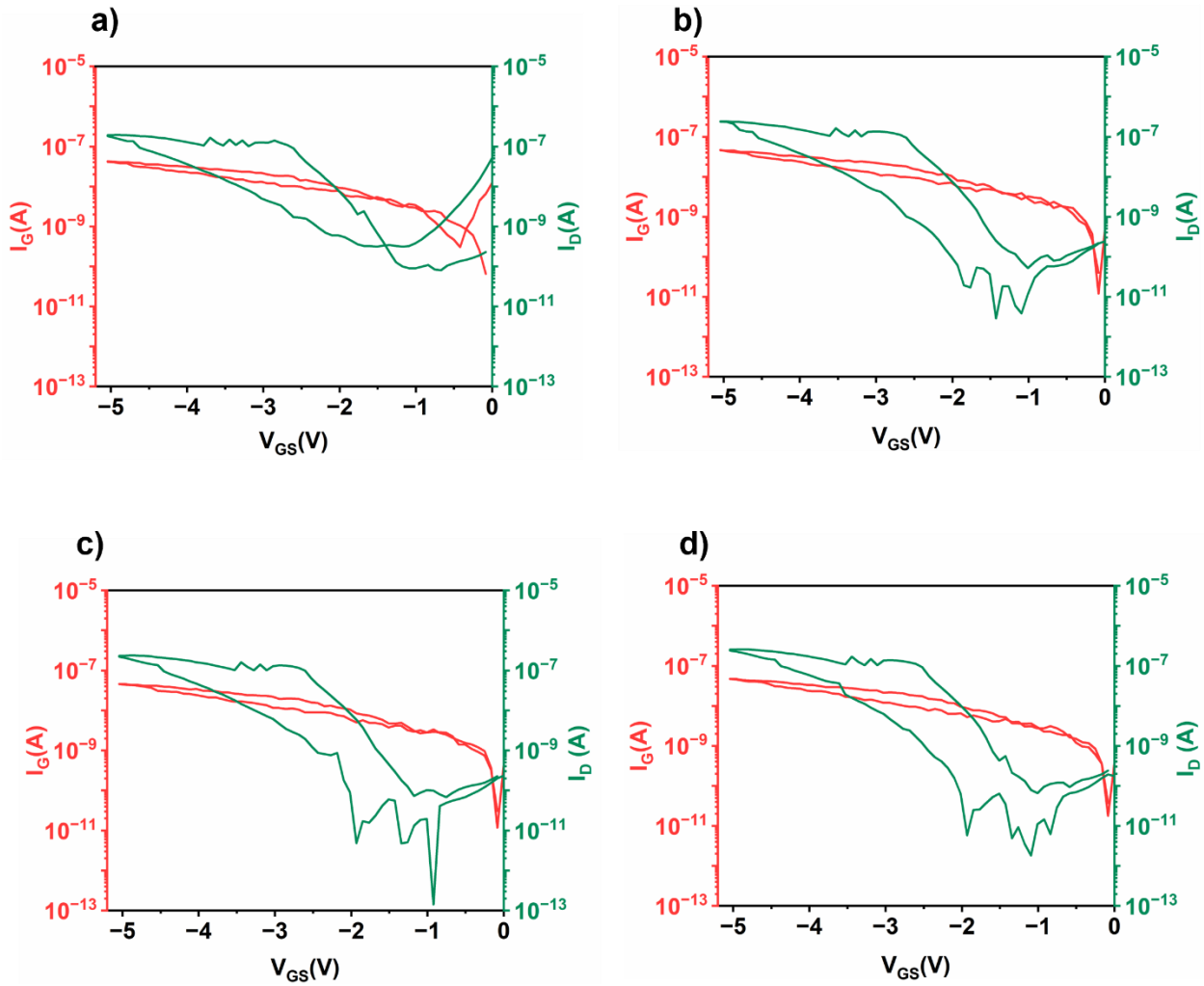


Figure S4.3. Transfer curves and leakage current are plotted under identical bias conditions for four times for a representative device.

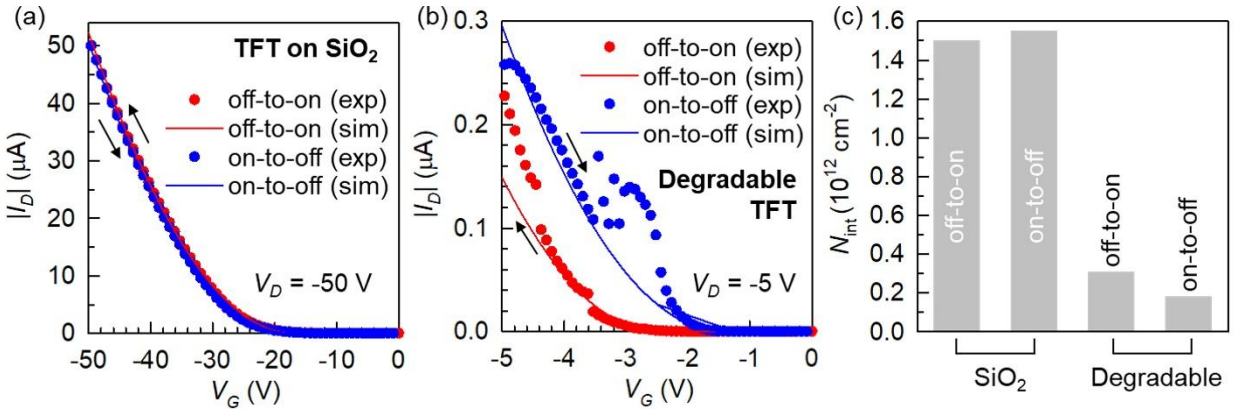


Figure S4.4. Experimental and theoretically reconstructed transfer curves for (a) non-degradable and (b) degradable TFT. (c) Values of N_{int} estimated in (a) and (b).

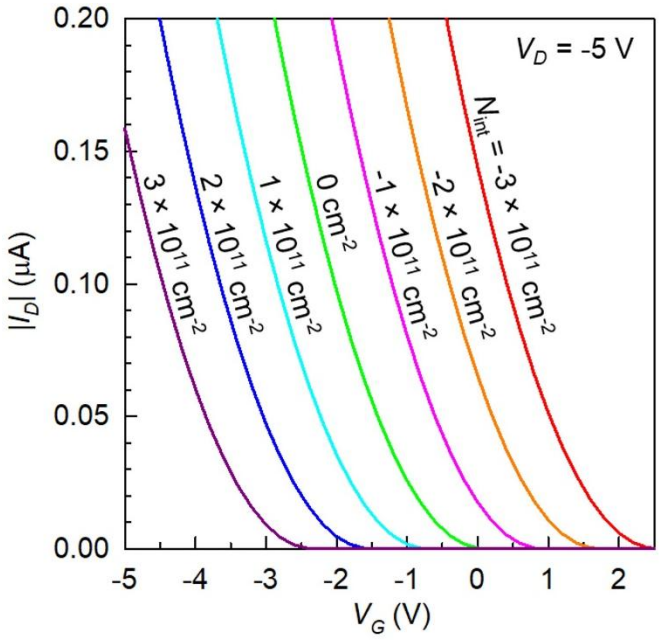


Figure S4.5. Simulation results visualizing the effects of N_{int} on transfer characteristics. N_{int} is the only variable between these seven curves. All the other materials parameters were kept identical to those extracted for the degradable TFT in **Figure S4.4**.

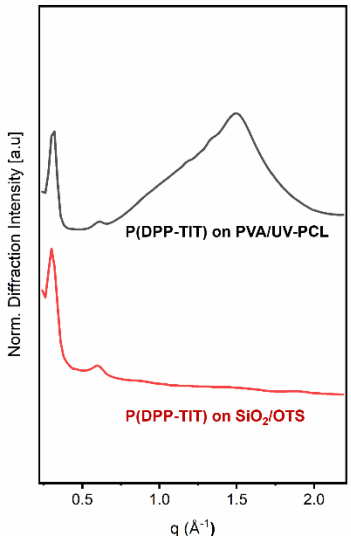


Figure S4.6. Corresponding azimuthally integrated diffraction profiles of P(DPP-TIT) on PVA/UV-PCL and SiO_2/OTS

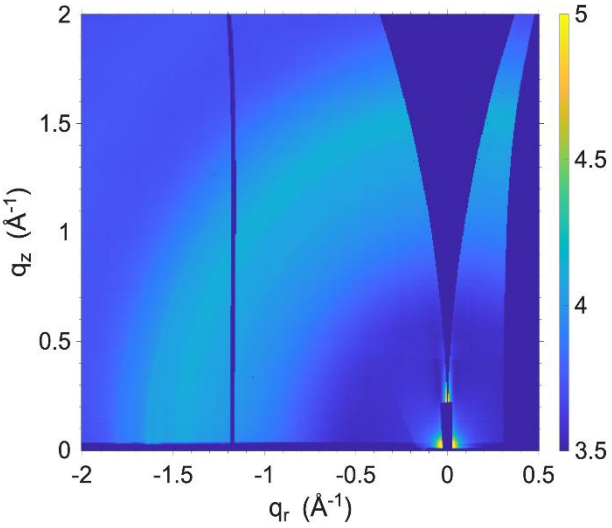


Figure S4.7. GIWAXS pattern of PVA/UV-PCL dielectric on PLA substrate

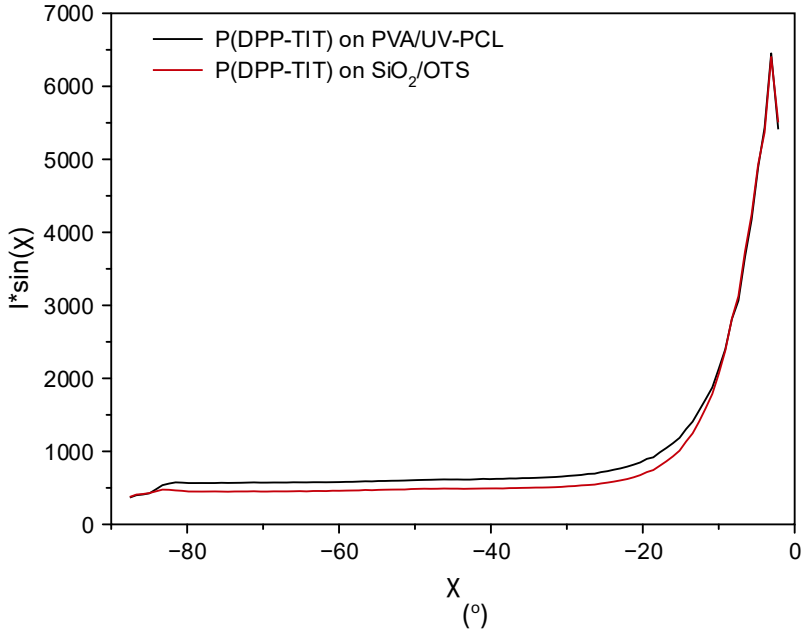


Figure S4.8. χ-cuts of the (100) diffraction peak extracted from the GIWAXS patterns of P(DPP-TIT) thin films deposited on SiO_2 and on the polymer substrate. The integrated (100) intensity was normalized by film thickness

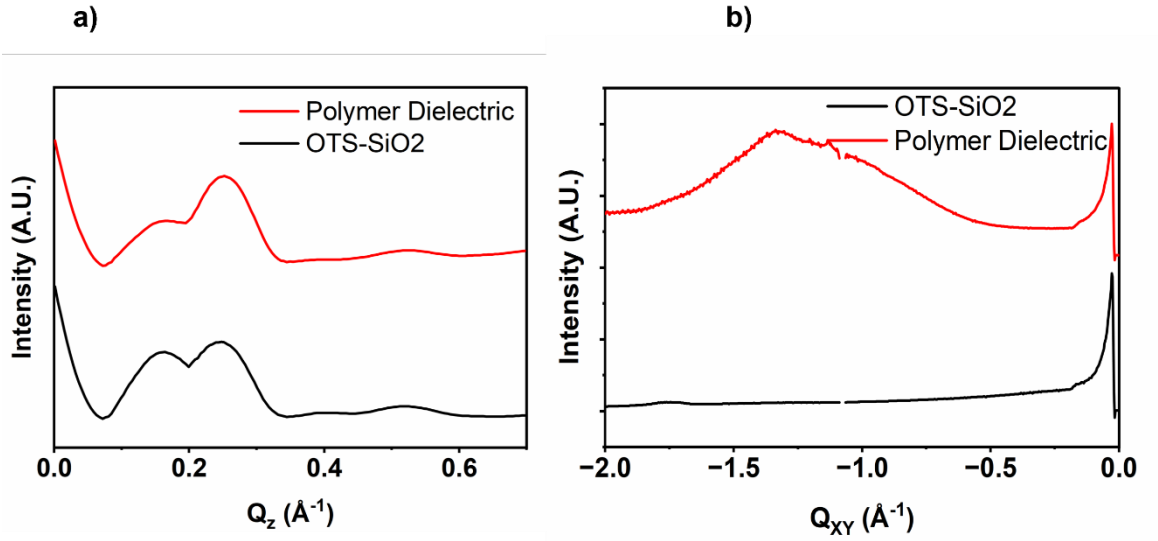
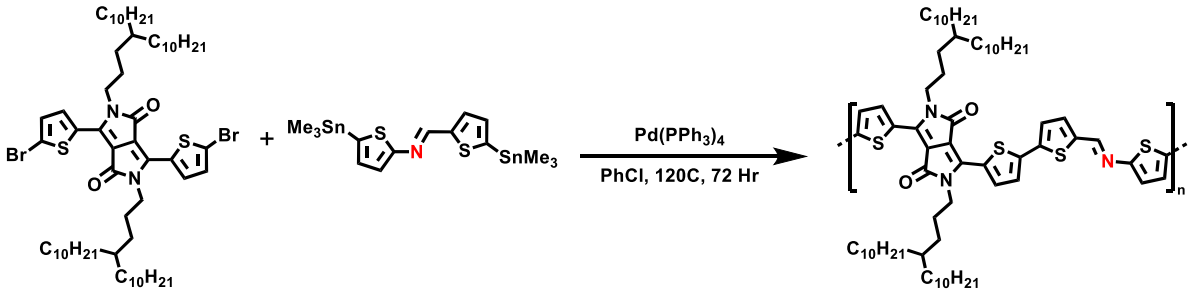


Figure S4.9. 1D line profiles of P(DPP-TIT) in a) Q_z out-of-plane vector direction and b) Q_{xy} in-plane vector direction. Data were processed with a standard Savitzky-Golay filter for clarity.

4.6.2 Synthesis of a degradable semiconductor: P(DPP-TIT)



To a reaction vessel equipped with a magnetic stir bar, 150 mg of 3,6-Bis(5-bromothiophen-2-yl)-2,5-bis(4-decyltetradecyl)-2,5-dihydropyrrolo[3,4-c]pyrrole-1,4-dione (0.133 mmol) and 69 mg of (E)-N,1-bis(5-(trimethylstannyl)thiophen-2-yl)methanimine (0.133 mmol) was added. The reaction vessel was moved into a nitrogen atmospheric glove box anti-chamber and thrice purged with vacuum and nitrogen before being transferred into the glovebox. 2.5 mL of anhydrous, degassed chlorobenzene was added into the reaction vessel to solubilize the monomers and 6.1 mg of Tetrakis (triphenylphosphine) palladium (0) (0.005 mmol) was added. The reaction vessel was then sealed under the nitrogen atmosphere, removed from the glovebox, and moved to a hotplate set to 120 ^{o}C and stirred for 72 hours. The reaction vessel was subsequently unsealed, and the chlorobenzene solution was pipetted into a beaker of cold methanol to precipitate the polymer. The polymer precipitate was loaded onto a Soxhlet thimble and was subsequently washed under reflux with methanol (12 hours), acetone (6 hours), hexanes (6 hours) and subsequently collected with 100 mL of chloroform (6 hours). The chloroform solution was reduced to approximately 25% of its original volume using rotary evaporation, upon which the solution was pipetted into a beaker of cold methanol to precipitate the purified polymer. The methanol was

subsequently drained using vacuum filtration to collect the polymer as a solid blue film (127 mg).

References

(1) Kang, S.-K.; Yin, L.; Bettinger, C. The Emergence of Transient Electronic Devices. *MRS Bull.* **2020**, *45* (2), 87–95.

(2) Fu, K. K.; Wang, Z.; Dai, J.; Carter, M.; Hu, L. Transient Electronics: Materials and Devices. *Chem. Mater.* **2016**, *28* (11), 3527–3539.

(3) Chiong, J. A.; Tran, H.; Lin, Y.; Zheng, Y.; Bao, Z. Integrating Emerging Polymer Chemistries for the Advancement of Recyclable, Biodegradable, and Biocompatible Electronics. *Adv. Sci.* **2021**, *8* (14), 2101233.

(4) Tan, M. J.; Owh, C.; Chee, P. L.; Kyaw, A. K. K.; Kai, D.; Loh, X. J. Biodegradable Electronics: Cornerstone for Sustainable Electronics and Transient Applications. *J. Mater. Chem. C* **2016**, *4* (24), 5531–5558.

(5) Chen, G.; Xu, L.; Zhang, P.; Chen, B.; Wang, G.; Ji, J.; Pu, X.; Wang, Z. L. Seawater Degradable Triboelectric Nanogenerators for Blue Energy. *Adv. Mater. Technol.* **2020**, *5* (9), 2000455.

(6) Hwang, S.-W.; Tao, H.; Kim, D.-H.; Cheng, H.; Song, J.-K.; Rill, E.; Brenckle, M. A.; Panilaitis, B.; Won, S. M.; Kim, Y.-S. A Physically Transient Form of Silicon Electronics. *Science.* **2012**, *337* (6102), 1640–1644.

(7) Gao, Y.; Zhang, Y.; Wang, X.; Sim, K.; Liu, J.; Chen, J.; Feng, X.; Xu, H.; Yu, C. Moisture-Triggered Physically Transient Electronics. *Sci. Adv.* **2017**, *3* (9), e1701222.

(8) King, B.; Lessard, B.H. Review Of Recent Advances In Sensing Mechanisms In Solid-State

Organic Thin-Film Transistor (OTFT) Sensors. *Journal of Materials Chemistry C.* **2024**, 5654-5683.

(9) Kaltenbrunner, M.; Sekitani, T.; Reeder, J.; Yokota, T.; Kuribara, K.; Tokuhara, T.; Drack, M.; Schwödiauer, R.; Graz, I.; Bauer-Gogonea, S. An Ultra-Lightweight Design for Imperceptible Plastic Electronics. *Nature.* **2013**, *499* (7459), 458–463.

(10) Sekitani, T.; Nakajima, H.; Maeda, H.; Fukushima, T.; Aida, T.; Hata, K.; Someya, T. Stretchable Active-Matrix Organic Light-Emitting Diode Display Using Printable Elastic Conductors. *Nat. Mater.* **2009**, *8* (6), 494–499.

(11) Tee, B. C.-K.; Chortos, A.; Berndt, A.; Nguyen, A. K.; Tom, A.; McGuire, A.; Lin, Z. C.; Tien, K.; Bae, W.-G.; Wang, H. A Skin-Inspired Organic Digital Mechanoreceptor. *Science.* **2015**, *350* (6258), 313–316.

(12) Klauk, H.; Zschieschang, U.; Pflaum, J.; Halik, M. Ultralow-Power Organic Complementary Circuits. *Nature* **2007**, *445* (7129), 745–748.

(13) Henson, Z. B.; Müllen, K.; Bazan, G. C. Design Strategies for Organic Semiconductors beyond the Molecular Formula. *Nat. Chem.* **2012**, *4* (9), 699–704.

(14) Li, R.; Wang, L.; Kong, D.; Yin, L. Recent Progress on Biodegradable Materials and Transient Electronics. *Bioact. Mater.* **2018**, *3* (3), 322–333.

(15) La Mattina, A. A.; Mariani, S.; Barillaro, G. Bioresorbable Materials on the Rise: From Electronic Components and Physical Sensors to in Vivo Monitoring Systems. *Adv. Sci.* **2020**, *7* (4), 1902872.

(16) Feig, V. R.; Tran, H.; Bao, Z. Biodegradable Polymeric Materials in Degradable Electronic

Devices. *ACS Cent. Sci.* **2018**, *4* (3), 337–348.

(17) Irimia-Vladu, M. “Green” Electronics: Biodegradable and Biocompatible Materials and Devices for Sustainable Future. *Chem. Soc. Rev.* **2014**, *43* (2), 588–610.

(18) Lei, T.; Guan, M.; Liu, J.; Lin, H.-C.; Pfattner, R.; Shaw, L.; McGuire, A. F.; Huang, T.-C.; Shao, L.; Cheng, K.-T. Biocompatible and Totally Disintegrable Semiconducting Polymer for Ultrathin and Ultralightweight Transient Electronics. *Proc. Natl. Acad. Sci.* **2017**, *114* (20), 5107–5112.

(19) Bettinger, C. J.; Bao, Z. Organic Thin-film Transistors Fabricated on Resorbable Biomaterial Substrates. *Adv. Mater.* **2010**, *22* (5), 651–655.

(20) Reichert, C. L.; Bugnicourt, E.; Coltelli, M.-B.; Cinelli, P.; Lazzeri, A.; Canesi, I.; Braca, F.; Martínez, B. M.; Alonso, R.; Agostinis, L. Bio-Based Packaging: Materials, Modifications, Industrial Applications and Sustainability. *Polymers (Basel).* **2020**, *12* (7), 1558.

(21) Chiellini, E.; Corti, A.; D’Antone, S.; Solaro, R. Biodegradation of Poly (Vinyl Alcohol) Based Materials. *Prog. Polym. Sci.* **2003**, *28* (6), 963–1014.

(22) Van Etten, E. A.; Ximenes, E. S.; Tarasconi, L. T.; Garcia, I. T. S.; Forte, M. M. C.; Boudinov, H. Insulating Characteristics of Polyvinyl Alcohol for Integrated Electronics. *Thin Solid Films* **2014**, *568*, 111–116.

(23) Tran, H.; Feig, V. R.; Liu, K.; Zheng, Y.; Bao, Z. Polymer Chemistries Underpinning Materials for Skin-Inspired Electronics. *Macromolecules* **2019**, *52* (11), 3965–3974.

(24) Ali, M.; Ronnasi, B.; Ourabi, M.; Park, J. H.; St-Pierre, J.-P.; Kim, C.-H.; Lessard, B. H.

Cytocompatible, Disintegrable, Low-Voltage Operation n-Type Organic Thin Film Transistors. *Mater. Adv.* **2025**, *6* (2), 557–568.

(25) Jin, S. H.; Yu, J. S.; Kim, J. W.; Lee, C. A.; Park, B.; Lee, J. D.; Lee, J. H. 34.2: PMMA Buffer-Layer Effects on Electrical Performance of Pentacene OTFTs with a Cross-linked PVA Gate Insulator on a Flexible Substrate. In *SID Symposium Digest of Technical Papers*; Wiley Online Library, 2003; Vol. 34, pp 1088–1091.

(26) Jin, S. H.; Yu, J. S.; Lee, C. A.; Kim, J. W.; Park, B.-G.; Lee, J. D. Pentacene OTFTs with PVA Gate Insulators on a Flexible Substrate. *Journal-Korean Phys. Soc.* **2004**, *44*, 181–184.

(27) Tousignant, M. N.; Lin, Z. S.; Brusso, J.; Lessard, B. H. Interfacial Ultraviolet Cross-Linking of Green Bilayer Dielectrics. *ACS Appl. Mater. Interfaces* **2023**, *15* (2), 3680–3688.

(28) Tousignant, M. N.; Ronnasi, B.; Tischler, V.; Lessard, B. H. N-Type Single Walled Carbon Nanotube Thin Film Transistors Using Green Tri-Layer Polymer Dielectric. *Adv. Mater. Interfaces* **2023**, *10* (14), 2300079.

(29) Rullyani, C.; Ramesh, M.; Sung, C.-F.; Lin, H.-C.; Chu, C.-W. Natural Polymers for Disposable Organic Thin Film Transistors. *Org. Electron.* **2018**, *54*, 154–160.

(30) She, X.-J.; Liu, J.; Zhang, J.-Y.; Gao, X.; Wang, S.-D. Operational Stability Enhancement of Low-Voltage Organic Field-Effect Transistors Based on Bilayer Polymer Dielectrics. *Appl. Phys. Lett.* **2013**, *103* (13).

(31) Chan, E. W. C.; Sun, X.; Travas-Sejdic, J. Recent Progress and Future Prospects in Transient Polymer Electronics. *Macromolecules* **2023**, *56* (11), 3755–3773.

https://doi.org/10.1021/acs.macromol.3c00254.

(32) Kenry; Liu, B. Recent Advances in Biodegradable Conducting Polymers and Their Biomedical Applications. *Biomacromolecules* **2018**, *19* (6), 1783–1803.

(33) Guimard, N. K. E.; Sessler, J. L.; Schmidt, C. E. Toward a Biocompatible and Biodegradable Copolymer Incorporating Electroactive Oligothiophene Units. *Macromolecules* **2009**, *42* (2), 502–511. https://doi.org/10.1021/ma8019859.

(34) Guo, B.; Finne-Wistrand, A.; Albertsson, A. C. Enhanced Electrical Conductivity by Macromolecular Architecture: Hyperbranched Electroactive and Degradable Block Copolymers Based on Poly(ε-Caprolactone) and Aniline Pentamer. *Macromolecules* **2010**, *43* (10), 4472–4480. https://doi.org/10.1021/ma100530k.

(35) Chakraborty, D.; Plajer, A. J. Recent Advances in Polyimine Chemistry: Synthesis, Functional Design, and Degradation. *J. Polym. Sci.* **2025**, 1–11. https://doi.org/10.1002/pol.20241199.

(36) Uva, A.; Kim, Y.; Michailovich, S.; Hsu, N. S. Y.; Bain, D. C.; Huang, S. H.; Musser, A. J.; Tran, H. Impact of Imine Bonds on the Electronic Properties of Degradable Carotenoid-Based Conjugated Polymers. *Polym. Chem.* **2025**, *16* (24), 2817–2828. https://doi.org/10.1039/d5py00235d.

(37) Tran, H.; Nikzad, S.; Chiong, J. A.; Schuster, N. J.; Peña-Alcántara, A. E.; Feig, V. R.; Zheng, Y.-Q.; Bao, Z. Modular Synthesis of Fully Degradable Imine-Based Semiconducting p-Type and n-Type Polymers. *Chem. Mater.* **2021**, *33* (18), 7465–7474.

(38) Zade, S. S.; Zamoshchik, N.; Bendikov, M. From Short Conjugated Oligomers to

Conjugated Polymers. Lessons from Studies on Long Conjugated Oligomers. *Acc. Chem. Res.* **2011**, *44* (1), 14–24. https://doi.org/10.1021/ar1000555.

(39) Hsu, N. S. Y.; Lin, A.; Uva, A.; Huang, S. H.; Tran, H. Direct Arylation Polymerization of Degradable Imine-Based Conjugated Polymers. *Macromolecules* **2023**, *56* (21), 8947–8955.

(40) Kotewicz, K.; Franco, L. R.; Araujo, M.; Wang, E. Acidochromic Behaviors of Indacenodithiophene-Based Conjugated Polymers Containing Azo, Imine, and Vinyl Bonds. *Macromolecules* **2025**, *58* (5), 2719–2729. https://doi.org/10.1021/acs.macromol.4c02700.

(41) David, J.; Weiter, M.; Vala, M.; Vyňuchal, J.; Kučerík, J. Stability and Structural Aspects of Diketopyrrolopyrrole Pigment and Its N-Alkyl Derivatives. *Dye. Pigment.* **2011**, *89* (2), 137–143. https://doi.org/10.1016/j.dyepig.2010.10.001.

(42) Liu, Q.; Bottle, S. E.; Sonar, P. Developments of Diketopyrrolopyrrole-Dye-Based Organic Semiconductors for a Wide Range of Applications in Electronics. *Adv. Mater.* **2020**, *32* (4), 1–46. https://doi.org/10.1002/adma.201903882.

(43) Chiong, J. A.; Zheng, Y.; Zhang, S.; Ma, G.; Wu, Y.; Ngaruka, G.; Lin, Y.; Gu, X.; Bao, Z. Impact of Molecular Design on Degradation Lifetimes of Degradable Imine-Based Semiconducting Polymers. *J. Am. Chem. Soc.* **2022**, *144* (8), 3717–3726. https://doi.org/10.1021/jacs.1c12845.

(44) Mei, J.; Bao, Z. Side Chain Engineering in Solution-Processable Conjugated Polymers. *Chem. Mater.* **2014**, *26* (1), 604–615. https://doi.org/10.1021/cm4020805.

(45) Yang, Y.; Liu, Z.; Zhang, G.; Zhang, X.; Zhang, D. The Effects of Side Chains on the Charge Mobilities and Functionalities of Semiconducting Conjugated Polymers beyond Solubilities. *Adv. Mater.* **2019**, *31* (46), 1–32. https://doi.org/10.1002/adma.201903104.

(46) Mooney, M.; Nyayachavadi, A.; Rondeau-Gagné, S. Eco-Friendly Semiconducting Polymers: From Greener Synthesis to Greener Processability. *J. Mater. Chem. C* **2020**, *8* (42), 14645–14664.

(47) Voskerician, G.; Shawgo, R. S.; Hiltner, P. A.; Anderson, J. M.; Cima, M. J.; Langer, R. In Vivo Inflammatory and Wound Healing Effects of Gold Electrode Voltammetry for MEMS Micro-Reservoir Drug Delivery Device. *IEEE Trans. Biomed. Eng.* **2004**, *51* (4), 627–635. https://doi.org/10.1109/TBME.2003.821034.

(48) Wilson, G. S.; Hu, Y. Enzyme-Based Biosensors for in Vivo Measurements. *Chem. Rev.* **2000**, *100* (7), 2693–2704. https://doi.org/10.1021/cr990003y.

(49) Peng, M.; Wang, J.; Li, Z.; Ren, G.; Li, K.; Gu, C.; Lin, Y. Three-Dimensional Flexible and Stretchable Gold Foam Scaffold for Real-Time Electrochemical Sensing in Cells and in Vivo. *Talanta* **2023**, *253*, 123891. https://doi.org/https://doi.org/10.1016/j.talanta.2022.123891.

(50) Edelman, E. R.; Seifert, P.; Groothuis, A.; Morss, A.; Bornstein, D.; Rogers, C. Gold-Coated NIR Stents in Porcine Coronary Arteries. *Circulation* **2001**, *103* (3), 429–434.

(51) Voskerician, G.; Shive, M. S.; Shawgo, R. S.; Von Recum, H.; Anderson, J. M.; Cima, M. J.; Langer, R. Biocompatibility and Biofouling of MEMS Drug Delivery Devices. *Biomaterials* **2003**, *24* (11), 1959–1967.

(52) Ali, M.; Ewenike, R. B.; Manion, J. G.; Lessard, B. H. Two Is Better than One: How the Addition of Multiple Biodegradable Polymers Can Improve Organic Thin-Film Transistor Performance. *ACS Appl. Mater. Interfaces* **2025**, *17* (1), 1734–1742.

(53) Manion, J.; Lessard, B. H. High-Throughput Characterization Is Key to Report Reliable Organic Thin-Film Transistor Performance. *Nat. Rev. Mater.* **2024**, *9* (6), 377–378. https://doi.org/10.1038/s41578-024-00689-8.

(54) Hemmerle, A.; Aubert, N.; Moreno, T.; Kékicheff, P.; Heinrich, B.; Spagnoli, S.; Goldmann, M.; Ciatto, G.; Fontaine, P. Opportunities and New Developments for the Study of Surfaces and Interfaces in Soft Condensed Matter at the SIRIUS Beamline of Synchrotron SOLEIL. *Synchrotron Radiat.* **2024**, *31* (1), 162–176.

(55) Jiang, Z. GIXSGUI: A MATLAB Toolbox for Grazing-Incidence X-Ray Scattering Data Visualization and Reduction, and Indexing of Buried Three-Dimensional Periodic Nanostructured Films. *Appl. Crystallogr.* **2015**, *48* (3), 917–926.

(56) Carvalho, J. R. G.; Conde, G.; Antonioli, M. L.; Dias, P. P.; Vasconcelos, R. O.; Taboga, S. R.; Canola, P. A.; Chinelatto, M. A.; Pereira, G. T.; Ferraz, G. C. Biocompatibility and Biodegradation of Poly (Lactic Acid)(PLA) and an Immiscible PLA/Poly (ε-Caprolactone)(PCL) Blend Compatibilized by Poly (ε-Caprolactone-b-Tetrahydrofuran) Implanted in Horses. *Polym. J.* **2020**, *52* (6), 629–643.

(57) Silva, C. C.; Thomazini, D.; Pinheiro, A. G.; Aranha, N.; Figueiro, S. D.; Góes, J. C.; Sombra, A. S. B. Collagen–Hydroxyapatite Films: Piezoelectric Properties. *Mater. Sci. Eng. B* **2001**, *86* (3), 210–218.

(58) Ortiz, R. P.; Facchetti, A.; Marks, T. J. High-k Organic, Inorganic, and Hybrid Dielectrics

for Low-Voltage Organic Field-Effect Transistors. *Chem. Rev.* **2010**, *110* (1), 205–239.

(59) Amin, E. M.; Karmakar, N. C.; Winther-Jensen, B. Polyvinyl-Alcohol (PVA)-Based RF Humidity Sensor in Microwave Frequency. *Prog. Electromagn. Res. B* **2013**, *54*, 149–166.

(60) Tsai, T.; Chang, J.; Wen, T.; Guo, T. Manipulating the Hysteresis in Poly (Vinyl Alcohol)-Dielectric Organic Field-Effect Transistors Toward Memory Elements. *Adv. Funct. Mater.* **2013**, *23* (34), 4206–4214.

(61) Tousignant, M. N.; Rice, N. A.; Peltekoff, A.; Sundaresan, C.; Miao, C.; Hamad, W. Y.; Lessard, B. H. Improving Thin-Film Properties of Poly (Vinyl Alcohol) by the Addition of Low-Weight Percentages of Cellulose Nanocrystals. *Langmuir* **2020**, *36* (13), 3550–3557.

(62) KV, S. B.; Rama Teja, A. S.; Srinivas Babu, N.; Arunachalam, V.; Maheswar, C. V. S.; Reddy, A. Methods of Decontamination of Toluene Di-Isocyanate (TDI) Spills and Leftovers. *Res. J. Chem. Sci. ISSN 2231*, 606X.

(63) Tousignant, M. N.; Rice, N. A.; Niskanen, J.; Richard, C. M.; Ritaine, D.; Adronov, A.; Lessard, B. H. High Performance Organic Electronic Devices Based on a Green Hybrid Dielectric. *Adv. Electron. Mater.* **2021**, *7* (10), 2100700.

(64) Grau, G.; Subramanian, V. Dimensional Scaling of High-Speed Printed Organic Transistors Enabling High-Frequency Operation. *Flex. Print. Electron.* **2020**, *5* (1), 14013.

(65) Khan, Y.; Thielens, A.; Muin, S.; Ting, J.; Baumbauer, C.; Arias, A. C. A New Frontier of Printed Electronics: Flexible Hybrid Electronics. *Adv. Mater.* **2020**, *32* (15), 1905279.

(66) Subbarao, N. V. V; Mandal, S.; Gedda, M.; Iyer, P. K.; Goswami, D. K. Effect of Temperature on Hysteresis of Dipolar Dielectric Layer Based Organic Field-Effect

Transistors: A Temperature Sensing Mechanism. *Sensors Actuators A Phys.* **2018**, *269*, 491–499.

(67) Brixi, S.; Radford, C. L.; Tousignant, M. N.; Peltekoff, A. J.; Manion, J. G.; Kelly, T. L.; Lessard, B. H. Poly (Ionic Liquid) Gating Materials for High-Performance Organic Thin-Film Transistors: The Role of Block Copolymer Self-Assembly at the Semiconductor Interface. *ACS Appl. Mater. Interfaces* **2022**, *14* (35), 40361–40370.

(68) Hadidi, M.; Jafarzadeh, S.; Forough, M.; Garavand, F.; Alizadeh, S.; Salehabadi, A.; Khaneghah, A. M.; Jafari, S. M. Plant Protein-Based Food Packaging Films; Recent Advances in Fabrication, Characterization, and Applications. *Trends Food Sci. Technol.* **2022**, *120*, 154–173.

(69) Zhang, H.; Zhang, F.; Sun, J.; Zhang, M.; Hu, Y.; Lou, Z.; Hou, Y.; Teng, F. Solution-Processed Organic Field-Effect Transistors with Cross-Linked Poly (4-Vinylphenol)/Polyvinyl Alcohol Bilayer Dielectrics. *Appl. Surf. Sci.* **2019**, *478*, 699–707.

(70) Nawaz, A.; Hümmelgen, I. A. Poly (Vinyl Alcohol) Gate Dielectric in Organic Field-Effect Transistors. *J. Mater. Sci. Mater. Electron.* **2019**, *30* (6), 5299–5326.

(71) Sun, Y.; Liu, Y.; Wang, Y.; Di, C.; Wu, W.; Yu, G. Polymer Gate Dielectrics with Self-Assembled Monolayers for High-Mobility Organic Thin-Film Transistors Based on Copper Phthalocyanine. *Appl. Phys. A* **2009**, *95*, 777–780.

(72) Puigdollers, J.; Voz, C.; Fonrodona, M.; Cheylan, S.; Stella, M.; Andreu, J.; Vetter, M.; Alcubilla, R. Copper Phthalocyanine Thin-Film Transistors with Polymeric Gate Dielectric. *J. Non. Cryst. Solids* **2006**, *352* (9–20), 1778–1782.

(73) Vasimalla, S.; Subbarao, N. V. V; Gedda, M.; Goswami, D. K.; Iyer, P. K. Effects of Dielectric Material, HMDS Layer, and Channel Length on the Performance of the Perylenediimide-Based Organic Field-Effect Transistors. *ACS omega* **2017**, *2* (6), 2552–2560.

(74) Park, J.; Kim, S.; Bae, J.; Cho, H.; Udaya Mohanan, K.; Baikie, I. D.; Kymissis, I.; Kim, C.-H. Inseparability between Charge-Injection Barrier and out-of-Plane Mobility in Staggered Thin-Film Transistors. *Appl. Phys. Lett.* **2025**, *127* (11).

(75) Lee, H.; Lim, K.-G.; Kim, C.-H. Vertical Organic Transistors with a Permeable Base: From Fundamentals to Performance Prediction. *J. Mater. Chem. C* **2023**, *11* (16), 5422–5430.

(76) Bae, J.; Park, S.; Jung, H.; Ko, E.-H.; Kymissis, I.; Kim, C.-H. Polymer Field-Effect Transistors with Inkjet-Printed Silver Electrodes: From Device Fabrication to Circuit Simulation. *J. Mater. Sci. Mater. Electron.* **2024**, *35* (2), 185.

(77) Kim, Y. E.; Jung, H.; Park, J. H.; Yoo, H.; Kim, C.-H. Energy Gap and Orbital Mixing in DNTT/PTCDI-C8 Heterostructure. *Org. Electron.* **2025**, *138*, 107195.

(78) Lee, H.; Kim, Y. E.; Bae, J.; Jung, S.; Sporea, R. A.; Kim, C.-H. High-Performance Organic Source-Gated Transistors Enabled by the Indium-Tin Oxide–Diketopyrrolopyrrole Polymer Interface. *ACS Appl. Mater. Interfaces* **2023**, *15* (8), 10918–10925.

(79) Müller, C.; Aghamohammadi, M.; Himmelberger, S.; Sonar, P.; Garriga, M.; Salleo, A.; Campoy-Quiles, M. One-Step Macroscopic Alignment of Conjugated Polymer Systems by Epitaxial Crystallization during Spin-Coating. *Adv. Funct. Mater.* **2013**, *23* (19), 2368–2377. https://doi.org/10.1002/adfm.201202983.

(80) Schulz, G. L.; Ludwigs, S. Controlled Crystallization of Conjugated Polymer Films from Solution and Solvent Vapor for Polymer Electronics. *Adv. Funct. Mater.* **2017**, *27* (1). https://doi.org/10.1002/adfm.201603083.

(81) Yu, S. H.; Park, K. H.; Kim, Y.-H.; Chung, D. S.; Kwon, S.-K. Fine Molecular Tuning of Diketopyrrolopyrrole-Based Polymer Semiconductors for Efficient Charge Transport: Effects of Intramolecular Conjugation Structure. *Macromolecules* **2017**, *50* (11), 4227–4234.

(82) Mukhopadhyay, T.; Puttaraju, B.; Roy, P.; Dasgupta, J.; Meyer, A.; Rudnick, A.; Tscheuschner, S.; Kahle, F.; Köhler, A.; Patil, S. Facile Synthesis and Chain-Length Dependence of the Optical and Structural Properties of Diketopyrrolopyrrole-Based Oligomers. *Chem. Eur. J.* **2017**, *23* (55), 13718–13723.

(83) McPherson, T. E. Characterizing the Morphology of Solvent Annealed PCBM/P3HT Bilayers Using GIXRD and Raman Spectroscopy. M.S. Thesis, University of Tennessee, Knoxville, 2014.

(84) Cranston, R. R.; Lanosky, T. D.; Ewenike, R.; Mckillop, S.; King, B.; Lessard, B. H. Polarized Raman Microscopy to Image Microstructure Changes in Silicon Phthalocyanine Thin-Films. *Small Sci.* **2024**, 2300350.

(85) Gao, Y.; Bai, J.; Sui, Y.; Han, Y.; Deng, Y.; Tian, H.; Geng, Y.; Wang, F. High Mobility Ambipolar Diketopyrrolopyrrole-Based Conjugated Polymers Synthesized via Direct Arylation Polycondensation: Influence of Thiophene Moieties and Side Chains. *Macromolecules* **2018**, *51* (21), 8752–8760. https://doi.org/10.1021/acs.macromol.8b01112.

(86) Opoku, H.; Nketia-Yawson, B.; Shin, E. S.; Noh, Y. Y. Organic Field-Effect Transistors Processed by an Environmentally Friendly Non-Halogenated Solvent Blend. *J. Mater. Chem. C* **2018**, *6* (3), 661–667. https://doi.org/10.1039/c7tc04823h.

(87) Kim, M.; Ryu, S. U.; Park, S. A.; Choi, K.; Kim, T.; Chung, D.; Park, T. Donor–Acceptor-Conjugated Polymer for High-Performance Organic Field-Effect Transistors: A Progress Report. *Adv. Funct. Mater.* **2020**, *30* (20), 1–25. https://doi.org/10.1002/adfm.201904545.

(88) Ma, H.; Yip, H. L.; Huang, F.; Jen, A. K. Y. Interface Engineering for Organic Electronics. *Adv. Funct. Mater.* **2010**, *20* (9), 1371–1388. https://doi.org/10.1002/adfm.200902236.

(89) Hendsbee, A. D.; Li, Y. Performance Comparisons of Polymer Semiconductors Synthesized by Direct (Hetero)Arylation Polymerization (DHAP) and Conventional Methods for Organic Thin Film Transistors and Organic Photovoltaics. *Molecules* **2018**, *23* (6). https://doi.org/10.3390/molecules23061255.

(90) Charland-Martin, A.; Collier, G. S. Understanding Degradation Dynamics of Azomethine-Containing Conjugated Polymers. *Macromolecules* **2024**, *57* (13), 6146–6155. https://doi.org/10.1021/acs.macromol.4c01168.

(91) Sims, M. B.; Patel, K. Y.; Bhatta, M.; Mukherjee, S.; Sumerlin, B. S. Harnessing Imine Diversity to Tune Hyperbranched Polymer Degradation. *Macromolecules* **2018**, *51* (2), 356–363. https://doi.org/10.1021/acs.macromol.7b02323.

(92) Jin, H.; Kim, K.; Park, S.; Rhee, J. H.; Ahn, H.; Kim, D. J.; Kim, K.; Noh, J. H.; Kim, T. S.; Shin, E. Y.; Son, H. J. Chemically Recyclable Conjugated Polymer and One-Shot Preparation of Thermally Stable and Efficient Bulk-Heterojunction from Recycled Monomer. *Adv. Funct. Mater.* **2023**, *33* (47), 1–11.

https://doi.org/10.1002/adfm.202304930.

(93) Ali, M.; Hoseyni, S. M.; Das, R.; Awais, M.; Basdogan, I.; Beker, L. A Flexible and Biodegradable Piezoelectric-Based Wearable Sensor for Non-Invasive Monitoring of Dynamic Human Motions and Physiological Signals. *Adv. Mater. Technol.* 2023, 8, 2300347.

(94) Martinelli, A.; Matic, A.; Jacobsson, P.; Börjesson, L.; Navarra, M. A.; Fernicola, A.; Panero, S.; Scrosati, B. Structural Analysis of PVA-Based Proton Conducting Membranes. *Solid State Ionics* **2006**, *177* (26–32), 2431–2435.

(95) Curry, E. J.; Ke, K.; Chorsi, M. T.; Wrobel, K. S.; Miller III, A. N.; Patel, A.; Kim, I.; Feng, J.; Yue, L.; Wu, Q. Biodegradable Piezoelectric Force Sensor. *Proc. Natl. Acad. Sci.* **2018**, *115* (5), 909–914.

(96) Bathaei, M. J.; Singh, R.; Mirzajani, H.; Istif, E.; Akhtar, M. J.; Abbasiasl, T.; Beker, L. Photolithography-Based Microfabrication of Biodegradable Flexible and Stretchable Sensors. *Adv. Mater.* **2023**, *35* (6), 2207081.

(97) Bi, H.; Wang, Z.; Sheng, H.; Shang, M.; Hu, J.; Guo, C.; Wan, D.; Li, F.; Yue, Q.; Su, Q. A Flexible Bioresorbable Implantable Sensor for Wireless Dynamic Monitoring of H2O2 Enabled by Pt-Decorated MoO3-x Nanozyme. *Small* **2025**, *21* (48), e08861.

(98) Öztürk, M. C.; Misra, V. *Electr. Eng. Handb.* **2004**, 109.

(99) Itagaki, M.; Suzuki, S.; Shitanda, I.; Watanabe, K. Electrochemical Impedance and Complex Capacitance to Interpret Electrochemical Capacitor. *Electrochemistry* **2007**, 75 (8), 649-655.

Chapter 5: Conclusion and Recommendations for Future Work

4.7 Overall Conclusion

The accumulation of e-waste and the growing demand for environmentally sustainable technologies make the development of fully degradable, high-performance OTFTs an important area of continued research. Ideally, these devices should combine strong electrical performance with materials that are non-toxic, biodegradable, and capable of controlled, multi-step disassembly, while also demonstrating functional relevance beyond simple proof-of-concept. This thesis explored strategies for designing sustainable OTFTs by optimizing biodegradable polymer dielectrics and substrates, tuning the semiconductor-dielectric interface, and engineering controlled degradation pathways.

Chapter 2 reported the development of a cytocompatible and disintegrable n-type OTFT device, integrating a fluorinated silicon phthalocyanine semiconductor with a bilayer PVA/PCL dielectric on a PLA substrate. I demonstrated that annealing temperature and gate electrode surface chemistry were critical to obtaining functional devices on the biodegradable substrate, and the resulting OTFTs showed a substantial V_T reduction relative to conventional SiO_2 dielectrics (from 12.7 V to −0.97 V) while maintaining comparable μ. I further demonstrated that these devices fully disintegrated in phosphate-buffered saline within a month and that the degradation products did not affect the viability of cultured fibroblasts, confirming their cytocompatibility. This established that fully cytocompatible, disintegrable, low-voltage n-type OTFTs are achievable using inexpensive, commercially available degradable polymers.

Chapter 3 investigated a blending strategy to reduce the amount of active semiconducting material required for functional OTFTs. I demonstrated that combining biodegradable PCL and

PLA additives with a diketopyrrolopyrrole-based semiconducting polymer could reduce active semiconductor loading by roughly 70–80% while maintaining or improving device performance. This establishes that meaningful, commercially relevant reductions in high-value semiconducting material are achievable without sacrificing OTFT function, an important consideration for scalable, cost-effective green electronics.

Chapter 4 built on the foundation of Chapter 2 by addressing two limitations of the earlier approach: the semiconductor employed in Chapter 2 was not fully degradable, and the assembled devices disintegrated as a single system, preventing the efficient separation and recovery of individual functional materials. To resolve this, I designed a p-type OTFT using an imine-linked degradable semiconducting polymer integrated with a PVA/UV-crosslinked-PCL bilayer dielectric and PLA substrate, engineered so each layer responded to a distinct degradation trigger. This bilayer dielectric again substantially reduced V_T (from −16.1 V to −2 V relative to OTS-treated SiO_2) while preserving comparable μ. I then demonstrated sequential, dual-trigger degradation: the semiconductor and dielectric dissolved under acidic conditions, while the PLA substrate degraded separately under basic conditions, leaving only recoverable gold micro/nanoparticles behind. This tiered degradation strategy enables selective separation and potential material recovery, offering a practical pathway toward environmentally responsible end-of-life management of transient electronics.

To summarize, this thesis demonstrates that degradable, commercially available polymers can be systematically combined and engineered through blending, bilayer stacking, and trigger-specific chemistry to fabricate OTFTs that match or exceed the performance of conventional devices while enabling controlled, multi-step degradation and material recovery. These studies show that active semiconductor loading can be substantially reduced through polymer blending,

that bilayer dielectrics can simultaneously lower V_T and improve device stability and biocompatibility, and that layer-specific degradation triggers can be used to engineer sequential, selective degradation pathways for improved end-of-life material recovery. Together, these contributions advance the design approach available for sustainable, high-performance, and fully degradable organic electronics.

4.8 Recommendations for Future Work

The work presented in this thesis establishes a foundation for the development of sustainable organic thin-film transistors by addressing several critical challenges, including the use of biodegradable materials, low-voltage operation, improved semiconductor efficiency, cytocompatibility, and controlled end-of-life degradation. While these advances represent important progress toward environmentally responsible organic electronics, several opportunities remain to further improve device performance, scalability, and sustainability.

The semiconductor-loading reduction strategy developed in Chapter 3 was demonstrated using a single diketopyrrolopyrrole-based semiconducting polymer (DPP2T) blended with PLA and PCL. Future work should test whether this blending approach generalizes to other conjugated polymer semiconductors, particularly n-type materials, to determine whether the same PLA-PCL ratio dependence and crystallinity enhancement hold more broadly. In addition, the devices in Chapter 3 showed considerable batch-to-batch variability in μ, particularly at intermediate PLA-PCL ratios. Future studies should investigate the sources of this variability, such as solvent selection, blend mixing time, or spin-coating parameters, to improve reproducibility.

One of the primary directions for future research is the development of high-performance, fully sustainable semiconductors. Although Chapter 4 demonstrated the feasibility of employing a

degradable conjugated polymer while maintaining competitive electrical characteristics,[1] the library of degradable organic semiconductors remains limited compared to conventional high-μ materials. Future efforts should therefore focus on designing conjugated polymers that simultaneously exhibit high charge-carrier μ, long-term operational stability, solution processability, and predictable degradation pathways. Achieving these characteristics without introducing complex synthetic routes will be essential for large-scale implementation.

Another important research direction involves the development of fully sustainable device architectures. Although the active materials employed throughout this thesis were selected with sustainability in mind, the devices still relied on vacuum-deposited gold electrodes.[1–3] Future work should investigate biodegradable, recyclable, or transiently conductive materials that can replace noble metals while maintaining low contact resistance and long-term electrical reliability. Such developments would move OTFTs closer to completely sustainable electronic systems.

The PVA/PCL-based bilayer dielectric devices developed in Chapters 2 and 4 substantially reduced V_T relative to conventional SiO_2 dielectrics, but this came with trade-offs. Devices in both chapters exhibited relatively low $I_{on/off}$ and, in Chapter 2, high off-currents attributed to the ambipolar nature of the F_{10}-SiPc semiconductor. Future work should focus on further dielectric or interface engineering to suppress this leakage and improve $I_{on/off}$ without sacrificing the low-voltage operation achieved in this work. Additionally, both bilayer dielectric systems exhibited measurable hysteresis, which was attributed to slow dipolar polarization and charge trapping associated with the hydroxyl groups in PVA. Future studies should explore alternative biodegradable dielectric materials or surface treatments with reduced hydroxyl content, or further refine the UV-PCL interlayer, to minimize this hysteresis while preserving the high dielectric constant PVA provides (**Figure 5.1**).

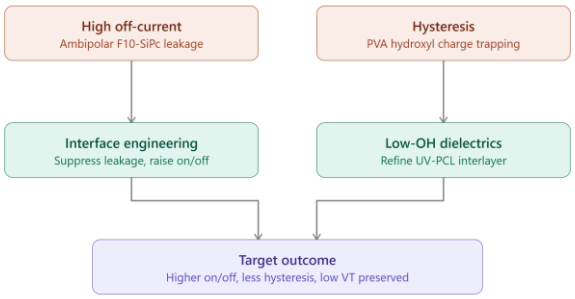


Figure 5.1. Proposed future research directions for addressing the current on/off ratio and hysteresis trade-offs observed in the PVA/PCL bilayer dielectric devices.

The devices developed in this thesis were characterized individually rather than as part of functional circuits. Since Chapter 2 demonstrated an n-type OTFT and Chapter 4 demonstrated a fully sustainable p-type OTFT, a natural next step is to combine both device types into complementary logic circuits **(Figure 5.2)** or other functional building blocks to evaluate whether the performance and degradation characteristics established here translate to circuit-level operation.

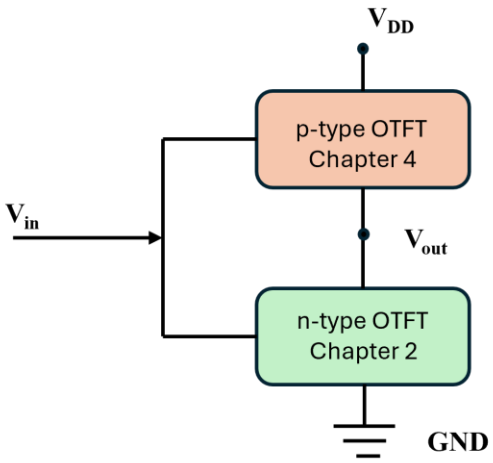


Figure 5.2. Proposed complementary inverter circuit combining the n-type OTFT developed in Chapter 2 with the p-type OTFT developed in Chapter 4, as a first step toward evaluating circuit-level performance and degradation.

The degradation studies presented in this thesis primarily focused on demonstrating controlled disintegration and sequential degradation under laboratory conditions. Future investigations should expand these studies to include real-world degradation environments, such as soil, compost, freshwater, seawater, and biological environments **(Figure 5.3).** Evaluating degradation kinetics, degradation products, and environmental impacts under realistic disposal conditions will provide a more comprehensive understanding of the complete life cycle of sustainable electronic devices.

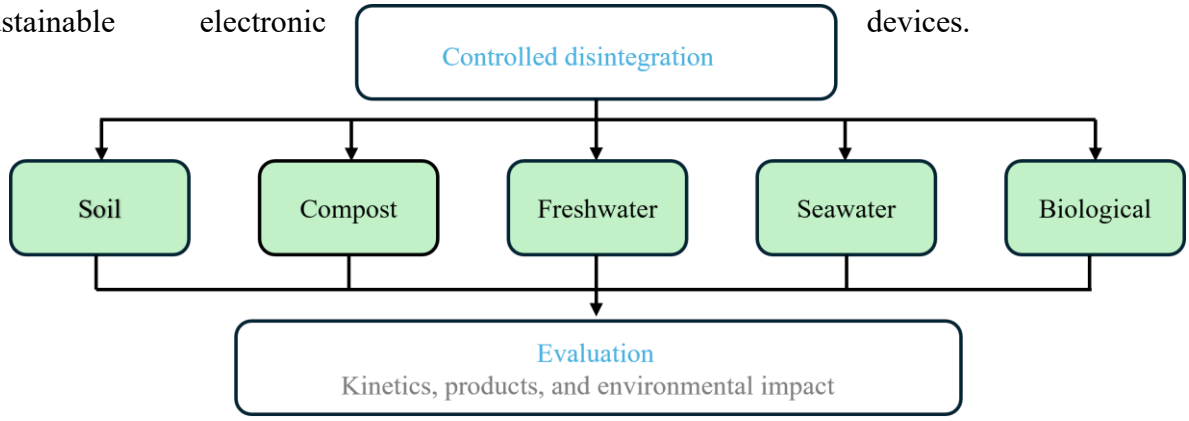


Figure 5.3. Future expansion of degradation analyses from laboratory conditions to real-world environments (soil, compost, freshwater, seawater, and biological systems), with degradation kinetics, degradation products, and environmental impact evaluated across each.

The fully sustainable OTFT developed in Chapter 4, integrating a biodegradable substrate, a degradable semiconductor, and a green dielectric, establishes a compelling and complete materials platform that is well-positioned for translation into next-generation gas and vapor sensing applications. An immediate extension of this work would be the systematic evaluation of the sustainable OTFT as a gas sensor by exposing the fabricated devices to a range of analyte vapors of environmental and industrial relevance, including ammonia and carbon dioxide, quantifying the sensor response in terms of sensitivity, limit of detection, response time, and

recovery time. Given that organic semiconductor thin films are intrinsically sensitive to molecular interactions at their surface (**Figure 5.4**),[4–10] it is anticipated that the sustainable OTFT platform could deliver sensing performance competitive with conventional non-degradable OTFT sensors reported in the literature. The inherent flexibility and mechanical conformability of the fully sustainable device stack further open the door to wearable[11] and disposable gas-sensing formats, such as skin-worn environmental monitors,[11] where the sensor's end-of-life degradability represents a transformative advantage over conventional flexible electronics, which contribute to growing e-waste. Looking further ahead, integrating the sustainable OTFT sensor into a fully printed, roll-to-roll-fabricated sensor array, combined with wireless data transmission, would represent a significant step toward a genuinely sustainable, low-cost, and scalable sensing platform suitable for deployment in resource-limited or remote environmental monitoring scenarios. Collectively, these directions position the sustainable OTFT developed in this thesis not merely as a proof of concept in green materials design, but as the foundation for a new generation of environmentally responsible sensing technologies.

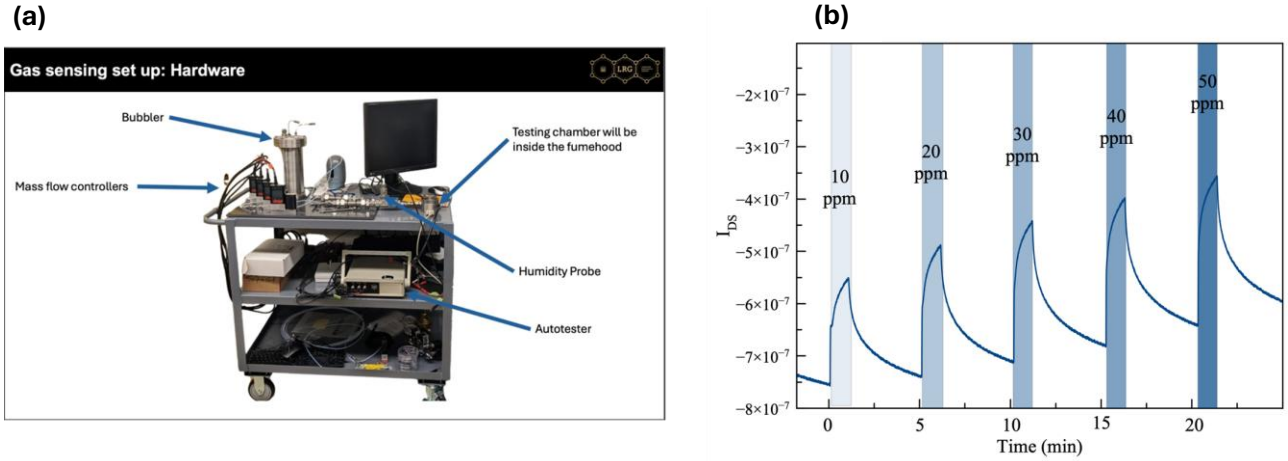
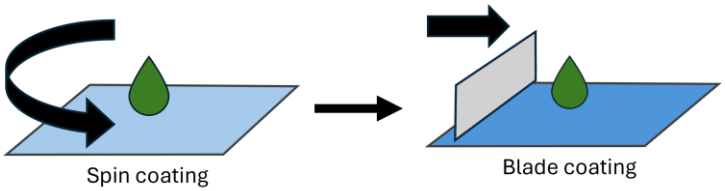


Figure 5.4. (a) Custom-built gas-sensing setup used to evaluate the sensing performance of the OTFTs under controlled analyte exposure.[12] (b) Preliminary sensing results from OTFTs under ammonia exposure fabricated using P(DPP-TIT) semiconductor and SiO_2 dielectric.

Building on the sustainable blending strategy established in Chapter 3, future work should extend this approach toward a scalable, industry-compatible blade-coating deposition method to evaluate the viability of DPP2T/PLA-PCL blend OTFTs beyond laboratory-scale spin coating. This would involve systematically varying semiconductor blend concentration, blade speed, and substrate temperature to identify a suitable processing window for consistent film formation. Establishing this window would demonstrate whether OTFTs made sustainable with DPP2T/PLA-PCL are not restricted to bench-scale fabrication but are instead amenable to higher-throughput deposition routes, a critical step toward their practical deployment in printable, flexible, and sustainable electronics.



Overall, the research presented in this thesis demonstrates that sustainability and high-performance organic electronics are not mutually exclusive objectives. Continued advances in biodegradable materials, scalable processing, recyclable device architectures, and environmentally responsible design are expected to accelerate the transition of organic electronics from proof-of-concept laboratory devices toward practical sustainable technologies.

References

(1) Ali, M.; Nyayachavadi, A.; Pascual, S. G.; Park, J.; Manion, J. G.; Hemmerle, A.; Kim, C.-H.; Lessard, B. H. Degradation by Design: Sequentially Degradable Organic Transistors for Sustainable Electronics. *Soft Sci. 2026, 6, 42.*

(2) Ali, M.; Ronnasi, B.; Ourabi, M.; Park, J. H.; St-Pierre, J.-P.; Kim, C.-H.; Lessard, B. H. Cytocompatible, Disintegrable, Low-Voltage Operation n-Type Organic Thin Film Transistors. *Mater. Adv.* **2025**, *6* (2), 557–568.

(3) Ali, M.; Ewenike, R. B.; Manion, J. G.; Lessard, B. H. Two Is Better than One: How the Addition of Multiple Biodegradable Polymers Can Improve Organic Thin-Film Transistor Performance. *ACS Appl. Mater. Interfaces* **2025**, *17* (1), 1734–1742.

(4) King, B.; Lessard, B. H. Review of Recent Advances and Sensing Mechanisms in Solid-State Organic Thin-Film Transistor (OTFT) Sensors. *J. Mater. Chem. C* **2024**.

(5) Jeong, J. W.; Lee, Y. D.; Kim, Y. M.; Park, Y. W.; Choi, J. H.; Park, T. H.; Soo, C. D.; Won, S. M.; Han, I. K.; Ju, B. K. The Response Characteristics of a Gas Sensor Based on Poly-3-Hexylithiophene Thin-Film Transistors. *Sensors Actuators B Chem.* **2010**, *146* (1), 40–45.

(6) Nketia-Yawson, B.; Noh, Y.-Y. Organic Thin Film Transistor with Conjugated Polymers for Highly Sensitive Gas Sensors. *Macromol. Res.* **2017**, *25* (6), 489–495.

(7) Mukhopadhyaya, T.; Wagner, J. S.; Fan, H.; Katz, H. E. Design and Synthesis of Air-Stable p-Channel-Conjugated Polymers for High Signal-to-Drift Nitrogen Dioxide and Ammonia Sensing. *ACS Appl. Mater. Interfaces* **2020**, *12* (19), 21974–21984.

(8) Tang, Y.; Ma, Q.; Lu, J.; Jiang, X.; Huang, L.; Chi, L.; Sun, L.; Wang, B. Nanofiber-Textured Organic Semiconductor Films for Field-Effect Ammonia Sensors. *IEEE Open J. Nanotechnol.* **2022**, *3*, 116–123.

(9) Jeong, S.-H.; Lee, J. Y.; Lim, B.; Lee, J.; Noh, Y.-Y. Diketopyrrolopyrrole-Based Conjugated Polymer for Printed Organic Field-Effect Transistors and Gas Sensors. *Dye. Pigment.* **2017**, *140*, 244–249.

(10) Cheon, H. J.; An, T. K.; Kim, Y.-H. Diketopyrrolopyrrole (DPP)-Based Polymers and Their Organic Field-Effect Transistor Applications: A Review. *Macromol. Res.* **2022**, *30* (2), 71–84.

(11) Baek, S.; Jo, Y.; Lee, Y.; Kwon, J.; Jung, S. Design and Integration of Organic Printed Thin-Film Transistor-Based Soft Biosensors for Wearable Applications. *ACS Appl. Electron. Mater.* **2024**, *6* (11), 7657–7678.

(12) Gallardo-Pascual, S.; King, B.; Ganesh Moorthy, S.; Lessard, B. H. Gate Voltage Effect on Fluorinated and Non-Fluorinated Copper Phthalocyanine OTFT-Based Ammonia Sensors. *Sensors & Diagnostics* **2025**, *4* (11), 1006–1013.